Energie & Umwelt
Energy & Environment

328

Conductivity and Structure of Sputtered ZnO

Nicolas Sommer

Member of the Helmholtz Association

Conductivity and Structure of Sputtered ZnO:Al on Flat and Textured Substrates for Thin-Film Solar Cells

Nicolas Sommer

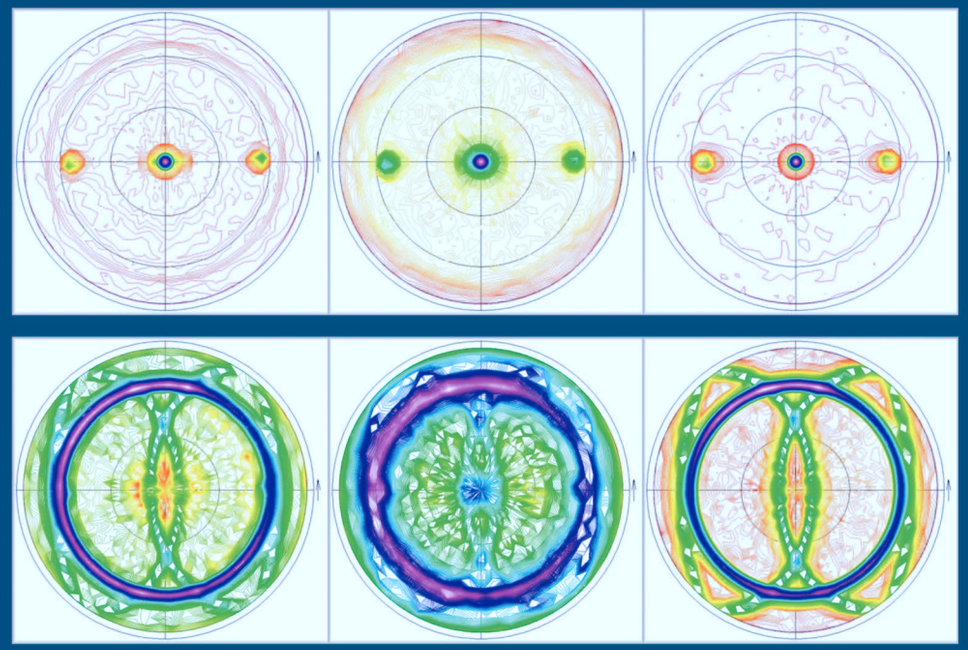

Energie & Umwelt / Energy & Environment
Band / Volume 328
ISBN 978-3-95806-156-9

JÜLICH
FORSCHUNGSZENTRUM

Energie & Umwelt / Energy & Environment
Band / Volume 328
ISBN 978-3-95806-156-9

JÜLICH
FORSCHUNGSZENTRUM

Schriften des Forschungszentrums Jülich
Reihe Energie & Umwelt / Energy & Environment Band / Volume 328

Forschungszentrum Jülich GmbH
Institute of Energy and Climate Research
IEK-5 Photovoltaics

Conductivity and Structure of Sputtered ZnO:Al on Flat and Textured Substrates for Thin-Film Solar Cells

Nicolas Sommer

Schriften des Forschungszentrums Jülich
Reihe Energie & Umwelt / Energy & Environment Band / Volume 328

ISSN 1866-1793 ISBN 978-3-95806-156-9

Bibliographic information published by the Deutsche Nationalbibliothek.
The Deutsche Nationalbibliothek lists this publication in the Deutsche
Nationalbibliografie; detailed bibliographic data are available in the
Internet at http://dnb.d-nb.de.

Publisher and Distributor: Forschungszentrum Jülich GmbH
Zentralbibliothek
52425 Jülich
Tel: +49 2461 61-5368
Fax: +49 2461 61-6103
Email: zb-publikation@fz-juelich.de
www.fz-juelich.de/zb

Cover Design: Grafische Medien, Forschungszentrum Jülich GmbH

Printer: Grafische Medien, Forschungszentrum Jülich GmbH

Schriften des Forschungszentrums Jülich
Reihe Energie & Umwelt / Energy & Environment, Band / Volume 328

D 82 (Diss. RWTH Aachen University, 2016)

ISSN 1866-1793
ISBN 978-3-95806-156-9

The complete volume is freely available on the Internet on the Jülicher Open Access Server (JuSER)
at www.fz-juelich.de/zb/openaccess.

Abstract

Aluminum-doped zinc oxide (ZnO:Al) is a prominent representative of the material class denoted as transparent conductive oxides (TCO). TCOs feature electrical conductivity while being transparent in the visible range. These unique properties constitute the wide application of TCOs in opto-electronic devices. This work targets the application of TCOs for thin-film silicon and chalcopyrite-based solar cells. Generally, TCOs are deposited onto flat substrates. However, TCO growth on textured, light scattering substrates for thin-film silicon solar cells and on the rough chalcopyrite absorber also call for the optimization of TCO deposition on textured substrates. Therefore, the deposition of sputtered ZnO:Al on flat as well as on textured substrates is elaborated. The focus is the understanding and optimization of electrical conductivity accompanied by a detailed investigation of the material's structural properties.

On flat substrates, I propose a conductivity model that comprises three scattering mechanisms, namely ionized-impurity, electron-phonon, and grain boundary scattering. The prominent feature of the model is the analytical description of grain boundary scattering by field emission, i.e. quantum mechanical tunneling of electrons through potential barriers at grain boundaries. For this purpose, a theory of Stratton (R. Stratton, *Theory of Field Emission from Semiconductors*, Phys. Rev. **125** (1962), 67 - 82) is adapted to double Schottky barriers at grain boundaries. The conductivity model is applied to a wide range of literature data to show its applicability and explanatory power. After establishing the basic understanding of ZnO:Al conductivity, two optimization routes are presented. The first route allows for a reduction of deposition temperature by 100 °C without deteriorating conductivity, transparency, and etching morphology by means of a seed layer concept. Seed and subsequently grown bulk layers were deposited from ZnO:Al_2O_3 targets with 2 wt% and 1 wt% Al_2O_3, respectively. I investigated the effect of bulk and seed layer deposition temperature as well as seed layer thickness on electrical, optical, and structural properties of ZnO:Al films. The positive effect of the highly doped seed layer was attributed to the beneficial role of the dopant aluminum that induces a surfactant effect. Furthermore, the seed layer induced increase of tensile stress is explained on the basis of the grain boundary relaxation model. Finally, temperature-dependent conductivity measurements, optical fits, and etching characteristics revealed that seed

layers reduce grain boundary scattering. It is particularly compelling that smaller grains correlate with enhanced charge carrier mobility. The second optimization route elaborates the effect of post-deposition heat treatments on ZnO:Al films that boost or degrade ZnO:Al conductivity depending on whether or not a capping layer protects the ZnO:Al film. Raman, XRD, and temperature-dependent Hall effect measurements in conjunction with the newly developed conductivity model are used to analyze the annealing effects. The results provide evidence that annealing with capping layer induces decreased ionized impurity and grain boundary scattering while annealing without capping layer leads to an enhancement of both scattering mechanisms.

On textured substrates, ZnO:Al growth is challenging due to the occurrence of extended grain boundaries that reduce charge carrier mobility and damp heat stability. ZnO:Al deposition conditions and substrate morphology are investigated in order to optimize ZnO:Al conductivity and damp heat stability on textured substrates. I found optimized deposition conditions such that ZnO:Al charge carrier mobility on randomly textured glass and on flat reference substrates were similar. A qualitative model is proposed that explains the impact of various deposition conditions on the basis of grain orientation. ZnO:Al showed higher charge carrier mobility and damp heat stability on U-shaped than on V-shaped substrates. This observation is attributed to a lower number of extended grain boundaries on U-shaped in contrast to V-shaped substrates. To further the evaluation of various textures for ZnO:Al growth, a quantitative electrical simulation is developed to predict the suitability of textured substrates for the growth of ZnO:Al films. Indeed, the simulation may calculate ZnO:Al charge carrier mobility if calibrated for a particular deposition condition. Furthermore, evidence is provided that the charge carrier mobility is not only determined by the density of extended grain boundaries but also by their distribution.

Kurzfassung

Aluminium-dotiertes Zinkoxid (ZnO:Al) ist ein wichtiger Vertreter der Materialklasse der transparenten, leitfähigen Oxide (TCO). TCOs sind sowohl elektrisch leitfähig als auch transparent im sichtbaren Spektralbereich. Diese einzigartigen Eigenschaften begründen die breite Anwendung von TCOs im Bereich der optoelektronischen Bauelemente. Die vorliegende Arbeit zielt auf die Anwendung von TCOs in Silizium- und Chalcopyrit-basierten Dünnschichtsolarzellen. Im Regelfall werden TCOs auf flachen Substraten aufgebracht. Allerdings verlangt das TCO-Wachstum auf texturierten, lichtstreuenden Substraten für Silizium-basierte Dünnschichtsolarzellen und raue Chalcopyrit-Absorber zusätzlich nach der Optimierung der TCO-Deposition auf texturierten Substraten. Daher wird im Folgenden die Deposition von gesputtertem ZnO:Al sowohl auf flachen als auch auf texturierten Substraten erörtert. Der Fokus liegt auf dem Verständnis und der Optimierung der elektrischen Leitfähigkeit begleitet von einer detaillierten Untersuchung der Materialstruktur.

Auf flachen Substraten schlage ich ein Leitfähigkeitsmodell vor, das drei Streumechanismen umfasst: Streuung an ionisierten Störstellen, an Phononen und an Korngrenzen. Das besondere Merkmal des Modells ist die analytische Beschreibung der Korngrenzenstreuung durch Feldemission, d.h. durch das quantenmechanische Tunneln von Elektronen durch Potentialbarrieren an den Korngrenzen. Zu diesem Zweck wird eine Theorie von Stratton (R. Stratton, *Theory of Field Emission from Semiconductors*, Phys. Rev. **125** (1962), 67 - 82) für Doppel-Schottky Barrieren an Korngrenzen angepasst. Das Leitfähigkeitsmodell wird an einer großen Auswahl von Literaturdaten getestet, um seine Anwendbarkeit und Erklärungskraft aufzuzeigen.

Nachdem ein grundlegendes Verständnis der Leitfähigkeitsmechanismen in ZnO:Al geschaffen wurde, werden im Weiteren zwei Optimierungskonzepte vorgestellt. Mit Hilfe einer Saatschicht ermöglicht das erste Konzept die Verringerung der Depositionstemperatur um 100 °C ohne dass Leitfähigkeit, Transparenz und Ätzmorphologie negativ beeinflusst werden. Saat- und die anschließend deponierte Bulkschicht werden von einem ZnO:Al-Target mit 2 wt% bzw. 1 wt% Al_2O_3 gesputtert. Ich habe den Effekt der Bulk- und Saatschichttemperatur sowie der Saatschichtdicke auf die elektrischen, optischen und strukturellen Eigenschaften der ZnO:Al-Filme untersucht. Der positive Einfluss der hochdotierten Saatschicht wurde auf die vorteilhafte Rolle des Dotanten Aluminium zurückgeführt, der einen Surfactant-Effekt induziert. Weiterhin

kann ich die durch die Saatschicht induzierte Zunahme der tensilen Verspannung auf der Basis des Korngrenzenrelaxationsmodells erklären. Schlussendlich zeigen temperaturabhängige Leitfähigkeitsmessungen, optische Fits und Ätzcharakteristika, dass Saatschichten die Korngrenzenstreuung reduzieren. Es ist insbesondere erstaunlich, dass kleinere Körner mit erhöhter Ladungsträgermobilität korrelieren. Das zweite Optimierungskonzept basiert auf dem Effekt eines nachträglichen Temperprozesses der ZnO:Al-Filme, der die Leitfähigkeit entweder erhöht oder verringert je nachdem ob eine Abdeckschicht den ZnO:Al-Film schützt oder nicht. Raman-, XRD- und temperaturabhängige Halleffektmessungen in Verbindung mit dem neu entwickelten Leitfähigkeitsmodell werden benutzt, um die Tempereffekte zu analysieren. Die Ergebnisse belegen, dass das Tempern mit Schutzschicht eine Reduktion der Streuung an ionisierten Störstellen und Korngrenzen induziert wohingegen das Tempern ohne Schutzschicht zu einer Verstärkung beider Mechanismen führt.

Auf texturierten Substraten ist das Wachstum von ZnO:Al Filmen herausfordernd, da Makrokorngrenzen auftreten, die die Ladungsträgermobilität und die Stabilität in feuchter Wärme reduzieren. ZnO:Al-Depositionsbedingungen und die Substratmorphologien werden untersucht, um die Leitfähigkeit und die Stabilität unter feuchter Wärme auf texturierten Substraten zu optimieren. Ich habe optimierte Depositionsbedingungen gefunden bei denen die Ladungsträgermobilität auf texturierten und flachen Substraten ähnlich ist. Ein qualitatives Modell wird vorgeschlagen, dass den Einfluss der unterschiedlichen Depositionsbedingungen auf der Basis der Kornorientierung erklärt. ZnO:Al zeigt höhere Ladungsträgermobilität und Stabilität unter feuchter Wärme auf U- als auf V-förmigen Substraten. Diese Beobachtung wird mit der geringeren Anzahl an Makrokorngrenzen auf U- im Vergleich zu V-förmigen Substraten erklärt. Um die Bewertung von texturierten Substraten für das ZnO:Al-Wachstum zu verbessern, wird eine quantitative elektrische Simulation entwickelt, die die Eignung der texturierten Substrate für das Wachstum der ZnO:Al Filme vorhersagt. In der Tat kann die Simulation die Ladungsträgermobilität berechnen, falls sie für die genutzte Depositionsbedingung kalibriert wurde. Weiterhin werden starke Hinweise präsentiert, dass die Ladungsträgermobilität nicht nur durch die Dichte der Makrokorngrenzen sondern auch durch ihre Verteilung bestimmt ist.

Contents

1. Introduction

Transparent conductive oxides (TCO) are used in various fields of application due to their unique property of possessing electrical conductivity and transparency in the visible range at the same time. Fields of application comprise low-emissivity, electrochromic, and smart windows [1, 2], as well as optoelectronic devices such as flat panel displays [3], organic light emitting diodes, and solar cells [4–6].

The most commonly used TCOs, namely fluorine-doped tin oxid (SnO_2:F), tin-doped indium oxid (In_2O_3:Sn), and aluminum-doped zinc oxide (ZnO:Al), are polycrystalline materials. Polycrystalline materials consist of small crystalline grains that are separated by grain boundaries, i.e. a disordered region of atoms between adjacent grains. In order to reach higher conductivity in these polycrystalline materials, one can either tune the charge carrier concentration or mobility to higher values, or increase the film thickness. Thicker films are not advisable due to higher parasitic absorption and costs. The increase of charge carrier concentration improves the conductivity. Unfortunately, it also implies enhanced absorption in the near infrared region which is particularly undesirable for thin-film solar cells [5, 7, 8]. Therefore, the improvement of charge carrier mobility is the favored path to high conductivity TCOs.

Understanding the mechanisms that limit the charge carrier mobility in degenerately doped, polycrystalline TCOs is of crucial importance in order to further increase the conductivity in these materials. Scattering mechanisms that reduce the mobility can be located either within the grain or at grain boundaries. Intra-grain scattering mechanisms are well understood. In contrast, grain boundary scattering is predominantly described by thermionic emission theory [9–12]. However, grain boundary scattering can comprise two further mechanisms, namely field emission, also denoted as quantum mechanical tunneling, and thermionic field emission. It is the aim of this work to reveal the importance of field emission as dominant scattering mechanism at grain boundaries of highly doped, polycrystalline semiconductors.

The investigation focuses on the sputter-deposited material ZnO:Al. ZnO:Al consists of abundant, non-toxic elements and possesses excellent properties in terms of conductivity and transparency. It is particularly interesting for thin-film silicon solar cells because it grows either self-textured in a low pressure chemical vapor deposition

process [13] or it can be textured by etching after sputter deposition [14–16]. The texture is needed for efficient light incoupling and scattering in order to improve the short-circuit current density and thus, the efficiency of solar cells [8, 17, 18].

Improving the conductivity of ZnO:Al films comprises two aspects. First, it is desirable to deposit the films at low temperatures without deteriorating their electrical properties. Thin, optimized seed layers have been proven to determine the further growth of subsequently grown ZnO:Al bulk layers [19–21]. Thus, seed layers are an interesting approach to enable low temperature deposition while maintaining high conductivity. Second, post-deposition heat treatments have been shown to boost the mobility in ZnO:Al [22–24]. Notably, ZnO:Al layers have to be capped by an amorphous silicon film in order to induce the beneficial effects of heat treatment. In contrast, ZnO:Al films without capping layer degrade upon annealing. Post-deposition heat treatments therefore pose an interesting subject to study scattering mechanisms that limit the charge carrier mobility in ZnO:Al. The conductivity characteristics of ZnO:Al films applying a seed layer or annealing approach will be interpreted in terms of my newly developed understanding of grain boundary scattering.

Besides acquiring an understanding of ZnO:Al conductivity mechanisms on flat substrates, some ZnO:Al applications such as thin-film silicon or chalcopyrite-based solar cells require the optimization of ZnO:Al films on textured substrates. It has been addressed before that textured, light scattering ZnO:Al films induce an elongated light path in the thin absorber layer of thin-film silicon solar cells whereby short-circuit current density and efficiency increase. Sputter-deposited and subsequently etched ZnO:Al needs a careful adjustment of deposition parameters such as pressure, temperature [25], or film thickness [26] in order to ensure an etch morphology with appropriate light scattering properties. Furthermore, conflicting requirements in terms of deposition conditions may prevail when conductivity, transparency, and surface morphology need to be optimized simultaneously, e.g. a thicker layer may enhance the light trapping capability of the textured ZnO:Al, but it increases at the same time the parasitic absorption in the ZnO:Al layer [27].

Textured glass substrates, prepared by wet-chemical etching, nano-imprint lithography [28–30], or reactive ion etching [31, 32], may relax the trade-off between electro-optical properties and surface morphology because the rough surface is provided by the substrate and subsequently deposited ZnO:Al layers can be optimized regarding electrical and optical properties only. For this purpose, ZnO:Al growth on textured substrates has to be investigated, understood, and optimized. However, the

topic of ZnO:Al growth on rough surfaces is mostly neglected in literature and only sparse studies may be found.

The most extensive study in this respect was conducted by Greiner et al. with a strong emphasis on ZnO:Al damp heat stability on textured substrates [33–35]. Their investigations were motivated by the fact that ZnO:Al serves as a window layer on the rough absorber of chalcopyrite-based solar cells. Greiner et al. identified growth disturbances, which they denoted as extended grain boundaries, as the reason for deteriorated ZnO:Al conductivity in the as-deposited but in particular in the damp heat degraded state. This thesis extends the studies of Greiner et al. by elaborating the effect of various deposition conditions and substrates textures on charge carrier mobility and damp heat stability of ZnO:Al on textured substrates.

In summary, one extracts the following objectives that shall be addressed in this thesis:

On flat substrates, a conductivity model for highly doped, polycrystalline semiconductors, e.g. sputter-deposited ZnO:Al, shall be developed that satisfactorily describes the dependence of charge carrier mobility on charge carrier concentration and measurement temperature. Particular emphasis is placed on the description of grain boundary scattering. Furthermore, two concepts to improve ZnO:Al conductivity shall be implemented and investigated. The first concept is based on a seed layer approach. It aims at a reduction of deposition temperature such that electro-optical and etching properties are deteriorated as little as possible. The second concept relies on a post-deposition heat treatment. The focus is to elucidate the different mechanisms that govern the annealing process depending on whether or not an amorphous silicon capping layer is applied. The explanation will strongly base upon the previously developed conductivity model.

On textured substrates, ZnO:Al shall be developed that possesses similar charge carrier mobility and damp heat stability than its counterpart on flat substrates. Textures with excellent suitability for ZnO:Al coating in terms of mobility and stability are supposed to be identified. Furthermore, a model shall be developed that features the predictive power to determine the suitability of a texture for ZnO:Al growth.

The above outlined objectives are reflected in the following structure:

Chapter 2 introduces TCOs in a general manner and describes in more detail structural and optical properties of ZnO, the main subject of investigation in this work. Subsequently, the general concept of sputter deposition and the physical

mechanisms that govern this process are discussed. The chapter closes with a short presentation of materials and device concepts for thin-film silicon solar cells, as well as basic solar cell parameters.

Chapter 3 details the preparation of textured substrates and the deposition systems that were applied for ZnO:Al and silicon film growth. Thin-film characterization techniques, their advantages and disadvantages, and technical concepts are presented. Finally, the practical implementation of post-deposition processes is specified.

Chapter 4 deals with the conductivity and the structural properties of ZnO:Al on flat substrates. In Section 4.1, I develop a conductivity model for highly doped, polycrystalline semiconductors which is then, in Section 4.2, applied to data from literature to prove its explanatory and predictive power. Sections 4.3 and 4.4 are dedicated to concepts towards highly conductive ZnO:Al films. Section 4.3 presents the application of a seed layer approach in order to use low-temperature deposition conditions without deteriorating the films' electrical, optical, and etching properties. In Section 4.4, a post-deposition heat treatment of ZnO:Al films is comprehensively investigated with special emphasis on the influence of an amorphous silicon capping layer.

Chapter 5 is dedicated to the deposition, characterization, and optimization of ZnO:Al films on textured substrates. Sections 5.1 and 5.2 detail the influence of deposition conditions and substrate texture, respectively. In Section 5.3, an electrical simulation is presented that is able to predict the suitability of various substrate textures for the growth of ZnO:Al films. At last, thin-film silicon solar cells on double-textured substrates were investigated. The double-texture consisted of thin, etched ZnO:Al that was deposited onto textured glass substrates.

The thesis is finalized in Chapter 6 by summarizing the results and outlining further work.

2. Physical and technological basics

This section gives a short overview about the physical and technological basics that this work relies on. The material class of transparent conductive oxides (TCO) and their applications will be introduced. The focus of this work is the investigation of the TCO zinc oxide. Its crystal structure, optical properties, and deposition using the sputtering process will be presented. Growth models for polycrystalline films are discussed in order to understand the processes during film growth. Finally, materials and device concepts for thin-film silicon solar cells as well as important solar cell parameters are introduced.

2.1. Transparent conductive oxides (TCO)

Optoelectronic devices such as displays or thin-film solar cells need contact layers that are conductive and transparent for emitted or incident light. Thin metal layers [36, 37], conductive polymers [38], or graphene [39] are possible candidates for such transparent conducting films. Furthermore, degenerately doped metal oxides such as tin-doped indium oxid (In_2O_3:Sn), fluorine-doped tin oxid (SnO_2:F) and aluminum-doped zinc oxide (ZnO:Al) exhibit the desired properties. These materials are called transparent conductive oxides (TCO). After their first description [40], a broad field of application as anti-reflex and heat insulation layers has been developed that is completed by the above mentioned optoelectronic devices.

Displays apply predominantly In_2O_3:Sn due to its high conductivity even in very thin films. Thin-film silicon solar cells use ZnO or SnO_2 as transparent front contact layers. For thin-film silicon solar cells, the TCO must be textured in order to assure light-scattering while possessing high conductivity and transparency. ZnO:Al can be deposited by sputtering and it is subsequently etched to induce a rough surface [7, 8, 17]. Furthermore, chemical vapor deposition processes can produce self-textured ZnO:B [13] or SnO_2:F. Chalcopyrite-based solar cells need ZnO:Al that possesses high conductivity and damp heat stability although the TCO is deposited on the rough absorber layer [33, 34, 41].

The optimization of ZnO:Al is thus needed for thin-film solar cells. Additionally, ZnO:Al is a candidate for the replacement of In_2O_3:Sn which is desired due to the scarcity of the element indium.

2.2. Zinc oxide

2.2.1. Crystal structure

ZnO is a group II-VI binary compound semiconductor. ZnO crystallizes in a wurtzite structure. Fig. 2.1 shows the wurtzite crystal structure that consists of two entangled hexagonal sublattices. One hexagonal lattice is occupied by zinc atoms whereas the other hexagonal lattice possesses solely oxygen atoms. Each oxygen atom is surrounded by four zinc atoms and vice versa. Although this tetrahedral coordination is typical for covalent bonding, one finds the bonding between zinc and oxygen to have an ionic share of 50 to 60% [42]. The two lattice parameters have values of $d_0 = 5.21\,\text{Å}$

Fig. 2.1. Wurtzite crystal structure of ZnO. Zinc- and oxygen-terminated facets are indicated. The two lattice constants d_0 and a_0 are shown.

and $a_0 = 3.25$ Å [43]. The c-axis is the symmetry axis of the hexagonal lattice. The ZnO structure can be seen as a sequence of double-layers perpendicular to the c-axis. Each double layer consists of a layer of zinc and oxygen atoms, respectively. Within the double-layers, each zinc atom is bonded to three oxygen atoms and vice versa. Only one bond per atom interconnects the double-layers. Due to the ionic character of the Zn-O bonds, one finds positively charged zinc and negatively charged oxygen

planes. Zinc and oxygen terminate the (001)- and (00$\bar{1}$)-surface, respectively. The piezoelectric property, that is the internal generation of an electric field resulting from an applied mechanical force, is a consequence of the polarization of the lattice planes.

2.2.2. Optical properties

The transparency in the visible region of the spectrum is characteristic for transparent conductive oxides (TCO). It is a direct consequence of the large band gap of these materials (e.g. $E_\mathrm{g}(\mathrm{ZnO}) = 3.4\,\mathrm{eV}$ [43]). The following short introduction is based on [35, 44–47].

Electromagnetic waves The combination of the two Maxwell equations

$$\nabla \times \vec{E} = -\frac{\partial \vec{B}}{\partial t} \tag{2.1}$$

$$\nabla \times \vec{B} = \mu^\mathrm{M}\mu_0^\mathrm{M}\left(\vec{j} + \frac{\partial \vec{D}}{\partial t}\right) \tag{2.2}$$

leads to the equation of motion of an electromagnetic wave[1]

$$\Delta\vec{E} - \mu_0^\mathrm{M}\epsilon\epsilon_0\frac{\partial^2\vec{E}}{\partial t^2} = 0 \tag{2.3}$$

whereby $\vec{E}$ and $\vec{B}$ are the electric and magnetic field, respectively. Furthermore, the magnetic permeability μ^M, the vacuum permeability μ_0^M, the dielectric constant ϵ_0, and the dielectric function or permittivity ϵ are introduced. $\vec{D}$ represents the electric displacement field. The one-dimensional solution of Eq. (2.3) is a plane wave

$$E(x,t) = E_0\exp\left(\imath kx - \imath\omega t\right) = E_0\exp\left(\imath\frac{\omega}{c_0}\sqrt{\epsilon}x - \imath\omega t\right) \tag{2.4}$$

with the wave vector $k = (\omega/c_0)\sqrt{\epsilon}$ and the angular frequency ω. The phase velocity $v_\mathrm{ph} = \omega/k$ in vacuum ($\epsilon = 1$) corresponds to the speed of light $c_0 = 1/\sqrt{\epsilon_0\mu_0^\mathrm{M}}$.

[1] Non-magnetic ($\mu^\mathrm{M} \approx 1$), non-conductive ($\vec{j} = 0$) and electrically neutral ($\rho = 0$) materials are assumed.

The dielectric function ϵ may be rewritten as

$$\epsilon = \epsilon(\omega) := 1 + \chi(\omega) \tag{2.5}$$

introducing the electric susceptibility $\chi(\omega)$. Inserting Eq. (2.5) in Eq. (2.3) yields

$$\Delta E - \frac{1}{c_0^2}\,\frac{\partial^2 E}{\partial t^2} = \frac{1}{c_0^2}\,\chi(\omega)\,\frac{\partial^2 E}{\partial t^2}. \tag{2.6}$$

The left side of Eq. (2.6) describes the equation of motion of an electromagnetic wave in vacuum. The right side characterizes the interaction of the electromagnetic wave with the material. The interaction produces secondary waves. Superposition of the primary and secondary electromagnetic waves results in a new, phase-shifted wave with modified wavelength. In conclusion, one can evaluate the interaction between material and incident wave if the electric susceptibility or the dielectric function is known.

Lorentz oscillator The Lorentz oscillator is a model to compute the dielectric function. It assumes an isotropic atomic charge distribution. An incident electromagnetic wave $E(t)$ deforms this charge distribution inducing a microscopic dipole moment $p(t)$. In a classical picture, the electric field stimulates the charge distribution to oscillate around its equilibrium position with the amplitude $\mathrm{u}(t)$. As the oscillating charges are accelerated, they emit secondary electromagnetic waves damping the system. Thus, the system's equation of motion

$$\ddot{\mathrm{u}}(t) + \Gamma\dot{\mathrm{u}}(t) + \Omega_0^2\mathrm{u}(t) = -\frac{q}{m}E_0\exp(-\imath\omega t) \tag{2.7}$$

corresponds to a damped, externally driven harmonic oscillator. Γ is a damping constant, Ω_0 is the eigenfrequency of the non-damped oscillator, and ω is the already mentioned angular frequency of the incident wave. The microscopic dipole moment $p(t)$ appears macroscopically as a polarization of the material P. The solution of Eq. (2.7) enables the determination of the polarization as N oscillating dipole moments in a volume V

$$P = \frac{\mathrm{N}}{V}\,q\,\mathrm{u}(t) = \frac{\mathrm{N}\,q^2}{V\,m}\,\frac{1}{\sqrt{(\Omega_0^2 - \omega^2)^2 + \Gamma^2\omega^2}}E_0\exp\left(\imath(\varphi - \omega t)\right) \tag{2.8}$$

with the phase shift

$$\varphi = \arctan\left(\frac{\Gamma\omega}{\Omega_0^2 - \omega^2}\right) \tag{2.9}$$

between the polarization and the external field. The polarization reflects the interaction between electromagnetic wave and material. One can therefore identify the polarization with the electric susceptibility χ and the dielectric function ϵ:

$$P := \epsilon_0 \chi E(t) = \epsilon_0(\epsilon - 1)E(t) \tag{2.10}$$

Hence, one obtains the dielectric function of the Lorentz oscillator divided into real and imaginary part

$$\begin{aligned} \epsilon(\omega) &= \epsilon'(\omega) + \imath\epsilon''(\omega) \\ \text{with} \qquad \epsilon'(\omega) &= 1 + \frac{\mathrm{N}q^2}{V\epsilon_0 m} \frac{\Omega_1^2 - \omega^2}{(\Omega_1^2 - \omega^2)^2 + \Gamma^2\omega^2} \\ \epsilon''(\omega) &= \frac{\mathrm{N}q^2}{V\epsilon_0 m} \frac{\Gamma\omega}{(\Omega_1^2 - \omega^2)^2 + \Gamma^2\omega^2} \end{aligned} \tag{2.11}$$

whereby the new, shifted resonance frequency is defined as

$$\omega_1^2 = \omega_0^2 - \frac{\mathrm{N}q^2}{3V\epsilon_0 m}. \tag{2.12}$$

Transmission, reflection, absorption Experimentally, one measures three quantities to characterize the TCO's optical properties: transmittance (T), reflectance (R), and absorptance (A)[2]. They are defined as the ratios between transmitted (I_T), reflected (I_R), absorbed (I_A) light intensity and incident light intensity (I_I):

$$T := \frac{I_\mathrm{T}}{I_\mathrm{I}} \qquad R := \frac{I_\mathrm{R}}{I_\mathrm{I}} \qquad A := \frac{I_\mathrm{A}}{I_\mathrm{I}} \tag{2.13}$$

The conservation of energy $I_\mathrm{I} = I_\mathrm{T} + I_\mathrm{R} + I_\mathrm{A}$ implies

$$T + R + A = 1 \tag{2.14}$$

The three quantities T, R, and A can be deduced from the dielectric function ϵ. The

[2]The *measurement quantities* transmittance, reflectance, and absorptance have to be distinguished from the *physical processes* transmission, reflection, and absorption.

relationship between ϵ and the refractive index n_{op}, the extinction coefficient κ, and the complex index of refraction $\tilde{n}_{\mathrm{op}}$ is given by

$$\epsilon = \epsilon' + \imath\epsilon'' = (n_{\mathrm{op}} + \imath\kappa)^2 = \tilde{n}_{\mathrm{op}}^2 \qquad \Leftrightarrow \qquad \begin{pmatrix} \epsilon' \\ \epsilon'' \end{pmatrix} = \begin{pmatrix} n_{\mathrm{op}}^2 - \kappa^2 \\ 2n'_{\mathrm{op}}\kappa \end{pmatrix} \tag{2.15}$$

Note that ϵ' and ϵ'' respectively n_{op} and κ are not independent. They are connected via the Kramers-Kronig relations. The implication of the complex index of refraction $\tilde{n}_{\mathrm{op}} = \sqrt{\epsilon}$ onto the electromagnetic field may be seen by inserting $\tilde{n}_{\mathrm{op}}$ into Eq. (2.4). One obtains

$$\begin{aligned} E(x,t) &= E_0 \exp\left(\imath \frac{\omega}{c_0} \tilde{n}_{\mathrm{op}}\, x - \imath\omega t\right) \\ &= E_0 \exp\left(\imath\, k_0\, n_{\mathrm{op}}\, x - \imath\omega t\right) \exp\left(-\kappa\, k_0\, x\right). \end{aligned} \tag{2.16}$$

The real part $n_{\mathrm{op}}(\omega)$ of the complex refractive index induces dispersion[3] whereas the imaginary part κ leads to absorption. The equation connecting κ with the transmitted intensity $I_{\mathrm{T}}(x)$

$$I_{\mathrm{T}}(x) = \frac{1}{2} c_0 \epsilon_0 \left|E(x)^2\right| = I_0 \exp\left(-2\kappa k_0 x\right) = I_0 \exp\left(-\alpha_{\mathrm{op}} x\right) \tag{2.17}$$

is know as Lambert-Beer law. $\alpha_{\mathrm{op}} = 2\kappa k_0$ is called absorption coefficient. Light impinging vertically on a coplanar layer experiences multiple reflections at the internal interfaces. We take this effect into account and obtain the transmittance

$$T = (1 - R) \exp\left(-\alpha_{\mathrm{op}} d\right) \tag{2.18}$$

of a coplanar layer of thickness d. The corresponding reflectance R is calculated by

$$R = \left|\frac{\sqrt{\epsilon} - 1}{\sqrt{\epsilon} + 1}\right|^2 = \frac{(n_{\mathrm{op}} - 1)^2 + \kappa^2}{(n_{\mathrm{op}} + 1)^2 + \kappa^2}. \tag{2.19}$$

Classical Drude model In this work, highly doped metal oxid films are investigated. These films are degenerate semiconductors. Therefore, the optical description must take into account the interaction between irradiation and quasi-free electrons[4]. Similar to the Lorentz oscillator, one assumes the electric field to induce oscillations of the electrons. In contrast to the Lorentz model, the quasi-free electrons do not experience

[3] Dispersion is a frequency dependent phase velocity $v_{\mathrm{ph}}(\omega) = c_0/n_{\mathrm{op}}(\omega)$.

[4] Often the entity of quasi-free electrons is denoted as electron gas. The absorption due to the interaction between incident waves and electron gas is called free carrier absorption.

a repulsive force because they are not bound to the atom nuclei. The system's equation of motion (compare to Eq. (2.7)) thus becomes

$$\ddot{\mathrm{u}}(t) + \Gamma_{\mathrm{Dr}}\dot{\mathrm{u}}(t) = -\frac{q}{m^*}E_0 \exp(-\imath\omega t). \tag{2.20}$$

The damping constant $\Gamma_{\mathrm{Dr}} = 1/\tau$ is connected to the mean free or relaxation time τ. The mean free time describes the time between between two collisions. Note the introduction of the effective mass[5] m^*. The solution of Eq. (2.20)

$$\mathrm{u}(t) = \frac{q\,E(t)}{m^*}\frac{1}{\omega^2 + \imath\Gamma_{\mathrm{Dr}}\omega} \tag{2.21}$$

may be used to compute the polarization $P = -nqu(t)$ of the quasi-free electrons. Here, n denotes the carrier concentration. Adding the polarization of the quasi-free and bound electrons, one obtains the dielectric function

$$\epsilon = \epsilon_\infty - \Omega_{\mathrm{Dr}}^2\frac{1}{\omega^2 + \imath\Gamma_{\mathrm{Dr}}\omega} = \epsilon_\infty - \frac{\Omega_{\mathrm{Dr}}^2}{\omega^2 + \Gamma_{\mathrm{Dr}}^2} + \imath\frac{\Omega_{\mathrm{Dr}}\Gamma_{\mathrm{Dr}}}{\omega^3 + \omega\Gamma_{\mathrm{Dr}}^2}. \tag{2.22}$$

ϵ_∞ contains the contribution of the bound electrons. The plasma frequency[6] Ω_{Dr} is defined as

$$\Omega_{\mathrm{Dr}}^2 := \frac{nq^2}{\epsilon_0 m^*}. \tag{2.23}$$

Eq. (2.23) may be used to derive the carrier concentration n from the plasma frequency Ω_{Dr}. The mobility

$$\mu_{\mathrm{op}} = \frac{q}{m^*}\Gamma_{\mathrm{Dr}} \tag{2.24}$$

can be computed from the damping constant $\Gamma_{\mathrm{Dr}} = 1/\tau$. In the case of low damping $\Gamma_{\mathrm{Dr}} \approx 0$, one can rewrite Eq. (2.22) as

$$\epsilon \approx \epsilon_\infty - \frac{\Omega_{\mathrm{Dr}}^2}{\omega^2}. \tag{2.25}$$

[5] The Drude model describes the electrons as classical particles. A quantum mechanical extension of the theory by Sommerfeld took the effective mass into account. Furthermore, Drude assumed all electrons to participate in the current. Effectively however, only the electrons at the Fermi surface do so. The mean free time τ has hence to be interpreted as the relaxation time $\tau(E_{\mathrm{F}})$ of the electrons at the Fermi surface.

[6] Literature mostly denotes Ω_{Dr} as plasma frequency although the physical plasma frequency is actually $\Omega_{\mathrm{P}}^2 = \Omega_{\mathrm{Dr}}^2/\left(\epsilon_\infty - \Gamma_{\mathrm{Dr}}^2\right)$ [35, 48].

One might distinguish two interesting cases[7]: (1) If $\omega^2 \ll \Omega_{\mathrm{Dr}}^2$, the dielectric function ϵ becomes negative and $\widetilde{n}_{\mathrm{op}} = \sqrt{\epsilon}$ is imaginary. Such waves incident on the electron gas are reflected as can be seen from Eq. (2.19). (2) If $\omega^2 \gg \Omega_{\mathrm{Dr}}^2$, ϵ is positive and $\widetilde{n}_{\mathrm{op}}$ is real. The electron gas becomes transparent. This behavior of high reflection at low frequencies and high transparency at high frequencies is typical for metals or highly doped metal oxides. The onset of the high reflection regime may be shifted via the carrier concentration because the carrier concentration determines the plasma frequency Ω_{Dr}.

Extended Drude models The classical Drude model assumes the damping constant to be frequency-independent. However, a more detailed analysis reveals that the scattering of charge carriers implies a frequency-dependent damping factor above the physical plasma frequency Ω_{P} [49]. The damping constant obeys a power law $\Gamma_{\mathrm{Dr}} \propto \omega^{\nu}$. The exponent ν depends on the specific scattering mechanism, e.g. the exponent $\nu = -3/2$ corresponds to ionized impurity scattering. Mergel and Qiao [48] and Pflug et al. [50] developed empirical models that take into account the frequency-dependent damping factor. Here, the model introduced by Mergel and Qiao is used to fit transmittance and reflectance spectra. Further information about this model and related fits may be found in Section 3.3.9.

Optical spectra of ZnO:Al Fig. 2.2 shows a typical transmittance, reflectance, and absorptance spectrum of ZnO:Al. Three spectral regions may be differentiated:

Region I: The incident photons provide enough energy to excite electrons from the valence into the conduction band. Therefore, the spectrum is dominated by the strong band gap absorption and the vanishing transmittance. ZnO:Al is a degenerate semiconductor. The lowest electronic states in the conduction band are already occupied (Fig. 2.3(b)). The Pauli exclusion principle then implies that electrons can only be excited into higher electronic states. The optical band gap thus depends on the carrier concentration because the carrier concentration correlates to the amount of occupied states in the conduction band. The increase of optical band gap $\Delta E_{\mathrm{g}}^{\mathrm{BM}}$ with increasing carrier concentration n

$$\Delta E_{\mathrm{g}}^{\mathrm{BM}} = \frac{\hbar^2}{2\,m^*}\left(3\,\pi^2\,n\right)^{2/3} \tag{2.26}$$

is known as Burstein-Moss shift [51, 52]. $\hbar$ is the Planck constant and m^* is the electron effective mass. The model assumes a parabolic band structure. In other words, it assumes the effective mass to be independent of carrier concentration.

[7] For the sake of simplicity, ϵ_∞ is assumed to be positive and real.

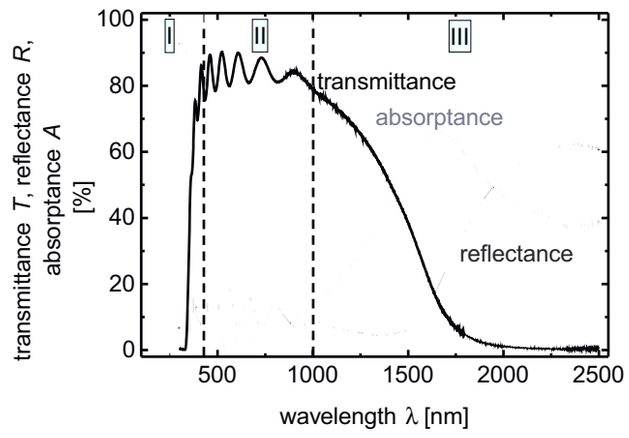

Fig. 2.2. Typical transmittance (black), reflectance (grey), and absorptance (light grey) of a common ZnO:Al layer as a function of wavelength. Three regions (I) - (III) are distinguished.

Although this hypothesis seems incorrect for ZnO:Al [53–55], the general trend is well described within the simple model. Fig. 2.3(c) shows that the Burstein-Moss shift is counteracted by many body effects such as electron-electron interaction [56]. However, the Burstein-Moss shift remains the dominating effect. Defects in the material induce tail states extending into the band gap [57]. As a result, sub band gap absorption is observed. The sub band gap absorption broadens the transmission edge and reduces its steepness [58].

Region II: The energy of the incident photons does not suffice to excite electrons from the valence into the conduction band. Therefore, one observes low absorptance and high transmittance in this wavelength range. High carrier concentrations might induce free carrier absorption already in region II. Fabry-Pérot interferences occur as a result of reflections at the layer's front and back side. The transmittance is mainly limited by the reflection at the interfaces between air, glass, and ZnO:Al. The absorption within the glass substrates can be neglected [59].

Region III: An increasing free carrier absorption with increasing wavelength is observed. As predicted by the Classical Drude model, the reflection starts to rise close to the plasma frequency. Consequently, the light intensity penetrating the material decreases and the absorptance drops[8]. The transmittance drops drastically at

[8]Some authors connect the free carrier absorption to the longitudinal oscillations of the electron gas.

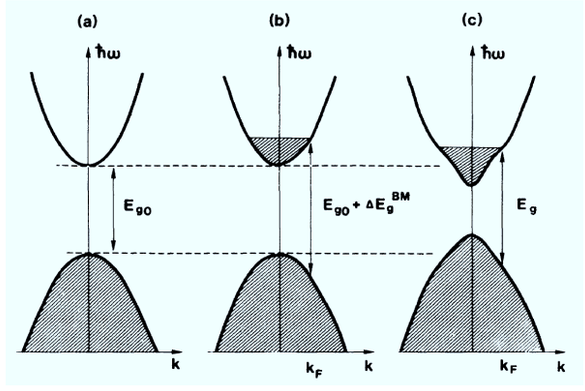

Fig. 2.3. Schematic representation of the band structure from [56]. Undoped semiconductor (a), degenerate semiconductor with Burstein-Moss shift (b) and additional many body interactions (c).

higher wavelength and it finally vanishes. The free carrier absorption can be controlled by the carrier concentration. Lower carrier concentrations shift the absorptance maximum to higher wavelengths and reduce the absorptance in the visible spectrum. Furthermore, higher charge carrier mobilities do not shift the absorptance peak but decrease its height. This result is revealed by the rather cumbersome evaluation of the absorption coefficient α as a function of damping constant Γ_{Dr}.

2.3. Sputter deposition

In this work, ZnO:Al films were grown by magnetron sputtering. In the following, the process of sputtering will be introduced and explained in brevity. First, the simple case of direct current (dc) sputtering will be presented. Second, the process of radio frequency (rf) sputtering, that is used for non-conductive targets, will be discussed. A detailed description of sputtering can be found in the book of Chapman [60].

Dc-sputtering Fig. 2.4 shows schematically the processes that take place during sputtering. Sputtering is performed within a vacuum chamber. The target consists of the material that is to be deposited onto the substrate. The substrate is placed

However, longitudinal oscillations cannot couple to the transverse waves of the electromagnetic field. Therefore, the free carrier absorption is the coupling of the transverse electromagnetic field to transverse oscillations of the electron gas [44].

opposite to the target. A noble gas, in our case argon, is introduced into the chamber. A small fraction of the argon atoms are initially ionized due to e.g. cosmic radiation. An electric field is applied between target and substrate. The electric field accelerates argon ions towards the negatively charged target and electrons towards the anode. On their way through the chamber, argon ions and electrons may collide with other argon atoms. If the kinetic energy of the charged particles is sufficiently high, the collisions may ionize further atoms, thus increasing the number of ions and electrons. One ends up with a self-sustaining plasma glow discharge consisting of ions, neutral atoms, and electrons. Ions that hit the target may eject target material which can then travel through the plasma towards the substrate.

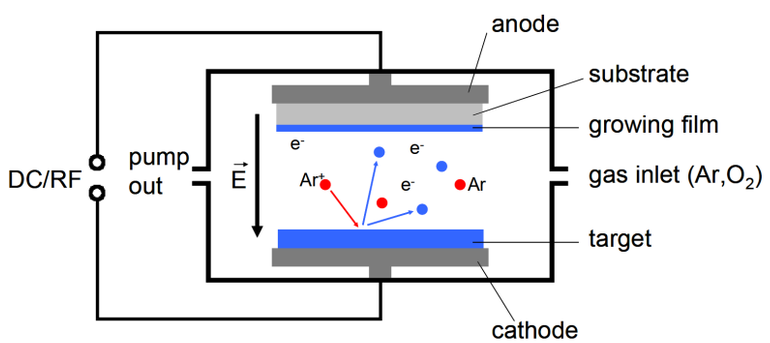

Fig. 2.4. Scheme of the sputtering process [61]

The growth rate is determined by the amount of target material that is not scattered backwards within the plasma on its way to the substrate. Therefore, a low argon pressure is desirable to obtain a high growth rate. However, the plasma cannot be sustained if the argon pressure is too low because the amount of ionization events would not be sufficient. The issue can be resolved by the application of a magnetic field. As a result of the Lorentz force, a carefully designed magnetic field induces the electrons to circle above the target. The electrons are confined to a small volume and their average path length is increased. Consequently, the ionization probability is increased and the plasma can be sustained at lower pressures. Note that the heavy ions are not affected by the magnetic field. The presented magnetic field supported sputtering process is called magnetron sputtering. Due to the plasma confinement, magnetron sputtering induces an inhomogeneous erosion of the target. The predominantly sputtered area of the targets forms a trench that is called racetrack.

Rf-sputtering For isolating or lowly conducting target material, the above described dc-process induces a positively charged target surface due to the positive argon ions that hit the target. In the extreme case of isolating targets, the charged target surface builds up an electric field that counteracts the external field. As a consequence, the argon ions are no longer accelerated and the plasma ceases.

The charging of the target surface can be prohibited by using an alternating electric field. Typically, a radio frequency (rf) of 13.56 MHz is used. The light electrons can follow the alternating electric field in contrast to the heavier ions. Electrons are driven towards the target when the external, alternating field charges the cathode positively. When the electric field switches and the cathode becomes negatively charged, the heavy and slow argon ions are not able to compensate the negative electric charge that has been transferred before by the electrons. Thus, the target builds up a negative charge that increases until the charge transfer of electrons and ions to the target is similar. This process is called self-biasing. As a consequence, argon ions are constantly accelerated towards the negatively charged cathode and sputter target material.

ZnO:Al targets are lowly conducting. Rf-sputtering will hence be used throughout this work to deposit ZnO:Al.

2.4. Polycrystalline growth models of sputtered films

The growth conditions determine electrical, optical, and etching properties of the material. In this section, the processes that occur on the surface during the sputtering process will be discussed. A growth model for ZnO will be presented followed by the detailed description of the stress within the films.

2.4.1. Surface processes during sputtering

Fig. 2.5 shows the processes on the surface during the sputtering process. Particles are ejected from the target and travel as atoms or clusters through the plasma towards the substrate. Particles may collide within the plasma with other particles or with argon ions resulting in a broadening of the angular distribution of incoming material. Also, some particles may be reflected and thus they do not reach the substrate.

If the energy of the impinging particles is high, they may be implanted into the growing film right where they first hit the film. There, they disturb the crystal lattice and may induce defects. Furthermore, high energy particles can transfer their energy to other atoms or clusters which are ejected consequently. Such a process is called resputtering. In contrast, particles with lower energies are absorbed and may diffuse on the surface to reach an energetically favorable site. The diffusion length depends on the energy and the mass of the particles. Obviously, single atoms have a longer diffusion length than clusters.

Fig. 2.5. Schematic representation of the processes that take place on the surface of the growing film during sputtering [15].

Atoms may also move within the bulk. However, the energy needed for this process is high rendering it less probable.

The roughness of the growing film induces shadowed areas. Particles that arrive under a certain angle may not reach this area for pure geometrical reasons. Note that this process is self-enforcing as the screening peaks grow faster than the shadowed area.

The deposition conditions influence severely the probability of the just described processes. A higher deposition temperature increases the particles' energy, thus leading to a higher surface diffusion length. A higher deposition pressure increases the probability of collisions within the plasma. As a consequence, the angular distribution is broadened and the growth rate decreases because more particles are reflected. A higher amount of collisions also induces a reduction of the impinging particles' energy. Further deposition parameters comprise the deposition time, i.e. the film thickness, and the deposition power.

2.4.2. Growth models for sputtered ZnO

ZnO texture For ZnO on flat substrates, one observes the c-axis to be oriented perpendicular to the substrate. The combination of two effects explains this behavior. First, the c-axis orientation has a minimum of surface free energy in ZnO [62]. A preferential growth and thus a high growth rate of this orientation is energetically favorable. Second, the domination of certain crystal orientations can be attributed to the survival-of-the-fastest mechanism, where the fastest growing orientation overgrows all other orientations [63]. Consequently, fast growing, c-axis oriented grains that are aligned perpendicular to the substrate overgrow all other grains leading to the characteristic ZnO texture.

Modified Thornton model The surface processes that have been discussed in the previous section were summarized by Thornton to describe the growth of metal films [64]. Kluth et al. adopted the model for the growth of ZnO:Al [25].

Fig. 2.6 shows the schematic representation of ZnO:Al film structure as a function of deposition temperature and pressure. Additionally, SEM images of the layers before and after etching in dilute hydrochloric acid (HCl 0.5 wt%) are presented [25].

High deposition pressures induce strong shadowing and a lower surface diffusion length. As a result, the formation of voids is promoted. The resulting grainy film structure is further promoted if the deposition temperature is low because then, the low surface diffusion length cannot compensate the high amount of shadowing. Kluth et al. denote such films with low compactness as type A.

The decrease of deposition pressure and the increase of deposition temperature reduce shadowing and promote surface diffusion. Consequently, the void formation is suppressed and the films become more compact. Such films are called type B. A further decrease and increase of pressure and temperature, respectively, leads to even more compact films denoted as type C.

2.4.3. Etching of polycrystalline ZnO:Al

The modified Thornton model correlates the deposition conditions and the layer properties to the etching behavior [25]. According to the model, the compactness of the film is the parameter that defines the etching morphology.

Grain boundaries in type A films with low compactness are prone to attack by the acid. Therefore, every grain boundary is etched and the morphology after etching

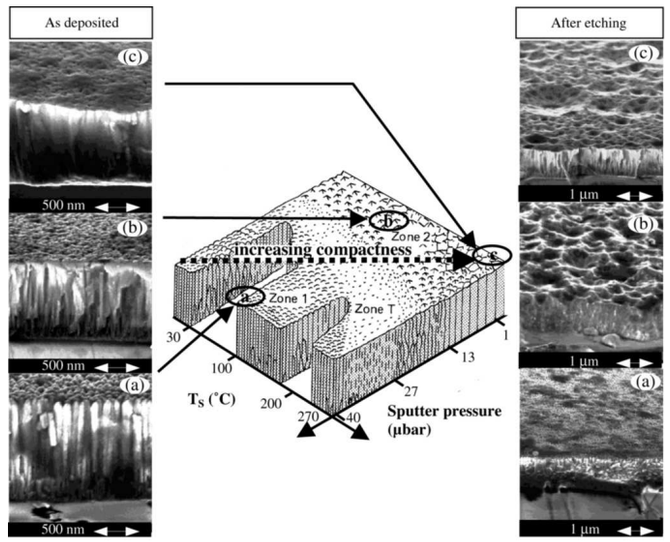

Fig. 2.6. Depiction of the modified Thornton model as developed by Kluth et al. [25].

consists of the exposed grains. In type B films with increased compactness, "the highly oriented ZnO:Al films are only attacked by the etchant from one crystallite site. This leads to an anisotropic etching process, which produces the observed crater structure." [25] A further increase of compactness leads to a type C morphology that rarely shows craters.

The etching model was expanded by Owen and Hüpkes et al. to take into account the effect of different etch species [61, 65]. The compactness was replaced by a parameter called etch potential which defines the probability of a grain boundary to be attacked by the acid.

2.4.4. Stress in sputtered films

The total stress in ZnO:Al consists of thermal and intrinsic stress: "The thermal stress is due to the difference in the thermal expansion coefficients of the coating and substrate materials. The intrinsic stress is due to the accumulating effect of the

crystallographic flaws that are built into the coating during deposition." [66] If one assumes isotropic mechanical properties in the substrate plane, the biaxial stress σ

$$\sigma = \mathrm{E}\,\frac{d_{\mathrm{xy}} - a_0}{a_0} \tag{2.27}$$

$$\sigma = \frac{\mathrm{E}}{1-\nu}\,\frac{d_0 - d_{\mathrm{z}}}{d_0} \tag{2.28}$$

can be related to the lattice spacing parallel (d_{xy}) or perpendicular (d_{z}) to the substrate. E and ν denote the Young modulus and the Poisson ratio, respectively. The Poisson ration can be computed using elastic constants by $\nu = \mathrm{C}_{13}/(\mathrm{C}_{11} + \mathrm{C}_{12})$. a_0 and d_0 are the unstrained lattice spacings in xy- and z-direction. In the following, $\mathrm{E} = 111.2 \times 10^9$ Pa [67] and $\nu = 0.365$ are employed using elastic constants from [68]. Positive and negative stress values are called tensile and compressive stress, respectively.

Thermal stress in the xy-plane is computed from the thermal expansion coefficients of substrate (Corning glass: $\alpha_{\mathrm{glass}} \approx 3.8 \times 10^{-6}\ \mathrm{K}^{-1}$ [59], float glass: $\alpha_{\mathrm{glass}} \approx 9 \times 10^{-6}\ \mathrm{K}^{-1}$ [69]) and ZnO ($\alpha_{\mathrm{ZnO}} \approx 6 \times 10^{-6}\ \mathrm{K}^{-1}$ [43]), and the difference ΔT between deposition and room temperature:

$$\sigma_{\mathrm{therm}} = \mathrm{E}\,(\alpha_{\mathrm{ZnO}} - \alpha_{\mathrm{glass}})\,\Delta T \tag{2.29}$$

On Corning glass, a maximal deposition temperature of 400 °C induces tensile stress in the order of 100 MPa after cooling.

Intrinsic stress can have multiple reasons. Possible explanations and models for intrinsic stress in sputtered films based on the readable review by Windischmann [70] are shortly discussed.

Two models have been predominately used to describe the occurrence of tensile stress: (1) The buried layer model by Klokholm and Berry assumes an advancing, disordered growth front [71]. Windischmann states that "the stress magnitude corresponds to the amount of disorder initially present before being buried by successive layers." High temperatures and low deposition rates induce low disorder and hence low tensile stress. Windischmann notes however that tensile stress relief will only become significant above $T_{\mathrm{dep}}/T_{\mathrm{m}} \approx 0.3$. T_{m} is the melting temperature of the growing material. As the melting temperature T_{m} of ZnO is approximately 2000 °C [43] and the maximum deposition temperatures T_{dep} were around 400 °C, one assumes the tensile stress relief as proposed by the buried layer model to be negligible. (2) The

grain boundary relaxation model is used to describe tensile stress in polycrystalline materials [72]. Interatomic attractive forces between adjacent grains impose tensile stress. One can relate the ionic radius r_0, the Young modulus E, the Poisson ratio ν, and the grain size L by the expression

$$\sigma \approx \frac{\mathrm{E}}{1-\nu}\,\frac{r_0}{L} \tag{2.30}$$

to the tensile stress σ. Note the inverse relationship between grain size and tensile stress.

Compressive stress is described by two models: (a) Impurity atoms may distort the lattice. Lattice distortion may be induced by "[..] incorporation of atoms of a size different from the host, or [..] reaction at grain boundaries (e.g., oxidation or hydrogenation) producing a phase with a different molar volume, or [..] grain surface energy reduction." [70] Water vapor, hydrogen, and inert gases are named as the dominant impurities. (b) The forward sputtering or atomic peening model introduced by D'Heurle and Harper assumes energetic particles impinging on the growing film to distort the lattice [73]. At low deposition temperatures $T_{\mathrm{dep}}/T_{\mathrm{m}} < 0.25$, "mass transport and defect mobility are sufficiently low to freeze the volumetric distortion in place" [70]. The expression describing the compressive stress

$$\sigma = \mathrm{k}\,\Phi\,\sqrt{\mathrm{E_p}}\,\mathrm{Q} \tag{2.31}$$

contains a numerical factor k , the ion flux Φ, the particle energy $\mathrm{E_p}$, and the quantity Q combining elastic constants and physical properties of the target. Köhl et al. could verify this mechanism for the growth of sputtered ZnO [74]. They found the effect to increase with increasing mass of the impinging ions. It is noteworthy that argon ions showed atomic peening, oxygen ions however did not.

Tensile and compressive stress inducing effects may be present simultaneously. Windischmann underlines this fact for the impurity model: "Consequently, superimposed on the tensile stress may be an impurity-induced compensating compressive stress that may merely reduce the tensile stress (and therefore not manifest itself overtly) or, in the extreme, produce a net compressive stress (even though the atomic peening mechanism is absent)."

Stress determination The stress was determined by x-ray diffraction (XRD) measurements (see Section 3.3.6). The (002) peak position is a measure for the vertical lattice spacing d_z. The (002) peak position shifts to either higher angles for tensile stress or lower angles for compressive stress. If the (002) peak position of unstrained

material is known, one can compute the effective stress in the films. Undoped and unstrained ZnO shows a (002) peak position at 34.4 ° [43]. This peak position will be employed although other authors have argued that the unstrained peak position of aluminum-doped ZnO may be at 34.5 ° [46].

2.5. Thin-film silicon solar cells

ZnO:Al is applied as transparent front contact in thin-film silicon solar cells. One of the motivations for a better understanding of ZnO:Al conductivity mechanisms is to increase solar cell efficiencies by improved ZnO:Al front contacts. Here, the basic concepts of thin-film silicon solar cells and parameters, which characterize a solar cell, shall be introduced.

Materials and device concepts Solar cells are devices that use the photovoltaic effect to convert light into electricity. An overview about the different concepts and materials used for solar cells can be found in [75–77].

Thin-film silicon solar cells consist of amorphous or microcrystalline silicon or a combination of both materials in a tandem device. A schematic structure of such a solar cell is shown in Fig. 2.7. The solar cell contains p- and n-doped silicon layers that enclose an intrinsic silicon layer. The doped layers induce an internal electric field. Incident light generates electron-hole pairs. The charge carriers are separated by the internal electric field and driven towards the contacts.

Amorphous silicon is deposited using plasma enhanced chemical vapor deposition (PECVD). Amorphous silicon contains more defects than its crystalline counterpart due to the lack of a long range order. The defects can be passivated by hydrogen. Hydrogenated, amorphous silicon (a-Si:H) has a sufficiently high conductivity for the application in solar cells. It exhibits a quasi-direct band gap of 1.7 eV and high absorption that allows the use of thin films. However, the material degrades under illumination. This effect is known as Staebler-Wronski effect [78]. It can account for efficiency losses of 15 to 25 % after 1000 h of illumination.

Microcrystalline silicon is, similar to amorphous silicon, hydrogenated and deposited using a PECVD process. Suitable material for solar cells consists of a mixture of microcrystalline and amorphous silicon. Hydrogenated, microcrystalline silicon (µc-Si:H) possesses an indirect band gap of 1.1 eV. Further details about this material can be found in [79].

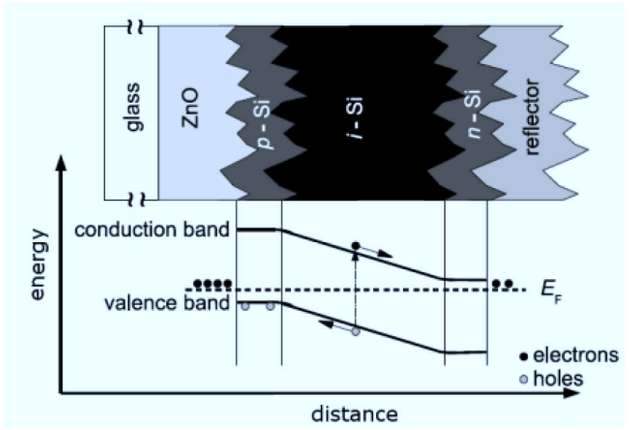

Fig. 2.7. Schematic structure and band diagram of a thin-film silicon solar cell in pin configuration. [61]

Microcrystalline silicon shows lower absorption in the visible range than amorphous silicon due to its indirect band gap. A significant amount of photons thus enters the solar cell, runs through the silicon layers, but leaves them without being absorbed. As a consequence, light trapping schemes based on substrate texturing have been introduced in order to elongate the light path in the cell [8, 17, 18]. Textured ZnO:Al films, that serve as substrate, can be obtained by chemical etching in e.g. dilute hydrochloric acid (see Section 2.4.3).

Amorphous and microcrystalline silicon have different band gaps. Thus, they absorb light in different wavelength regions. A combination of both materials in a tandem device is able to use and convert a broader wavelength spectrum of the incident sunlight. However, such a device is more difficult to fabricate and one has to assure that the subcells produce similar current since they are connected in series.

Solar cell parameters An important characterization technique for solar cells is the measurement of the cell's current I in the dark and under illumination as function of voltage V. The current will be normalized to the area to obtain the current density j.

A characteristic jV-curve under illumination is shown in Fig. 2.8. The operating point of the solar cell will be chosen such that the cell produces the maximum output power density P_{mpp}. The corresponding current density and voltage at the maximum power point are denoted as j_{mpp} and V_{mpp}. In the case of zero voltage, one obtains

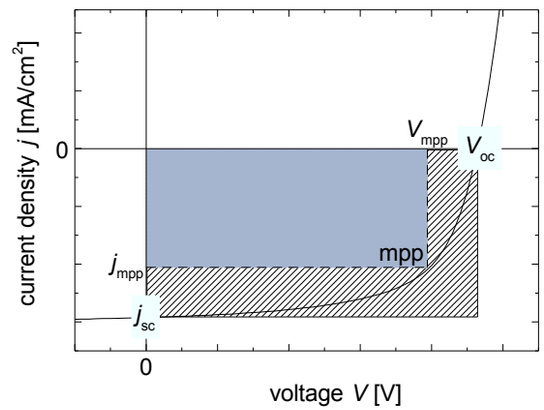

Fig. 2.8. The characteristic jV-curve of a solar cell under illumination.

the short-circuit current density j_{sc}. The voltage measured at vanishing current density is called open-circuit voltage V_{oc}. The ratio of the product of $j_{\mathrm{mpp}}\,V_{\mathrm{mpp}}$ and $j_{\mathrm{sc}}\,V_{\mathrm{oc}}$

$$FF = \frac{j_{\mathrm{mmp}}\,V_{\mathrm{mmp}}}{j_{\mathrm{sc}}\,V_{\mathrm{oc}}} \tag{2.32}$$

is called fill factor FF. The efficiency of a solar cell η is the ratio between the maximum power P_{mpp} and the power density of the incident radiation P_0. The efficiency

$$\eta = \frac{P_{\mathrm{mpp}}}{P_0} = \frac{FF\,V_{\mathrm{oc}}\,j_{\mathrm{sc}}}{P_0} \tag{2.33}$$

can be rewritten using Eq. (2.32).

A further characterization method for solar cells is the measurement of the external quantum efficiency (EQE). The external quantum efficiency

$$EQE(\lambda) = \frac{n_{\mathrm{e}}(\lambda)}{n_{\gamma}(\lambda)} \tag{2.34}$$

is defined as the ratio between the number of extracted electrons and the number of incident photons at a given wavelength.

A detailed description of important solar cell parameters can be found in [80].

3. Experimental details

This chapter describes the preparation of textured substrates and details the deposition systems for ZnO:Al and silicon growth. Furthermore, various characterization techniques of films and devices and post-deposition processes will be presented.

3.1. Preparation of textured substrates

3.1.1. Texture-etched glass

Flat, low-iron solar glass *Eurowhite* [69] produced by the company *Euroglas* was subjected to a first etching step. Depending on the specific etching conditions, one can vary the lateral width of the etching texture from approximately 1 to 7 µm. This first etching step was developed by our project partner, the company *Berliner Glas*. They possess detailed knowledge about the first etching step. The texture after the first etching step can be further modified by a second etching step in an acid mixture consisting of 45 wt% of sulfuric acid and 0.5 wt% of hydrofluoric acid. A detailed description of the resulting textures can be found in Section 5.2.

3.1.2. Nano-imprint substrates

Nano-imprint processes are used to replicate structures that possess features in the nanometer scale. A foil or resist is pressed onto the surface that one wants to replicate. Foil or resist adopt the inverse surface texture. In a subsequent step, one hardens either the foil by heat or the resist by UV light. Finally, the structured foil or resist represent a mold that can be used to prepare structured glass. For this purpose, resist is brought upon a glass substrate. Thereafter, the resist is structured by the mold. Further details about the process can be found in Meier et al. [29].

3.1.3. Lithographically produced model structure

(100) oriented silicon wafers were cleaned by a standard RCA clean followed by a thermal oxidation (*RTP AS One150, AnnealSys*) whereby 50 nm of a protective SiO_2 were grown. Subsequently, a positive lithography (*MA4, Süss Microtech*) was performed using a mask that contained 2 µm × 2 µm lines and spaces. The resist was removed by applying an O_2 plasma for 20 s (*ClusterTool CT100 ECR-RIE, Oxford Instruments*). A short dip in buffered hydrofluoric acid removed the SiO_2 layer. Then, the wafers were etched for 23 min in 60 wt% of potassium hydroxide (KOH) at 40 °C. Another RCA clean and a further thermal oxidation ended the process. The thermal oxidation yielded a SiO_2 layer that served as an isolator between silicon wafer and subsequently deposited ZnO:Al.

KOH etches silicon in the (110) direction approximately 700 times faster than in the (111) direction [81]. Thus, the (111) direction serves as an etch stop. The (111) planes form an angle of 54.74 ° with the surface of a (100) oriented wafer. As a result, the above described KOH etching process yields V-shaped trenches (see Section 5.1.2).

It was furthermore aimed at smoothing the sharp valleys of the initial V-shaped morphology. For this purpose, the V-shaped trenches were subjected to hydrogen for 60 s at a temperature of 1050 °C. The flow rate was 100 sccm at a pressure of 65 Pa. The process was performed in the same system that was used for the thermal oxidation (*RTP AS One150, AnnealSys*).

The smoothing process was difficult to control. Thus, only a very slight effect was finally observed, e.g. Fig. 5.11(b) and (c) show the smoother and the original structure, respectively.

3.2. Layer deposition

3.2.1. ZnO:Al deposition

ZnO:Al films were deposited in a small area and a large area sputtering system. Two main differences characterize the systems: The maximal possible substrate size in the small sputtering system is 10 cm × 10 cm whereas it is 30 cm × 30 cm in the large area system. Additionally, a static deposition process is used in the small area system in contrast to a dynamic deposition process in the large area sputter chamber. In the following, both systems will be described in more detail.

Small area sputtering system The small area sputtering system was built by the company *Kurt J. Lesker*. It consists of a main chamber, which contains the sputtering targets, and a loading chamber. Both chambers are separated by a shutter. The loading chamber assures that the atmospheric contamination in the main chamber is kept to a minimum. The base pressure in the main chamber is approximately 2×10^{-5} Pa. The chamber contains four targets with a diameter of 15.24 cm (6 inch). Furthermore, four heatable substrate holders are available that can be moved above the desired targets. Shutter separate the substrate and the target.

Each heater consists of two halogen lamps that heat an isothermal metal plate. The metal plate is situated 1 cm above the back surface of the substrate. A thermocouple determines the metal plate's temperature, which will be called heater temperature in the following. The substrate temperature differs from the heater temperature. The difference depends on the substrate, e.g. Corning glass [59] or float glass [69], and on the amount of metal that the substrate holder consists of. More metal induces a faster heat transport. Thus, the substrate temperature is lower. In this work, only heater temperatures are given. Generally, the substrate temperature is roughly two third of the heater temperature. The heater reached the adjusted temperature within a few minutes. However, an overall heating-up time of at least one hour was adhered in order to assure a constant substrate temperature.

Ceramic ZnO:Al targets were subjected to an rf-sputtering process. A power of 250 W was chosen that corresponds to a power density of 1.4 W/cm^2. The sputtering gas was pure argon. The argon gas flow rate was 8 standard cubic centimeters per minute (sccm). The sputtering process was started while the shutter was closed. After a minimum of 5 min, the process was assumed to be stable and the shutter was opened to begin the actual deposition. The thickness of the grown film deviates by about 10 to 20% at the edges of the 10 cm $\times$ 10 cm substrate. Thus, all measurements were performed in the relatively homogeneous center of the substrate. Further details about the homogeneity and the small area sputtering system in general can be found in [47, 82, 83].

Large area sputtering system The dynamic large area deposition took place in a vertical inline sputtering system *VISS 300* built by *von Ardenne Anlagentechnik*. The system consists of two loading chambers and two process chambers. The base pressure is around 2×10^{-5} Pa. The substrates with maximal size of 30 cm $\times$ 30 cm oscillate in front of planar, rectangular targets with dimensions of 75 cm $\times$ 10 cm. Instead of a single 30 cm $\times$ 30 cm substrate, a 3×3 matrix of 10 cm $\times$ 10 cm substrates may also be coated.

The substrates are heated from the back surface by radiative heaters. Similar to the small sputtering system, the substrate temperature depends on various parameters and cannot be measured directly during the process. Thus, only heater temperatures will be given in this work. The substrate temperature is approximately two third of the heater temperature.

Rf-sputtering was used to deposit ZnO:Al from a ceramic target with a doping concentration of 1 wt% Al_2O_3. The deposition pressure and argon flow rate were 0.1 Pa and 100 sccm, respectively. The deposition power was 1.5 kW which corresponds to a power density of 2.0 W/cm^2.

Industrially relevant float glass [69] was used as substrate in Section 5. Float glass contains contamination such as sodium ions that may diffuse out of the glass and into the ZnO:Al layers [84, 85]. Thereby, it degrades the ZnO:Al layers [86]. To prevent contamination, SiO_xN_y layers were sputtered onto float glass to serve as barrier layer. Reactive mid-frequency (mf) sputtering was used to deposit the SiO_xN_y interlayers. Details about the mf-sputtering process can be found in [46]. The thickness of the SiO_xN_y layer was 70 nm. In conjunction with an appropriate refractive index, which can be adjusted by the relation between nitrogen and oxygen, one obtains an anti-reflection effect. Detailed deposition conditions and properties of the SiO_xN_y interlayer are given in [86, 87].

3.2.2. Solar cell deposition

Single junction µc-Si:H and a-Si:H/µc-Si:H tandem solar cells were deposited using plasma enhanced chemical vapor deposition (PECVD). A plasma excitation frequency of 13.56 MHz was applied to decompose the precursors. Precursors were hydrogen (H_2) and silane (SiH_4). Furthermore, trimethylborane ($B(CH_3)_3$) and phosphine (PH_3) were used for p- and n-doping, respectively.

µc-Si:H and a-Si:H/µc-Si:H solar cells were prepared in different PECVD systems. Details about the µc-Si:H deposition can be found in [88, 89]. The tandem process is described in [90].

The back contact of the solar cells consisted of 80 nm thin ZnO:Al which was rf-sputtered in the large area sputtering system from a target with 1 wt% Al_2O_3. Subsequently, a 200 nm thick silver layer and another 80 nm thin ZnO:Al were sputtered onto the solar cell. The aperture area of the cells was carefully defined by laser patterning [91].

3.3. Characterization

3.3.1. Thickness determination

The thickness was determined using a surface profiler *Dektak 3030* built by the company *Veeco* equipped with a 12 µm stylus. A thickness measurement with a surface profiler needs a step between the substrate and the film. For this purpose, a small circle of hydrophobic ink with a diameter of 1 mm was applied to the film's surface. Then, the film that surrounded the circle was etched until it was removed completely. The hydrophobic ink was subsequently removed with isopropyl alcohol. The start of the measurement was set to be the point where the film was etched away. The stylus hit the film that had been secured by the ink at some point. The resulting step was taken as the film thickness. The thickness of flat layers can be determined with an accuracy of 10 nm [46].

3.3.2. Electrical measurements

Charge carrier mobility μ, charge carrier concentration n, and resistivity ρ of ZnO:Al films were determined using the Hall effect in van der Pauw geometry [92].

The resistivity

$$\rho = \frac{1}{e\,n\,\mu} = \frac{1}{\sigma} = R_{\mathrm{sh}}\,d \tag{3.1}$$

is connected to the mobility μ and the carrier concentration n. e is the elementary charge. Furthermore, the conductivity σ is the inverse of the resistivity ρ. Also, the resistivity may be determined as the product of sheet resistance R_{sh} and the layer thickness d. The sheet resistance is the resistance of a thin film of conducting material with quadratic area.

For Hall effect measurements[1], a direct current I is injected into the sample. Additionally, a magnetic field B is applied perpendicular to the substrate. The Lorentz force drives the flowing electrons to one side of the sample. As a consequence, an

[1] For the sake of clarity, Hall effect measurements will be denoted as Hall measurements throughout this work.

electric field occurs that counteracts the Lorentz force. The electric field is measured as the Hall voltage

$$V_{\mathrm{H}} = \frac{I\,B}{e\,d\,n}. \tag{3.2}$$

I, B, and the sample thickness d are known. Thus, from the measurement of the Hall voltage, one can determine the carrier concentration n. Additionally, the resistivity can be obtained by measurements of the sheet resistance R_{sh}. Finally, one receives the mobility

$$\mu = (e\,n\,\rho)^{-1} = \left(e\,\frac{I\,B}{e\,d\,V_{\mathrm{H}}}\,R_{\mathrm{sh}}\,d\right)^{-1} = \left(\frac{I\,B}{V_{\mathrm{H}}}\,R_{\mathrm{sh}}\right)^{-1} \tag{3.3}$$

by replacing n and ρ. Note that the mobility μ is independent of the thickness d.

Van der Pauw showed Hall measurements with four contacts to be feasible as long as the sample is homogeneous and much thinner than wide [92]. Furthermore, the four contacts have to be placed at the edges of the sample.

Three Hall measurement setups have been used in the course of this work. One setup was dedicated to measurements at room temperature, whereas two other setups were applied for temperature-dependent Hall measurements.

One of the two temperature-dependent Hall setups is a home-made experiment located at the IEK5 at Forschungszentrum Jülich. It was used for measurements presented in Section 4.3.3. The setup is cooled by liquid nitrogen and can thus attain temperature of 80 K. Contacts consist of small wires that are fixed to the sample by conductive silver. Samples were of size 8 mm × 8 mm. A magnetic field of 2.1 T was used. Further details about this measurement setup can be found in [93].

The second temperature-dependent Hall setup is located at RWTH Aachen University at the I. Physical Institute (IA). It was used for measurements presented in Section 4.4. The setup is a *Physical Property Measurement System (PPMS)* built by *Quantum Design*. The setup is cooled by liquid helium. Measurement temperatures as low as 2 K were attained. The sample size was 8 mm × 8 mm. The magnetic field strength was 1 T. Further details about the setup can be found in [94].

Hall measurements at room temperature were performed in a commercial setup *RH2030* produced by the company *PhysTech*. Quadratic samples of size 11 mm × 11 mm were connected to the setup by four metallic contact pins. Due to the high carrier concentration of the investigated samples, a simple mechanical contact between film

and metal pin was sufficient to obtain an ohmic contact. The ohmic characteristic was controlled before each measurements. The magnetic field possessed a strength of 0.7 T.

Relative errors of Hall measurements of ZnO:Al films on flat substrates (Section 4) have been estimated to be $< 5\%$ for mobility and carrier concentration and $< 1\%$ for resistivity [46]. Furthermore, the error estimation of carrier concentration and resistivity needs to take into account the uncertainty of thickness determination (see Section 3.3.1). Under the assumption of 500 nm thick ZnO:Al films, the final relative error of carrier concentration and resistivity is $< 7\%$ and $< 3\%$, respectively.

Errors of Hall measurements of ZnO:Al films on textured substrates (Section 5) contain two contributions. The first contribution is the just described error of the measurement setup. The second contribution arises from the slight, uncontrollable differences between each deposition process. In particular, the surface morphology of randomly textured substrate varies slightly from substrate to substrate and thus, the mobility might also vary. The second error source was determined by reproducing samples several times using nominally identical deposition parameters. The final errors are given as error bars in the respective graphs.

3.3.3. Optical characterization

A dual beam photospectrometer *Lambda 950* constructed by the company *Perkin Elmer* was used to determine optical properties of ZnO:Al films. The films' transmittance and reflectance can be measured in the wavelength range from 250 to 2500 nm. The wavelength is selected by a grating monochromator. The setup consists of a tungsten-halogen and a deuterium lamp as light sources. An Ulbricht sphere is placed in the light path behind or in front of the sample to determine transmittance or reflectance, respectively. The transmitted or reflected light is measured by a photomultiplier in the ultraviolet to visible wavelength range and by a Peltier-cooled PbS detector in the near infrared wavelength range. The measurement error was estimated to be below 1 %.

3.3.4. Scanning electron microscopy (SEM)

A scanning electron microscope (SEM) relies an the scanning of a surface with a focused electron beam. Thereby, these electrons can either be scattered back or they

induce secondary electrons to be emitted from the surface. Both kinds of electrons can be detected. The number of electrons can be translated into a two-dimensional image of the surface. The image depends on the surface topography and the material properties [95].

A disadvantage of SEMs is their need of conductive samples. Non-conductive materials such as glass can be investigated only if a thin conductive film is deposited upon the surface that might however alter the surface features. Furthermore, SEMs give only a qualitative impression of the surface and lack quantitative information. Advantages of SEMs are the fast and easy measurement process and the possibility to image samples from the milli- to the nanometer scale.

SEM images have been recorded with a *Magellan 400* produced by *FEI* and by a *LEO Gemini 1550* setup from *Carl Zeiss*. Both systems offer an in-lens detector, which detects back scattered and secondary electrons, and a detector of the Everhart-Thornley type, which is sensitive to back scattered electrons only. Furthermore, both SEM systems feature field emissions cathodes with adjustable acceleration voltages to prevent, for example, charging effects at the surface. The cathode of the *LEO Gemini 1550* is a cold-cathode type whereas the *Magellan 400* possesses a Schottky type cathode. The former SEM yields a maximum resolution of 1 to 10 nm in contrast to the latter setup, which offers a resolution below 1 nm.

3.3.5. Atomic force microscopy (AFM)

In this work, the surface morphology of textured substrates and ZnO:Al films is investigated by an atomic force microscope (AFM). The basic principle of an AFM is the interaction of a tip, with a diameter of ideally only a few nanometers, and the sample surface. The tip is mounted on a cantilever. Two major operation modes may be differentiated: contact and non-contact mode.

In contact mode, the tip is brought in close contact to the surface. Van der Waals forces pull the tip towards the surface, thereby inducing a measurable deflection of the cantilever. The tip is now scanned across the surface. The tip height is varied by piezo elements to fulfill the condition of constant deflection, i.e. constant height above the surface. The tip height is recorded and results in the surface topography.

In non-contact mode, an oscillation is applied to the cantilever. When the oscillating tip approaches the surface, it starts to experience van der Waals forces. The van der Waals forces damp the external oscillations. The amplitude changes and a phase shift

between externally applied and actual cantilever oscillation occurs. Both changes are a measure for the force acting on the tip. Similar to the contact mode, the tip is scanned across the surface while adjusting the height such that the force stays constant.

The advantages of atomic force microscopy are the simple sample preparation, the fact, that the surface is not destroyed or altered by the measurement, and the possibility to investigate non-conductive materials. Also, AFMs offer quantitative information about the surface morphology in contrast to e.g. SEMs. Disadvantages result from the fact that AFM images are always a convolution of tip geometry and real surface. Artifacts might thus occur that have to be identified. Exemplarily, steps can never be depicted unaltered and the tip geometry might change resulting in measurement changes. Furthermore, the horizontal movement of the piezo scanners is not completely planar and the piezo scanners might drift in general. Also the scan size is limited to a few tens of micrometers.

AFM images in this work were recorded with a *Nanostation 300* by *SIS*. Non-contact measurements were performed using tips with diameters of 40 nm. Scan size and resolution were usually 10 µm × 10 µm or 20 µm × 20 µm and 512 × 512, respectively. Measurements in contact mode were recorded with tips having diameters below 10 nm. The scan size was between 1 and 2 µm using a resolution of 256 × 256. Non-contact mode was applied to investigate the surface morphology of textured substrates (see Section 5). Contact mode was performed to gain insight into the small structures of flat, as grown ZnO:Al (see Section 4.3).

Two statistical quantities are used in this work to characterize vertical and lateral feature sizes of a given surface. A measure of the vertical feature height is the root mean square (rms) roughness σ_{rms}. It denotes the root mean square deviation of the individual height points with respect to the average height. A measure of the lateral feature size is the autocorrelation length l_{corr} which can be obtained from a fit to the height-height correlation function (HHCF). The one-dimensional height-height correlation function based on profiles along the fast scanning AFM axes is given as

$$H(\tau) = \frac{1}{N(M-m)} \sum_{k=1}^{N} \sum_{n=1}^{M-m} (z_{\mathrm{n+m,\,k}} - z_{\mathrm{n,k}})^2 \tag{3.4}$$

where $m = \tau/\Delta d$. Δd denotes the distance between two neighboring image points in scan direction, N and M represent the number of rows and columns, respectively, that the image consists of, and z is the height at a given x- and y-coordinate. The

experimentally determined HHCF can be fitted by the relation

$$H(\tau) = 2\sigma_{\mathrm{rms}}^2 \left(1 - \exp\left(-\frac{\tau^2}{l_{\mathrm{corr}}^2}\right)\right) \tag{3.5}$$

where σ_{rms} and l_{corr} denote the rms roughness and the autocorrelation length.

3.3.6. X-ray diffraction (XRD)

X-ray diffraction is a non-destructive method to gain information about the crystallographic structure of TCO materials. Interatomic distances are in the range of Ångström ($\sim 10^{-10}$ m). The Abbe diffraction limit implies that the resolution of such structures with electromagnetic waves requires irradiation of wavelength similar to the interatomic distances. X-ray beams fulfill this requirement as their wavelength is between 10^{-8} m and 10^{-12} m.

If monochromatic x-ray irradiation impinges onto the sample under the angle θ, diffraction of the incident beam induces interferences. If furthermore the Bragg condition

$$n\lambda = 2d_{\mathrm{hkl}} \sin\theta \tag{3.6}$$

is fulfilled, constructive interference will occur. n is an integer, λ denotes the wavelength of the incident beam, and d_{hkl} describes the distance between two lattice planes, (hkl) being the Miller indices. Eq. (3.6) accommodates the periodicity of the lattice, but it neglects the actual crystal structure. The information about the crystal structure is contained in the structure factor F_{hkl} which is the Fourier transform of the electron density. The intensity of the diffracted beam is proportional to the square of the absolute value of the structure factor F_{hkl}. As a result, some peaks are forbidden whereas others possess high intensity.

Three different measurement geometries have been used in this work, namely Bragg-Brentano, rocking curve, and pole figure. They will be presented in the following.

Bragg-Brentano (BB) Fig. 3.1(a) illustrates the BB geometry. Incident and diffracted beam exhibit the same angle θ with respect to the substrate surface. Simultaneous variation of θ reveals the lattice plains that fulfill the Bragg condition. The position, intensity, and width of the BB peaks can be analyzed to gain insights into the crystal structure of the sample. The position θ of the reflexes can be used to determine the crystal lattice spacing d_{hkl}. The comparison of the lattice spacing

with literature or with other layers lets us draw quantitative conclusions about the stress in the films (see Section 2.4.4). The peak intensity reveals the relative prevalence of crystal orientations. The peak width, determined as the full width at half maximum (FWHM), may be used to calculate the size of coherently scattering regions g by applying the Scherrer formula [96]. g is often referred to as vertical grain size [47, 97]. In my opinion, this nomenclature is misleading. Often the vertical grain size g is taken as a measure for the lateral grain size although the relation between both quantities is unclear and not well-established[2]. As a consequence, the peaks' FWHM in BB geometry will be used without the evaluation of the Scherrer formula as a measure of crystalline quality.

Fig. 3.1. The scheme [98] illustrates two different XRD measurement geometries. (a) Bragg-Brentano geometry: The incident beam possesses the same angle θ as the diffracted beam. By simultaneously varying both angles, one detects the lattice plains that fulfill the Bragg condition. Note that only lattice plains parallel to the surface contribute to the diffracted signal. (b) Rocking curve measurement: The angle θ is fixed to a value showing the desired diffraction peak in Bragg-Brentano geometry. One rotates the substrate to detect the lattice plains perpendicular to the scan normal.

Rocking curve (RC) Fig. 3.1(b) illustrates the RC geometry. X-ray source and detector are set to an angle of interest θ that fulfills the Bragg condition (3.6). Then the substrate is tilted ("rocked") parallel to incident and diffracted beam. Only crystallites possessing lattice plains perpendicular to the scan normal contribute to the signal. Thereby, one can evaluate the degree to which the crystallites of a

[2] Note that the lateral grain size in highly c-textured ZnO:Al matters e.g. for the electronic transport in the material (see Section 4.1.3).

certain orientation are aligned. The FWHM in RC geometry is a measure of the orientational order. The better the crystallite alignment, the smaller the FWHM.

Pole figure RC measurements detect the crystallite tilt in one direction only. Pole figures however allow the measurement of the orientational distribution in two dimensions. Fig. 3.2 shows the relevant geometry and measurement angles. Similar

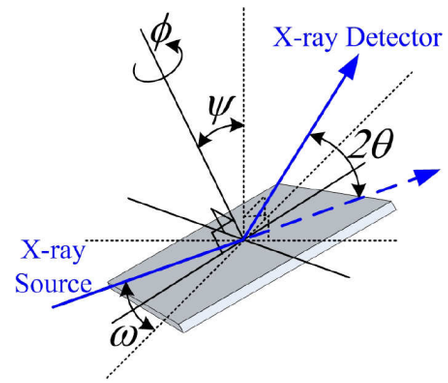

Fig. 3.2. Scheme [99] of pole figure measurements. The Bragg condition is fulfilled for a particular angle θ. For each angle $\psi = 0 - 90\,^{\circ}$, one varies $\phi = 0 - 360\,^{\circ}$.

to the rocking curve, one chooses a particular angle for an orientation (hkl) of interest. Then the polar angle ψ is varied step by step. For each value of ψ, one scans the azimuthal angle ϕ. The resulting intensities are plotted in a two dimensional graph in polar coordinates. The radial axes and the polar angle in the graph correspond to the polar and azimuthal angles of the measurement. Examples of pole figures can be found in Section 5.1.2.2.

Experimental setting BB and RC measurements have been performed in a diffractometer *Bruker D8 Advance*. Electrons with a power of 1.6 kW are accelerated onto a copper anode. A characteristic x-ray spectrum occurs of which one uses the most intense irradiation, the CuKα line with a wavelength of 1.54 Å. Pole figures were recorded by a *Philips X'Pert Pro MRD* with an Eulerian cradle again using CuKα radiation.

3.3.7. Raman spectroscopy

Raman spectroscopy relies on the interaction of monochromatic light with molecular vibrations or phonons [100]. The inelastically scattered photons either gain or loose energy. The energy shift can be detected and gives information about the vibrational modes and thus, the bonding and microstructural properties of the investigated solid. Raman spectra were measured with an excitation wavelength of 488 nm using a diode pumped solid state laser *Saphhire 488-100* from *Coherent*. A laser power of 3.5 µW was applied during a measurement time of 60 s. Measurements were performed from layer and substrate side, respectively. The latter measurement is subsequently subtracted from the former to extract the signals that are related to the film under investigation.

3.3.8. Characterization of solar cells

Current-voltage characteristic The current was measured under illumination as function of voltage using a *SMU 238* by *Keithley*. A class A sun simulator that features xenon and halogen lamps was applied to produce an AM1.5 solar spectrum with a radiation power density of 100 mW/cm^2 at a temperature of 25 °C. The measurement error was estimated to be less than 2 %. Further details about current-voltage measurements of thin-film solar cells can be found in [101].

External quantum efficiency The measurement of the external quantum efficiency (EQE) is based on the evaluation of the spectral response (SR) of the solar cell as a function of wavelength λ. The spectral response is given by the ratio between the generated current density and the radiation power density. The EQE

$$EQE(\lambda) = SR(\lambda)\,\frac{hc}{e\lambda} \tag{3.7}$$

can be expressed in terms of the spectral response. h, c, and e denote Planck's constant, the speed of light in vacuum, and the electron charge, respectively. The subcells of tandem devices are measured by applying a bias light that is only absorbed in one of the subcells. Consequently, this subcell does not limit the current and the other subcell may be measured. Additional information about the measurement of external quantum efficiencies can be found elsewhere [101, 102].

3.3.9. Optical fits

Description of fit model Simulations of transmittance and reflectance spectra have been performed with the programm SCOUT [103]. The optical data was fitted using a harmonic oscillator, an O'Leary-Johnson-Lim (OJL) model, and an extended Drude model with a frequency-dependent damping factor. The basic physical concepts of the Drude model have been described in Section 2.2.2. The frequency-dependent damping factor

$$\Gamma_{\mathrm{Dr}}(\omega) = \Gamma_{\mathrm{L}} - \frac{\Gamma_{\mathrm{L}} - \Gamma_{\mathrm{H}}}{\pi} \left[\arctan\left(\frac{\omega - \Omega_{\Gamma\mathrm{Dr}}}{\Gamma_{\Gamma\mathrm{Dr}}}\right) + \frac{\pi}{2}\right] \tag{3.8}$$

consists of the low-frequency (Γ_{L}, $\omega = 0$) and high-frequency (Γ_{H}, $\omega = \infty$) damping factors, the changeover frequency $\Omega_{\Gamma\mathrm{Dr}}$, and the function width $\Gamma_{\Gamma\mathrm{Dr}}$. More details about this model approach can be found in [48, 104]. Optical mobilities μ_{opt} and carrier concentrations n can be derived from the damping frequency $\Gamma_{\mathrm{Dr}}(\omega)$ and the plasma frequency Ω_{Dr}:

$$\mu_{\mathrm{opt}} = \frac{e}{m^*} \Gamma_{\mathrm{Dr}}(\Omega_{\mathrm{Dr}}) \tag{3.9}$$

$$n = \frac{\epsilon_0\, m^*}{e^2}\, \Omega_{\mathrm{Dr}}^2 \tag{3.10}$$

e is the elementary charge, ϵ_0 and m^* denote the vacuum permittivity and the effective mass of charge carriers. Note that I evaluated the damping frequency $\Gamma_{\mathrm{Dr}}(\Omega_{\mathrm{Dr}})$ at the plasma frequency Ω_{Dr}. Optical and Hall carrier concentrations were assumed to be equal. The effective mass was tuned to meet this requirement. Then, one can compute the optical mobility μ_{opt} using the predetermined effective mass. Note however that the optical resistivity is independent of the effective mass. Therefore, the uncertainty of the optical resistivity is lower than the uncertainty of the optical mobility. As a consequence, discussions will focus on the optical resistivity. Error bars were obtained by fitting the same spectrum several times with different starting conditions. Fig. 3.3 shows an example of an optical fit. Experimental and simulated transmittance and reflectance spectra exhibit a reasonable agreement.

Discussion of the optical model Many authors in the field of TCO research use optical fits for reasons discussed in the next paragraph. Three models may be distinguished: (1) The classical Drude model [105–110], modified Drude models using frequency dependent damping terms by (2) Mergel and Qiao [48, 104, 111, 112] or by (3) Pflug et al. [33, 50, 112, 113].

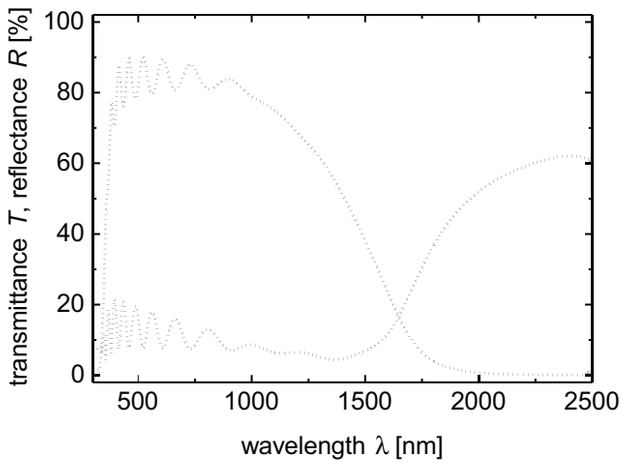

Fig. 3.3. Transmittance and reflectance of flat ZnO:Al layer. The grey lines represent the experimental spectra. The black dotted lines show the simulated spectra. In this case, the ratio between the optically determined thickness and the one obtained from a surface profiler (see Section 3.3.1) was $d_{\mathrm{opt}}/d_{\mathrm{sylus}} = 1.05$.

It is striking that all authors except for Mergel and Qiao [48] derived optical resistivities similar to or higher than the Hall resistivity. In contrast, my derived optical resistivity was significantly lower than the Hall resistivity (e.g. compare Fig. 4.18 in Section 4.3.3). Furthermore, I calculated optical mobilities in the range of $80\,\mathrm{cm}^2/\mathrm{Vs}$ in contrast to mobility values of $< 40\,\mathrm{cm}^2/\mathrm{Vs}$ as given in literature.

Mergel and Qiao compared the classical Drude model to the extended Drude model. First, the extended Drude model yielded better fit results as compared to the classical Drude model. Second, the optical mobility obtained with the extended Drude model was generally higher than the mobility calculated with the classical Drude model. But even the application of extended Drude models yielded a rather low optical mobility [33, 111]. I attribute the low optical mobilities to the evaluation of the damping constant. Most authors determine the optical mobility using the low-frequency damping constant Γ_{L} [33, 50, 111–113], whereas Mergel and Qiao employ the damping constant at the plasma frequency $\Gamma_{\mathrm{Dr}}(\Omega_{\mathrm{Dr}})$ to calculate the optical mobility applying Eq. (3.9). Mergel and Qiao showed that, at least for their extended Drude model, the optical mobility derived from the low-frequency damping constant yielded lower mobility values than the Hall measurements. The next paragraph will

show that optical mobilities lower than the Hall mobilities are physically unlikely. Therefore, the evaluation of the damping constant at the plasma frequency will be adopted in this work. Generally, one must discuss if the obtained optical mobility or resistivity is reasonable within the general understanding of conductivity in the investigated material. I will do so in Section 4.3.

Application of optical fits The resistivity of polycrystalline ZnO:Al consists of two components: Scattering within the grain ρ_g and at grain boundaries ρ_{gb}. Following Matthiessen's rule, they add up to the total resistivity of the film $\rho_{tt} = \rho_g + \rho_{gb}$. Hall measurements determine the total resistivity of the film because the current is forced to flow through grains and grain boundaries. In contrast, optical measurements induce an electric field that causes the charge carriers to oscillate within a few nanometers. As the average electron path length is smaller than the grain size, the charge carriers are only scattered within the grain and hardly at grain boundaries [105, 107, 113]. The determination of electrical properties using both techniques, Hall measurements and optical fits, enables to identify the relative fraction of intra-grain and inter-grain scattering.

3.4. Post-deposition processes

3.4.1. Annealing

Post-deposition annealing was performed in a small oven (*ROK/A 4/300*, *Heraeus*), which offers a homogeneous area of approximately 3 cm × 3 cm, and in a larger oven (*FRH-150/250/1100*, *Linn High Therm*), where substrates of size 10 cm × 10 cm could be treated.

The small oven was used for the annealing of ZnO:Al on textured substrates (see Section 5.1.1.4). Only samples of size 11 mm × 11 mm dedicated to Hall measurements were processed. The larger oven was applied to ZnO:Al on flat substrates in order to prepare enough material for different characterization techniques (see Section 5.1.1.4).

Capping layers consisted of 60 nm phosphorus doped a-Si:H films and were deposited by PECVD. After the annealing, further characterization required the capping layers to be removed. This was done by reactive ion etching in an *AMR* system by *Plasma Technology* using a gas mixture of CHF_3/CF_4. Power, pressure, and flow were 300 W, 3 Pa, and 20 sccm, respectively. After 3 min, the silicon capping layer was removed.

One sample was capped but not annealed. After cap removal, no difference was found between the electrical properties before and after capping. Hence, the cap deposition and removal did not influence the layer's electrical properties.

3.4.2. Damp heat degradation

Damp heat degradation was carried out in a climatic chamber *NCC4020* built by the company *Nema*. The degradation was performed at 85 °C and 85 % humidity. Hall effect samples were attached to glass substrates using a polyimide film (*Kapton*, *Du Pont*). The glass substrates were then vertically positioned within the climatic chamber in order to prevent accumulation of condensed water on the samples' surface.

After approximately 24, 100, 250, 500, and 1000 h, the degradation process was interrupted, the samples were removed from the climatic chamber and subjected to Hall measurements.

4. ZnO:Al on flat substrates

Understanding the conductivity mechanisms in ZnO:Al is of crucial importance to optimize the material for the application in optoelectronic devices. Therefore, Sections 4.1 and 4.2 are dedicated to my current understanding of conductivity mechanisms in ZnO:Al. In Section 4.1, common conductivity models proposed in literature are discussed. Problems and limitations are identified. Based on this evaluation, a more advanced conductivity model is deduced that resolves inconsistencies and offers a better description of experimental data. This model comprises the tunneling of charge carriers through potential barriers at grain boundaries. In Section 4.2, this new model is applied to data from literature to show its applicability and explanatory power. Section 4.3 and 4.4 are dedicated to the optimization of ZnO:Al conductivity. Here, optimization implies two aspects: On the one hand, it is desirable to use stable and low cost deposition conditions without deteriorating the film properties. An important deposition parameter in this respect is the deposition temperature. A concept for the reduction of deposition temperature based on a seed layer approach is presented in Section 4.3. On the other hand, from a rather scientific point of view, one wants to explore the limits of conductivity and improve it irrespective of time and effort. A post-deposition annealing process has been shown to boost the mobility. Thus, Section 4.4 presents a comprehensive investigation of the annealing process. The results of seed layer and annealing approach are interpreted on the basis of the conductivity model that has been proposed in Section 4.1.

4.1. ZnO:Al conductivity model

Two contributions to ZnO:Al resistivity may be differentiated: scattering of charge carriers within the grain ρ_g and at grain boundaries ρ_{gb}. Two mechanisms that describe effects within the grain, ionized impurity and electron-phonon scattering, will be included into the proposed conductivity model. Grain boundary scattering comprises three possible mechanisms: thermionic emission, field emission, and thermionic field emission.

Further scattering mechanisms within the grain such as dislocation scattering [114–117], neutral impurity scattering [115, 117, 118], or scattering due to weakly localized

electrons [119–121] will not be considered in the proposed model. Reasons for the disregard of dislocation and neutral impurity scattering can be found in [115, 117]. Weak localization scattering is beyond the scope of this work. However, it might explain certain features of temperature-dependent Hall measurements such as a decreasing resistivity with increasing temperature.

The focus of this section is threefold: (1) A critical review of ionized impurity scattering and thermionic emission theory is presented. (2) I elaborate the mathematical description of thermionic field emission and field emission at grain boundaries. (3) Two criteria will be given that hint to the dominant scattering process at grain boundaries.

4.1.1. Ionized impurity scattering

ZnO:Al with high carrier concentrations exceeding $\sim 10^{19}\,\mathrm{cm}^{-3}$ possesses a large amount of ionized donors. They can be intrinsic donors such as oxygen vacancies or extrinsic donors such as aluminum. Ionized donors are charged. Therefore, they scatter charge carriers. The development of the description of ionized impurity scattering is illustrated in detail by Ellmer [54]. Here, the theory will be shortly summarized and material parameters are determined. A critical discussion ends this section.

Theory Conwell and Weisskopf assumed the ionized impurity to induce a truncated Coulomb potential [122]. However, one has to take into account the screening of the Coulomb potential by free charge carriers reducing the Coulomb potential's strength and scattering ability. Brooks [123] and Herring, and Dingle [124] incorporated the screening into the description of ionized impurity scattering[1]. The formula for ionized impurity scattering as derived by Dingle

$$\mu_{\mathrm{ii}} = \frac{3\,(\epsilon_{\mathrm{r}}\epsilon_0)^2\,h^3}{m^{*2}\,e^3}\,\frac{Z_{\mathrm{D}} - Z_{\mathrm{A}}\,K}{Z_{\mathrm{D}}^2 + Z_{\mathrm{A}}^2\,K}\,\frac{1}{F_{\mathrm{ii}}} \tag{4.1}$$

contains the screening function F_{ii}, the static dielectric constant ϵ_{r}, the vacuum permittivity ϵ_0, and the Planck constant h. Further parameters are the effective mass m^* and the compensation ratio $K = n_{\mathrm{A}}/n_{\mathrm{D}}$ of acceptor n_{A} and donor n_{D} concentrations. Z_{D} and Z_{A} denote the charge of donors and acceptors, respectively.

[1] Brooks and Herring derived an expression for non-degenerate semiconductors. Dingle adapted it for degenerate semiconductors.

Note that Eq. (4.1) assumes only one type of acceptor and donor charge. The analytical expression for the screening function [53][2]

$$F_{\mathrm{ii}}(\xi_0, \xi_1) = \left\{1 + \frac{4\xi_1}{\xi_0}\left(1 - \frac{\xi_1}{8}\right)\right\}\ln(\xi_0 + 1) - \frac{\xi_0}{\xi_0 + 1} - 2\xi_1\left(1 - \frac{5}{16}\,\xi_1\right) \tag{4.2}$$

with

$$\xi_0 = (3\pi^2 n)^{1/3}\,\frac{\epsilon_{\mathrm{r}}\epsilon_0\,h^2}{e^2\,m^*}, \tag{4.3}$$

and

$$\xi_1 = 1 - \frac{m_0^*}{m^*} \tag{4.4}$$

accounts for the non-parabolicity of the ZnO conduction band by the introduction of a n-dependent effective mass

$$m^*(n) = m_0^*\left\{1 + 2C\,\frac{\hbar^2}{m_0^*}\,(3\pi^2 n)^{2/3}\right\}. \tag{4.5}$$

m_0^* is the effective mass at the minimum of the conduction band and C is a non-parabolicity parameter.

Ellmer fitted data of single crystalline ZnO by an empirical formula proposed by Masetti et al. to estimate an upper mobility limit for ZnO:Al [54, 126]. The empirical model developed originally for highly doped silicon takes into account phonon scattering, and scattering at single ionized impurities as well as clusters. Scattering at ionized impurity clusters assumes the creation of dopant clusters for highly doped materials that scatter carriers more efficiently due to their higher effective charge.

Material parameters The description of ionized impurity scattering by Eq. 4.1 contains three material parameters that are not well-known as they are difficult to measure directly:

1. **Donor and acceptor charge $Z_{\mathrm{D,A}}$**
   Two main doping mechanisms are discussed in literature [54]. The first one is the doping by extrinsic dopants such as boron, aluminum, or gallium. These extrinsic dopants possess a charge of $Z_{\mathrm{D}} = 1$. The second doping mechanism could be intrinsic doping by oxygen vacancies resulting in $Z_{\mathrm{D}} = 2$. Look et al. showed

[2] Note that the expression for ξ_0 has a minor fault in [53] as for example mentioned by [125].

the main donor to be gallium in their ZnO:Ga films [127]. Furthermore, they identified Zn-vacancies as main acceptor which is supported by theoretical investigations [128]. Thus the further assumption in this work will be $Z_D = 1$ (extrinsic doping by aluminum) and $Z_A = 2$ (Zn-vacancy acceptor). Note that this assumption implies, firstly, the neglect of ionized impurity clusters and, secondly, a maximum compensation ratio of $K = 50\%$.

2. **Compensation ratio *K***
   The compensation ratio's impact on the mobility is shown in Fig. 4.1 for $K = 5\%$ and $K = 10\%$. Look et al. determined compensation ratios between 3% and 12% for ZnO:Ga films with carrier concentrations between $7.8 \times 10^{20}\,\mathrm{cm}^{-3}$ and $12.8 \times 10^{20}\,\mathrm{cm}^{-3}$ [127, 129]. If not otherwise stated, I assume a compensation ratio of $K = 0\%$.

3. **Effective mass** m^*
   The effective mass is controversially discussed in literature. Values of $m^* = 0.28m_e$ [33, 105, 106], $m^* = 0.34m_e$ [127], $m^* = 0.5m_e$ [109] and $m^* = 0.6m_e$ [104] may be found. Of course, these constant values assume implicitly a parabolic conduction band, i.e. the effective mass is independent of carrier concentration. However, a more realistic description takes into account the non-parabolicity of the conduction band. As a consequence, the effective mass becomes dependent on carrier concentration. This dependence is described by Eq. 4.5 which contains two free parameters, m_0^* and C, that need to be fixed.

Fig. 4.1 shows the mobility as a function of carrier concentration for three different parameter sets of m_0^* and C. The mobility determined solely by ionized impurity scattering for $K = 0\%$ should be an upper limit because all other scattering mechanisms, that might further decrease the mobility, were neglected. For the as-grown layers (solid symbols) in Fig. 4.1, all three theoretical curves (solid lines) may represent this upper limit because the experimental data does not exceed them. However, the annealed samples and the optically characterized as-grown films show mobility values close to or even slightly above the curve determined by parameters of Young and coworkers.

The effect of phonon scattering was eliminated by measuring the mobility at low temperatures (see Section 4.4). The value presented in this work clearly exceeded the limit computed after Young and coworkers. Therefore, it is assumed that this parameter set overestimates the impact of ionized impurity scattering. Both, the parameter sets of Ruske et al. and Fujiwara

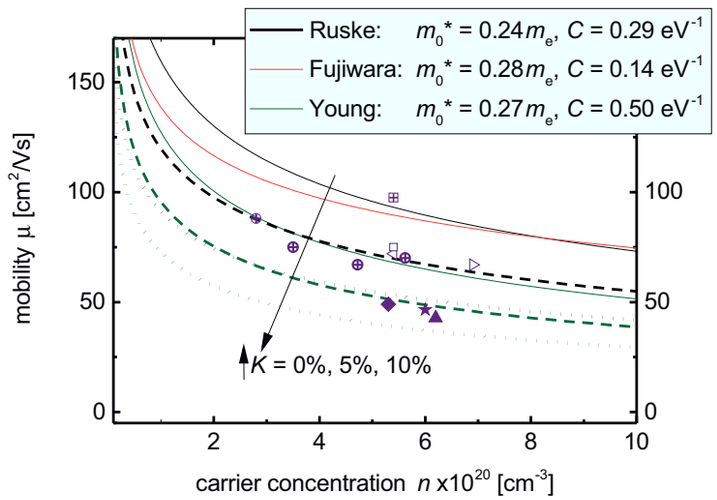

Fig. 4.1. The mobility limited by ionized impurity scattering was computed as a function of carrier concentration using Eq. 4.1. Three different parameters sets for the effective mass were evaluated: Ruske et al. [113] (black lines), Fujiwara and Kondo [110] (red lines), and Young et al. [130] (green lines). The parameters m_0^* and C are given in the graph. For Ruske et al. and Young et al., the compensation ration K was varied from 0% (solid lines), to 5% (dashed lines), and 10% (dotted lines). Here, $Z_\mathrm{D} = 1$ and $Z_\mathrm{A} = 2$ was assumed. The experimental data was divided into as-grown layers (▲ [55], ♦ [8], ⋆ [131]), as-grown layers whose mobility was determined by optical fits (⊕ this work), layers annealed under a capping layer and measured at room temperature (□ this work, ◁ [24], ▷ [113]), annealed samples measured at low temperatures to eliminate phonon scattering (⊞ this work).

and Kondo, seem reasonable. They have been obtained by fitting optical data. Ruske et al. used an extended Drude model whereas Fujiwara and Kondo applied the classical Drude model. The extended Drude model is believed to be more appropriate for reasons outlined in Section 3.3.9. Although further uncertainties with regard to the optical fits of Ruske et al. remain (see again Section 3.3.9), their parameter set will be used simply because further values for m_0^* and C are lacking. This parameter set yields an effective mass of $0.35 m_\mathrm{e}$ for a carrier concentration of 5×10^{20} cm^{-3}. This value is close to $m^* = 0.34 m_\mathrm{e}$ determined by Look [127]. Yet it is lower than the values of $m^* = 0.39 - 0.45 m_\mathrm{e}$ that have been extracted from optical fits in this work.

Discussion Ionized impurity scattering is often denoted as the dominant scattering mechanism in highly doped ZnO with carrier concentrations in the range of 10^{20}-10^{21} cm^{-3} [54, 55, 106, 113, 115, 127, 131–135]. This conclusion is mostly drawn from the evaluation of Hall mobility data as a function of carrier concentration [54, 55, 115, 131, 134] or temperature [127, 132, 133]. Also optical fits were employed [106, 113]. Temperature-independent mobility is often declared as an indicator for ionized impurity scattering. However, temperature-independent mobility does not imply necessarily a mobility limitation by ionized impurity scattering. The conductivity model developed in this section is able to explain temperature-independent mobility although scattering at grain boundaries limits the mobility. In addition, the $\mu - n$ dependence may be well explained using the proposed conductivity model. The similarity of mobility or resistivity values derived by optical fits and Hall measurements is also used as an indicator for ionized impurity scattering. Yet optically determined values are open to several doubts (see Section 3.3.9). Moreover, the comparison of optical and Hall resistivity in Section 4.3 revealed significantly higher optical than Hall resistivities. In conclusion, the often used indicators for the domination of ionized impurity scattering are controversial and rather doubtful.

4.1.2. Electron-phonon scattering

The scattering of electrons by phonons in metals is described by the Bloch-Grüneisen law [44, 136, 137]. The equation for electron-phonon interaction

$$\rho_{\mathrm{ph}} = \lambda_{\mathrm{tr}} \frac{4\pi^3 m^* k_{\mathrm{B}}}{he^2} \frac{1}{n} \Theta \left(\frac{T}{\Theta}\right)^5 \int_0^{\Theta/T} \frac{x^5 \mathrm{d}x}{(\exp(x)-1)(1-\exp(-x))} \tag{4.6}$$

contains the electron-phonon coupling constant λ_{tr}, the Debye temperature Θ, the electron charge e, the Boltzmann constant k_{B}, the Planck constant h, the effective mass m^* and the carrier concentration n. λ_{tr} and Θ are used as fit parameters to describe temperature-dependent resistivity measurements. Note the reciprocal dependence of ρ_{ph} and n. Assuming constant m^*, λ_{tr}, and Θ, the resistivity due to electron-phonon scattering decreases with increasing carrier concentration. However, the mobility defined by $\mu_{\mathrm{ph}} = (\rho_{\mathrm{ph}} ne)^{-1}$ is independent of the carrier concentration. Fig. 4.2 shows the mobility derived from Eq. (4.6) as a function of measurement temperature for various Debye temperatures. First, the electron-phonon scattering is only relevant for temperatures exceeding 150 - 200 K. Second, Fig. 4.2 shows a lower

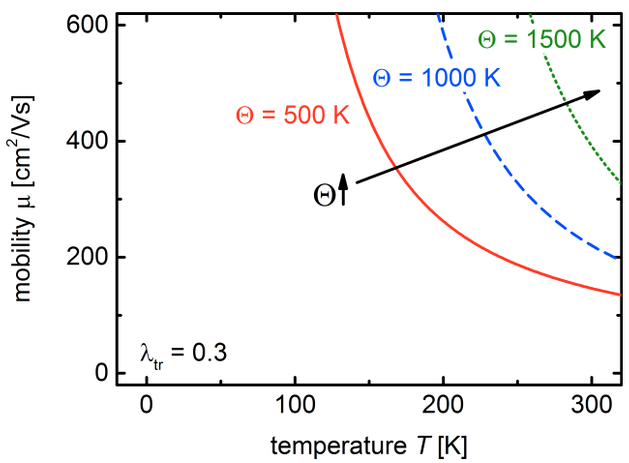

Fig. 4.2. The mobility is shown as a function of measurement temperature. Three different values of the fit parameter Θ are evaluated. The electron-phonon coupling constant was fixed at $\lambda_{tr} = 0.3$.

Debye temperature to imply a stronger electron-phonon scattering and thus a lower mobility.

The Bloch-Grüneisen law has been used to describe electron-phonon scattering in highly doped TCOs [133, 135, 138]. Instead of the Bloch-Grüneisen law, some authors explicitly compute the scattering by optical phonons and by acoustic phonons interacting through deformation or piezoelectric potentials [114, 127, 139–141]. To my knowledge, a detailed comparison between both descriptions of electron-phonon scattering has not yet been performed and it is out of the scope of this work to do so. Certainly, future investigations should comprise the differences and applicability of both theories. Until then, the more general and simpler Bloch-Grüneisen law will be applied.

4.1.3. Grain boundary scattering

Polycrystalline films are composed of small crystalline grains separated by grain boundaries. A grain boundary is a region of disordered atoms between adjacent grains. Disordered atoms imply incomplete atomic bonding resulting in a large number of defects. The defects can trap electrons. The trapping of electrons induces

potential energy barriers at the grain boundaries that may scatter mobile electrons traveling from one grain to another.

Fig. 4.3 illustrates three possible transport paths across such potential barriers at grain boundaries: thermionic emission, thermionic field emission, and field emission[3]. I will firstly focus on thermionic emission because most of the concepts involving grain boundaries were developed assuming this transport mechanism. Furthermore, the section about thermionic emission will critically and in detail review literature about this mechanism. I will identify possible inconsistencies and problems. Subsequently, a description of field and thermionic field emission is presented. Here, Stratton's field emission theory [142, 143] is for the first time adapted to grain boundaries, that is to double Schottky barriers. In a final step, I review criteria that reveal which of the three transport processes across grain boundaries dominate for a given material.

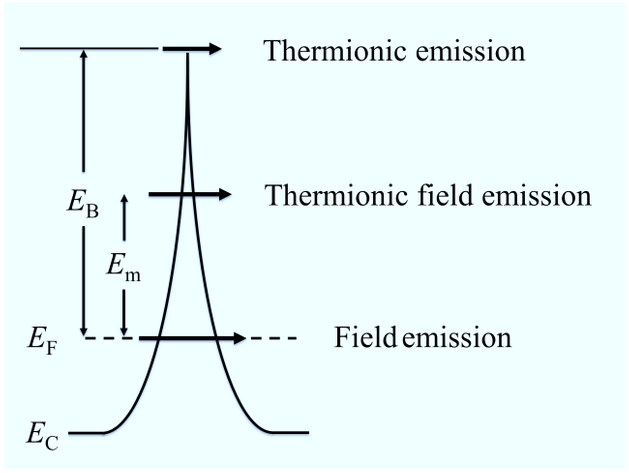

Fig. 4.3. A potential barrier at a grain boundary in degenerate semiconductors is illustrated. E_C and E_F denote the energy level of the conduction band and the Fermi level, respectively. The Fermi level lies within the conduction band. E_B measures the barrier height from the Fermi level to the top of barrier. Electrons can pass the potential barrier by thermionic emission over the barrier, by thermally activated tunneling (thermionic field emission) at the energy E_m, and by tunneling (field emission) at the Fermi level.

[3]Note that "field emission" is also denoted as "tunneling".

4.1.3.1. Thermionic emission

Thermionic emission over Schottky barriers Thermionic emission theory across Schottky barriers is developed following Rhoderick and Williams [144] and subsequently applied to double Schottky barriers, i.e. grain boundaries.

The thermionic emission theory assumes the transfer of electrons over the barrier to be the dominant transport path across Schottky barriers. The concentration of electrons with energies larger than the barrier

$$\tilde{n} = \int_{E_\mathrm{B}}^{\infty} D(E) f(E,T,V) \mathrm{d}E \approx N_\mathrm{c} \exp\left\{-\frac{E_\mathrm{B} - eV}{k_\mathrm{B} T}\right\} \tag{4.7}$$

is determined by the density of states $D(E)$ multiplied by the occupancy represented by the Fermi-Dirac function $f(E,T,V)$, and integrated for energies larger than the barrier. Using the Boltzmann approximation to the Fermi-Dirac function, $\tilde{n}$ may be expressed by the effective density of states $N_\mathrm{c} = 2(2\pi m^* k_\mathrm{B} T/h^2)^{3/2}$, the barrier height E_B, and the external applied voltage V. Further parameters are the electron charge e, the Boltzmann constant k_B, and the temperature T. Note that the Fermi level was taken to be the reference level at zero energy. The area density of electrons hitting the barrier per second is given by $\tilde{n}\bar{v}/4$. $\bar{v}$ is the average thermal velocity of electrons. Assuming a Maxwellian distribution of electron velocities, $\bar{v}$ can be computed as $\bar{v} = (8k_\mathrm{B}T/\pi m^*)^{1/2}$. One further assumes that such electrons incident on the barrier are not reflected by e.g. phonons. Moreover, one has to take into account the electrons flowing from the metal into the semiconductor. Then, the thermionic current J_TE across a Schottky barrier of height E_B is

$$J_\mathrm{TE} = \frac{e\bar{v}}{4} N_\mathrm{c} \exp\left(-E_\mathrm{B}/k_\mathrm{B}T\right) \left\{\exp\left(eV/k_\mathrm{B}T\right) - 1\right\}. \tag{4.8}$$

With the effective density of states N_c and the average thermal velocity $\bar{v}$, Eq. (4.8) becomes the familiar relation

$$J_\mathrm{TE} = A^* T^2 \exp\left(-E_\mathrm{B}/k_\mathrm{B}T\right) \left\{\exp\left(eV/k_\mathrm{B}T\right) - 1\right\} \tag{4.9}$$

containing the Richardson constant $A^* = 4\pi m^* e k_\mathrm{B}^2/h^3$. The neglected effect of reflection at the barrier can be integrated into the model by modifying the Richardson constant [11]. The synthesis of thermionic and diffusion theory yields the relation $J = J_\mathrm{TE}/(1 + \bar{v}/v_\mathrm{D})$ where v_D is an effective diffusion velocity [145]. If $\bar{v} \gg v_\mathrm{D}$ then

$J \approx J_{\mathrm{TE}}$ and thermionic emission theory applies. Orton showed thermionic emission theory to be appropriate for polycrystalline materials [11, 12].

Thermionic emission across grain boundaries Let us now apply Schottky barrier theory to double Schottky barriers, that is grain boundaries. As a consequence of the generally high number of grain boundaries within the material, one can assume the voltage drop across one grain boundary to be small[4]. Then, the grain boundary limited conductivity σ of a polycrystalline material with grain size L can be computed using the relation

$$\sigma = \frac{L}{2} \left.\frac{\mathrm{d}J_{\mathrm{TE}}}{\mathrm{d}V}\right|_{V=0}. \tag{4.10}$$

The factor 1/2 occurs because the voltage drops across two equal Schottky barriers [12, 146]. The grain size L appears because the conductivity is after Matthiessen's rule proportional to the reciprocal number of grain boundaries #gb, i.e. $\sigma \sim 1/\#\mathrm{gb}$. As the number of grain boundaries equals furthermore the reciprocal grain size, it follows $\sigma \sim (1/\#\mathrm{gb} = 1/(1/L) = L)$. Using Eq. (4.9) in conjunction with the just outlined modifications, the conductivity of a polycrystalline material is obtained by

$$\sigma_{\mathrm{TE}} = L \frac{eA^*}{2k_{\mathrm{B}}} T \exp\left(-\frac{E_{\mathrm{B}}}{k_{\mathrm{B}}T}\right). \tag{4.11}$$

Similar expressions have been derived by Petritz [10] and Seto [9]. However, Seto uses Eq. (4.8) in the form

$$J_{\mathrm{TE}} = \frac{e\bar{v}}{4} \underbrace{N_{\mathrm{c}} \exp\left(-E_{\mathrm{C}}/k_{\mathrm{B}}T\right)}_{=n} \exp\left[-(E_{\mathrm{B}} - E_{\mathrm{C}})/k_{\mathrm{B}}T\right] \Big\{ \exp\left(eV/k_{\mathrm{B}}T\right) - 1 \Big\} \tag{4.12}$$

where E_{C} is the energy of the conduction band with respect to the Fermi level. The expression for the carrier concentration n is only valid for non-degenerate semiconductors because it is based on Boltzmann statistics. Thus, Seto's model must not be applied to degenerate materials! For degenerate semiconductors, Eq. (4.11) is

[4] A voltage of 1 V is applied during Hall effect measurements across a sample size of approximately 1 cm. Assuming a grain size of 40 nm, the voltage of 1 V is distributed across 1 cm/40 nm = 250 000 grain boundaries. The voltage drop at each of these 250 000 grain boundaries is thus roughly 1 µV. Consequently, it holds at room temperature that 1×10^{-6} eV $\ll 25 \times 10^{-3}$ eV $= k_{\mathrm{B}}T$.

appropriate given that $E_\mathrm{B} \gg k_\mathrm{B}T$. The conductivity derived by Seto

$$\sigma_\mathrm{TE} = Ln \frac{e^2}{2\sqrt{2\pi m^* k_\mathrm{B}}} \frac{1}{\sqrt{T}} \exp\left[-(E_\mathrm{B} - E_\mathrm{C})/k_\mathrm{B}T\right] \tag{4.13}$$

and Eq. (4.11) differ in their temperature dependence and in the exponent. Seto gives the barrier height relative to the conduction band whereas Schottky theory measures the barrier with respect to the Fermi level. Note that, similar to Eq. (4.11), a factor 1/2 was also appended to Seto's equation.

Uniform barriers The barrier height E_B was derived by Seto based on the trapping of electrons at grain boundaries [9]. Depending on the doping concentration n_D, two different expressions for the barrier height

$$E_\mathrm{B} = \frac{e^2 L^2}{8\epsilon_0\epsilon_\mathrm{r}} n_\mathrm{D} + E_\mathrm{C} \qquad Ln_\mathrm{D} < Q_\mathrm{t} \tag{4.14a}$$

$$E_\mathrm{B} = \frac{e^2 Q_\mathrm{t}^2}{8\epsilon_0\epsilon_\mathrm{r}} \frac{1}{n_\mathrm{D}} + E_\mathrm{C} \qquad Ln_\mathrm{D} > Q_\mathrm{t} \tag{4.14b}$$

may be computed. Here, Q_t denotes the density of occupied traps per area at grain boundaries, ϵ_0 and ϵ_r are the vacuum permittivity and the static dielectric constant. The barrier height as derived by Seto is measured relative to the bottom of the conduction band. As the barrier height in Schottky theory is given with respect to the Fermi level, one has to modify Seto's barrier height to make it suitable for Schottky theory. The condition $Ln_\mathrm{D} < Q_\mathrm{t}$ describes a situation of only partially filled traps, and grains that are completely depleted of electrons. For $Ln_\mathrm{D} > Q_\mathrm{t}$, the traps are completely filled with electrons and the grains are partially depleted. Neglecting the n-dependence of the Fermi level, one sees from Eqs. 4.14a and 4.14b that E_B firstly increases linearly with n_D, reaches a maximum at $Ln_\mathrm{D} = Q_\mathrm{t}$ and then decreases as $1/n_\mathrm{D}$. The highly doped ZnO layers investigated in this work all fulfill the condition $Ln_\mathrm{D} \gg Q_\mathrm{t}$. Then, the convenient assumption $n_\mathrm{D} \approx n$ is justified.

Seto's model assumes the trap energy E_t to have δ-shaped distribution and to be smaller than the Fermi energy. Interestingly, Baccarani et al. found in silicon samples for this monovalent case under specific conditions a temperature-dependent barrier height [147]. Furthermore, Baccarani et al. modified the grain boundary trapping model taking into account energetically distributed traps. However, they found their data of polycrystalline silicon samples to be better described by the monovalent than by the continuous trapping states model.

Fluctuating barriers A further assumption of the presented models is the uniform

barrier height. Spatial fluctuations of Schottky barrier heights were introduced by Werner and Güttler to explain current/voltage and capacitance/voltage measurements [148]. Werner applied this model to grain boundaries to elucidate curved Arrhenius plots as observed for many polycrystalline materials [149]. Werner assumed

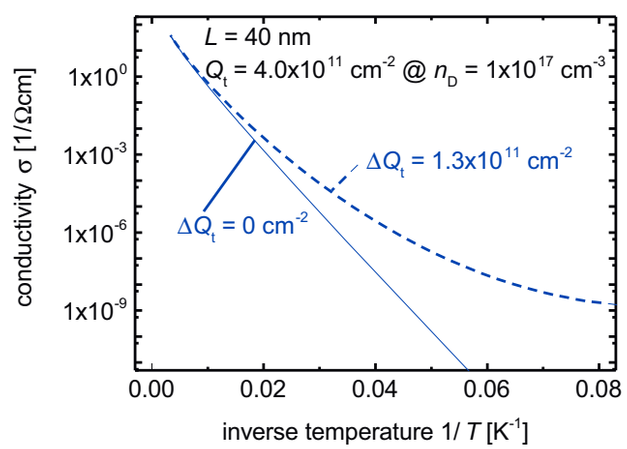

Fig. 4.4. An Arrhenius plot of the mobility is shown with (dashed line) and without (solid line) fluctuating barriers. Curved Arrhenius plots are observed when the barrier height fluctuates. The fluctuations are induced by variations of the trap density ΔQ_t. The barrier height was computed using Eq. (4.14b) for a donor concentration $n_\mathrm{D} = 1 \times 10^{17}\ \mathrm{cm}^{-3}$. For simplicity it was assumed that the Fermi level lies close to the conduction band so that the term E_C in Eq. (4.14b) is negligible. Note that the chosen carrier concentration $n < n_\mathrm{D}$ implies that the criterion for thermionic emission outlined in Section 4.1.3.4 is fulfilled.

the barrier heights to have a Gaussian distribution $P(E_\mathrm{B})$ with standard deviation $\tilde{\sigma}_\mathrm{B}$ around a mean value $\bar{E}_\mathrm{B}$. He included the barrier fluctuations into the thermionic emission theory by performing an integration of the thermionic emission current described by Eq. (4.9) over all potentials E_B. The application of fluctuating barriers to grain boundaries of polycrystalline materials yields

$$\sigma_\mathrm{TE} = L\,\frac{eA^*}{2k_\mathrm{B}}\,T\,\exp\left\{-\frac{1}{k_\mathrm{B}T}\left(\bar{E}_\mathrm{B} - \frac{\tilde{\sigma}_\mathrm{B}^2}{2k_\mathrm{B}T}\right)\right\}. \tag{4.15}$$

The fluctuating barriers induce a reduction of the effective current barrier by $\tilde{\sigma}_\mathrm{B}^2/2k_\mathrm{B}T$. This reduction is more pronounced for lower temperatures leading to the upwardly bend Arrhenius curves for high $1/T$ values. An example is shown in Fig. 4.4. Several

authors used the Werner model to fit data of polycrystalline materials [132, 139, 150]. However, some authors ignored the temperature dependence of the prefactor of the exponential function [132, 139]. Others modified the Werner model according to the relation $N_c \exp(-E_C/k_B T) = n$ which is only valid for non-degenerate materials [150]. Nevertheless, such a model was applied to degenerate materials. I will use the barrier heights derived from these questionable models further down, because other values are lacking,

Degenerate semiconductors Several authors claim the Seto or Werner model to be inaccurate for highly doped materials because they do not take into account the degeneracy [119, 135, 151, 152]. In agreement with my conclusions, Bruneaux et al. stated Eq. (4.11) to apply to a degenerate electron gas and Seto's equation to a non-degenerate electron gas [152]. Zhang and Ma cited Bruneaux et al. but gave a slightly different expression for the mobility in degenerate samples [135]. Explanatory remarks regarding their modification were not given by Zhang and Ma. Therefore, the expression used by Zhang and Ma is problematic as e.g. pointed out by Liu et al. [133]. The expression was nevertheless used by other authors [119].

Kajikawa argued that the Boltzmann approximation is applicable only when the relation $E_c - E_F \gg k_B T$ holds [151]. Although this argument is certainly true in the case of the Seto model, it does not apply to Eq. (4.11) and thus the Werner model. The criterion for the applicability of Boltzmann statistics with respect to thermionic emission at grain boundaries is $E_B \gg k_B T$. Only then, the approximation in Eq. (4.7) and the expression for the average thermal velocity $\bar{v}$ are valid. Values found in literature for E_B are $0.3-8$meV [139], 3meV [132], and $6.8-37.7$meV [150]. Note that these values have been obtained with the above discussed, modified Werner models that comprise an exponent similar to the Werner model but modified prefactors. As these values are mostly lower than $k_B T \approx 25$ meV at room temperature, the criterion $E_B \gg k_B T$ is not fulfilled and the application of the Werner model seems questionable.

The integration of Fermi-Dirac statistics into a model of fluctuating grain boundary barrier heights has been presented by Kajikawa [151]. He evaluated the expression for the conductivity

$$\sigma_{TE} = \frac{e^2 n \langle \tau \rangle}{m^*} = \int_0^\infty \left\{ \int_{E_B}^\infty D(E,T)\, f(E,T)\, \tau(E,T)\, \mathrm{d}E \right\} P(E_B)\, \mathrm{d}E_B \qquad (4.16)$$

with $\tau(E,T) = \lambda_g/\nu$ being the relaxation time defined as the fraction of electron

mean free path λ_g and electron group velocity ν. The inner integral can be solved and gives the conductivity for uniform barrier heights

$$\sigma_{TE}^{u} = \frac{4}{3}\lambda_g \frac{eA^*}{k_B} T \left[\frac{E_B + E_F}{k_B T} \left(1 + \exp\left(\frac{E_B}{k_B T} \right) \right)^{-1} + \ln\left(1 + \exp\left(-\frac{E_B}{k_B T} \right) \right) \right]. \tag{4.17}$$

For $E_B \gg k_B T$, Eq. (4.17) should reproduce equation (4.11). However, Eq. (4.17) differs from Eq. (4.11) by a factor of $8(E_B + E_F)/3k_B T$. Kajikawa's expression gives hence a different temperature dependence than the expression derived by Schottky barrier theory. The outer integral of Eq. (4.16) has to be evaluated numerically. Kajikawa fitted temperature-dependent conductivity data of various polycrystalline semiconductors with the three fitting parameters mean free path λ_g, standard deviation and mean value of the barrier fluctuations. His model includes specifically the condition $E_B \leq k_B T$. The price to pay is the lacking analytical solution in case of fluctuating barriers.

4.1.3.2. Field Emission

Field Emission is the quantum mechanical tunneling of electrons through thin potential barriers. Field emission was considered by several authors to be an important transport path across grain boundaries in polycrystalline materials [109, 135, 139, 153–156]. Therein, if any, expressions of Holm [157] or Simmons [158] have been used. Holm's equation predicts temperature-independent field emission currents. As Stratton and Simmons obtained a slightly quadratic dependence of current on temperature, Holm's equation will not be considered further [142, 159].

To my knowledge, the only publication that implemented an analytical field emission model is the one by Garcia-Cuenca et al. [155]. They used the expressions derived by Simmons to explain temperature-dependent conductivity measurements of CdS:In films [158]. However, Simmons formula only takes into account the averaged barrier height. It is, in a manner of speaking, blind for the actual shape of the barrier. Consequently, his model does not contain thermionic field emission.

In this work, I adapted equations derived by Stratton [142, 143]. Stratton's equations include the specific barrier shape and deal explicitly with thermionic field emission. To my knowledge, it is the first time that Stratton's theory is applied to grain boundaries in highly doped polycrystalline semiconductors.

The field emission current

$$J_{\mathrm{FE}} = e\frac{4\pi m^*}{h^3}\int_0^\infty \left[(f_1(E) - f_2(E)) \int_0^E P(E_\mathrm{x})\mathrm{d}E_\mathrm{x} \right] \mathrm{d}E \tag{4.18}$$

is given by the integral of the difference between the two Fermi Dirac function f_1 and f_2 at each side of the barrier multiplied with the integral over the tunneling probability $P(E_\mathrm{x})$. $P(E_\mathrm{x})$ may be computed using the WKB approximation [160,161] by

$$P(E_\mathrm{x}) = \exp\left\{ -\frac{2}{3}\frac{(E_\mathrm{B} - E_\mathrm{x})^{3/2}}{E_{00}\sqrt{\phi_\mathrm{B}}} \right\} \tag{4.19}$$

with E_B and ϕ_B being the barrier height measured with respect to the Fermi level and the conduction band, respectively [144]. E_{00} is defined as

$$E_{00} = \frac{2e}{\alpha}\sqrt{\frac{n}{2\epsilon_0\epsilon_\mathrm{r}}} = \frac{\hbar}{2}\sqrt{\frac{n}{\epsilon_0\epsilon_\mathrm{r}m^*}} \tag{4.20}$$

where $\alpha = 2(2m^*)^{1/2}/\hbar$ is a constant. Under the assumption that predominantly electrons close to the Fermi level contribute to the current,

$$P(E_\mathrm{x}) \approx \exp\left\{ -\left(b_1 + c_1\epsilon_\mathrm{x} + f_1\epsilon_\mathrm{x}^2\right) \right\} \tag{4.21}$$

can be expanded with respect to the variable $\epsilon_\mathrm{x} = E_\mathrm{F} - E_\mathrm{x}$. The computation of the tunneling coefficients b_1, c_1, f_1 for double Schottky barriers at grain boundaries may be found in Appendix A.1. Here, just the results

$$b_1 = 2\,\frac{E_\mathrm{F}}{E_{00}}\left[\sqrt{\widetilde{E}^2 + \widetilde{E}} - \ln\left(\sqrt{\widetilde{E}+1} + \sqrt{\widetilde{E}}\right)\right] \tag{4.22}$$

$$c_1 = 2\,\frac{1}{E_{00}}\,\ln\left(\sqrt{\widetilde{E}+1} + \sqrt{\widetilde{E}}\right) \tag{4.23}$$

$$f_1 = 2\,\frac{1}{4E_{00}E_\mathrm{F}}\sqrt{\frac{\widetilde{E}}{\widetilde{E}+1}} \tag{4.24}$$

are presented. The parameter $\widetilde{E}$ is given by

$$\widetilde{E} = \frac{E_\mathrm{B} - eV}{E_\mathrm{F}}. \tag{4.25}$$

Note the difference between the expression of f_1 as presented here and as given by Padovani [162]. A short discussion regarding this difference can be found in Appendix A.1.

The combination of Eqs. (4.18) and (4.21), and the evaluation of b_1 and c_1 for small applied voltages V yields the J-V characteristic given by Padovani [162]

$$J_{\mathrm{FE}} = \frac{A^* \exp\left(-b_1\right)}{(c_1 k_{\mathrm{B}})^2} \left\{ \left(\frac{\pi c_1 k_{\mathrm{B}} T}{\sin\left(\pi c_1 k_{\mathrm{B}} T\right)} \left[1 - \exp\left(-c_1 e V\right)\right] \right) - c_1 e V \exp\left(-c_1 E_{\mathrm{F}}\right) \right\} \tag{4.26}$$

with $A^* = 4\pi m^* e k_{\mathrm{B}}^2 / h^3$ being the Richardson constant. Using the relation

$$\sigma = L \left. \frac{\mathrm{d}J}{\mathrm{d}V} \right|_{V=0}, \tag{4.27}$$

I obtained for the field emission conductivity σ_{FE} in polycrystalline semiconductors the expression

$$\sigma_{\mathrm{FE}} = \frac{e L A^* c_1}{(c_1 k_{\mathrm{B}})^2} \exp\left(-b_1\right) \left\{ \frac{\pi c_1 k_{\mathrm{B}} T}{\sin\left(\pi c_1 k_{\mathrm{B}} T\right)} - \exp\left(-c_1 E_{\mathrm{F}}\right) \right\}. \tag{4.28}$$

The same formula has been derived by Yu with the exception that his expression already contained the relation $c_1 = E_{\mathrm{B}}/E_{00}$ deduced from Eq. (4.23) for $V \approx 0$ [163]. The variation of conductivity respectively mobility[5] with temperature as derived from Eq. (4.28) is shown in Fig. 4.5. The temperature dependence of

$$\sigma_{\mathrm{FE}} \sim \frac{\pi c_1 k_{\mathrm{B}} T}{\sin\left(\pi c_1 k_{\mathrm{B}} T\right)} \approx 1 + \frac{1}{6} \left(\pi c_1 k_{\mathrm{B}} T\right)^2 \tag{4.29}$$

is approximately quadratic. For representative values of n, L, and Q_{t}, this quadratic dependence translates into a charge carrier mobility that is almost constant for low temperatures up to 100 K. Higher temperatures induce a slight mobility increase.

The trap density hardly influences the general shape of the curve. However, it determines strongly the overall mobility level.

Eq. (4.28) describes tunneling through barriers with uniform height. Similar to thermionic emission theory, an extension of the tunneling expression for fluctuating barriers would be desirable. However, it is shown in Appendix A.2 that the derivation

[5] Note that the carrier concentration is temperature-independent in highly doped semiconductors under investigation in this work.

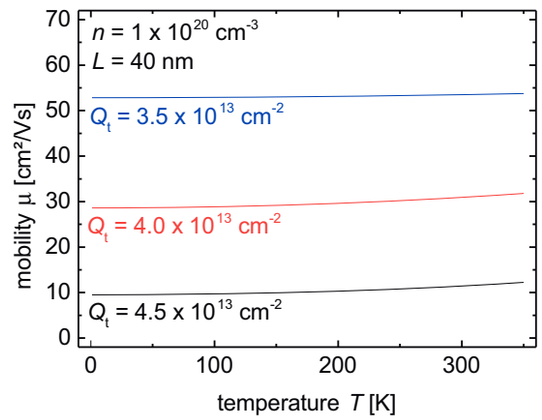

Fig. 4.5. The temperature-dependent mobility is plotted for three different trap densities Q_t. A constant carrier concentration of 1×10^{20} cm^{-3} and a grain size of 40 nm were assumed. The mobility is almost constant for temperatures up to 100 K and increases approximately quadratic for higher temperatures. Note that the trap density influences predominantly the overall level of the mobility and not so much the general shape of the curve.

of an analytical expression for tunneling through fluctuating barriers needs strong simplifying assumptions. These simplification predominate the benefits of the more detailed barrier description. Therefore, Eq. (4.28) will be the expression of choice for tunneling through potential barriers at grain boundaries.

Of course, a numerical solution for the expression of field emission through fluctuating barriers would be possible. However, it is my aim in this work to rely on analytical expressions because they can be more easily applied by others researchers.

4.1.3.3. Thermionic Field Emission

Thermionic field emission describes the tunneling of electrons at an energy E_m exceeding the Fermi energy E_F, but being below the barrier height E_B. E_m is defined by the relation

$$c_\mathrm{m} k_\mathrm{B} T = 1 \tag{4.30}$$

and the J-V characteristic for thermionic field emission is described by [143,162,164]

$$J_{\mathrm{TFE}} = \frac{A^* T}{2\pi k_{\mathrm{B}}} \exp\left(\frac{E_{\mathrm{F}}}{k_{\mathrm{B}}T} - b_{\mathrm{m}} - \frac{E_{\mathrm{m}}}{k_{\mathrm{B}}T}\right)\left(\frac{\pi}{f_{\mathrm{m}}}\right)^{1/2}\left[1 - \exp\left(-\frac{eV}{k_{\mathrm{B}}T}\right)\right]. \tag{4.31}$$

b_{m}, c_{m}, and f_{m} are the tunneling coefficients derived in the previous section. The expressions for the thermionic field emission coefficients b_{m}, c_{m}, and f_{m} differ from those of pure field emission b_1, c_1, and f_1 only by the replacement of the Fermi level E_{F} by the characteristic energy E_{m}. Note that this does not only imply the modification of the integrand, but also of the integration limits now defined by $\phi(x) = E_{\mathrm{m}}$. Evaluating the coefficients according to Appendix A.1 results in

$$b_{\mathrm{m}} = 2\,\frac{1}{E_{00}}\left[\sqrt{\bar{E} - E_{\mathrm{m}}}\sqrt{\bar{E}} - \frac{E_{00}E_{\mathrm{m}}}{2k_{\mathrm{B}}T}\right] \tag{4.32}$$

$$c_{\mathrm{m}} = 2\,\frac{1}{E_{00}}\ln\left\{\frac{\sqrt{\bar{E} - E_{\mathrm{m}}}\sqrt{\bar{E}}}{\sqrt{E_{\mathrm{m}}}}\right\} \tag{4.33}$$

$$f_{\mathrm{m}} = 2\,\frac{1}{4E_{00}E_{\mathrm{m}}}\sqrt{\frac{\tilde{E}^{\mathrm{m}}}{\tilde{E}^{\mathrm{m}} + 1}} \tag{4.34}$$

$$\approx 2\,\frac{\cosh^2\left(E_{00}/2k_{\mathrm{B}}T\right)}{4E_{00}\bar{E}}\,\frac{1}{\sqrt{2 - \tanh^2\left(E_{00}/2k_{\mathrm{B}}T\right)}} \tag{4.35}$$

with the parameters

$$\bar{E} = E_{\mathrm{B}} + E_{\mathrm{F}} - eV \tag{4.36}$$

$$\tilde{E}^{\mathrm{m}} = \frac{E_{\mathrm{B}} - eV}{E_{\mathrm{m}}} \tag{4.37}$$

$$E_{\mathrm{m}} = \frac{\bar{E}}{\cosh^2\left(E_{00}/2k_{\mathrm{B}}T\right)}. \tag{4.38}$$

The expression for E_{m} was deduced by inserting c_{m} into Eq. (4.30). Eq. (4.30) was also used to derive the term $E_{00}E_{\mathrm{m}}/k_{\mathrm{B}}T$ in the expression for b_{m}. Eq. (4.35) is obtained from Eq. (4.34) by applying the expression for E_{m} and by evaluating the square root term in (4.34). The examination of the exponent in Eq. (4.31) reveals

that

$$b_{\mathrm{m}} - \frac{E_{\mathrm{m}}}{k_{\mathrm{B}}T} = 2\,\frac{\bar{E}}{E_0} \tag{4.39}$$

$$\text{where} \qquad E_0 = E_{00}\,\coth\Big(\frac{E_{00}}{2k_{\mathrm{B}}T}\Big). \tag{4.40}$$

The thermionic field emission current J_{TFE} can thus be expressed as

$$\begin{aligned} J_{\mathrm{TFE}} =& \frac{A^*T\sqrt{E_{00}\bar{E}}}{\sqrt{2\pi}\,k_{\mathrm{B}}\cosh\left(E_{00}/2k_{\mathrm{B}}T\right)}\,\Big(2-\tanh^2\left(E_{00}/2k_{\mathrm{B}}T\right)\Big)^{1/4} \\ & \times \exp\left\{\frac{E_{\mathrm{F}}}{k_{\mathrm{B}}T} - 2\,\frac{E_{\mathrm{B}}+E_{\mathrm{F}}}{E_0}\right\}\,\exp\left(2\,\frac{eV}{E_0}\right)\left[1-\exp\left\{-\frac{eV}{k_{\mathrm{B}}T}\right\}\right]. \end{aligned} \tag{4.41}$$

Using Eq. (4.27), one obtains the conductivity

$$\begin{aligned} \sigma_{\mathrm{TFE}} =& \frac{eLA^*\sqrt{E_{00}(E_{\mathrm{B}}+E_{\mathrm{F}})}}{\sqrt{2\pi}\,k_{\mathrm{B}}^2\cosh\left(E_{00}/2k_{\mathrm{B}}T\right)}\,\Big(2-\tanh^2\left(E_{00}/2k_{\mathrm{B}}T\right)\Big)^{1/4} \\ & \times \exp\left(\frac{E_{\mathrm{F}}}{k_{\mathrm{B}}T}\right)\,\exp\left\{-2\,\frac{E_{\mathrm{B}}+E_{\mathrm{F}}}{E_0}\right\}. \end{aligned} \tag{4.42}$$

Expression (4.42) differs from the one derived by Yu [163]. Instead of the term $\Big(2-\tanh^2\left(E_{00}/k_{\mathrm{B}}T\right)\Big)^{1/4}$, Yu's equation contains the expression $\sqrt{\coth\left(E_{00}/k_{\mathrm{B}}T\right)}$. This difference is a direct consequence of the discrepancy between Padovani's expression for f_1 and the one derived in this work (see Appendix A.1).

Fluctuating barriers can be implemented into the model of thermionic field emission according to the procedure proposed by Werner. The procedure was outlined in Section 4.1.3.1 and Appendix A.1. As a result, Eq. (4.42) is modified by an additional factor. The conductivity $\sigma_{\mathrm{TFE}}^{\mathrm{f}}$ comprising fluctuating barriers is thus given by

$$\sigma_{\mathrm{TFE}}^{\mathrm{f}} = \sigma_{\mathrm{TFE}} \times \exp\left(\frac{\tilde{\sigma}_{\mathrm{B}}^2}{2E_{00}}\right). \tag{4.43}$$

Similar to the thermionic emission case, fluctuating barriers induce a reduction of barrier height. The reduction is given by $\tilde{\sigma}_{\mathrm{B}}^2/2E_{00}$.

4.1.3.4. Which process dominates the transport across grain boundaries? – Criteria

Depending on doping concentration and temperature, one of the three transport paths across grain boundaries dominates. Crowell and Rideout [165] and Stratton [142, 143] have developed criteria revealing the dominant transport mechanism.

Crowell and Rideout's criterion is based on the parameter $k_\mathrm{B}T/E_{00}$. Following Rhoderick and Williams, E_{00} can be interpreted as the barrier height, measured relative to the conduction band, such that an electron at the bottom of the conduction band and at the edge of the depletion region has the field emission probability equal to $\exp(-1)$. "Therefore the ratio $k_\mathrm{B}T/E_{00}$ is a measure of the relative importance of thermionic emission and tunneling. As a rough guide, we should expect field emission if $k_\mathrm{B}T \ll E_{00}$, thermionic field emission if $k_\mathrm{B}T \approx E_{00}$, and thermionic emission if $k_\mathrm{B}T \gg E_{00}$." [144]

More exact criteria have been given by Stratton [142, 143]. Field emission occurs if the inequality

$$1 > k_\mathrm{B}T\left(c_1 + \sqrt{2f_1}\right) \tag{4.44}$$

is fulfilled. If the inequalities

$$1 < c_1 k_\mathrm{B}T \tag{4.45}$$

$$\text{and} \qquad 1 < b_\mathrm{m} + c_\mathrm{m}\left(E_\mathrm{F} - E_\mathrm{m}\right) + f_\mathrm{m}\left(E_\mathrm{F} - E_\mathrm{m}\right)^2 \tag{4.46}$$

are complied with, the process is described by thermionic field emission. The criterion for thermionic emission is given by

$$1 > b_\mathrm{m} + c_\mathrm{m}\left(E_\mathrm{F} - E_\mathrm{m}\right) + f_\mathrm{m}\left(E_\mathrm{F} - E_\mathrm{m}\right)^2. \tag{4.47}$$

In the next section, the presented criteria will be applied to highly doped, polycrystalline semiconductors, e.g. ZnO:Al.

4.2. Field emission model: Application and evaluation

The application of conductivity models developed in Section 4.1 will be presented below. Mobility and conductivity data from literature and own experiments will therefor be investigated as a function of charge carrier concentration n and measurement temperature T. The observed dependencies will be fitted taking into account ionized impurity scattering, electron-phonon scattering, and grain boundary scattering.

The charge transport across potential barriers at grain boundaries comprises three mechanisms: field emission, thermionic field emission, and thermionic emission. Criteria to decide on the dominant transport path have been given in Section 4.1.3.4. As the highest measurement temperature is generally 300 K, and as the lowest carrier concentrations are around $5 \times 10^{19}\,\mathrm{cm}^{-3}$, Crowell and Rideout's criterion

$$k_\mathrm{B}T \approx 25\,\mathrm{meV} < 88\,\mathrm{meV} = E_{00} \tag{4.48}$$

suggests field emission to be the dominant transport path for all investigated samples. This hypothesis has been checked and verified for each fit by evaluating Stratton's more detailed criteria with the obtained barrier heights. Thus, for the highly doped, polycrystalline semiconductors under investigation in this work, it is certain to state the important result that *field emission is the dominant transport path across grain boundaries!*

Altogether, the conductivity model consists of ionized impurity scattering (ii), electron-phonon scattering (ph), and field emission at grain boundaries (FE). The three scattering mechanisms were combined using Matthiessen's rule. It states that the total resistivity

$$\rho_\mathrm{tt} = \rho_\mathrm{ii}(n, K) + \rho_\mathrm{ph}(n, T, \Theta, \lambda_\mathrm{tr}) + \rho_\mathrm{FE}(n, T, Q_\mathrm{t}, L) \tag{4.49}$$

is the sum of the resistivities of the individual scattering mechanisms. Three fit parameters occur: Debye temperature Θ, electron-phonon coupling constant λ_tr, and grain boundaries trap density Q_t. If not otherwise stated, a compensation ratio of $K = 0\%$ and a grain size of $L = 40\,\mathrm{nm}$ [46, 47] will be assumed. Note that ρ_ph is a function of n whereas μ_ph is independent of n (see Section 4.1.2).

4.2.1. Mobility vs. carrier concentration

Within the presented conductivity model, the mobility μ depends amongst others on the carrier concentration n. It will be shown that the model can fit the observed $\mu - n$ dependencies. The only fit parameter will be the grain boundaries trap density Q_t because electron-phonon scattering cannot be extracted from $\mu - n$ data. Anticipating results of $\mu - T$ fits, one estimates reasonable values for Θ and λ_{tr} to be 1000 K and 0.3, respectively, resulting in an electron-phonon scattering mobility of 200 cm^2/Vs. Note that this value is comparable to 210 cm^2/Vs derived by Ellmer [54].

"Jülich" data Fig. 4.6 shows mobility data of ZnO:Al films obtained by Berginski et al. [8]. By varying target doping concentration (TDC) and deposition temperature, samples with various carrier concentrations and mobilities were obtained. Additionally, data from Section 4.3 dealing with seed layers is shown. In a first approach, the data was modeled with the conductivity model assuming a trap density that is independent of carrier concentration (dashed lines). They fit the samples with TDC of 0.2 wt% and 0.5 wt%, and the seed layer data reasonably well. Layers with TDC

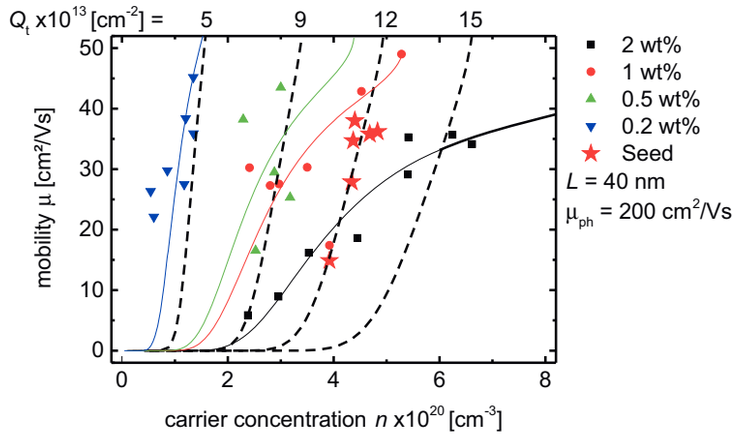

Fig. 4.6. The mobility is plotted against the carrier concentration for four different target doping concentrations. The data was extracted from [8]. Furthermore, data from Section 4.3 dealing with a seed layer approach was added. Dashed lines represent the results of the conductivity model assuming the trap density to be independent of the carrier concentration. Four different grain boundary trap densities were evaluated ($Q_t = 5, 9, 12, 15 \times 10^{13}\,cm^{-2}$). Solid lines show the fits under the assumption of a trap density being dependent on the carrier concentration.

of 1 wt% and 2 wt% however are not well described. A second approach is inspired by results in CdS [155] and silicon [156] where the trap density was found to be dependent on carrier concentration. Thus, the trap density Q_t was assumed to be linked to the carrier concentration by the most simple functional dependence, that is a linear relationship. The obtained relation

$$Q_t = Q_t(n) = Q_{t0} + C_t\, n \tag{4.50}$$

contains two unknown parameters Q_{t0} and C_t that were used to fit the data in Fig. 4.6 again. C_t was restrictively assumed to be the same for all TDCs. The fit results, shown as solid lines in Fig. 4.6, reproduce the data very well. Only the seed layer is still described best by the model without n-dependent trap density. Hence, the seed layer approach seems to enable the increase of carrier concentration without affecting the density of occupied grain boundary traps. The fit parameters

Table 4.1. Parameters of fits to data in Fig. 4.6 according to Eq. (4.50)

TDC [wt%]	0.2	0.5	1	2
Q_{t0} [cm^{-2}]	2.65×10^{13}	4.38×10^{13}	4.76×10^{13}	5.98×10^{13}
C_t [cm]	1.5×10^{-7}			

in Table 4.1 show an increase of Q_{t0} with increasing TDC. The dopant aluminum might thus be an important factor for the traps at grain boundaries as also suggested by other authors [108]. A qualitative explanation for the n-dependent trap density will be given in Section 4.2.2.2.

Minami data Fig. 4.7 shows data that was extracted from Minami et al. [55]. The reasonable fit is based on the assumption of n-dependent trap densities at grain boundaries. It reproduces both the mobility increase of ZnO and the mobility decrease of ZnO:Al with increasing carrier concentration.

The mobility increase of ZnO is easily explained by the increasing field emission through grain boundaries at higher carrier concentrations. The mobility decrease of ZnO:Al can be accounted for by two effects: (1) The effective mass increases with increasing carrier concentration due to the non-parabolic ZnO conduction band. As a consequence, the mobility as determined by ionized impurity scattering decreases. Minami et al. explained the data in this way. However, Ellmer pointed out that Minami's effective mass of $m^* = 1.04 m_e$ at $n = 1 \times 10^{21}$ cm^{-3} is rather high and possibly problematic [54]. In our case, a lower effective mass is used. Thus, only a

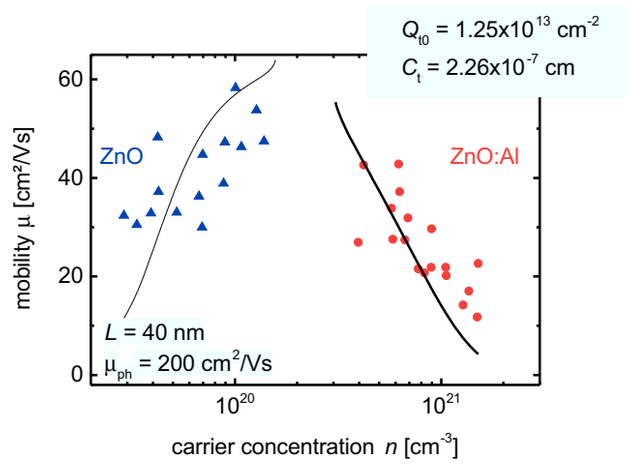

Fig. 4.7. The mobility is shown as a function of carrier concentration for intrinsic (blue triangles) and aluminum-doped (red circles) ZnO. The data has been extracted from [55]. The black solid line represents a fit with the conductivity model assuming a grain boundary trap density that is dependent on the carrier concentration according to Eq. (4.50). The fit parameters Q_{t0} and C_t are given in the graph. The fit represents the increasing mobility for ZnO and the decreasing mobility for ZnO:Al. The fit is not a continuous line because the Fermi level is situated above the potential barriers at grain boundaries for $1.5 \times 10^{20}\,\mathrm{cm}^{-3} < n < 3.1 \times 10^{20}\,\mathrm{cm}^{-3}$.

part of the mobility decrease can be explained and a further explanation is needed. (2) Higher carrier concentrations need to induce an increasing barrier height at the grain boundaries to explain the reduction of mobility due to field emission of electrons through grain boundaries. This would be the case if the amount of additional traps induced by the higher carrier concentration was high, e.g. C_t was high. Such a situation is predicted by the fit in Fig. 4.7. Hence, the specific energetic distribution of the traps at grain boundaries in conjunction with the field emission model might explain the mobility drop at high carrier concentrations.

Conclusion The conductivity model comprising uncompensated ionized impurity scattering, electron-phonon scattering, and field emission at grain boundaries describes the carrier concentration dependence of the mobility satisfactorily. In most cases, reasonable fits could be obtained only by assuming the grain boundary trap density to be dependent on carrier concentration.

4.2.2. Mobility vs. measurement temperature

Electron-phonon scattering and field emission through grain boundaries are dependent on temperature. Thus, the evaluation of the proposed conductivity model has to comprise the investigation of temperature-dependent conductivity and mobility measurements. In total, six different measurement series have been analyzed. Seed layer and annealing experiments will be discussed in Sections 4.3 and 4.4, respectively. In the following, data from literature is the subject of interest.

4.2.2.1. Fit curves

First, indium-doped cadmium sulfide (CdS:In) films will be discussed because their conductivity has been interpreted in terms of a different field emission model than the one used here [155]. Most importantly, these films exemplify the importance of electron-phonon scattering for the interpretation of conductivity data. Furthermore, sputtered ZnO:Al and LPCVD grown ZnO:B with various carrier concentrations will be investigated. They will underline that different dopants, grain sizes, and growth methods do not alter the applicability of the model. At the end, damp heat degraded ZnO:Al will be discussed because damp heat degradation is supposed to predominantly influence grain boundaries. Therefore, it is an interesting system for the application of the field emission model.

Garcia-Cuenca et al. data Fig. 4.8 shows temperature-dependent conductivity measurements of CdS:In films. The data was obtained from Garcia-Cuenca et al. [155]. Garcia-Cuenca et al. proposed a conductivity model comprising field emission through grain boundaries to interpret their data. Field emission model is based on the description by Simmons [158], whereas the model developed here uses equations of Stratton [142, 143]. Generally, the two models yield similar results because both models predict an approximately quadratic temperature dependence. Garcia-Cuenca et al. used the expression $\sigma = \sigma_0(1 + \beta T^2)$ as fit function. Fit parameters are σ_0 and β. Both parameters are essentially a function of the trap density Q_t. Garcia-Cuenca et al. were however not able to reproduce the data such that σ_0 and β yield the same trap density. In contrast, the model based on Stratton and applied in Fig. 4.8 is able to fit the data with one unique trap density.

Garcia-Cuenca et al. obtained a reasonable agreement of their data and the tunneling model only for low temperatures. It is suspected that the reason lies in the neglect of electron-phonon scattering.

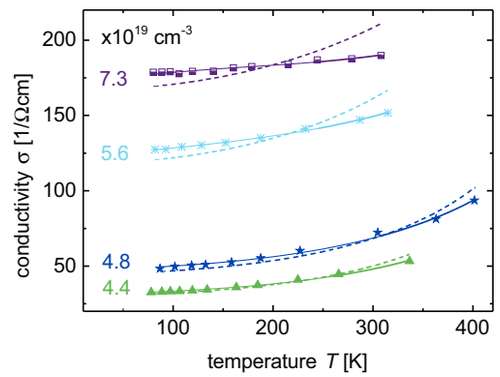

Fig. 4.8. temperature-dependent conductivity measurements of polycrystalline CdS:In films with various carrier concentrations are shown. The data is obtained from Garcia-Cuenca et al. [155]. The dashed lines are fits taking into account field emission at grain boundaries only. Solid lines comprise field emission and electron-phonon scattering. Note that, in contrast to ZnO:Al films, a parabolic conduction band was assumed. Garcia-Cuenca et al. specified a grain size of 500 nm.

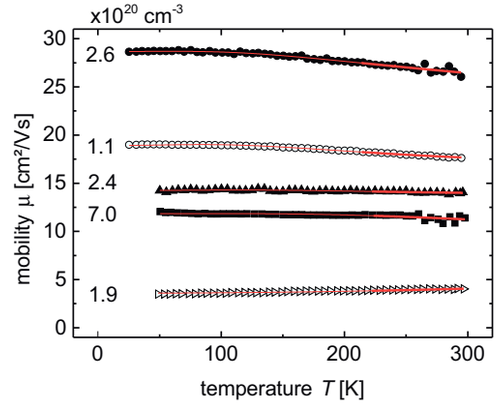

Fig. 4.9. The mobility of sputtered polycrystalline ZnO:Al was measured as a function of temperature. Films with various carrier concentrations have been investigated. The data was extracted from Ellmer and Mientus [132]. Red lines represent fits comprising uncompensated ionized impurity scattering, electron-phonon scattering, and field emission through grain boundaries. Fit parameters are Θ, λ_{tr}, and Q_{t}. No information was given by Ellmer and Mientus about the grain size. Therefore, it was assumed to be 40 nm.

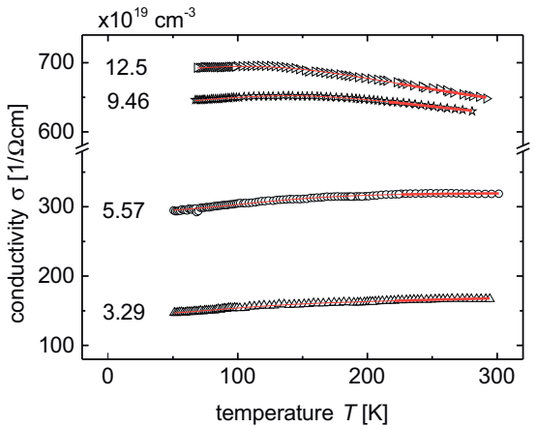

Fig. 4.10. The conductivity of polycrystalline ZnO:B films was measured at various temperatures. The films have been grown by LPCVD. The carrier concentration was changed by varying the flow of the dopant precursor during deposition. The data was taken from Myong et al. [166]. Red lines are fits according to the conductivity model under investigation. Myong et al. obtained grain sizes of around 330 nm by SEM measurements.

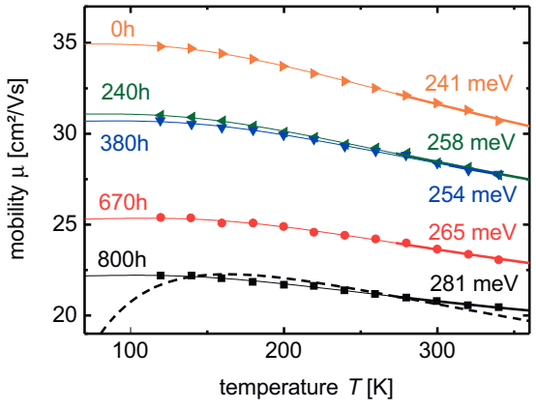

Fig. 4.11. The mobility of ZnO:Al films was measured at temperatures from 100 K to 350 K. The investigated films underwent damp heat treatments for various durations. The data has been taken from Kim et al. [167]. The measurements have been fitted with the proposed conductivity model. The barrier heights deduced from the model are given in the graph. The dashed line is a fit according to the Seto model. Kim et al. give a grain size of 75 nm.

Fig. 4.8 clearly shows that the application of field emission and electron-phonon scattering (solid lines) reproduces the data much better than the pure field emission model (dashed lines). The disregard of electron-phonon scattering might be a reason why an unambiguous value for Q_t could not be obtained by Garcia-Cuenca et al. Thus, I stress the important result that *only the combination of field emission and electron-phonon scattering leads in most cases to a satisfying description of temperature-dependent conductivity data.*

Ellmer et al. data Fig. 4.9 shows mobility measurements of sputtered, polycrystalline ZnO:Al as a function of temperature. The data was obtained by Ellmer and Mientus [132]. The samples possessed different carrier concentrations. Although the grain size was unknown and thus a representative value for ZnO:Al of 40 nm was used, excellent fits have been obtained. Some samples showed a slight mobility increase at higher temperatures, whereas for others, a mobility decrease was observed. In the framework of the proposed conductivity model, the positive and negative slopes correspond to field emission and electron-phonon scattering, respectively. Field emission dominated the temperature behavior in the low mobility film. In fact, the best fit for this sample was obtained by neglecting electron-phonon scattering. In contrast, the two samples with the highest mobility showed a temperature dependence that is dominated by electron-phonon scattering. The two other samples possessed an almost constant mobility. Here, the temperature dependence of field emission and electron-phonon scattering compensated each other.

I stated at the beginning of Section 4.2 that the total resistivity is obtained by the combination of three scattering mechanisms: ionized impurity scattering (ii), electron-phonon scattering (ph), and grain boundary scattering represented by the field emission model (FE). Of course, not only the total resistivity but also the total mobility can be computed as a combination of the individual scattering mechanisms.

The three scattering processes have been plotted separately in Fig. 4.12. Note that similar plots with similar conclusions can also be derived for the other data. It is clearly illustrated that the limiting mechanism is field emission through grain boundaries because field emission shows the lowest mobility. The slight temperature dependence of field emission is hidden in the strongly temperature-dependent electron-phonon scattering. Thus it seems as if the mobility is, apart from electron-phonon scattering, temperature-independent, although the slightly temperature-dependent field emission is limiting the overall mobility.

The above outlined argumentation focusing on grain boundary scattering is not unambiguous due to its assumption of vanishing compensation. A different argumen-

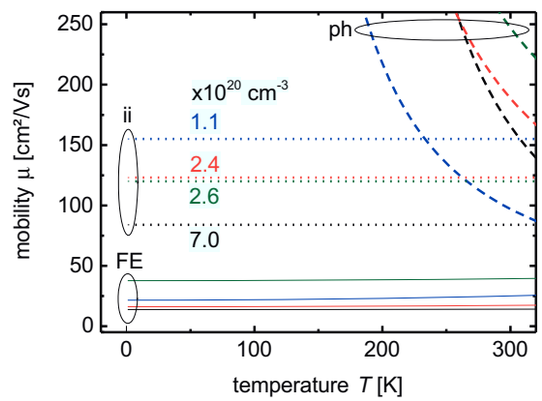

Fig. 4.12. Fits to data obtained from Ellmer and Mientus [132] shown in Fig. 4.9 have been split into the three scattering mechanisms contained within the model, which are ionized impurity scattering (ii), electron-phonon scattering (ph), and field emission at grain boundaries (FE).

tation could assume grain boundary scattering to be negligible. Consequently, the low mobility would be induced solely by ionized impurity scattering that is amplified by compensation. Under this assumption, fits of most of the temperature-dependent measurements would also be possible.

Exemplarily, the mobility of the sample with $n = 1.1 \times 10^{20}\,\mathrm{cm}^{-3}$ could be limited by ionized impurity scattering if a compensation ratio of $K = 30\%$ is assumed. Note that, within my model, $K = 30\%$ means that 60% of the electrons, that have been provided by extrinsic donors, are absorbed by acceptors. Also, Look et al. determined by SIMS measurements and positron annihilation spectroscopy a maximum compensation value of $K = 12\%$ in a ZnO:Ga film with $n = 12.8 \times 10^{20}\,\mathrm{cm}^{-3}$. Without having a clear proof, it is reasonable to suppose the compensation to increase with increasing dopant concentration. A value of $K = 30\%$ seems under this assumption high. Furthermore, the positive slope of the sample with $n = 1.9 \times 10^{20}\,\mathrm{cm}^{-3}$ cannot be explained without an additional scattering mechanism because ionized impurity scattering is temperature-independent. This additional mechanism is likely grain boundary scattering. Hence, field emission is the mechanism to apply following the criteria derived in Section 4.1.3.4.

Myong et al. data The data of Ellmer et al. contained only one sample showing the upwardly bend mobility curve that is characteristic for field emission. Temperature-dependent conductivity measurements extracted from Myong et al. are

shown in Fig. 4.10. Their data contained more samples with positive slope indicating field emission [166]. Both low conductivity samples showed a positive slope, i.e. increasing conductivity with increasing temperature. The sample with $n = 9.46 \times 10^{19}\,\mathrm{cm}^{-3}$ illustrates nicely both effects, field emission at grain boundaries and electron-phonon scattering. A positive slope in the low temperature range was observed that corresponds to field emission, and a negative slope in the high temperature range was observed that corresponds to electron-phonon scattering. Evaluating the shares of the three scattering mechanisms showed field emission to be the limiting mechanism in these samples.

Kim et al. data Temperature-dependent measurements of damp heat treated ZnO:Al films have been presented by Kim et al. [167]. Their data is shown in Fig. 4.11. Damp heat treatment degrades mobility and carrier concentration of doped ZnO [13, 23, 107, 168]. Agreement exists in literature that damp heat degradation affects predominantly grain boundaries. Therefore, it is interesting to investigate such degradation with the proposed model of field emission through grain boundaries. Fig. 4.11 shows the temperature dependence to be dominated by electron-phonon scattering, because only downwardly bend curves were observed. However, according to the proposed model, the overall mobility level is defined by field emission at the grain boundaries. Indeed, the expected results of increased barrier height with increasing damp heat time were obtained. The field emission model thus agrees with the literature conception of damp heat degradation.

Kim et al. used the Seto model to fit their data. Here, I also applied the Seto model to their data and obtained the dashed line in Fig. 4.11. In contrast to Kim et al., I extended the fit to temperatures below the lowest measurement temperature and I did not use an Arrhenius plot. As a result, one observes clearly that the agreement between fit and measurement is poor. Note especially that the Seto fit predicts a rather improbable mobility decrease at low temperatures. This is hence a good example of how misleading certain fits can be if they are not carefully evaluated.

4.2.2.2. Fit parameter

Fit parameters of the investigated measurement series will be evaluated regarding their consistency and their implications for the trap distribution at grain boundaries.

Field emission The field emission model contains one fit parameter: the grain boundary trap density Q_t. Various Q_t values extracted from fits of temperature-dependent measurements have been plotted in Fig. 4.13(a) as a function of carrier concentration

n. One observes that the trap density increased with increasing carrier concentration. Note again that the Q_t values have been obtained from fits of temperature-dependent measurements. Let me shortly remind you of the fits to $\mu - n$ data. There, satisfying fits could only be obtained under the assumption of a trap density that depends on carrier concentration. A simple linear relation between Q_t and n with the parameters Q_{t0} and C_t was proposed (see Eq. (4.50)). The same linear relationship was used to fit the $Q_t - n$ dependence that was obtained from various temperature-dependent measurements. The dashed line in Fig. 4.13(a) represents this fit. The agreement between experimental data and fit is reasonable well. Note that the carrier concentration is given on a logarithmic scale. The values for Q_{t0} and C_t obtained from the fit to temperature-dependent measurements are similar to the values obtained by the fitting of $\mu - n$ data (see Table 4.1). Thus, the results of $\mu - n$ and $\mu - T$ data are consistent. Both predict an increasing trap density at the grain boundaries with increasing carrier concentration.

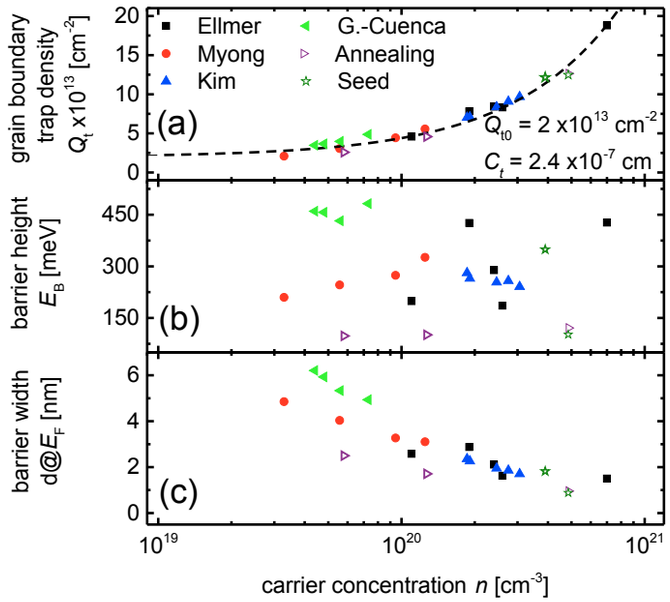

Fig. 4.13. (a) The grain boundary trap density Q_t is shown as a function of carrier concentration. The dashed line is a fit according to Eq. (4.50). The fit parameters Q_{t0} and C_t are presented. Note that the CdS:In films of Garcia-Cuenca et al. were not included into the fit. From Q_t, one can derive the barrier height E_B (b) and the barrier width d at the Fermi level (c).

The n-dependent trap density might be explained by the energetic distribution of the trap states. Fig. 4.14 illustrates the hypothesis of trap states being distributed in energy. Only the trap states with energies equal to or below the Fermi level are occupied. The increase of carrier concentration induces a rising Fermi level. Thus, trap states that were formerly unoccupied can now be filled with electrons and the density of occupied traps is boosted. Support of this hypothesis is given by scanning tunneling measurements of ZnO:Al. The investigation showed that trap states are broadly distributed in energy and that trap states above the Fermi level exist [169].

Fig. 4.14. The dependence of trap density Q_t at grain boundaries as a function of carrier concentration n is illustrated. Trap states are distributed energetically. An increasing carrier concentration is accompanied by an increase of Fermi level. Thus, more traps can be filled and Q_t is raised. If n decreases, the Fermi level drops and less traps are occupied.

The fits to the "Jülich" $\mu - n$ data showed that different target doping concentrations (TDC) needed different values for $Q_{\mathrm{t}0}$ to fit the $\mu - n$ data (see Fig. 4.6 and Table 4.1). The dopant aluminum is supposed to be an important source for trap states at grain boundaries [108]. The increase of TDC might thus induce more traps. As only $Q_{\mathrm{t}0}$ was influenced by the TDC, I suggest only deep traps to be possibly affected by the dopant aluminum.

Fig. 4.13(b) and (c) show the barrier height and width. Both parameters were derived from the trap density. Note that the obtained barrier heights are one order of magnitude higher than the ones found in literature. This is a direct result of the generally higher trap densities. Exemplarily, Ellmer and Mientus give a maximum trap density of $3 \times 10^{13}\,\mathrm{cm}^{-2}$ [115]. The barrier height (with respect to the Fermi level) varies more strongly than the trap density. The reason is that, firstly, the

barrier height is calculated as the difference between the barrier height relative to the conduction band and the Fermi level, and that, secondly, the barrier height with respect to the conduction band is a quadratic function of the trap density (see Eq. 4.14b). Thus, the quadratically varying minuend, i.e. the barrier height with respect to the conduction band, induces a strong variation of the barrier height relative to the Fermi level. The barrier height shows no correlation with carrier concentration. In contrast, the barrier width at the Fermi level decreases slightly with increasing carrier concentration. The reason might be the higher barrier height measured with respect to the conduction band at higher carrier concentrations. Consequently, the barrier at the Fermi level can be narrower although the barrier height given relative to the Fermi level might be the same. Generally, no correlation between either barrier height or width, and mobility was found. Only the combination of both, barrier height and width, determine the field emission mobility.

Electron-phonon scattering Fig. 4.15 depicts the fit parameters of electron-phonon scattering: electron-phonon coupling constant λ_{tr} and Debye temperature Θ. λ_{tr} varies between 0 and 0.6 with the exception of one ZnO:B sample and the CdS:In films where values exceeding 0.6 were obtained. The results seem to be reasonable because Allen obtained for metals values in the range of 0.5 [137]. Also, the determined values for Θ of 500 to 1500 K are similar to Allen's results. Additional experiments such as specific heat measurements would be required to further check the obtained fit values.

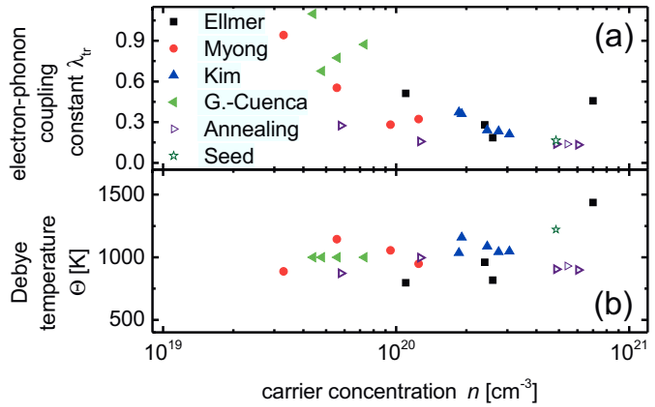

Fig. 4.15. The electron-phonon scattering contains two fit parameters. They are presented in this graph: (a) electron-phonon coupling constant λ_{tr} and (b) Debye temperature Θ.

4.3. Seed layers with increased aluminum concentration

4.3.1. Introduction

Literature overview Several groups have developed seed layers in order to improve the properties of polycrystalline ZnO and ZnO:Al.

Köhl et al. used ion beamed assisted sputtering to improve the c-axis orientation of ZnO deposited at room temperature [19, 74]. The Xe^+ ion bombardment induced highly oriented grains already in the nucleation stage of the growth process via an atomic peening mechanism [70, 73]. A competitive growth mode of the subsequently deposited layer was suppressed without further ion bombardment because the film adopted the preferential orientation of the seed layer.

Dewald et al. aimed at producing suitable ZnO:Al layers for solar cell applications with industrially applicable, high deposition rate processes using direct current (dc) sputtering [20]. However, a simple dc-process did not yield the desired results especially with regard to the etch morphology[6]. Therefore, they applied a low rate, radio frequency (rf) sputtering process to deposit a thin seed layer knowing that the rf-process leads to films with suitable etch morphology. They attributed the advantage of the rf- over the dc-process to enhanced Ar^+ ion bombardment increasing the adatom mobility and reducing inter-crystalline shadowing effects. Consequently, the rf-deposition resulted in better oriented grains and denser layers. dc-sputtered films deposited on top of rf-grown layers showed appropriate etch characteristics and improved electrical properties. Similar to the work of Köhl et al., the seed layer with improved film structure dictates the properties of the subsequently grown ZnO:Al.

Claeyssens et al. deposited ZnO films by pulsed laser deposition (PLD) using a high-temperature seed layer [21]. Increasing the deposition temperature to a certain limit improved the grains' orientation and crystal structure. Therefore, they applied an optimized high-temperature seed layer whose ameliorated film structure determined the further low-temperature growth.

Approach The investigation of ZnO:Al with different amounts of the dopant aluminum revealed a need for elevated deposition temperatures with decreasing aluminum concentration in order to meet the required electrical, optical, and etching

[6] Details about the etching of ZnO:Al and the connection of deposition parameters and etch morphology can be found in Section 2.4

properties [8]. While ZnO:Al with a target doping concentration (TDC) of 2 wt% of Al_2O_3 offers low resistivity and suitable etching characteristics already for room temperature deposition, the absorptance in the near infrared region (NIR) is high due to free carrier absorption. The reduction of TDC to increase transparency in the NIR region however calls for increased deposition temperatures to achieve high mobility and Type B etch morphology [8, 25]. The presented approach aims at a deposition temperature reduction of ZnO:Al with TDC of 1 wt% (ZnO:Al = 1 wt%) by applying a seed layer with TDC of 2 wt% (ZnO:Al = 2 wt%). Thereby, one hopes to combine the suitable etch characteristics at low deposition temperatures of ZnO:Al = 2 wt% with the high transparency of ZnO:Al = 1 wt% while maintaining low resistivity.

Nomenclature In the following, thin ZnO:Al = 2 wt% films are called "seed layers". Subsequently deposited thick ZnO:Al = 1 wt% films are named "bulk layers". Thin ZnO:Al = 1 wt% films will be referred to as "thin bulk layers".

Experimental details Seed layers were deposited in the small area sputtering system. The large area deposition system was used to grow the bulk layers. The temperatures are heater temperatures. For both deposition systems, substrates temperatures are roughly two third of the heater temperatures. The deposition pressure was 0.3 Pa in the case of the seed layers and 0.1 Pa for the bulk layers. The thickness of the bulk layer was approximately 800 nm if not otherwise stated. More details about the deposition systems can be found in Section 3.2.1.

Outline of investigation The section divides into four parts. Firstly, the seed layer deposition conditions were kept constant and the bulk layer deposition temperature was varied. Secondly, various seed layer temperatures were investigated using the same bulk layer deposition conditions. The third part deals with the impact of seed layer thickness on bulk layer properties again keeping the bulk layer growth conditions constant. A discussion closes this section.

4.3.2. Bulk layer: temperature variation

The bulk layer deposition temperature was varied from 100 °C to 430 °C keeping the seed layer constant. Seed layer deposition temperatures were 350 °C for all samples. Electrical, optical, and etching properties were investigated.

Electrical properties The electrical properties are summarized in Table 4.2. Samples with and without seed layer only showed slight differences except for a bulk deposition temperature of 300 °C. There, a substantially higher charge carrier

Table 4.2. Charge carrier mobility and concentration for four different bulk deposition temperatures with and without seed layer. Seed layer deposition parameters were: $d = 40\,\text{nm}$, $T_{\text{seed}} = 350\,°\text{C}$

temperature T [°C]	mobility μ [cm^2/Vs]		carrier concentration n x 10^{20}[cm^{-3}]	
	seed	no seed	seed	no seed
100	27.1	27.3	2.6	2.8
200	32.5	30.3	3.2	3.5
300	36.0	17.4	4.5	3.9
430	46.4	46.4	5.3	5.6

mobility and concentration was obtained for the film with seed layer. However, the difference between the samples with and without seed layer resulted predominately from the strong mobility decrease of the film without seed layer. The seed layer prevented this mobility drop.

Optical properties Fig. 4.16(a) shows the transmittance and absorptance of bulk layers deposited at various temperatures on seed layers. In the wavelength range close to the band gap around 400 nm, the absorption edge shifted to longer wavelengths due to a decrease of carrier concentration (confirmed by Hall measurements, Table 4.2) resulting in a Burstein-Moss shift (see Section 2.2.2). A slight change in the slope of the curves however hints to additional sub band gap absorption probably related to additional defects because of the lower deposition temperatures [58]. In general, the absorptance of samples employing a seed layer in combination with low deposition temperatures was higher in the wavelength range between 350 nm and 600 nm. Yet the seed layer induced lower absorptance compared to films deposited at the same temperatures but without seed layer (Fig. 4.16(b)). Indeed, the absorptance reduction was to a large fraction determined by the lower sub band gap absorption as can be deduced from the steeper slope of the seed layer curves.

Etch characteristics Films with and without seed layer were etched for 40 s in HCl 0.5 wt%. SEM measurements were used to investigate the resulting surface morphology (see Fig. 4.17). The films without seed layer showed a surface with small, grainy structures except for a deposition temperature of 430 °C. One determines the grainy surface texture to be a Type A morphology after the modified Thornton model of Kluth et al. (see [25] and Section 2.4). The application of seed layers induced a crater-like morphology already for bulk deposition temperatures as low as 100 °C. The crater-like surface texture, also called Type B following Kluth et al., was fully developed for bulk deposition temperatures above 200 °C when a seed layer was

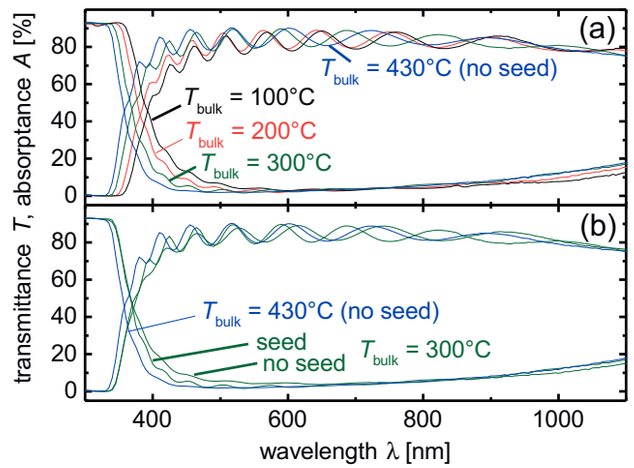

Fig. 4.16. Transmittance and absorptance of ZnO:Al layers: (a) Bulk layers deposited at three different T_{bulk} in combination with a seed layer ($d = 40\,\mathrm{nm}$, $T_{\mathrm{seed}} = 350\,^{\circ}\mathrm{C}$) were measured. (b) Bulk layers using $T_{\mathrm{bulk}} = 300\,^{\circ}\mathrm{C}$ were deposited with and without seed layer. For comparison, both graphs show a standard high-temperature process ($T_{\mathrm{bulk}} = 430\,^{\circ}\mathrm{C}$) without any seed layer.

applied. Without the use of seed layers, deposition temperatures as high as 430 °C were necessary to obtain a Type B texture. In that case, ZnO:Al films with and without seed layer showed the same etch morphology.

4.3.3. Seed layer: temperature variation

A bulk deposition temperature of 300 °C was chosen to be suitable to investigate the influence of seed layer deposition temperatures. As described in the last section, the deposition temperature of 300 °C yielded the best optical properties. Additionally, the difference regarding charge carrier mobility between samples with and without seed layer was most pronounced for this temperature. Hence, the seed layer's influence on the electrical properties was investigated for this deposition temperature. The following investigation was thus performed using a bulk deposition temperature of 300 °C. The seed layer thickness was 40 nm. Seed layer deposition temperatures were varied from 250 °C to 450 °C in 50 °C steps. Bulk layer coating was performed in the large area sputtering system in a single deposition process.

Fig. 4.17. SEM images of etched ZnO:Al layers. The bulk deposition temperature was varied from 100 °C to 430 °C (left to right). References without seed layer (upper row) and samples with seed layers ($d = 40$ nm, $T_{\mathrm{seed}} = 350$ °C, lower row) were co-deposited.

4.3.3.1. Electrical, optical, and etching properties

Electrical properties at room temperature The influence of various seed layer deposition temperatures on the electrical properties at room temperature are summarized in Fig. 4.18. Charge carrier mobility (a) and concentration (b) were determined by Hall measurements. The resistivity (c) was obtained by Hall measurements and additionally, by fits to optical data (see Section 3.3.9).

Application of seed layers induced a mobility increase of more than a factor 2 (Fig. 4.18(a)), e.g. the sample without seed layer showed a mobility of 15 $\mathrm{cm}^2/\mathrm{Vs}$ whereas a seed layer grown at 350 °C resulted in a mobility of 35 $\mathrm{cm}^2/\mathrm{Vs}$. The carrier concentration (Fig. 4.18(b)) was higher for seed layer samples. It increased with temperature until 400 °C and then dropped slightly. The Hall resistivity (Fig. 4.18(c), black squares) was dominated by the increase of Hall mobility. It decreased with the use of seed layers by a factor of 3. The optically determined resistivity (Fig. 4.18(c), blue triangles) however decreased only by about 20%. The only slightly changed optical resistivity, hence the almost constant intra-grain resistivity, implies seed layers to mainly influence grain boundary scattering. Indeed, seed layers induced a reduction of grain boundary scattering in the subsequently deposited bulk layers. The share of resistivity attributed to grain boundary scattering (red circles in Fig. 4.18(c)) decreased by a factor of 4 when a seed layer grown at 350 °C was applied.

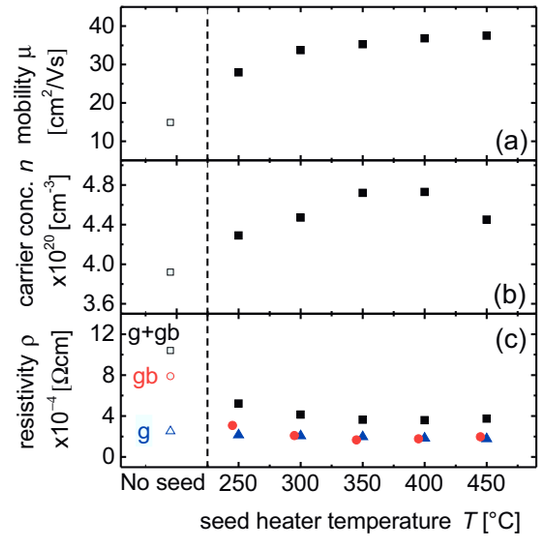

Fig. 4.18. Charge carrier mobility (a) and concentration (b), and resistivity (c) for a sample without seed layer (open symbols) and samples with seed layer (closed symbols). Black squares and blue triangles are data points derived from Hall measurements and optical fits, respectively. In figure (c), I used Matthiessen's rule $\rho_{tt} = \rho_g + \rho_{gb}$ to split up the resistivity derived from Hall measurements (g+gb) into the part belonging to the intra-grain scattering (g) derived from optical fits and a part belonging to grain boundary scattering (gb). Note that the gb-data is slightly shifted to assure better clarity.

Temperature-dependent conductivity measurements Fig. 4.19(a) shows the temperature-dependent conductivity of a sample without seed layer (circles) and a sample with seed layer grown at 350 °C (squares). The measurement temperature was varied from 90 K to 330 K. The obtained data was fitted with the conductivity model developed and applied in Sections 4.1 and 4.2. The model takes into account three different scattering mechanisms: ionized impurity scattering, electron-phonon scattering, and grain boundary scattering described by field emission. The temperature-dependence of the sample with seed layer was dominated by electron-phonon scattering although the overall conductivity level was still determined by grain boundary scattering.

In contrast, the sample without seed layer could be fitted using the field emission model only. Thus, the increased conductivity of the seed layer sample in comparison to the sample without seed layer was due to a reduction of grain boundary scattering.

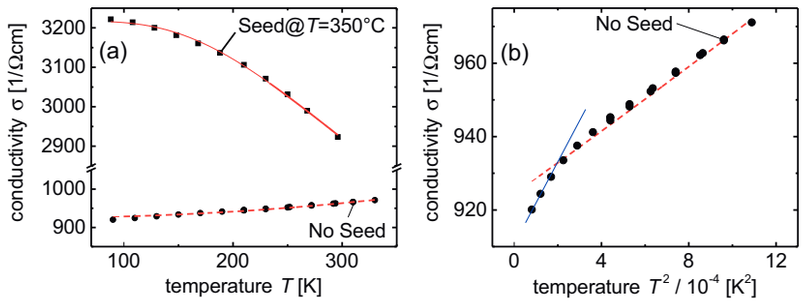

Fig. 4.19. Temperature-dependent conductivity measurements: (a) A sample without seed layer (circles) and a sample with seed layer deposited at 350 °C (squares) was investigated. Red lines are fits using the conductivity model discussed in Sections 4.1 and 4.2. Note that the sample without seed layer was fitted using the field emission model only. (b) The conductivity of the sample without seed layer is plotted over the squared temperature. The red dashed line represents the fit also shown in (a). However, two different slopes were present in the measurement. The blue solid line is a guide to the eye for the steeper slope.

In conclusion, the temperature-dependent conductivity measurements underlined the hypothesis that the application of seed layers improved the transport across grain boundaries.

The sample without seed layer provided an interesting feature that is observed when the conductivity is depicted as a function of the squared measurement temperature. The field emission model exhibited quadratic temperature dependence. Therefore, one should observe a single straight line in Fig. 4.19(b). However, not a single but two straight lines with different slopes were observed. The fit, depicted as the red dashed line, is an average of both slopes. It agrees well with the smaller slope since the smaller slope dominated over most of the temperature range. Such measurements showing two straight lines have also been reported for polycrystalline silicon films [156]. The observation was explained by disorder in the films, i.e non-uniform barrier heights and dopant distribution.

Optical properties Fig. 4.20 shows transmittance and absorptance of samples without seed layer and with seed layers deposited at $T_{\mathrm{seed}} = 250\,^{\circ}\mathrm{C}$ and $T_{\mathrm{seed}} = 450\,^{\circ}\mathrm{C}$. As already presented in the previous section, the seed layer reduced the absorptance in the wavelength range between 350 nm and 600 nm in comparison to the reference sample without seed layer. However, the absorptance was not as low as for the

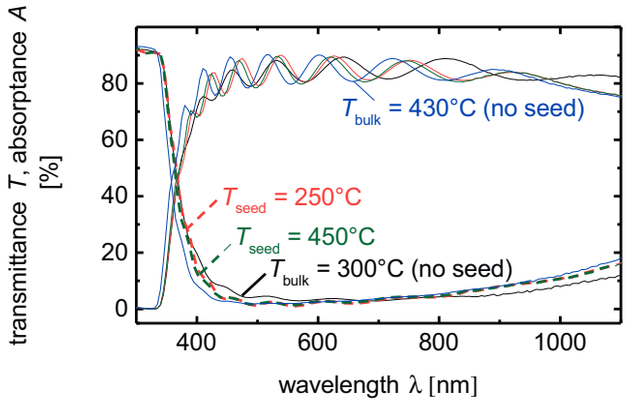

Fig. 4.20. Transmittance and absorptance of ZnO:Al layers. A sample without seed layer (black solid line) and two samples with seed layers (dashed lines) deposited at $T_{\mathrm{seed}} = 250\,^{\circ}\mathrm{C}$ and $T_{\mathrm{seed}} = 450\,^{\circ}\mathrm{C}$ are shown. For comparison, a standard high-temperature process ($T_{\mathrm{bulk}} = 430\,^{\circ}\mathrm{C}$) without any seed layer is plotted as well (blue solid line).

high-temperature reference. A higher seed temperature induced a slight absorptance decrease. But this effect was not as pronounced as the effect that was observed when comparing samples with and without seed layer. In the long wavelength range above 800 nm, the absorptance was governed by free carrier absorption and therefore correlated with the carrier concentration. The sample without seed layer possessed a carrier concentration of $3.9 \times 10^{20}\,\mathrm{cm}^{-3}$, the samples with seed layer featured a carrier concentration of $4.3 \times 10^{20}\,\mathrm{cm}^{-3}$ and $4.5 \times 10^{20}\,\mathrm{cm}^{-3}$ for temperatures of 250 °C and 450 °C, respectively (see also Fig. 4.18(b)). Consequently, the sample without seed layer showed the lowest absorptance in the long wavelength range.

Etch characteristics Fig. 4.21 shows SEM images of etched ZnO:Al layers with various seed layer deposition temperatures. When no seed layer was used, the surface morphology was of Type A [25]. Applying a seed layer deposited at 250 °C, a clear change of surface texture was found compared to samples without seed layer. The texture shifted to a crater-like morphology although craters are still rather small. However, increasing the seed temperature further to 350 °C, led to a crater-like surface texture of Type B. No change of texture was observed by further increasing the seed temperature.

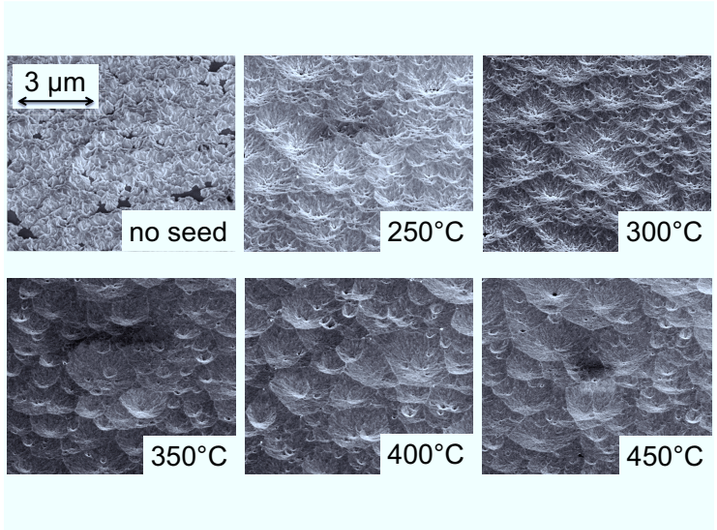

Fig. 4.21. SEM images of etched ZnO:Al layers. The seed deposition temperature was varied from 250 °C to 450 °C. The bulk deposition temperature was 300 °C.

4.3.3.2. Structural properties

AFM measurements The surface morphology of flat ZnO:Al layers was measured with atomic force microscopy (AFM). The layers have not been etched at this stage. Fig. 4.22 shows the rms roughness (a) and height-height correlation length (HHCL)(b) of seed and seed+bulk layers. The definition and practical determination of rms roughness and HHCL may be found in Section 3.3.5. Generally, all samples exhibited a lower rms roughness and HHCL than the reference sample without seed layer. Both quantities showed only a small decrease with increasing seed temperature. Nevertheless, the overall effect of the seed layer was pronounced. The rms roughness of the bulk reference sample without seed layer was 18.1 nm whereas the rms roughness of the seed+bulk sample with seed layer deposited at 300 °C was determined to be 4.2 nm only.

XRD measurements X-ray diffraction (XRD) measurements have been performed to evaluate the influence of seed layers on the structural properties of ZnO:Al films. Fig. 4.23(a) shows that the (002) peak position of seed+bulk layers increased when applying a seed layer. In particular, the seed+bulk sample with seed deposition

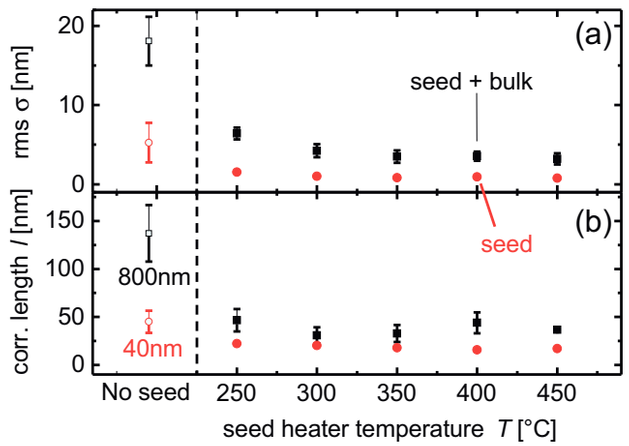

Fig. 4.22. Rms roughness (a) and height-height correlation length (b) for samples without seed layer (open symbols) and samples with seed layer (closed symbols). 40 nm thin seed layers (red circles) and 800 nm thick combinations of seed and bulk layers (black squares) are shown. The samples without seed layer were deposited using bulk layer deposition conditions.

temperature of $T = 250\,°C$ showed a clear increase of (002) peak position in comparison to the bulk layer sample without the application of a seed layer. The (002) peak position of seed+bulk layers saturated for temperatures exceeding 300 °C. In contrast, the (002) peak position of seed layers did not saturate until temperatures exceeding 400 °C were reached.

The full width at half maximum (FWHM) of the (002) peak determined in Bragg-Brentano geometry is presented in Fig. 4.23(b). Seed and seed+bulk layers showed decreasing FWHM with increasing seed layer temperature. The comparison of the samples without seed layer and with seed layer deposited at 250 °C revealed differences between seed and seed+bulk layers. Seed layers had a higher FWHM for all temperatures in comparison to the thin bulk sample, whereas the FWHM of seed+bulk samples was smaller than the FWHM of the sample without seed layer.

The FWHM of the (002) peak determined in rocking curve geometry gives information about the ZnO:Al grain orientation. Fig. 4.23(c) shows the FWHM of rocking curves for seed and seed+bulk layers. Generally the FWHM decreased with increasing seed layer deposition temperature. The seed layers' FWHM were for all samples higher than for the thin bulk layer film. A seed heater temperature of at least 300 °C was

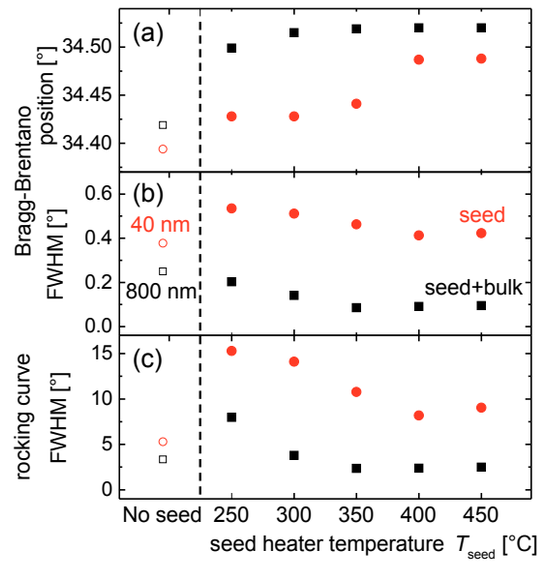

Fig. 4.23. XRD investigations in Bragg-Brentano geometry and rocking curves for a samples without seed layer (open symbols) and samples with seed layer (closed symbols). Bragg-Brentano: (002) peak position (a) and FWHM (b). Rocking curve of (002) peak: FWHM (c). The 40 nm thin seed layers (closed, red circles) and the 800 nm thick combination of seed and bulk layers (closed, black squares) are shown. Bulk layer deposition conditions were used to deposit a 40 nm thin layer (open, red circles) and a 800 nm thick film (open, black squares).

needed so that the seed+bulk samples showed FWHM values comparable to or lower than the sample without seed layer.

4.3.4. Seed layer: thickness variation

4.3.4.1. Electrical, optical, and etching properties

The influence of seed layer thickness on bulk layer properties was investigated. The seed layer thickness was varied from 5 to 100 nm. The seed layer deposition temperature was 350 °C. Similar to the previous Section 4.3.3, a bulk layer deposition temperature of 300 °C was chosen.

A seed layer thickness of 5 nm was sufficient to induce the beneficial effects with regard to electrical, optical, and etching properties. A further increase of seed layer thickness up to 100 nm did not alter the films' properties significantly. Exemplary, the charge carrier mobility is shown as a function of seed layer thickness (Fig. 4.24). A strong mobility increase was observed when applying a seed layer of only 5 nm. Charge carrier concentrations of all samples were in the range of 4.7×10^{20} cm^{-3} to 4.9×10^{20} cm^{-3} and did not show any trend related to seed layer thickness.

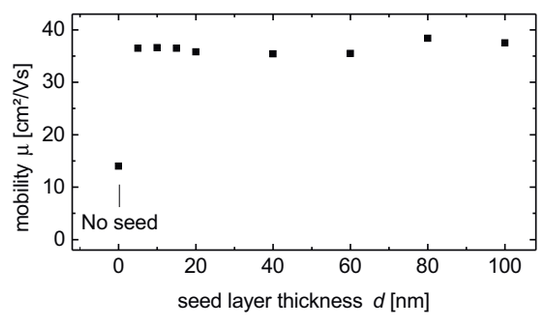

Fig. 4.24. Charge carrier mobility for a sample without seed layer and films with various seed layer thicknesses. The seed layer thickness was varied from 5 nm to 100 nm. The seed deposition temperature was 350 °C. The bulk layer deposition temperature was 300 °C.

4.3.4.2. Microcrystalline silicon solar cells

Microcrystalline silicon μc-Si:H solar cells were deposited on etched ZnO:Al. The results for seed+bulk layers and a high-temperature reference (0 nm) are summarized in Table 4.3. Solar cells with comparable or even slightly higher conversion efficiencies ν than the high-temperature reference could be achieved on ZnO:Al with seed layer approach. Note that ZnO:Al deposition temperatures of the seed layer approach were approximately 100 °C lower than of the high-temperature reference. The open circuit voltage V_{oc} of μc-Si:H solar cells on seed+bulk layers was significantly higher compared to the reference. The fill factor FF was similar for all samples, but there was a small trend to higher fill factors for seed layers of 10 to 15 nm thickness. However, the short-circuit current density j_{sc} of seed+bulk layer samples was lower in comparison to the high-temperature reference. Moreover, the seed+bulk layer sample with thickness of 5 nm had lower j_{sc} than the seed+bulk layer samples with seed thicknesses of 10 and 15 nm.

Table 4.3. Solar cell parameters efficiency η, fill factor FF, open-circuit voltage V_{oc}, and short-circuit current density j_{sc} of µc-Si:H solar cells. The solar cells were deposited on etched ZnO:Al with seed layer thicknesses of 5 to 15 nm. The seed heater temperature was 350 °C. The bulk heater temperature was 300 °C. The reference without seed layer (0 nm) was an etched, high-temperature ZnO:Al bulk film deposited at 430 °C using a TDC of 1 wt%.

thickness [nm]	η [%]	FF [%]	V_{oc} [mV]	j_{sc} [mA]
0	8.4	66.9	507	24.9
5	8.1	66.0	536	22.8
10	8.5	68.8	526	23.5
15	8.6	68.6	531	23.5

4.3.5. Discussion

In the following, the beneficial effect of aluminum for the growth of aluminum-doped ZnO will be discussed in terms of the surfactant concept. Furthermore, the seed layer induced changes regarding intrinsic stress will be interpreted using the grain boundary relaxation model. Finally, an explanation for the improved electrical properties, which go along with the application of seed layers, will be presented.

Aluminum as surfactant Fig. 4.22(a) shows a reduction of rms roughness with the application of seed layers. The roughness reduction is interpreted as a transition from 3D- to 2D-growth. The transition is attributed to the beneficial role of the dopant aluminum. Other authors have also reported on the positive role of aluminum during growth of sputtered ZnO:Al [97, 170, 171]. Aluminum-doped ZnO films showed an improved (002) texture, an increased crystalline quality, and reduced intrinsic stress [97, 170]. Furthermore, the rms roughness was lower for doped layers, similar to our results [171]. Boron-doped ZnO grown by low pressure chemical vapor deposition (LPCVD) also showed lower rms roughness compared to undoped films [172]. In the case of sputtered ZnO:Al, the authors speculate aluminum to act as surface-active species (surfactant) [173–175]. Surfactants are commonly applied during growth of III-V semiconductors to suppress 3D-growth. Surfactants mainly alter the surface diffusion length of the impinging atoms. Depending on the surfactant used, they can either increase or decrease the surface diffusion length [175].

Highly strained material, e.g. ZnO:Al, might show 3D-growth because this growth mode decreases the intrinsic stress in the layer. Atoms impinging on the growing film diffuse to lattice sites that reduce stress. It could thus be beneficial to decrease the

diffusion length to prevent 3D-growth. However, 3D-growth might also occur because the surface diffusion length is too short for the atoms to reach optimal lattice sites. The increase of the surface diffusion length applying a surfactant might overcome this obstacle.

In our case, I suspect aluminum to enhance the surface diffusion length. Lower deposition pressures or higher deposition temperatures increase the surface diffusion length: the former because of additional energy input into the film by means of higher ion bombardment during growth [25, 64, 97], the latter due to an enhancement of the thermal energy of adatoms [8, 25]. Furthermore, lower deposition pressures or higher deposition temperatures induce a shift of etch morphology from Type A to Type B (see Section 2.4 and [25]). Thus, lower deposition pressures or higher deposition temperatures lead to an enhanced surface diffusion length resulting in a change of etch morphology from Type A to Type B. As seed layers with higher aluminum concentration induced exactly this change of etch morphology from Type A to Type B, I conclude that the surfactant aluminum enhances the surface diffusion length.

Note the interesting fact that higher deposition temperatures enhance the surface diffusion length not only because of the already mentioned increase of the adatoms' thermal energy but also because of aluminum accumulation. Higher deposition temperatures induce augmented zinc evaporation from the surface. Aluminum however is not influenced as its evaporation temperature is higher than the zinc evaporation temperature. Consequently, the aluminum concentration at the surface increases for increasing deposition temperatures. Warzecha, for example, raised the concentration of the dopant gallium in ZnO:Ga films by a factor of two by increasing the deposition temperature from 25 °C to 500 °C [176]. Therefore, high deposition temperatures induce an enhancement of surface diffusion length due to two effects, namely the increased thermal energy of adatoms and the higher concentration of the surfactant aluminum.

In conclusion, the dopant aluminum acts as a surfactant that increases the surface diffusion length. As a result, 3D-growth of the highly aluminum-doped seed layer is prevented and further growth of bulk layers is ameliorated.

Stress and grain boundary relaxation model Fig. 4.23(a) shows the (002) peak position to increase with the application of seed layers. The peak shift to higher angles is equivalent to rising tensile stress. Tensile stress might be explained by the grain boundary relaxation model (GBRM) outlined in Section 2.4.4. It predicts an inverse relationship of stress and lateral grain size. Here, the grain size was

determined by the height-height correlation length (HHCL) as determined from AFM measurements. The equalization of grain size and HHCL is justified since Owen showed the surface's lateral feature size to describe the grain size [61].

The application of seed layers led to an increase of tensile stress with respect to the sample without seed layer. The tensile stress increase was computed using XRD measurements and compared to stress values obtained by the grain boundary relaxation model.

The (002) peak position measures the total stress. As bulk layers were grown at the same deposition temperature, the thermal stress should be the same for all investigated films. Thus, a correction of XRD stress measurements by thermal stress is not necessary. The increase of tensile stress

$$\sigma_{\mathrm{Seed}} - \sigma_{\mathrm{NoSeed}} = \frac{E}{1-\nu}\left\{\frac{d_0 - d_{\mathrm{z}}^{\mathrm{Seed}}}{d_0} - \frac{d_0 - d_{\mathrm{z}}^{\mathrm{NoSeed}}}{d_0}\right\} = \frac{E}{1-\nu}\left\{\frac{d_{\mathrm{z}}^{\mathrm{NoSeed}} - d_{\mathrm{z}}^{\mathrm{Seed}}}{d_0}\right\} \tag{4.51}$$

comprises strained and unstrained vertical lattice spacing d_{z} and d_0, Young modulus E and Poisson ratio ν.

The tensile stress increase with respect to the sample without seed layer is given by the grain boundary relaxation model as

$$\sigma_{\mathrm{Seed}} - \sigma_{\mathrm{NoSeed}} = \frac{E}{1-\nu}\, r_0 \left\{\frac{1}{L_{\mathrm{Seed}}} - \frac{1}{L_{\mathrm{NoSeed}}}\right\}. \tag{4.52}$$

L denotes the grain size determined by AFM. r_0 is the ionic radius and unknown. Here, it was used as a parameter to fit the GBRM stress data to the values of the XRD measurements.

Fig. 4.25 shows the tensile stress increase as determined by the GBRM and XRD measurements. One notices a reasonable agreement between both methods of stress determination. The exception was the sample with seed layer grown at 400 °C. Here, the grain size was slightly larger than for films at 350 °C and 450 °C. Therefore, the GBRM predicted a slightly lower tensile stress than the XRD measurements.

Generally, the grain boundary relaxation model explained the increasing tensile stress well. Consequently, the tensile stress of seed layer samples resulted from smaller grains as compared to the film without seed layer.

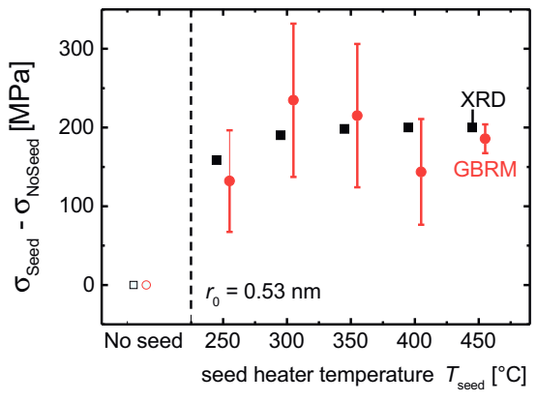

Fig. 4.25. The relative tensile stress obtained by the grain boundary relaxation model (GBRM) (red circles) and by XRD measurements evaluating the (002) peak position (black squares) are shown for seed+bulk layers whereby seed layers were deposited at various temperatures. The value of the fit parameter r_0 is given in the graph.

Film structure and mobility The seed layer did hardly influence the electrical properties for bulk deposition temperatures of 100 °C and 200 °C (see Table 4.2). Only for bulk deposition temperatures of 300 °C, a significant improvement was achieved by the application of seed layers. This difference is mainly attributed to the mobility decrease of the sample without seed layer. However, for all three bulk deposition temperatures, one observed a change of etch morphology from Type A without seed layer to Type B with seed layer (see Fig. 4.17). I extracted from the data of Berginski et al. [8] that the peculiar mobility dip prevails for various TDC, and that it shifts to lower deposition temperatures when increasing the TDC. Moreover, I observed that the etch morphology was Type A for deposition temperatures smaller or equal to the dip temperature, and that Type B prevailed for higher deposition temperatures. The change of etch morphology when using a seed layer could thus be interpreted as shifting the material from the lower to the higher temperature side of the mobility dip. This interpretation could also explain the seemingly unchanged electrical parameters for bulk deposition temperatures of 100 °C and 200 °C, because mobilities in the same range occur on either side of the mobility dip.

Fig. 4.23(b) and (c) show the FWHM of the (002) peak using Bragg-Brentano (BB) geometry and rocking curves (RC). As described in Section 3.3.6, the Bragg-Brentano FWHM is a measure for the crystalline quality. The rocking curve FWHM describes

the tilt of the crystallites. Lower FWHM values imply a better crystalline quality and better grain orientation. Both FWHM values decreased with increasing seed layer deposition temperature. Thus, higher seed layer deposition temperatures resulted in a better crystalline quality and grain orientation of the ZnO:Al films. The improved structural quality of the films might explain the enhanced mobility that was observed for higher seed layer deposition temperatures. However, the 250 °C seed layer sample showed only a slightly lower BB-FWHM and actually a higher RC-FWHM than the sample without seed layer although the mobility of the former was significantly higher than the mobility of the latter film. Hence, crystallographically improved or better oriented grains were not the reason for the enhanced mobility of samples using seed layers.

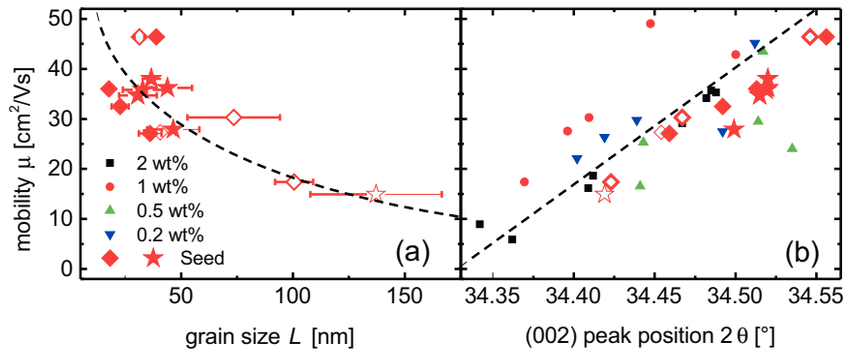

Fig. 4.26. The charge carrier mobility is plotted as a function of grain size (a) and (002) peak position (b), respectively. Bulk (red diamonds) and seed layer (red asterix) deposition temperatures were varied. Samples with (closed symbols) and without (open symbol) seed layer are shown. The grain size was determined by AFM measurements. Data from [8] was added to figure (b). The dotted lines are guides to the eye. Note that AFM and XRD data of the bulk layer temperature variation series have not been shown in the respective Section 4.3.2.

It was shown before that seed layers reduced the grain size (see the previously discussed GBRM). If grain boundaries determined the mobility in the films, the mobility would be expected to decrease with decreasing grain size because the number of electron scattering grain boundaries increased. This is certainly not the case as the sample without seed layer showed the largest grain size but the lowest mobility. One interpretation of this observation might be that grain boundaries did not influence the electrical transport in the films. However, optical fits, temperature-dependent conductivity measurements, and fits to $\mu - n$ data (see Fig. 4.6) suggested grain

boundary scattering to be the limiting transport mechanism. These measurements furthermore suggested grain boundary scattering to be reduced as a result of seed layer application. Note also that etch characteristics supported a change in grain boundary morphology. Therefore, I propose the hypothesis that a decrease of grain size goes along with an improvement of grain boundary morphology due to an overall ameliorated growth of the films. To support the hypothesis, Fig. 4.26 shows the mobility as function of grain size (a) and (002) peak position (b), respectively. According to the GBRM, grain size and (002) peak position are correlated. Fig. 4.26(a) and (b) should hence be redundant and give the same results. Indeed, both quantities, grain size and (002) peak position, show a reasonable correlation to the mobility, which supports my hypothesis that smaller grains have more but also more conductive grain boundaries. More importantly, my hypothesis leads to a counterintuitive relationship between mobility and grain size: the smaller the grains, the higher the mobility.

Conclusion ZnO:Al = 1% films grown on ZnO:Al = 2% seed layers possessed reduced grain size and surface roughness, higher tensile stress and improved electrical and etch properties. The surfactant effect of the dopant aluminum was proposed as explanation for lower grain size and roughness. The higher aluminum content in the seed layers increased the surface diffusion length resulting in preferential 2D-growth. The beneficial 2D-growth was then adopted by the subsequently grown bulk layers with lower aluminum content. The tensile stress was interpreted in terms of the grain boundary relaxation model. In the framework of this model, the augmented tensile stress applying seed layers resulted from reduced grain size. Furthermore, fits to $\mu - n$ data, temperature-dependent conductivity measurements, optical fits, and etching characteristics suggested that the use of seed layers reduced grain boundary scattering although the number of grain boundaries increased due to lower grain sizes. Thus, the application of seed layers significantly improved the grain boundary morphology resulting in higher mobility and more suitable etching characteristics. A seed layer thickness of 5 nm was sufficient to set the beneficial 2D-growth mode.

4.4. ZnO:Al Annealing

Literature overview Several authors have conducted post-deposition annealing of doped, polycrystalline ZnO to improve electrical and optical properties. The annealing process can be distinguished into furnace, laser, and rapid thermal annealing. The annealing behavior of doped, polycrystalline ZnO depends predominantly on annealing temperature and atmosphere. Here, I differentiate the literature overview by the annealing atmosphere. I focus on charge carrier mobility and concentration, optical transmittance, and structural properties determined by Raman spectroscopy and XRD measurements.

Vacuum: Furnace annealing in vacuum with temperatures up to 500 °C increased the charge carrier mobility [47, 177, 178]. The charge carrier concentration decreased [47], increased [178], or did not show a clear trend [177]. The optical transmittance in the 400 to 1000 nm range improved [177]. Raman spectra showed a decreasing intensity of the peak at roughly 570 cm^{-1} [177, 179]. The intensity drop of the 570 cm^{-1} peak was attributed to improved crystallinity [177] or to a diminution of electric fields induced by charge trapping at grain boundaries [179]. For further information about Raman spectroscopy of ZnO films, I refer to Section 4.4.4. The crystalline quality as deduced from XRD measurements in Bragg-Brentano geometry[7] increased upon annealing [177, 179].

H_2: Several authors reported a lower resistivity and higher mobility after furnace annealing in H_2 or H_2/N_2 at temperatures between 300 and 400 °C [177, 180, 181]. However, annealing temperatures of 500 °C deteriorated the mobility [177]. Rapid thermal annealing under H_2/Ar atmosphere for 10 min at 500 °C increased the mobility [127]. The carrier concentration and the optical transmittance increased. Charpentier et al. noted that the crystalline quality improved, whereas Oh et al. did not observe an improvement [177, 181]. The intensity of the Raman peak at 570 cm^{-1} decreased [177].

Air/N_2: Furnace annealing in air or N_2 atmosphere decreased charge carrier mobility and concentration [22, 177, 180, 182]. However, rapid thermal annealing for 3 min at 900 °C induced an enhancement of carrier mobility and concentration when the samples were cooled down in Ar ambient [183]. Laser annealing mostly increased the resistivity [184, 185]. A slight amelioration of electric properties can be achieved by carefully choosing the treatment parameters [186]. Optical transmittance increased after annealing [58]. Improved crystalline quality was reported by several

[7] In this work, I defined the crystalline quality as the FWHM of the (002) peak (see Section 3.3.6).

authors [177, 183], whereas Wimmer et al. did not observe clear structural changes after annealing [182].

Annealing under capping layer: The influence of the atmosphere may be reduced by the use of capping layers on top of the doped ZnO films [22, 24, 182, 187]. Thereby, mobilities as high as $70\,\mathrm{cm^2/Vs}$ can be achieved without deteriorating the carrier concentration [24]. Additionally, the optical transmittance was increased by the reduction of sub band gap absorption [58]. Consistent trends relating the mobility to Raman spectroscopy or XRD measurements have not been observed yet. The advantage of the capping layer annealing is attributed to the reduction of the deteriorating effect of oxygen [22]. Remarkably, one can partially reverse the deteriorating effect of annealing without cap by applying a second annealing step under a protective capping layer [182].

Objective The literature overview suggests a lack of investigations connecting detailed structural experiments to comprehensive Hall effect measurements. To my knowledge, only Charpentier et al. have tried to correlate Raman spectroscopy and XRD experiments on the one hand and temperature-dependent Hall effect measurements on the other hand [177]. However, their investigation missed the most interesting annealing procedure, namely the annealing under a protective capping layer. Here, I investigated ZnO:Al films that were subject to annealing procedures at various temperatures with and without capping layer. The aim was to combine structural investigations and temperature-dependent Hall effect measurements with the new ZnO:Al conductivity model developed in Section 4.1.

Experimental details The initial ZnO:Al films were deposited in the large area deposition system (see Section 3.2.1) using a heater temperature of 430 °C and a pressure of 0.1 Pa. The thickness as determined by a surface profiler was 785 nm. ZnO:Al films with the same thickness were carefully chosen by measuring the optical transmittance and comparing the position of interference fringes. The resistance was checked by 4-point measurements. A variation of no more than $0.2\,\Omega$ was observed. All samples were capped in a single PECVD run assuring comparability. Samples with and without protective capping layer were annealed simultaneously. The annealing temperatures were 400, 500, 600, and 650 °C. The plateau time was 6 h. The heating rate was 1.7 K/min. The annealing took place under vacuum with a residual pressure of 1×10^{-4} Pa. For the temperature-dependent Hall effect measurements, an additional sample was prepared that was annealed twice for 24 h at 600 °C.

Outline of investigation First, electrical and optical measurements at room temperature are shown to assure that the process yielded comparable results to literature. Then, temperature-dependent electrical measurements are presented followed by XRD and Raman spectroscopy investigations. A discussion closes this chapter.

4.4.1. Electrical and optical properties at room temperature

Electrical properties Hall effect measurements were performed at room temperature. Fig. 4.27 shows charge carrier mobility (a), concentration (b), and resistivity (c) of ZnO:Al samples annealed at various temperatures with and without capping layer. Annealing under a protective capping layer increased the mobility up to a

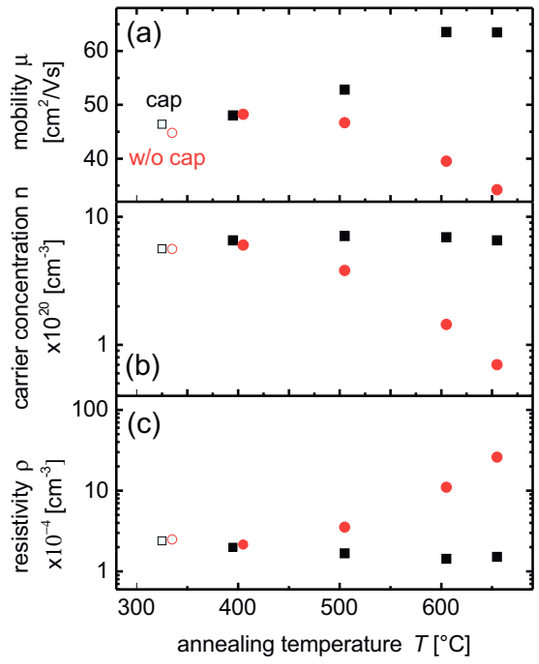

Fig. 4.27. Charge carrier mobility (a), carrier concentration (b), and resistivity (c) are plotted as a function of annealing temperature. Samples were annealed with (black, closed squares) and without (red, closed circles) capping layer. Open symbols represent the non-annealed reference samples. For better clarity, the reference and the 400 °C samples are slightly shifted on the temperature scale.

maximum of 64 cm^2/Vs. The carrier concentration augmented to $7.1 \times 10^{20}\,cm^{-3}$ at annealing temperatures of 500 °C and decreased to $6.5 \times 10^{20}\,cm^{-3}$ at annealing temperatures of 650 °C. Correspondingly, the resistivity decreased from $2.4 \times 10^{-4}\,\Omega\,cm$ for the reference sample to $1.4 \times 10^{-4}\,\Omega\,cm$ at annealing temperatures of 600 °C. Only for annealing temperature of more than 400 °C, the samples without capping layer showed a different behavior than the capped samples. For uncapped ZnO:Al films, the mobility decreased down to 34 cm^2/Vs and the carrier concentration fell to $7 \times 10^{19}\,cm^{-3}$. Consequently, the resistivity increased by one order of magnitude from $2.5 \times 10^{-4}\,\Omega\,cm$ to $2.6 \times 10^{-3}\,\Omega\,cm$.

Optical properties Fig. 4.28 shows the absorptance of samples annealed with (a) and without (b) capping layer. The absorptance peak is induced by free carrier absorption (see Section 2.2.2). The peak's position is mainly determined by the carrier concentration. All films that were annealed under a capping layer showed higher carrier concentrations than the reference sample. Thus, the absorption peak of capped and annealed samples shifted slightly to lower wavelengths. In contrast, decreasing carrier concentrations for the samples without capping layer resulted in a shift of the absorption peak to higher wavelengths.

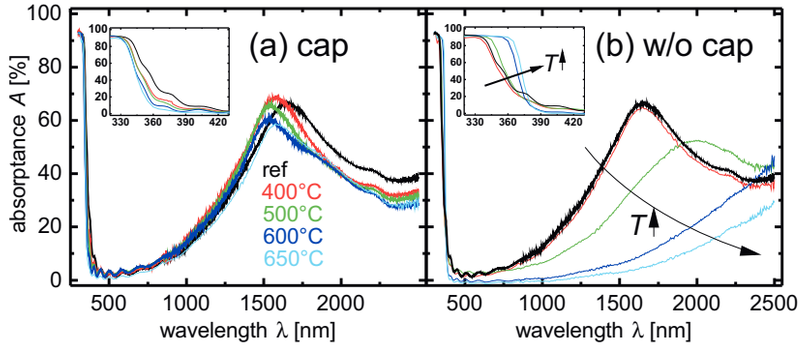

Fig. 4.28. Absorptance of samples annealed at various temperatures with (a) and without (b) capping layer. Small graphs show the wavelength region around the ZnO:Al band gap.

Insets show the improved steepness of the absorption edge after annealing. The tail states that extend into the band gap were reduced by capped and uncapped annealing [57, 58]. Furthermore, the position of the band gap is determined by the carrier concentration. The relationship between band gap and carrier concentration

is described by the Burstein-Moss shift (see Section Fig. 2.2). A lower carrier concentration leads to a smaller band gap and vice versa. This behavior can exemplarily be observed for the samples without capping layer. A reduction of carrier concentration induced a band gap shift to higher wavelengths.

In conclusion, the electrical and optical properties of the samples under investigation agreed with data from literature [22, 24, 182, 187]. Therefore, they are suitable for more detailed investigations.

4.4.2. Temperature-dependent Hall effect measurements

Fig. 4.29 shows temperature-dependent measurements of charge carrier mobility and concentration. Both quantities were measured between 2 and 300 K. The non-annealed reference and samples annealed at 600 °C and 650 °C with and without capping layer were subject of interest. Additionally, I investigated a sample that was annealed twice for 24 h at 600 °C without capping layer.

Comparison of Hall effect measurement tools The temperature-dependent measurements have been performed with a different measurement tool[8] than the simple room-temperature measurements presented at the beginning of this section. A comparison between both tools revealed that the mobility values determined by the room-temperature tool were lower and the carrier concentrations were higher than for the temperature-dependent measurement tool. Exemplarily, the mobility of the reference sample was 46 cm^2/Vs when determined by the room-temperature tool and 51 cm^2/Vs as measured with the temperature-dependent tool. Similar differences were observed for the other samples.

In a round robin test with several project partners, the room-temperature tool's accuracy was evaluated. It was found that the room-temperature tool underestimates the mobility and overestimates the carrier concentration in comparison to the project partners' values[9]. A mobility difference of roughly 2 cm^2/Vs was found. It might be possible that the temperature-dependent measurements slightly overestimate the mobility. The measurement inaccuracies of both tools might thus lead to the observed mobility and carrier concentration differences of roughly 10%.

[8] The temperature-dependent measurements were conducted by partners at the I.Institute of Physics (IA) of RWTH Aachen University.

[9] Project partners were the Helmholtz-Zentrum Berlin (HZB), the Fraunhofer Institute for Surface Engineering and Thin Films (IST), and the company Euroglass.

Charge carrier mobility Fig. 4.29(a) shows temperature-dependent mobility measurements. With the exception of the uncapped film that was annealed twice at 600 °C, the mobility decreased for all investigated samples in the temperature range from 100 to 300 K. The higher the mobility at 2 K, the more pronounced was the mobility decrease. In the temperature range between 2 to 100 K, a constant or slightly decreasing mobility was observed for most samples. However, Fig. 4.29(a') reveals a small mobility increase in this temperature range for the sample annealed at 650 °C without capping layer. A more pronounced mobility increase was observed for the film that was annealed twice at 600 °C.

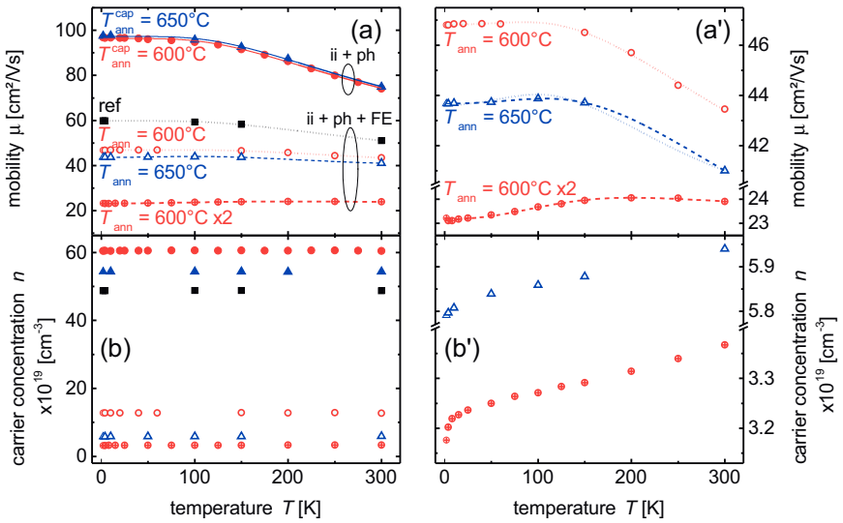

Fig. 4.29. Charge carrier mobility (a) and concentration (b) have been measured from 2 to 300 K. Measurements of a reference and samples annealed at 600 °C and 650 °C with and without capping layer, respectively, were performed. Additionally, a sample that was annealed twice for 24 h at 600 °C without capping layer is depicted (600 °C x2). Fits of capped and annealed samples (solid lines) take into account ionized impurity (ii) and electron-phonon scattering (ph). Fits of uncapped and annealed samples, and the reference sample (dotted and dashed lines) comprise additionally field emission through grain boundaries (FE). Graphs (a') and (b') show mobility and carrier concentration of samples without capping layer in more detail. Dotted lines represent fits where the value of ionized impurity scattering is computed from theory (see Section 4.1.1). In particular, $K = 0\%$ was assumed. Dashed lines are fits where the compensation ratio K was taken into account as an additional fit parameter. Table 4.4 shows an overview about the fit parameter values.

Solid, dotted, and dashed lines in Fig. 4.29(a) denote fits according to the model proposed in Section 4.1. Samples annealed under a capping layer were fitted considering ionized impurity and electron-phonon scattering. Grain boundary scattering was omitted because uncompensated ionized impurity scattering was sufficient to describe the low-temperature mobility of the samples. Note that electron-phonon scattering is negligible at low temperatures. Actually, ionized impurity scattering could not be implemented according to Eq. (4.1) because the mobilities at low temperatures were even under the assumption of $K = 0\%$ higher than predicted by Eq. (4.1). For example, the mobility at 2 K was measured to be 97 $\mathrm{cm^2/Vs}$ for the sample annealed at 600 °C but Eq. (4.1) yields only a value of 89 $\mathrm{cm^2/Vs}$. The difference might be explained by measurement inaccuracies. Also, the free parameters of ionized impurity scattering theory such as the effective mass might be slightly imprecise. In any case, the mobility due to ionized impurity scattering was implemented as a simple fit parameter without recourse to Eq. (4.1).

The reference and the samples annealed without capping layer were fitted considering ionized impurity, electron-phonon, and grain boundary scattering through field emission. Fig. 4.29(a') shows fits of temperature-dependent Hall effect measurements of samples that were annealed without protective layer. Two films, namely the sample annealed at 650 °C and the sample annealed twice for 24 h at 600 °C (600 °C x2), showed a slight mobility increase in the low temperature range that is characteristic for field emission. The dotted lines assume the layer to be uncompensated ($K = 0\%$). In contrast, dashed lines are fits where the compensation ratio K was taken into account as an additional fit parameter. In case of the 650 °C layer, the fit with K as variable parameter (dashed line) is certainly better than the fit with $K = 0\%$ (dotted line). The 600 °C x2 films could not be fitted under the assumption of $K = 0\%$. Only the implementation of a variable K led to the satisfactory fit result that is shown in Fig. 4.29(a'). The reference and the 600 °C sample did not show the peculiar mobility increase at low temperatures. Thus, one cannot determine the exact share of ionized impurity and grain boundary scattering. Satisfying fits can be obtained by either assuming $K = 0\%$ and taking into account grain boundary scattering or by neglecting grain boundary scattering and assuming $K = 8.5\%$.

Table 4.4 presents the parameters of fits shown in Fig. 4.29(a'). In addition, the mobility values for the scattering mechanisms ionized impurity (ii), electron-phonon (ph), and grain boundary scattering through field emission (FE) are given. For the reference and the 600 °C sample, two different assumptions with regard to the share of ionized impurity and grain boundary scattering have been evaluated.

Table 4.4. Parameters of fits to temperature-dependent Hall effect measurements (Fig. 4.29(a')) are shown: compensation ration K, electron-phonon coupling constant λ_{tr}, Debye temperature Θ, and trap density at grain boundaries Q_t. Furthermore, mobility μ values at room temperature for the scattering mechanisms ionized impurity (ii), electron-phonon (ph), and grain boundary scattering through field emission (FE) are depicted.

		fit parameter				μ [cm^2/Vs]		
sample	cap	K [%]	λ_{tr}	Θ [K]	Q_t [cm^{-2}]	ii	ph	FE
650 °C	Y	0	0.138	930	–	97	328	–
600 °C	Y	0	0.132	899	–	96	362	–
650 °C	N	16	0.210	1142	2.4×10^{13}	77	352	117
600 °C x2	N	28	0.503	1096	1.7×10^{13}	45	144	79
ref	–	0	0.138	904	1.3×10^{14}	97	326	65
ref	–	8.5	0.132	925	–	60	348	–
600 °C	N	0	0.157	996	4.6×10^{13}	149	375	73
600 °C	N	21	0.212	1143	–	47	585	–

Charge carrier concentration Fig. 4.29(b) demonstrates the films to be degenerate semiconductors because the charge carrier concentrations are temperature-independent. The donor ionization energy vanishes and the dopant electrons are not localized even at low temperatures. The transition to a metal-like behavior takes place at a certain carrier concentration which is typically in the range of 5×10^{18} cm^{-3} for ZnO [154]. However, Fig. 4.29(b') shows the samples annealed without capping layer to have a small activation energy. Following Ada-Hanifi et al., the activated carrier concentration can be explained by disorder [156]. Disorder comprises non-uniform barrier heights and dopant distribution. For high carrier concentrations, the disorder is screened and the carrier concentration is not activated. But for low carrier concentration, the disorder induces an activation of the carrier concentration.

4.4.3. XRD investigations

Bragg-Brentano measurements have been performed to investigate the structural changes during the annealing process. Fig. 4.30(a) shows the mobility as a function of (002) peak position. Data points are labeled by annealing temperatures. Black squares and red circles denote the samples annealed with and without capping layer, respectively. A reduction of mobility with increasing peak position was observed.

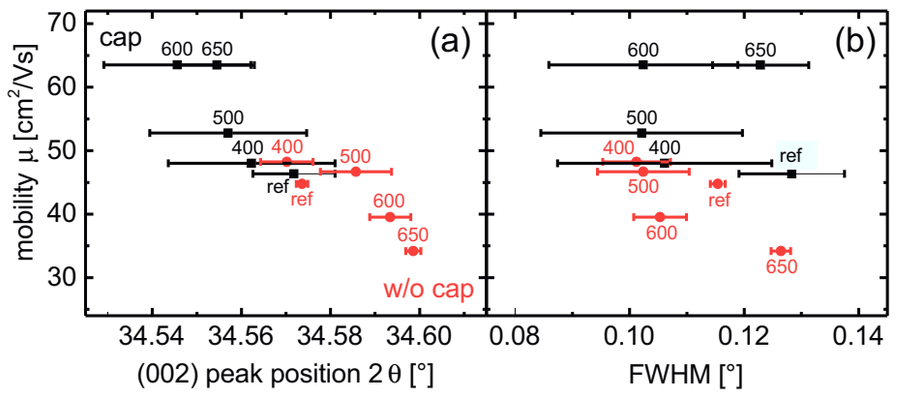

Fig. 4.30. The mobility is depicted over the (002) peak position (a) and the FWHM (b) as determined from XRD measurements in Bragg-Brentano geometry. Black squares and red circles denote the samples annealed with and without capping layer, respectively. Numbers close to the data point represent the annealing temperatures.

Moreover, the annealing with capping layer induced a peak shift to lower angles, whereas one noted a peak position increase for the annealing without capping layer. Fig. 4.30(b) points out that, within the measurement error, there is no correlation between the FWHM of the (002) peak and the mobility. One can thus state that the annealing process induced merely a slight variation of the crystalline quality as deduced from the FWHM.

4.4.4. Raman spectroscopy

In addition to XRD measurements, Raman spectroscopy was performed in order to study the microstructural properties of annealed ZnO:Al. Fig. 4.31 shows Raman spectra of ZnO:Al films that were annealed with and without capping layer. In the following, I will discuss the origin of the various peaks with regard to literature.

$\nu = 566\,\mathrm{cm}^{-1}$: A broad, asymmetric peak at $566\,\mathrm{cm}^{-1}$ was observed. A comparison to Table 4.5 reveals that the $566\,\mathrm{cm}^{-1}$ peak might correspond to the A_1(LO) mode. Tzolov et al. explained the high intensity of the A_1(LO) mode by electric field induced Raman scattering (EFIRS) [191]. They assumed the electric fields prevailing at grain boundaries due to charge trapping to enhance the intensity of the A_1(LO) mode. Furthermore, they related the low wavenumber part of the asymmetric A_1(LO) mode

Table 4.5. Group theory predicts the following active and silent Raman modes and shifts in single-crystalline ZnO [188–190]. The measurement geometry, where the incident light was perpendicular to the substrate, implies that only E_2 and A_1(LO) modes should be observable [43].

active modes	E_2^{low}	E_2^{high}	A_1(TO)	E_1(TO)	A_1(LO)	E_1(LO)
Raman shift ν [cm^{-1}]	102	437	380	407	570	583

silent modes	B_1^{low}	B_1^{high}
Raman shift ν [cm^{-1}]	275	580

to localized phonon modes continuously spread in energy because of disordered crystallites[10].

In contrast, Manjón et al. argued that the discussed Raman mode at 566 cm^{-1} belongs to the silent B_1^{high} mode [190]. They supposed the occurrence of the silent Raman mode to be "likely disorder-activated Raman scattering (DARS). This scattering is induced by the breakdown of the translation symmetry of the lattice caused by defects or impurities either because of the dopant nature or because of the growth conditions [..]". Their hypothesis is supported by the detection of the silent B_1^{low} mode at 274 cm^{-1}. A discussion of the B_1^{low} mode is found further down. Note that besides DARS also EFIRS might activate silent Raman modes.

In my opinion, Lorite et al. proved the EFIRS hypothesis convincingly by applying an external electric field during Raman spectroscopy measurements [193]. They observed that the application of the external electric field reduced the intensity of the 566 cm^{-1} peak. According to their interpretation, the external electric field reduced the electric potentials at grain boundaries thereby reducing the effect of EFIRS. Note that disorder and defects are a prerequisite for the charge trapping and thus the electric potentials at the grain boundaries. Thus, EFIRS might be seen as a special case of DARS.

In conclusion, it is not clear whether the 566 cm^{-1} peak is related to the A_1(LO) or the B_1^{high} mode. Yet I will base my further argumentation on the assumption that

[10] Charpentier et al. evaluated the low and high wavenumber contribution of the A_1(LO) mode to gain "qualitative information about the crystallinity of the films." They assumed the low wavenumber part to represent disordered material and the high wavenumber part to correspond to crystalline material [192].

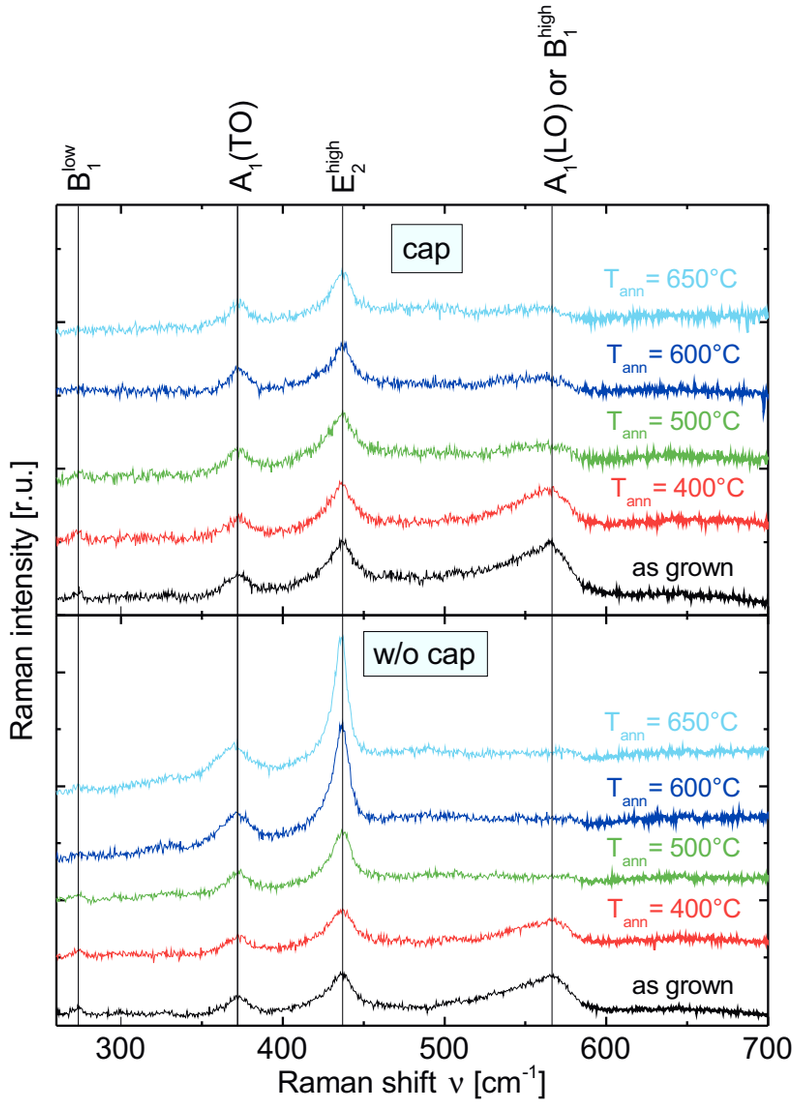

Fig. 4.31. The graph shows Raman spectroscopy of samples annealed at various temperatures with and without capping layer. As-grown, non-annealed layers are presented as reference. The peaks at 274 cm^{-1}, 372 cm^{-1}, 437 cm^{-1} and 566 cm^{-1} correspond to the B_1^{low}, $A_1(TO)$, E_2^{high}, and $A_1(LO)$ or B_1^{high} mode, respectively.

electric potentials at grain boundaries, which induce electric field induced Raman scattering, are the reason for occurrence and intensity of the observed 566 cm^{-1} peak.

Fig. 4.31 reveals decreasing intensity of the 566 cm^{-1} peak with increasing annealing temperature. More importantly, the intensity reduction was found for samples annealed with and without capping layer. For samples without capping layer, this observation is consistent with literature [177,179,191]. I stated that electric potentials at grain boundaries might be the reason for the 566 cm^{-1} peak. In view of this fact, I suppose these electric potentials to be reduced by the annealing procedure. In other words, I suspect the amount of trap states at grain boundaries to decline as a consequence of the annealing process irrespective of the presence of a capping layer.

$\nu = 437\,cm^{-1}$: The peak at 437 cm^{-1} corresponds to the E_2^{high} mode [43, 188, 191, 192, 194]. Several authors ascribe this peak to vibrations of oxygen atoms [43, 192, 193, 195, 196].

One extracts from Fig. 4.31 that the peak at 437 cm^{-1} did not change if the annealing process was conducted with capping layer. However, annealing executed without capping layer resulted in increasing peak intensities with increasing annealing temperature. Thus, I speculate that annealing without capping layer led to incorporation of oxygen whereas the capping layer prevented oxygen from diffusing into the ZnO:Al layer[11]. Note that the assumption of oxygen incorporation during annealing without capping layer is supported by SIMS measurements[12].

$\nu = 372\,cm^{-1}$: This peak is assigned to the A_1(TO) mode. Actually, the used measurement geometry implies that this mode should not be observable in single-crystalline ZnO. However, the polycrystalline character [192] or the doping [198] of the films activate it.

The A_1(TO) mode showed a similar behavior as the 437 cm^{-1} peak, namely it increased with higher annealing temperatures for annealing without cap whereas it stayed constant when a capping layer was applied. Yet I lack a connection between the A_1(TO) mode and specific features of the microstructure. Therefore, I cannot comment on the peak intensity change as a function of annealing parameters.

[11] Lupan et al. even deduced a better crystalline quality after annealing from an increase of the E_2^{high} peak [197].
[12] J. Hüpkes, private communication

$\nu = 274\,\mathrm{cm}^{-1}$: I suspect this peak to be the B_1^{low} mode [190, 191]. It is supposed to occur for the same reason as its high wavelength counterpart, the B_1^{high} mode, that is to say, the electric potentials at grain boundaries.

As a result of its intensity reduction during annealing, it is concluded, equivalent to the $566\,\mathrm{cm}^{-1}$ peak, that the electric fields at the grain boundaries were diminished by the annealing process. Note also that the intensity reduction was observed for capped and uncapped samples.

4.4.5. Discussion

Two mechanisms will be considered and discussed to explain the impact of annealing on the electrical properties of ZnO:Al. These two mechanisms are a change of compensation ratio K and an altered grain boundary trap density Q_t.

Temperature-dependent Hall effect measurements The samples that were annealed under a capping layer showed mobilities close to the ionized impurity limit for uncompensated material $K = 0\%$. Based on these results, it is reasonable to assume the compensation in cap annealed ZnO:Al layers to be zero. The mobility in capped layers is thus limited by ionized impurity scattering with $K = 0\%$ and electron-phonon scattering.

The mobility decreased after the annealing procedure without the use of capping layers. Assuming the deterioration of the mobility to be induced by the creation of acceptors only, thus neglecting grain boundary scattering completely, would lead to a compensation ratio of $K = 26\%$ for the 650 °C sample and $K = 36\%$ for the 600 °C x2 film. However, the temperature-independent ionized impurity scattering cannot explain the slight mobility increase in the low temperature range that was observed for both samples. The mobility increase is rather explained by additional grain boundary scattering. For the 650 °C and the 600 °C x2 films, the fits yield values of $117\,\mathrm{cm}^2/\mathrm{Vs}$ and $79\,\mathrm{cm}^2/\mathrm{Vs}$, respectively, for grain boundary scattering at room temperature. Ionized impurity scattering induced mobility values of $76\,\mathrm{cm}^2/\mathrm{Vs}$ and $45\,\mathrm{cm}^2/\mathrm{Vs}$ corresponding to $K = 16\%$ and $K = 28\%$. Since the mobility values of electron-phonon scattering were generally higher (see Table 4.4), one concludes the mobility of the uncapped samples to be mainly limited by ionized impurity scattering and field emission at grain boundaries.

Raman spectroscopy and grain boundary scattering The limiting scattering mechanisms of the reference sample are suggested to be ionized impurity scattering

and grain boundary scattering. Ionized impurity scattering is supposed to play a decisive role because the mobility is computed to be even in the uncompensated case as low as 97 $\mathrm{cm}^2/\mathrm{Vs}$. Grain boundary scattering is assumed to be important because Raman spectroscopy suggested potential barriers at the grain boundaries to exist in this material. The exact share of ionized impurity and grain boundary scattering however cannot be determined for the reference sample. Nevertheless, the maximum compensation ratio can be determined to be $K = 8.5\%$ if one assumes to have no grain boundary scattering. Note that this value is lower than the one estimated for the uncapped and annealed samples.

Fig. 4.32. The image illustrates the interaction between grain boundary trap density and carrier concentration. (a) Reference sample: A high grain boundary trap density Q_t and a high carrier concentration imply low barrier heights and small barrier widths. Grain boundary scattering exists but it is rather weak. (b) Annealing with capping layer: A high carrier concentration induces a Fermi level E_F situated highly above the conduction band E_C. Under the assumption of a rather low trap density at the grain boundaries, the Fermi level might lie above the barrier. Grain boundary scattering is negligible. (c) Annealing without capping layer: Low carrier concentrations in conjunction with low trap densities might lead to high barrier heights and large barrier widths. Grain boundary scattering is relatively strong.

Fig. 4.32(a) exemplifies the situation of the reference sample. Raman spectroscopy suggested the grain boundary trap density Q_t of the reference to be higher than for the annealed samples. The high trap density in conjunction with the rather high

carrier concentration implies grain boundary scattering to be active. However, based on the temperature-dependent mobility measurements, grain boundary scattering is supposed to be less important for the reference sample than for the samples annealed without capping layer. This was taken into account in Fig. 4.32(a) by the smaller barrier width and the lower barrier height in comparison to Fig. 4.32(c).

Raman spectroscopy suggested potential barriers at grain boundaries to decrease for the capped and uncapped annealing procedure. This result seems contradictory at first, because grain boundary scattering was on the one hand supposed to be important for the uncapped layers, but, on the other hand, it was proposed to be negligible for the capped samples. The contradictory result can be explained by the different carrier concentrations of capped and uncapped samples. Fig. 4.32(b) and (c) show exemplarily that the same amount of grain boundary trap states Q_t might induce different levels of grain boundary scattering. Fig. 4.32(b) illustrates the case of annealing with capping layer. Raman spectroscopy suggested the grain boundary trap density to be comparable to the case of uncapped annealing. However, the carrier concentration is significantly higher in the capped films. The Fermi level might thus be situated above the barrier. Grain boundary scattering would be negligible. Fig. 4.32(c) corresponds to the case of annealing without capping layer. The diminished carrier concentration implies the Fermi level to lie close to the conduction band minimum. Thus, barrier height and width are high and grain boundary scattering exists.

Effect of capping layer I suggested that ZnO:Al annealing reduced the trap density at the grain boundaries irrespective of the existence of a capping layer. Grain boundary scattering was supposed to be an important factor for the uncapped samples only because the carrier concentration decreased parallel to the decrease of grain boundary trap density. Thus, the vanishing grain boundary scattering with the application of a capping layer is eventually obtained because the capping layer prevented the carrier concentration to drop.

A further difference between the capped and uncapped ZnO:Al films is their different compensation ratio K. The compensation ration was determined to be $K = 0\%$ in the capped case and $K = 16\%$ respectively $K = 28\%$ in the uncapped case. A maximum compensation ratio of $K = 8.5\%$ was estimated for the reference sample. Therefore, it can be concluded that the annealing under capping layer reduced the compensation and that, in contrast, the annealing without capping layer increased the compensation.

Annealing induced microscopic changes Annealing might induce a reorganization of the crystal lattice within the grain boundary region that reduces the defect density at the grain boundaries [23]. The hypothesis of defect reduction at the grain boundaries is supported by Raman spectroscopy and temperature-dependent mobility measurements. I speculate that the reorganized grain boundaries might also reduce the interatomic attractive forces between adjacent grains. The grain boundary relaxation model presented in Section 2.4.4 predicts in this case a reduction of tensile stress in the annealed layers. And indeed, under the assumption of a constant compressive stress component, the decreasing (002) peak positions hint to a reduction of tensile stress in ZnO:Al films that were annealed under a capping layer.

Tensile stress increased when a capping layer was not applied although a decreasing tensile stress was expected following the grain boundary relaxation model. One can speculate that decreasing tensile stress resulting from grain boundary reconstruction was overcompensated by the escape of zinc atoms. The generated zinc vacancies act as acceptors. Acceptors reduce the carrier concentration and increase ionized impurity scattering. Both effects have been suggested before for annealed and uncapped ZnO:Al. However, the amount of acceptors needed to account for the carrier concentration drop of the uncapped, 650 °C sample would imply after Eq. (4.1) a mobility of 8 cm/Vs. Thus, acceptor generation cannot be the only reason for the lower carrier concentrations in samples without capping layer. Additional donor deterioration has to take place. Raman spectroscopy suggested incorporation of oxygen in the uncapped ZnO:Al. As a consequence, I speculate that either the filling of oxygen vacancies or the oxidation of aluminum might take place. Note that oxygen incorporation increases compressive stress and hence counteracts tensile stress. Thus, both processes, Zinc removal and oxygen assimilation, might be active, but Zinc removal dominates the stress measurements whereas oxygen assimilation dominates the Raman spectroscopy.

Conclusion Annealing with capping layer reduced the grain boundary trap density, prevented the carrier concentration to drop and reduced compensation in the films. Thus, ionized impurity and grain boundary scattering were diminished and the mobility increased. Annealing without capping layer reduced the grain boundary trap density as well, but it induced a carrier concentration decrease and a compensation increase. The result was enhanced ionized impurity and grain boundary scattering and thus a reduction of mobility. The decrease of carrier concentration cannot be explained by the enhanced compensation only. Additional donor deterioration has to take place.

5. ZnO:Al on textured substrates

ZnO:Al deposition on textured substrates poses challenges due to the decrease of conductivity and damp heat stability. These challenges need to be tackled for the application of ZnO:Al as transparent conductive front contact in thin-film solar cells such as thin-film silicon or chalcopyrite-based solar cells.

Motivation *Thin-film silicon solar cells* apply textured interfaces to improve the light trapping. Thereby the short-circuit current density increases and thus higher solar cell efficiencies are achieved. Commonly, the transparent conductive oxide (TCO) is textured [8, 17, 18]. Sputter deposition of aluminum-doped zinc oxide (ZnO:Al) layers onto flat substrates and subsequent etching in HCl, HF, or via electrochemical methods leads to textured ZnO:Al surfaces [14–16].

The texture and thus the quality of light trapping, however, depend on the specific growth conditions, such as deposition pressure, temperature [25], or layer thickness [13, 26]. Hence, the deposition parameters have to be carefully adjusted. Additionally, there is a trade-off between optical, electrical, and texture properties, e.g. a thicker layer may enhance the light trapping capability of the textured TCO, but it increases at the same time the parasitic absorption in the TCO layer [13, 27].

Textured glass substrates may overcome the above mentioned obstacles of textured zinc oxide. The texture is provided by the substrate. The subsequently sputtered ZnO:Al layer must be optimized regarding electrical and optical properties only. Hence, textured glass substrates allow the decoupling of texture on the one hand and electrical as well as optical properties on the other hand. Specifically, the layer thickness can be adjusted with regard to the layer resistance, thereby reducing the parasitic absorption in ZnO:Al layers. Textured substrates have been produced by wet-chemical etching [199], nano-imprint lithography [28–30], reactive ion etching [31, 32] or aluminum induced texturization [200].

ZnO:Al is also used as TCO in *chalcopyrite-based solar cells* [41, 201]. Here, the substrate configuration implies ZnO:Al to be deposited onto rough absorber layers.

Naturally, ZnO:Al properties on textured substrates need to be investigated for both solar cell applications. Despite the high need for optimized TCOs on textured substrates, studies about ZnO:Al growth on these substrates are very limited. The

growth of sputtered ZnO:Al on rough substrates with regard to its damp heat stability has been investigated by Greiner et al. for the application in chalcopyrite-based solar modules [33–35]. They found the challenge of ZnO:Al growth on textured substrates to be the decrease of charge carrier mobility in comparison to flat substrates. Moreover, damp heat treatment of ZnO:Al on rough substrates leads to a strong resistivity increase. ZnO:Al growth disturbances, also called extended grain boundaries, were given as reason for this behavior.

A comprehensive investigation regarding the influence of different deposition conditions and substrate morphologies on charge carrier mobility and damp heat stability is still lacking. Thus, in this work, various deposition conditions and substrate textures were investigated in order to understand their effect on mobility and damp heat stability. The objective is hence to understand and overcome ZnO:Al conductivity deterioration and damp heat instability on textured substrates.

Outline of investigation Section 5.1 details the influence of ZnO:Al deposition conditions on conductivity and damp heat stability. Randomly textured substrates and a model structure, that consisted of parallel trenches, were investigated. The deposition conditions comprised deposition temperature and pressure, and film thickness. ZnO:Al films were furthermore characterized by their etching behavior and their structural properties as determined by x-ray diffraction (XRD). Also, the impact of annealing was subject of interest.

Section 5.2 focuses on the influence of various substrate textures on conductivity and damp heat stability. Textured substrates under investigation were texture-etched and nano-imprinted glasses.

A description of ZnO:Al conductivity with a simple electrical model is presented in Section 5.3.

Section 5.4 presents a proof of concept of a-Si:H/µc-Si:H tandem solar cells on texture-etched glass that was coated with thin ZnO:Al layers. Furthermore, double textures were produced by etching thin ZnO:Al on textured substrates in dilute hydrofluoric acid (1 wt%). The influence of the double textures on a-Si:H/µc-Si:H tandem solar cells was investigated.

Experimental details In the course of investigations on ZnO:Al growth on textured substrates, two different configurations of magnets within the cathode, target fixation rings, and substrate holders had to be used. The magnetic fields differed in their strength. The target fixation rings were made of different materials. The important

distinction between both substrate holders was the amount of metal they consisted of.

The first configuration consisted of a magnetic field manufactured by the company *Lesker*. Therefore, this configuration will be referred to as "Lesker". The magnetic strength was measured to be about 15 mT. The target fixation ring was made of stainless steel. The substrate holder was built of more material in comparison to the one used later. The second configuration used a magnetic field produced by the company *Gencoa*. Its strength was determined to be 60 mT. The target fixation ring was made of aluminum. The substrate holder consisted of less material in comparison to the one used in the Lesker configuration. The just described configuration will be called "Gencoa". The similarities and differences between Lesker and Gencoa configuration will be discussed in Section 5.1.

The substrate size was 3 cm × 10 cm for texture-etched glass and 2.5 cm × 5 cm for nano-imprint substrates. Two substrates were always coated within a single deposition: a textured glass and a flat reference. The resulting 6 cm × 10 cm or 5 cm × 5 cm glass area was positioned over the center of the target. Measurements characterizing the layers were performed in the center of each substrate. Note that the racetrack had a diameter of roughly 10 cm.

The film thickness was measured on the flat reference substrates. It was assumed to be similar on flat and rough substrates.

5.1. Influence of deposition conditions

5.1.1. Randomly textured substrates

The influence of deposition temperature and pressure as well as layer thickness on electrical, damp heat, and etching properties was investigated. Post-deposition annealing was evaluated as a method to ameliorate the conductivity and damp heat stability. The randomly textured substrate C was used for the following investigations. It is shown in Fig. 5.15(b). Note that the SiO_xN_y interlayer (see Section 3.2.1) slightly smoothed the glass texture, but preserved the general morphology.

5.1.1.1. Electrical properties

Difference between Lesker and Gencoa configuration The difference between both configurations shall be illustrated by the mobility data presented in Fig. 5.1. Fig. 5.1(a) and (b) represent Lesker and Gencoa configuration, respectively. Three differences shall be discussed:

(1) The deposition temperatures were higher for Lesker than for Gencoa configuration. A good reference point to verify this statement is the striking mobility dip that occured for both configurations. The Lesker configuration showed the dip at roughly 400 °C whereas the Gencoa configuration exhibited the dip at 300 °C. The reason is assumed to be the reduced amount of metal that the Gencoa substrate holder consists of. Consequently, heat was less efficiently conveyed away from the substrate. Substrate temperatures were thus different although heater temperatures were similar.

(2) The mobility in the high temperature range at about 500 °C was higher for Gencoa than for Lesker configuration. Different target fixation rings were identified as the reason for this observation. During the deposition process, the target fixation rings are sputtered as well. The ring material is thus incorporated into the growing film. Secondary ion mass spectrometry (SIMS) measurements revealed the concentration of chrome and iron in the deposited layers to be higher in Lesker than in Gencoa configuration. Chrome and iron are suspected to originate from the stainless steel ring. These elements might have induced defects that reduced the ZnO:Al mobility for high deposition temperatures. Of course, the target fixation ring made of aluminum was less harmful as aluminum is the dopant material anyway.

(3) Fig. 5.1 shows high-pressure and low-pressure experiments. The same low pressure of 0.13 Pa yielded similar results for Lesker and Gencoa configurations. However, the high pressure had to be adjusted in order to obtain similar mobilities and trends. One might speculate the different magnetic fields to be the reason or different depths of race tracks. The depth of race tracks increases with target usage.

Charge carrier mobility Despite the above outlined differences, Lesker and Gencoa configuration showed similar features with regard to mobility as a function of temperature and pressure. The important features were (I) the striking mobility dip which was more pronounced for high pressure, (II) improved mobility on textured substrates at low temperature and pressure, (III) and the fact that, irrespective of temperature, high pressures induced significantly lower mobilities on textured than on flat substrates.

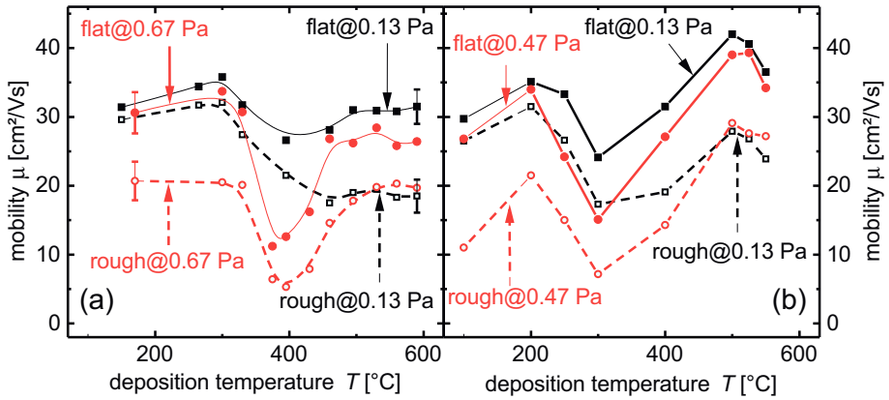

Fig. 5.1. ZnO:Al charge carrier mobility is shown as a function of heater temperature during deposition. A flat reference substrate (closed symbols, solid lines) and a texture-etched glass C (open symbols, dashed lines) were co-deposited. Two different deposition pressures are presented in each graph. Films were prepared using Lesker (a) and Gencoa (b) configuration.

(I) Fig. 5.1 shows a strong deterioration of mobility at temperatures between 300 and 400 °C. A similar mobility decrease was mentioned in Section 4.3. There, it was demonstrated that the mobility drop is caused by increased grain boundary scattering. Here, it is thus reasonable to assume differences in the strength of grain boundary scattering to dominate the mobility as well. Yet, knowledge about the detailed microscopic changes that induce different levels of grain boundary scattering is still lacking.

(II) The mobility on textured substrates (open symbols, dashed lines) was always lower than the mobility on flat substrates (closed symbols, solid lines). Fig. 5.1 shows the magnitude of mobility deterioration on textured substrates to be influenced by deposition conditions. Low-pressure and low-temperature conditions were observed to induce mobility values on textured substrates that were close to the values on flat substrates. Greiner et al. provided evidence that the lower mobility on textured substrates is due to growth disturbances which they called extended grain boundaries (eGB) [33, 34].

(III) Fig. 5.1 shows the mobility on textured substrates to be always lower for high-pressure (red circles) than for low-pressure (black squares) conditions. Only at high temperatures, the mobility level was not influenced by deposition pressure. The influence of pressure on mobility was investigated in more detail at temper-

atures of 200 °C in Lesker configuration. Fig. 5.2 shows ZnO:Al mobility on flat substrates (closed symbols) to be approximately constant between 0.07 Pa and 0.7 Pa. Higher deposition pressures deteriorated the mobility on flat substrates. In contrast, the mobility on rough substrates (open symbols) decreased from its maximum at 0.13 Pa with increasing deposition pressure. Consequently, the highest mobility on textured substrates and the lowest difference between flat and rough substrates were obtained at 0.13 Pa. It will be referred to these deposition conditions (300 °C, 0.13 Pa) as "optimized deposition conditions". The deposition conditions that comprised a pressure of 0.67 Pa at a temperature of 300 °C will be called "non-optimized deposition conditions" because the mobility difference between flat and rough substrates was the highest for these conditions. Note that the given conditions were determined for Lesker configuration. For the sake of completeness, optimized (200 °C, 0.13 Pa) and non-optimized (200 °C, 0.67 Pa) deposition conditions are given for Gencoa configuration as well. Note furthermore that deposition parameters for non-optimized deposition conditions had to be slightly adjusted for nano-imprint substrates and the model structure to obtain similar electrical properties.

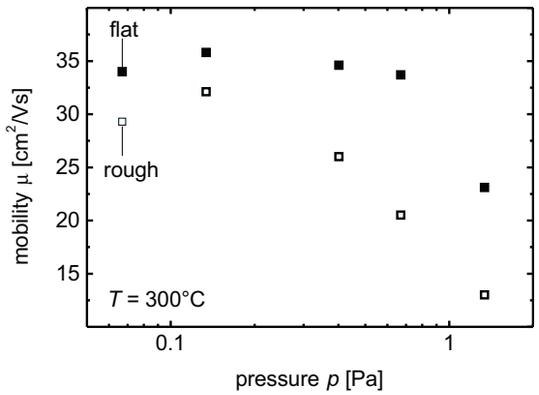

Fig. 5.2. Mobility values of ZnO:Al grown on flat (closed symbols) and rough (open symbols) substrates are plotted as a function of deposition pressure. The deposition temperature was 300 °C. Lesker configuration was used.

The dependence of mobility on film thickness is shown in Fig. 5.3. Optimized (black squares) and non-optimized deposition (red circles) conditions were investigated. For thin layers of 200 nm, the mobility of both deposition conditions was similar whereas it differed for thicker layers. For optimized deposition conditions, the mobility on flat and rough substrates increased with increasing film thickness. The absolute difference between the mobility on flat and rough substrates stayed approximately

the same. Non-optimized deposition conditions induced a slight mobility increase on flat substrates. On rough substrates however, the mobility was independent of thickness.

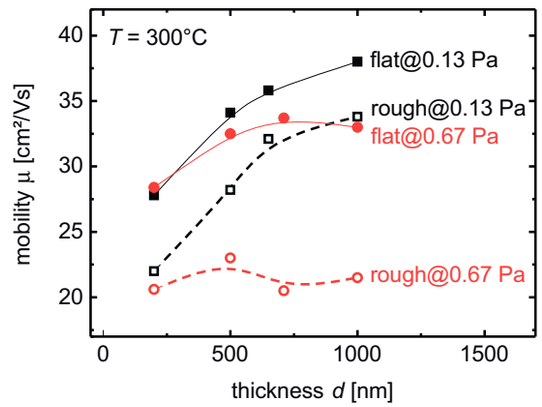

Fig. 5.3. The mobility was investigated for various film thicknesses. Optimized (black data) and non-optimized (red data) deposition conditions were used to grow the films. A flat reference (closed symbol) and a rough substrate (open symbol) were co-deposited. The films were sputtered in Lesker configuration.

Charge carrier concentrations were comparable for flat and textured substrates. They increased with increasing deposition temperature from $2 \times 10^{20}\,\mathrm{cm}^{-3}$ to $3 \times 10^{20}\,\mathrm{cm}^{-3}$. Carrier concentrations were hardly influenced by deposition pressure. At 300 °C, carrier concentrations varied between $2 \times 10^{20}\,\mathrm{cm}^{-3}$ to $2.3 \times 10^{20}\,\mathrm{cm}^{-3}$ without showing a trend related to deposition pressure. For optimized deposition conditions, increasing film thickness induced higher carrier concentrations, e.g. carrier concentrations increased from $1.8 \times 10^{20}\,\mathrm{cm}^{-3}$ for 200 nm to $2.5 \times 10^{20}\,\mathrm{cm}^{-3}$ for 1000 nm. Non-optimized deposition conditions showed no change of carrier concentration related to thickness. Note again that the mobility showed no dependence on thickness for non-optimized deposition conditions.

5.1.1.2. Damp heat stability

Under damp heat conditions, the resistivity of ZnO:Al films on textured substrates is known to degrade faster than on flat substrates [33, 34]. Growth disturbances,

also called extended grain boundaries (eGB), were given as reason for increased degradation.

ZnO:Al films have been deposited on textured substrates at various temperatures, pressures, and thicknesses. Subsequently, the films have been exposed to damp heat. Both, the films on flat and textured substrates, degraded. The degradation on textured substrates comprises degradation that takes place on flat substrates and an additional share that is related to extended grain boundaries. After Matthiessen's rule, one can thus express the resistivity on rough substrates

$$\rho_{\mathrm{rough}} = \rho_{\mathrm{flat}} + \rho_{\mathrm{eGB}} \tag{5.1}$$

as the sum of resistivity on flat substrates ρ_{flat} and extended grain boundaries ρ_{eGB}. Since ρ_{rough} and ρ_{flat} were known, one could compute ρ_{eGB} to evaluate the degradation of extended grain boundaries as a function of deposition conditions.

Fig. 5.4(a) shows ZnO:Al films that have been deposited at various temperatures using a deposition pressure of 0.13 Pa. ρ_{eGB} was calculated for each film and damp heat

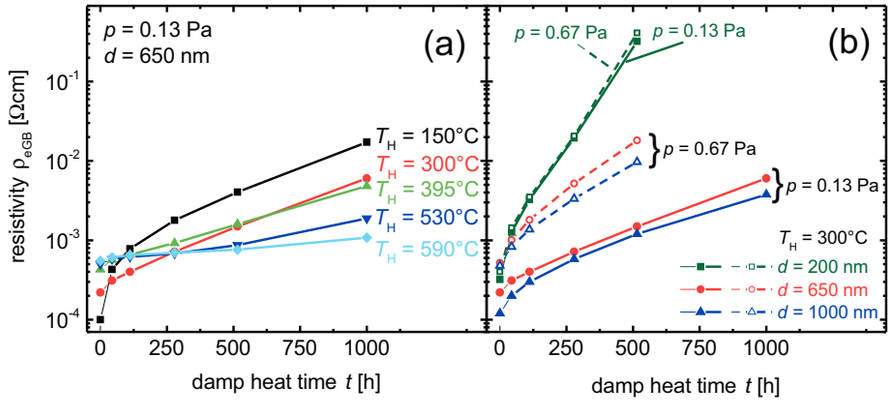

Fig. 5.4. The resistivity of extended grain boundaries ρ_{eGB} is shown as a function of damp heat time. ρ_{eGB} is calculated by applying Matthiessen's rule, i.e. $\rho_{\mathrm{eGB}} = \rho_{\mathrm{rough}} - \rho_{\mathrm{flat}}$. (a) ZnO:Al films were deposited at various temperatures on flat and rough substrates. Deposition pressure and film thickness were 0.13 Pa and 650 nm, respectively. Subsequently, the films were exposed to damp heat. (b) ZnO:Al films with thicknesses of 200, 650, and 1000 nm were deposited with optimized (0.13 Pa, closed symbols) and non-optimized (0.67 Pa, open symbols) deposition conditions. Note that all films were grown using Lesker configuration.

time. One discovers ρ_{eGB} to be more stable with increasing deposition temperature. Note that films which had the lowest resistivity before damp heat degradation were the ones to degrade the strongest and vice versa. Similar results have been obtained for a deposition pressure of 0.67 Pa.

Fig. 5.4(b) presents films that have been deposited with three different thicknesses using optimized (0.13 Pa, closed symbols) and non-optimized (0.67 Pa, open symbols) deposition conditions. The strongest increase of ρ_{eGB} was observed for the thinnest films of 200 nm. Moreover, the degradation was similar for both deposition conditions. In contrast, the degradation was influenced by deposition conditions for films with thickness of 650 nm and 1000 nm. Optimized deposition conditions (0.13 Pa) induced a less pronounced increase of ρ_{eGB} with increasing damp heat time in comparison to non-optimized deposition conditions (0.67 Pa).

5.1.1.3. Film structure

Etch characteristics ZnO:Al films on textured substrates were etched for 5 s in dilute hydrochloric acid (HCl 0.5 wt%). The films were deposited at various temperatures and two different pressures. Fig. 5.5 shows scanning electron microscopy (SEM) top view images that were recorded to qualitatively characterize the films. Black spots in the images indicate holes or, in extreme cases, trenches that were etched into the layers. Holes and trenches occurred at sharp valleys of textured substrates. A comparison of the etching pattern in e.g. Fig. 5.5(d) with the textured substrate (see Fig. 5.15(b)) reveals similarities. Further SEM investigations also supported the hypothesis of sharp valleys being dominant points of attack for the acid.

Fig. 5.5 shows different hole concentrations as a function of deposition conditions. Low temperatures in combination with high pressure (Fig. 5.5(b), (d), and (f)) induced a high amount of holes after etching. In contrast, low temperatures in combination with low pressure (Fig. 5.5(a), (c), and (e)) reduced the number of holes. Note that a low number of holes was obtained for optimized deposition conditions ($T = 300\,°C$, $p = 0.13\,Pa$) whereas a high number of holes was observed for non-optimized deposition conditions ($T = 300\,°C$, $p = 0.67\,Pa$), i.e. a low number of holes coincides with a high mobility and vice versa.

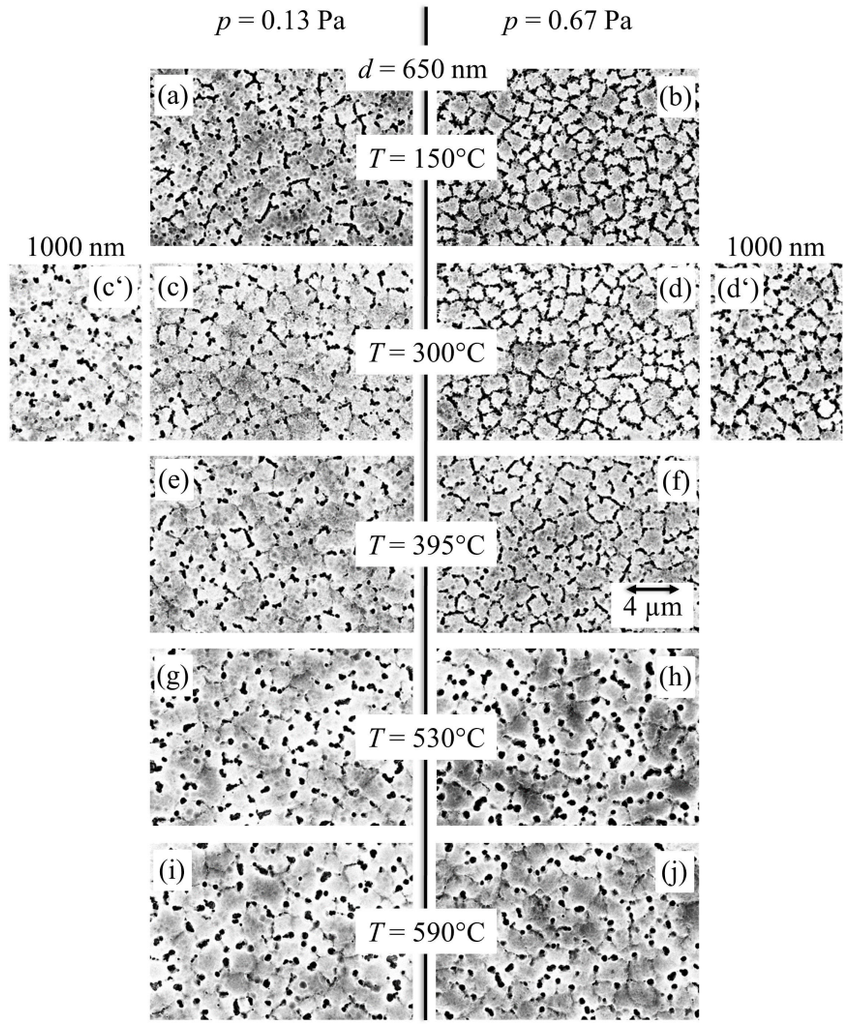

Fig. 5.5. SEM top view images of ZnO:Al layers on textured substrates that were etched for 5 s in dilute hydrochloric acid (HCl 0.5 wt%). The films were deposited at various temperatures. Furthermore, two different pressures, 0.13 Pa and 0.67 Pa, were used. The thickness was 650 nm except for two layers that possessed a thickness of 1000 nm. Black spots or lines in the images indicate holes or trenches in the layer. Note that all films were grown using Lesker configuration.

At high temperatures equal or above 530 °C, the number of holes stayed constant and was neither affected by temperature nor by pressure (Fig. 5.5(g) - (j)). Note that the mobility was also independent of pressure for high temperatures. The hole morphology changed in comparison to lower temperatures. For low temperatures, one observed trenches. For high temperatures however, the acid induced broad, mostly isolated holes.

Thicker films with $d = 1000$ nm were investigated for optimized (Fig. 5.5(c')) and non-optimized (Fig. 5.5(d')) deposition conditions. For non-optimized deposition conditions, the etching pattern was similar to the pattern of $d = 650$ nm. For optimized deposition conditions however, one observed the etching pattern to change from trenches to holes.

5.1.1.4. Annealing

On flat substrates, it is known that ZnO:Al mobility can be boosted with an annealing process that employs a-Si:H capping layers (see Section 4.4). Furthermore, annealing improves damp heat stability [23].
On textured substrates, it is thus reasonable to hope for improved mobility and damp heat stability after annealing as well.

In a first step, the influence of annealing temperature was investigated for two specific deposition conditions. Then, the annealing was applied to ZnO:Al films that were deposited with various deposition conditions. Finally, damp heat stability of as-grown and annealed films was compared.

The annealing process took place in Nitrogen atmosphere. The plateau time was 6 h. ZnO:Al layers were co-deposited on flat and textured substrates. Flat reference layers underwent the same process steps as films on rough substrates. Lesker configuration was used for all depositions.

Annealing temperatures of 300, 400, and 500 °C were applied to films deposited at low (300 °C, Fig. 5.6(a)) and high (530 °C, Fig. 5.6(b)) temperatures. The low-temperature films were grown with optimized deposition conditions. Thus, the mobility difference between flat (closed symbols) and rough (open symbols) substrates was low. On the contrary, the high-temperature film showed a higher mobility difference between flat and rough substrates.

Fig. 5.6 shows the mobility of as-grown and annealed ZnO:Al layers on flat and textured substrates. Three observations attract attention:

(1) Annealing at 300 °C induced a mobility decrease with respect to the as-grown films for the low deposition temperature film. In contrast, the same annealing process induced a mobility increase for the high deposition temperature film.

(2) The mobility gap between ZnO:Al on flat and rough substrates increased with increasing annealing temperature. The reason was the lesser increase or even decrease of mobility on rough substrates in comparison to flat substrates for $T_{\mathrm{ann}} > 300$ °C. As textured substrates induce defects in ZnO:Al, it is reasonable to assume textured substrates to create defects in the capping layers as well. It is furthermore known that annealing without capping layer at high temperatures deteriorates the mobility (see Section 4.4 and [182]). Thus, one might explain the increasing mobility gap between films on flat and rough substrates to originate from a less efficient capping effect.

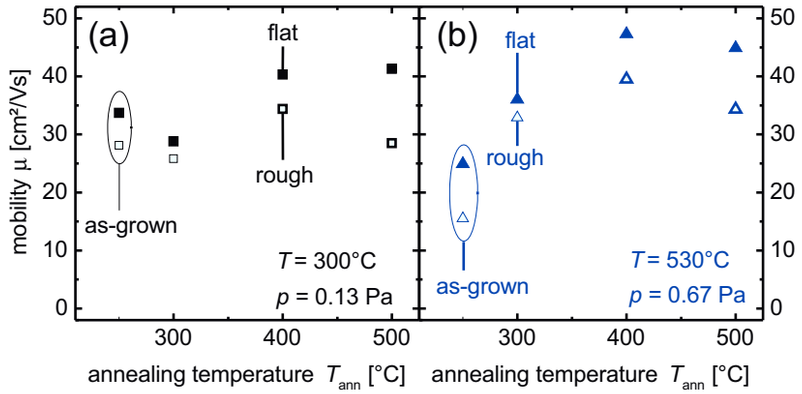

Fig. 5.6. ZnO:Al films on flat and textured substrates were annealed under capping layers at temperatures of 300, 400, and 500 °C. The annealing took place under Nitrogen atmosphere. The plateau time was 6 h. The capping layer consisted of a-Si:H with a thickness of 60 nm. The mobility was measured before and after annealing. Films that were grown with two different deposition conditions (a) and (b) have been investigated.

(3) Irrespective of deposition conditions, the mobility difference between films on flat and rough substrates was found to be small after annealing at 300 °C. Even more, Fig. 5.6(b) shows the annealing to have reduced the mobility difference for the high temperature film. This is particularly interesting because the annealing temperature was below the substrate temperature during deposition[1].

[1]Note that deposition temperatures were heater and not substrate temperatures. Substrate

Deposition conditions It was just pointed out that the impact of annealing depended on deposition conditions. Therefore, a more detailed investigation of annealing impact as a function of various deposition conditions shall be presented. Films that were deposited at 5 different temperatures and 2 different pressures underwent the annealing process at temperatures of 300 °C.

Fig. 5.7(a) and (b) show the mobility of as-grown (black symbols) and annealed (blue symbols) films on flat (closed symbols, solid lines) and rough (open symbols, dashed lines) substrates. One notices for all deposition temperatures that the annealing

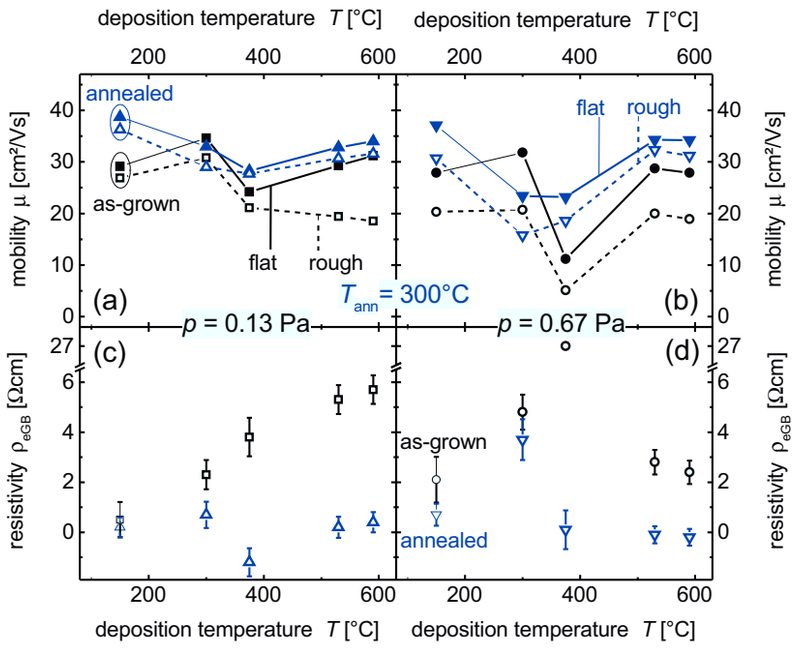

Fig. 5.7. ZnO:Al layers on flat (closed symbols) and textured (open symbols) substrates were annealed under a-Si:H capping layers at 300 °C for 6 h. ZnO:Al films were deposited at various temperatures and two different pressures: (a), (c) $p = 0.13$ Pa and (b), (d) $p = 0.67$ Pa. Mobility and resistivity were measured before and after annealing. The resistivity of extended grain boundaries (see Section 5.1.1.2) for as-grown and annealed films was plotted for pressures $p = 0.13$ Pa (c) and $p = 0.67$ Pa (d).

temperatures were roughly two third of the respective heater temperatures. In contrast, the given annealing temperatures were substrate temperatures.

process induced a mobility increase compared to as-grown films. The only exceptions were optimized (300 °C, 0.13 Pa) and non-optimized deposition conditions (300 °C, 0.67 Pa).

A deposition pressure of 0.13 Pa implied the mobility gap between flat and rough substrates to be small after annealing. For a deposition pressure of 0.67 Pa, the annealing process yielded a decrease of mobility gap as well. Yet the mobility difference between films on flat and rough substrates could not be eliminated completely for low deposition temperatures.

Fig. 5.7(c) and (d) depict the resistivity of extended grain boundaries ρ_{eGB} (see Section 5.1.1.2) for as-grown and annealed films. It is illustrated that the annealing process reduced the mobility deteriorating defects that have been induced by the textured substrates.

Damp heat stability of as-grown and annealed ZnO:Al films on flat and textured substrates has been investigated. Fig. 5.8 shows the resistivity of extended grain boundaries before (a) and after (b) annealing for various damp heat times as a function of deposition temperature.

One observes for as-grown and annealed samples that low deposition temperatures led to higher degradation in contrast to high deposition temperatures.

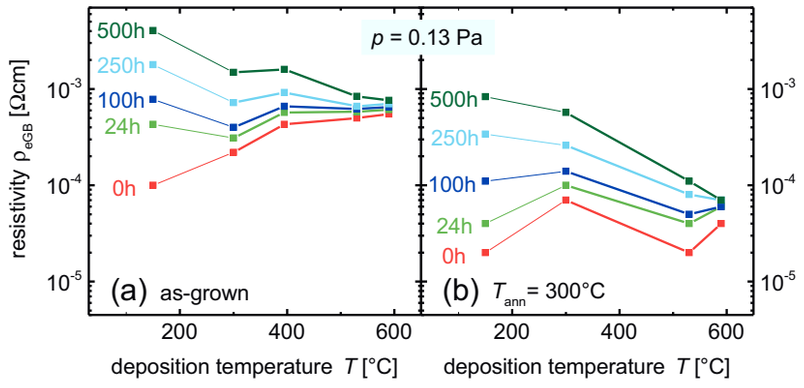

Fig. 5.8. (a) As-grown and (b) annealed ZnO:Al films were exposed to damp heat for up to 500 h. The annealing took place at 300 °C for 6 h with the use of 60 nm thin a-Si:H capping layers. For the damp heat treatment, the capping layers were removed. The resistivity of extended grain boundaries (see Section 5.1.1.2) is shown as a function of deposition temperature.

It was pointed out that annealing reduced ρ_{eGB}. Thus, annealed films showed a lower ρ_{eGB} in the non-degraded state (0 h) than as-grown films.

Generally, one might describe the ρ_{eGB} data of annealed films to be shifted down by roughly one order of magnitude in comparison to as-grown films. Thus, the annealing process reduced damp heat degradation no matter what deposition temperature was used. Note again that the annealing temperature of 300 °C was rather low and for some samples even below the substrate temperature during deposition.

5.1.2. Model structure

Prior investigations took place on randomly textured glass substrates. In the following, a clearly defined periodic surface structure was produced by a lithographic technique (see Section 3.1.3). Fig. 5.9 shows a scheme of the model structure that consisted of 2500 parallel, V-shaped trenches. The trenches had an opening angle of 70.5 °. This structure was used to confirm the observed mobility differences in terms of sputtering conditions. Furthermore, detailed structural characterization was performed using SEM and XRD measurements to clarify the reason for the electrical differences.

Fig. 5.9. Scheme of the model structure which consisted of 2500 parallel, V-shaped trenches (marked as grey). Each trench had a width of 1.6 µm and a depth of 1.1 µm. The trenches were separated by plateaus of width 2.5 µm. After ZnO:Al deposition, silver contacts (marked as blue) were thermally evaporated on both sides of the structure.

Three different deposition conditions were used to grow ZnO:Al layers on the model structure: optimized (200 °C, 0.13 Pa) and non-optimized (200 °C, 0.52 Pa) deposition conditions, and a high-temperature process (500 °C, 0.13 Pa) were applied[2]. Let me shortly remind you of the differences between the deposition conditions. Optimized and non-optimized deposition conditions led to similar mobilities on flat substrates. However, on textured substrates, optimized deposition conditions induced ZnO:Al mobilities close to the values obtained on flat substrate while non-optimized deposition conditions led to lower mobilities than on the flat reference. Similar to non-optimized deposition conditions, the high-temperature process showed a mobility gap between flat and textured substrates. Note that Gencoa configuration was used. Further details about the deposition conditions may be found in Section 5.1.1.1.

5.1.2.1. Electrical properties

The resistance was measured by contacting the silver pads. Four-point measurements were used in order to be able to neglect the contact resistance. Due to the sample geometry and the isolating SiO_2 layer between silicon and ZnO:Al, the current was forced to cross the trenches. The aim of the measurements was to determine the additional resistance that resulted from possible defects, also called extended grain boundaries [33, 34], induced by the sharp, V-shaped tips of the trenches. For this purpose, the resistance R_{flat} of ZnO:Al on a flat reference substrate was compared to the ZnO:Al resistance R_{rough} on the model structure.

Determination of path enhancement and ZnO:Al thickness variation To access the resistance of extended grain boundaries, one has to compute the additional resistance that results from the fact that the current has to cover a longer distance on rough than on flat substrates. Besides this geometric path enhancement, one has to take into account the variation of ZnO:Al thickness on rough substrate, e.g. ZnO:Al was thicker on the flat plateaus than within the trenches. Fig. 5.10 shows the proposed current flow through ZnO:Al on the model structure. The current is assumed to flow in the middle of the ZnO:Al layer. The theoretical resistance $R_{\text{rough}}^{\text{theo}}$ of ZnO:Al grown on the model structure, considering path enhancement and ZnO:Al thickness

[2] Note that the pressure of the non-optimized deposition process was slightly adjusted in comparison to the processes for texture-etched and nano-imprinted glass.

Fig. 5.10. Arrows depict the current flow through ZnO:Al grown on the model structure. The current is assumed to flow in the middle of the layer. The layer thickness was measured by SEM at three different points d_1, d_2, and d_3. The path enhancement of the current is computed via the lengths l_1, l_2, and l_3.

variation only, thus neglecting extended grain boundaries, is given as

$$\begin{aligned} R^{\text{theo}}_{\text{rough}} =& \rho_{\text{flat}} \frac{l^{\text{rough}}_{\text{total}}}{A} \\ =& \rho_{\text{flat}} \left(\frac{\overbrace{2500 \times 2.5\,\mu\text{m} + 2.7\,\text{mm}}^{\text{plateau}}}{9.6\,\text{mm} \times d_1} \right. \\ & \left. + \underbrace{2\,\frac{2500 \times l_1}{9.6\,\text{mm} \times d_{23}} + 2\,\frac{2500 \times l_2}{9.6\,\text{mm} \times d_{12}} + \frac{2500 \times l_3}{9.6\,\text{mm} \times d_3}}_{\text{trench}} \right) \end{aligned} \tag{5.2}$$

whereby $l^{\text{rough}}_{\text{total}}$ is the total length that the current has to pass through the trenches from one contact to the other. $A = l_{\text{trench}} \times d$ is the cross section area that is determined by the product of the trench length l_{trench} and the film thickness d. ρ_{flat} is deduced from the measured resistance R_{flat} as

$$\rho_{\text{flat}} = R_{\text{flat}} \frac{A}{l^{\text{flat}}_{\text{total}}} = R_{\text{flat}} \frac{9.6\,\text{mm} \times d_1}{12.7\,\text{mm}}. \tag{5.3}$$

$l^{\text{flat}}_{\text{total}}$ is the normal distance between the two silver contacts. The length of the flat plateaus between the trenches was 2.5 µm, 2.7 mm was the length between the last trench and the silver contacts. Furthermore, the lengths l_1, l_2, and l_3 were calculated

in the following way

$$l_1 = \frac{0.75\,\mu\text{m}}{\cos 54.74^\circ} - \frac{d_3}{\tan 35.26^\circ} \tag{5.4}$$

$$l_2 = \frac{\pi}{2}\, d_1\, \frac{54.74^\circ}{360^\circ} \tag{5.5}$$

$$l_3 = \pi\, d_3\, \frac{109.48^\circ}{360^\circ}. \tag{5.6}$$

d_{12} and d_{23} denote the average of d_1 and d_2, and d_2 and d_3, respectively. Note that l_2 and l_3 are approximated by a circular arc.

The resistance of extended grain boundaries

$$R_{\text{eGB}} = R^{\text{exp}}_{\text{rough}} - R^{\text{theo}}_{\text{rough}} \tag{5.7}$$

is given as the difference between the experimentally determined resistance $R^{\text{exp}}_{\text{rough}}$ and the theoretically computed resistance $R^{\text{theo}}_{\text{rough}}$ that takes into account path enhancement and thickness variation only. Subsequently, one can determine the resistivity of extended grain boundaries

$$\rho_{\text{eGB}} = R_{\text{eGB}}\, \frac{9.6\,\text{mm} \times d_3/\cos 35.26^\circ}{2500 \times l_{\text{eGB}}} \tag{5.8}$$

if the width l_{eGB} in current direction of the extended grain boundaries is known.

Note that the above outlined determination of $R^{\text{theo}}_{\text{rough}}$ is a purely heuristic approach. It is most certainly a strong simplification of the actual current flow.

Experimental results The resistance of ZnO:Al on flat reference substrates and on the model structure was determined for three different deposition conditions. For all deposition conditions, a higher resistance on the model structure than on the flat reference substrate was observed as can be seen in Table 5.1. To determine the resistivity of extended grain boundaries, one has to take into account path enhancement and thickness variation on the model structure. R_{theo} in Table 5.1 denotes the resistance if only these two effects are considered. One observes for optimized deposition conditions (200 °C, 0.12 Pa) that R_{theo} was higher than R_{exp}. This result reflects, on the one hand, the excellent suitability of the process for ZnO:Al deposition on textured substrates, and, on the other hand, the error due to the heuristic approach of computing R_{theo}. Also, for the high-temperature process (500 °C, 0.13 Pa), R_{theo} and R_{exp} were similar. As a consequence of the unknown error regarding the determination of R_{theo}, it is reasonable to estimate the resistivity of

Table 5.1. The experimentally determined resistance R_{exp} of ZnO:Al on a flat reference substrate and on the model structure is shown for three different deposition conditions. Additionally, the theoretically determined resistance R_{theo} that takes into account the path enhancement of the current and the thickness variation on the model structure is given.

Deposition conditions	Flat	Model structure	
	R_{exp} [Ω]		R_{theo} [Ω]
200 °C, 0.12 Pa	21.4	29.0	30.4
200 °C, 0.52 Pa	19.7	43.1	27.1
500 °C, 0.13 Pa	6.7	10.4	9.4

extended grain boundaries ρ_{eGB} only for non-optimized deposition conditions (200 °C, 0.52 Pa) because these deposition conditions showed a clear difference between R_{exp} and R_{theo}.

For the determination of ρ_{eGB}, one needed amongst others the length l_{eGB} of extended grain boundaries. As l_{eGB} is unknown, I will give ρ_{eGB} for two reasonable values of l_{eGB}. Under the assumption of l_{eGB} to be 5 and 40 nm, one obtained an extended grain boundary resistivity ρ_{eGB} of $5.72 \times 10^{-1}\,\Omega\,\mathrm{cm}$ and $7.15 \times 10^{-2}\,\Omega\,\mathrm{cm}$, respectively. These values correspond to sheet resistances of 12 260 Ω and 1533 Ω. Greiner at al. determined for ρ_{eGB} values of $1.67 \times 10^{-1}\,\Omega\,\mathrm{cm}$ to $5 \times 10^{-2}\,\Omega\,\mathrm{cm}$, which is comparable to my values [34].

The measured resistances on the model structure confirmed the results that were obtained for the randomly textured glass. Optimized deposition conditions (200 °C, 0.12 Pa) showed a resistance R_{exp} which was even below R_{theo}. Thus, extended grain boundaries contributed only very slightly to the resistance. In contrast, ZnO:Al grown by non-optimized deposition conditions (200 °C, 0.52 Pa) showed a high resistance on the model structure in comparison to R_{theo}. Therefore, extended grain boundaries contributed to the overall resistance. This corresponds to the ZnO:Al mobility reduction that was found on the texture-etched glass substrates for non-optimized deposition conditions. The contribution of extended grain boundaries to the resistance for the high-temperature process were stronger than for optimized deposition conditions but not as strong as for non-optimized deposition conditions. A similar observation was found for the mobility reduction on texture-etched glass (see Section 5.1.1.1).

5.1.2.2. Structural investigations

SEM cross section measurements SEM cross section measurements were performed to investigate structure, extent, and number of extended grain boundaries within ZnO:Al layers deposited on the model structure. Fig. 5.11 shows the resulting images. Three different ZnO:Al deposition conditions were investigated. Furthermore, Fig. 5.11(c), (f), and (i) show the original V-shaped trench, whereas the other images depict the slightly smoothened structure (see also Section 3.1.3). Note that the electrical properties were similar for both structures.

Fig. 5.11(a), (d), and (g) show an overview of ZnO:Al on the model structure. Fig. 5.11(b), (e), and (h) depict the tip of the structure that was slightly smoothened. Fig. 5.11(c), (f), and (i) illustrate the tip of the original, V-shaped trench.

Fig. 5.11. SEM cross section images of ZnO:Al deposited on the model structure. From top to bottom, the deposition conditions correspond to optimized and non-optimized deposition conditions, and a high-temperature process.

My subjective, qualitative observations may be summarized as follows: For all deposition conditions, extended grain boundaries were found on the original, V-shaped structure. On the slightly smoother structure, extended grain boundaries were observed as well, but the exemplarily shown measurements suggest that their extent is lower. More importantly, for optimized deposition conditions, I also found trenches where clear and obvious defect could not be observed at all. An example is depicted in Fig. 5.11(b).

In general however, whether or not an extended grain boundary might be observed depended severely on how the sample broke during the preparation process for the cross sections. Furthermore, there was no clear and unambiguous difference to be observed between the amount and extent of defects with respect to the various deposition conditions. Therefore, the SEM cross sections do not allow to conclude that one deposition condition induced more or less extended grain boundaries than the other.

One observation is nevertheless save to make: the grains are oriented almost perfectly perpendicular to the local substrate surface for the high-temperature process. In contrast, for the low-temperature processes, the grains are slightly bend upwards towards the particle flux during growth.

XRD measurements To gain further insight into ZnO:Al grain orientation, XRD pole figures were recorded. Fig. 5.12 shows XRD pole figure measurements of ZnO:Al layers grown on the model structure. (002) and (101) direction were investigated for three different deposition conditions.

The measurements of the (002) direction depict three distinct peaks. One was situated in the center, the other two were shifted on the ψ-axis to positive or negative values. The center peak belongs to grains that are aligned perpendicular to the global substrate surface. Thus, the center peak resulted from the material on the plateaus. The two satellite peaks are shifted by an angle of roughly 53°. This angle is very similar to the inclination angle of the trenches which was 54.74 °. The satellite peaks thus belong to grains that are located in the trenches. Note however that, for geometrical reasons, only grains close to the opening of the trenches contribute to the signal. Grains that are situated near the bottom of the trench are not probed using the (002) direction.

Measurements of the (101) direction show one centered ring and two half-rings that are shifted by approximately 53° on the ψ-axis. Two other signals are observed at high positive and negative ψ values.

Fig. 5.12. XRD pole figures of ZnO:Al layers deposited on the model structure with three different deposition conditions. The (002) direction (a) - (c) and the (101) direction (d) - (f) were investigated.

The (101) direction is inclined against the (002) direction by an angle of 61.6°. The centered ring in the (101) measurement thus corresponds to the center peak in the (002) measurement. The half-rings result from the grains that are located within the trenches. Note that, in contrast to the (002) direction, the measurement of the (101) direction takes into account all grains in the trenches, most notably the grains at the tip of the trench. The signals that were observed at high positive and negative ψ values belong to the (10-1) direction.

Depending on the deposition conditions, differences between the pole figures were observed. The obtained pole figures however possessed merely a resolution of 5°, i.e. ψ and ϕ were varied in 5° steps. This resolution was too low to get insight into the grain orientation in particular in the trenches. Therefore, more detailed measurements of the (101) direction were performed. ϕ was set to zero while ψ was varied. This measurement corresponds to a centered horizontal cut through the pole figures.

Fig. 5.13 shows measurements using the just described geometry. Four distinct peaks dominated the spectrum. The two outer peaks at roughly 60° correspond to the (101) direction of ZnO:Al on the plateaus of the model structure. In the pole figures, these peaks were part of the centered ring. The two inner peaks are induced by the grains in the trenches. The trenches are inclined by 54.74° against the plateaus of the structure. The outer and inner peaks show a difference of roughly 53°, which is close to the expected value of 54.74°. All films but in particular the high-temperature layer (blue line in Fig. 5.13) showed a high-angle shoulder that one can identify as the (10-1) direction. The low-temperature films (black and red lines in Fig. 5.13) additionally showed a pronounced low-angle shoulder (green, dotted rings). An explanation for this peak is lacking.

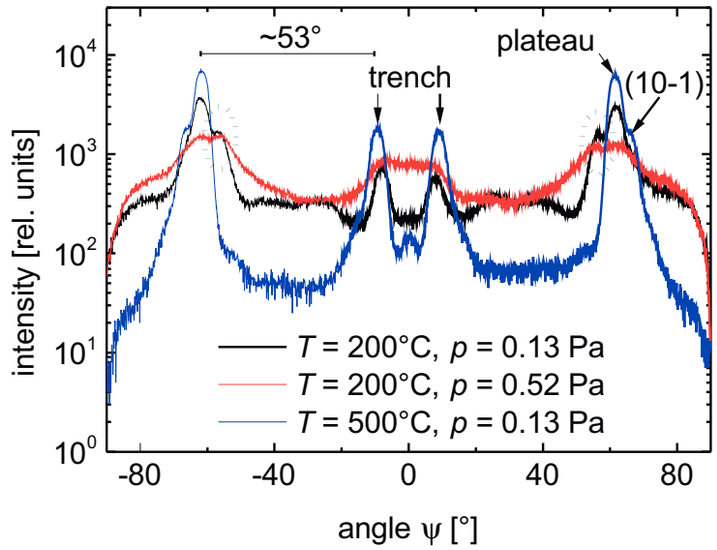

Fig. 5.13. XRD measurements of the (101) direction as a function of the angle ψ. The angle ϕ was chosen such that the measurement corresponds to a horizontal cut through the pole figures in Fig. 5.12. The investigated ZnO:Al films were deposited on the model structure using three different deposition conditions.

The comparison of the measurements revealed that the peak width differed as a function of deposition conditions. In particular, the peaks of non-optimized deposition conditions (red line in Fig. 5.13) were strongly smeared out, whereas the peaks of the high-temperature process (blue line) were clearly defined. Note furthermore that

the different peak widths on the flat plateaus should not be influenced by the texture of the model structure. As a consequence, an investigation of the grain orientation in the trenches has to take into account that the grain orientation on flat substrates already differs strongly as a function of deposition conditions. To divide the observed grain orientation in the trenches into an effect that is attributed to differences already observed for flat substrates and into an effect that one can trace back to the grains in the trenches only is difficult.

In conclusion, the only observation that is save to make is that the high-temperature process yielded grains that were clearly orientated perpendicular to the local substrate surface because the signal intensity between the inner and outer peaks was low. In contrast, the low-temperature processes showed a significantly higher intensity between the respective two main peaks. Thus, there were grains that were neither oriented perpendicular to the substrate surface on the plateaus nor in the trenches. However, it was not possible to reveal differences in grain orientation between optimized (200 °C, 0.13 Pa) and non-optimized (200 °C, 0.52 Pa) deposition conditions because particularly non-optimized deposition conditions induced peaks that were strongly broadened even on the flat plateaus. Note that the conclusions of XRD measurements coincide with to the conclusions of SEM investigations.

5.1.3. Discussion

The following discussion aims at qualitatively explaining the different behavior of ZnO:Al films on textured substrates with regard to mobility, damp heat stability, and etching. The various film properties need to be correlated and explained in terms of the varying deposition conditions.

Growth model Sputtered ZnO:Al thin films consist of crystalline columns. Generally, the orientation of crystalline columns in a sputtering process is determined by the angle between the particle flux and the substrate normal [202–208]. Several analytical expressions have been derived connecting substrate orientation and angle of incident particle beam with column orientation [202–204]. All expressions have in common that the column axis is inclined from the local substrate normal to the direction of particle flux. Note that, for oblique sputtered ZnO, the results are somewhat contradictory regarding the relation of column orientation and particle flux [205–208]. This seems to reflect the various deposition conditions and system geometries used in these studies. Besides substrate orientation and angle of incident particles, adatom mobility was shown to influence the column orientation [203].

If one neglects shadowing effects, ZnO:Al growth on textured substrates resembles oblique sputtering with locally very different substrate angles. Therefore, columns on textured substrates are to some extent oriented according to the local substrate angle [35, 209]. As outlined above, the column orientation is furthermore influenced by adatom mobility and incident particle flux.

The adatom mobility is amongst others influenced by the deposition temperature. Higher deposition temperatures relax the impact of incident particle flux direction and induce columns that are oriented rather perpendicular to the local substrate surface [203].

The direction of incident particle flux is amongst others determined by the deposition pressure. Lower deposition pressures induce less particle collisions in the plasma. Consequently, the particle flux for low deposition pressures is more direct in comparison to higher deposition pressures with rather diffuse particle flux [210, 211]. Thus, for lower deposition pressures one expects a parallel orientation of ZnO:Al columns rather than perpendicular growth on the local substrate facets.

Fig. 5.14 summarizes in a qualitative sketch the described effects of deposition temperature and pressure on grain orientation. I propose that the grain orientation affects size, harmfulness, and possibly also the number of extended grain boundaries. Low temperatures and pressures induce the grains to be oriented in the direction of particle flux. High temperatures and pressures lead to grains that grow vertically on the local substrate surface. It is suggested that the former case, that is a vertical column orientation, results in fewer or less harmful growth disturbances or extended grain boundaries (shadowed area in Fig. 5.14).

High- vs. low-temperature deposition conditions Two ZnO:Al films shall exemplify the behavior at low and high temperatures. Using Gencoa configuration, the low-temperature film was deposited at 200 °C, the high-temperature film was grown at 530 °C. I will focus on ZnO:Al films grown with pressure of 0.13 Pa.

The low-temperature film exhibited mobilities on textured substrates that were close to the flat reference (see Sections 5.1.1.1 and 5.1.2.1). The high-temperature film showed a gap between the mobility on textured substrates and on flat reference substrates. The high-temperature film was more stable under damp heat conditions than the low-temperature film (see Section 5.1.1.2). Etching produced slightly more holes in the high-temperature layer than in the low-temperature film (see Section 5.1.1.3).

Fig. 5.14. Qualitative sketch of grain orientation on textured substrates: (a) low temperature and pressure, (b) high temperature and pressure. Extended grain boundaries are marked in red. Because of the more vertical grain orientation, the extended grain boundary in the layer is less pronounced for low-temperature and low-pressure deposition conditions than for high-temperature and high-pressure growth conditions.

The small mobility gap between flat and textured substrates at low deposition temperatures and the large mobility gap at increased deposition temperatures can be explained in terms of the proposed growth model. According to the model, low temperatures induce less harmful extended grain boundaries than high temperatures due to a more vertical grain growth. As extended grain boundaries on textured substrates reduce the mobility [33,34], a diminution of these extended grain boundaries using lower deposition temperatures increases the mobility. Indeed, SEM and XRD measurements supported the hypothesis that grains grew perpendicular to the local substrate surface for high deposition temperatures and tilted towards the particle flux for low deposition temperatures (see Section 5.1.2.2).

Extended grain boundaries are supposed to decrease the damp heat stability of ZnO:Al layers [33, 34]. Thus, from mobility results and growth model, one would expect the damp heat stability to be lower for higher deposition temperatures due to more harmful extended grain boundaries. However, contrary results were obtained. Higher deposition temperatures led to higher damp heat stability. Note that similar results have been obtained for ZnO:Al growth on flat substrates [168]. I suspect that damp heat stable (extended) grain boundaries can restrict the mobility. Mobility and susceptibility to damp heat might thus be two independent properties of (extended) grain boundaries.

The number and morphology of holes after etching gave further insights into the number of extended grain boundaries because extended grain boundaries exhibit a higher etching rate than the bulk layer [65, 212]. Hence, the holes in ZnO:Al films are proposed to result from preferential etching of extended grain boundaries. A comparison of films deposited at low and high temperature reveals slightly more holes for high than for low-temperature films. This supports my assumption of more or more harmful extended grain boundaries in the high-temperature layer deteriorating the mobility.

High- vs. low-pressure deposition conditions I discuss the influence of deposition pressure for low-temperature (200 °C) and high-temperature (530 °C) deposition conditions. 0.13 Pa will be denoted as low-pressure deposition condition. Depending on the used configuration[3], 0.47 Pa or 0.67 Pa will be defined as high-pressure deposition conditions[4].

For low deposition temperatures, the deposition pressure had a strong impact on charge carrier mobility on textured substrates. Low deposition pressures induced mobilities on textured substrates that were similar to the mobility on flat reference substrates. In contrast, high pressures led to a strong mobility gap between the films on textured and on flat substrates. For high deposition temperatures however, the deposition pressure did not influence the mobility. Both, low- and high-pressure deposition conditions showed significantly lower mobility on textured than on flat substrates. I conclude that the impact of deposition temperature dominates over the influence of deposition pressure. In other words: If the adatom mobility is sufficiently high, then the angular distribution of impinging particles is negligible.

For low deposition temperatures, low or high deposition pressures induce a narrow or broad angular distribution of incident particles, respectively. According to the proposed growth model (see Fig. 5.14), fewer, smaller, and less harmful extended grain boundaries occurred for low deposition pressures due to a more vertical grain growth. However, the proposed difference of grain orientation as a function of deposition pressure could not be clearly verified (see Section 5.1.2.2). SEM measurements hint to the suggested mechanism, but differences were too small to make a definite statement. XRD measurements failed to give more insight due to the already different structural

[3] Two system configurations, namely Lesker and Gencoa configuration, were used in the course of this work (see Section 5.1)

[4] Note that, before, the low-temperature and -pressure deposition condition was denoted "optimized deposition condition" and the low-temperature and high-pressure deposition condition was called "non-optimized deposition condition".

properties of flat films for different deposition pressures. Consequently, the proposed mechanism could not be verified yet.

Damp heat stability and etching properties might also be explained in the framework of the growth model. Low-pressure films showed higher damp heat stability and significantly fewer holes after etching in comparison to high-pressure layers (see Sections 5.1.1.2 and 5.1.1.3). Fewer, smaller, and less harmful extended grain boundaries might lead to higher damp heat stability of the whole ZnO:Al layer. Furthermore, fewer holes after etching also indicate a lower number of extended grain boundaries. High mobility and damp heat stability as well as the observed etching behavior might thus be attributed to the same structural reason, that is fewer or smaller and therefore overall less harmful extended grain boundaries.

Note that such a clear interrelation between charge carrier mobility, damp heat stability, and etching behavior was not observed for films that were deposited at different temperatures. Indeed, I suggested that extended grain boundaries might be vulnerable to damp heat without being a strong scattering barrier for electrons reducing the mobility. Therefore, the attribution of increased damp heat stability to fewer or smaller extended grain boundaries is questionable. Nevertheless, the strong difference between low- and high-pressure deposition conditions in terms of etching behavior cannot, in my opinion, be reduced solely to a different vulnerability of the same amount and size of extended grain boundaries to acid. Their number and extent needs be higher to induce such a different amount of holes.

Thickness The thickness was varied for low-temperature deposition conditions only. For low-pressure deposition conditions, one observed an increase of mobility on flat and textured substrates, whereas the mobility of high-pressure ZnO:Al films increased only slightly on flat substrates and stayed constant on textured substrates (see Fig. 5.3). Low- and high-pressure deposition conditions showed similar damp heat degradation for the films with the lowest thickness of 200 nm. However, thicker films degraded stronger when high-pressure deposition conditions were used.

The correlation between mobility and damp heat degradation is noteworthy. For thin films, low- and high-pressure deposition conditions showed similar mobility values and damp heat stability on textured substrates. Increasing thickness induced a mobility gap between low- and high-pressure deposition conditions. The different mobility values of ZnO:Al on textured substrates coincided with stronger damp heat degradation of ZnO:Al films using high-pressure deposition conditions in comparison to low-pressure deposition conditions. Note again that the interrelation between mobility and damp heat degradation might be problematic. However, the obvious

correlation supports the hypothesis that different levels of mobility and damp heat degradation can be attributed to the same reason, namely more or less harmful extended grain boundaries.

One could argue that thin layers possessed the same number and harmfulness of extended grain boundaries irrespective of growth conditions. For thicker layers the mechanisms proposed in the growth model take effect. Consequently, with increasing thickness, the impact of extended grain boundaries on mobility and damp heat degradation decreased for low-pressure deposition conditions whereas it stayed constant for high-pressure deposition conditions.

5.1.4. Conclusion

The influence of various deposition conditions on ZnO:Al growth on textured substrates was investigated in order to reveal their influence on mobility and damp heat stability. The deposition of ZnO:Al on textured substrates is challenging due to a reduction of ZnO:Al mobility and damp heat stability resulting from extended grain boundaries. ZnO:Al films were deposited on randomly textured glass substrates and a model structure that consisted of parallel trenches with a clearly defined morphology.

On randomly textured glass substrates, I found optimized, low-temperature and low-pressure deposition conditions that led to ZnO:Al films on textured substrates with mobility values similar to those on flat reference substrates. Highly damp heat stable ZnO:Al films on textured substrates were obtained for films deposited at high temperatures.

Annealing at low temperatures of 300 °C induced a ZnO:Al mobility increase on textured substrates nearly up to the level of flat substrates irrespective of the initial mobility gap between flat and textured substrate. Furthermore, the damp heat stability was increased by the annealing process. In general, the impact of extended grain boundaries on mobility and damp heat stability was significantly reduced after annealing.

ZnO:Al deposited on the periodic model structure verified results with regard to electrical properties that had been obtained on randomly textured substrates. For non-optimized, low-temperature and high-pressure deposition conditions, the resistivity of extended grain boundaries was determined to be between $5.72 \times 10^{-1}\,\Omega\,\mathrm{cm}$ and $7.15 \times 10^{-2}\,\Omega\,\mathrm{cm}$.

A growth model was presented that qualitatively explains the observed mobility differences in terms of deposition conditions. The model assumes that grains which grow perpendicular to the local substrate surface induce more, larger, and more harmful extended grain boundaries. These more harmful extended grain boundaries then reduce the mobility. The grain orientation thereby depends on the deposition conditions.

For high-temperature deposition conditions, grain growth perpendicular to the substrate surface was observed by XRD and SEM investigations. For low-temperature deposition conditions, the grain orientation depended on the deposition pressure. I suspect that low pressures induce grains to be bent towards the incident particle flux whereas high deposition pressures led to grain growth that is rather perpendicular to the local substrate surface. Consequently, low-temperature and low-pressure deposition conditions were identified as optimal for the growth of ZnO:Al on textured substrates.

5.2. Influence of substrate texture

The influence of various substrate textures on ZnO:Al mobility and damp heat stability was investigated. Etch characteristics were evaluated to gain insight into the number of extended grain boundaries. Two types of textured substrates were used, namely texture-etched glass substrates and nano-imprint substrates.

Texture-etched glass substrates Texture-etched glass was fabricated in a two-step wet-chemical etching procedure (see Section 3.1.1).

Fig. 5.15(b) shows the surface morphology after the first etching step. The obtained substrate C is characterized by pyramids with sharp valleys and high plateaus. This first etching step can be modified such that it results in surface texture A that is characterized by larger but similar features.

The morphology of substrate C was further modified by a second etching step. The second etching step was applied for 40, 80, and 120 s resulting in textures C040, C080, and C120, respectively. One observes the sharp features of substrate C to be predominantly attacked by the acid, thus widening and rounding the valleys. Substrate C was hence modified by the second etching step towards round, smooth, crater-like surface structures.

Fig. 5.15. AFM measurements of various textured substrates. From left to right, the surface morphology changes from V- to U-shape. Substrates (a) - (e) are texture-etched glasses. Substrates (f) - (k) are nano-imprint substrates. Substrates Z5-I (j) and E-AZO-I (k) are inverted from Z5 (f) and E-AZO (h). Substrates A and C, and Z5 and Z25-5, respectively, possess similar surface features, but their lateral feature sizes differ. Note that substrate A has a different length scale than the other substrates.

Following the nomenclature of e.g. Python et al. [213], substrate C will be called "V-shaped" and substrate C120 "U-shaped". Substrates C040 and C080 present gradual steps between C and C120.

Nano-imprint substrates Nano-imprint lithography is a technique for the replication of microstructures. Amongst others, it has been applied to replicate surface textures beneficial for light scattering in thin-film silicon solar cells [28, 29]. In this work, nano-imprint lithography was used to produce various rough surfaces in order to investigate ZnO:Al growth. Further details about the replication of textured substrates using nano-imprint lithography may be found in Section 3.1.2.

Fig. 5.15(f) - (k) show the investigated nano-imprint substrate textures. The sub-

strates were derived from either sputtered and subsequently etched ZnO:Al [7, 14–16, 27] or from self-textured ZnO:B that was grown by low pressure chemical vapor deposition[5] (LPCVD) [13, 18].

Sputtered and etched aluminum-doped ZnO (E-AZO) possesses a crater-like, U-shaped surface morphology. In contrast, LPCVD-grown ZnO:B exhibits a pyramid-like, V-shaped surface morphology after deposition. Rms roughness and lateral feature size may be increased by increasing the layer thickness [13]. The sharp features of LPCVD-grown ZnO:B can be smoothened by a post-deposition plasma treatment [214, 215].

Substrate Z5 was replicated from a 5 µm thick ZnO:B layer. Substrate Z5-20 was also obtained from a 5 µm thick ZnO:B film. However, the film was furthermore plasma-treated for 20 minutes, thus shifting the surface morphology from V- to rather U-shaped features. Substrate Z25-5 was replicated from a layer of thickness 2.5 µm. The pyramidal features were thus smaller compared to substrate Z5. 5 minutes of plasma treatment rounded the sharp, V-shaped valleys. Note that problems occurred during the replication process of Z5-20. Therefore, the nano-imprint texture possessed less V-shaped features than the original texture. SEM measurements of the original texture may be found in [213]. However, it was checked that the texture changed consistently in all experiments.

Substrates E-AZO and Z5 were inverted. AFM measurements of E-AZO-I and Z5-I are found in Fig. 5.15(j) and (k).

5.2.1. Electrical properties

V- vs. U-shaped substrates The previous Section 5.1.1.1 showed optimized and non-optimized deposition conditions to exist that induce a low or high difference between mobilities on flat and rough substrates. In this section, both deposition conditions were applied to various substrate textures.

Fig. 5.16(a) presents ZnO:Al mobilities of films on texture-etched glass and a flat reference substrate. The modification of the substrate morphology from V- to U-shaped structures via a second etching step led to an increase of ZnO:Al charge

[5] The deposition of self-textured ZnO:B layers as well as their nano-imprint replication was performed at the Photovoltaics and Thin Film Electronics Laboratory of the Ecole Polytechnique Fédérale de Lausanne.

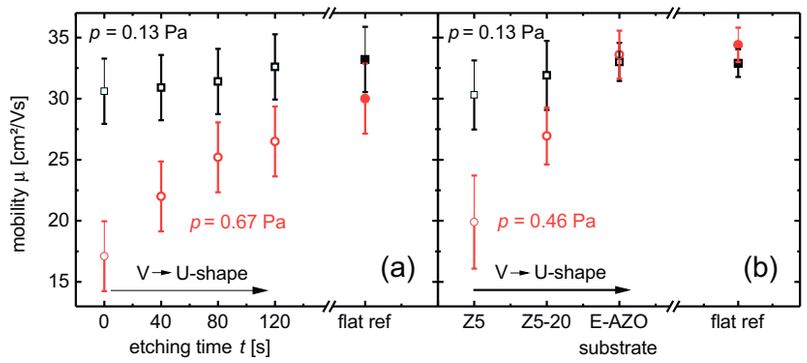

Fig. 5.16. The mobility is shown for optimized (low pressure) and non-optimized (high pressure) deposition conditions as a function of substrate morphology. (a) Texture-etched glass (Lesker) and (b) nano-imprint (Gencoa) substrates were used. Note that deposition parameters differed since different system configurations were used (see Section 5.1.1.1).

carrier mobility for both growth conditions. The trend however was much more pronounced for non-optimized than for optimized deposition conditions.

Fig. 5.16(b) shows similar observations for nano-imprint substrates. ZnO:Al on V-shaped Z5 substrates exhibited lower mobilities than films on crater-like, U-shaped E-AZO substrates.

In conclusion, ZnO:Al films on U-shaped substrate morphologies showed higher mobilities than films on V-shaped morphologies. Moreover, ZnO:Al layers on U-shaped morphologies exhibited mobilities close to the values of flat reference substrates irrespective of deposition conditions

Feature size Two sets of substrates were investigated that possessed similar surface morphologies but different lateral feature sizes. The height-height correlation length (HHCL) was used as a measure for the feature size (see Section 3.3.5).

Substrate A and C are texture-etched glass substrates with pyramid-like morphology and sharp trenches, but different feature sizes. The feature size of substrate A and C was 1633 nm and 289 nm, respectively. Thus, the number of sharp trenches was lower on substrate A. In Section 5.1, evidence was provided that sharp trenches induce extended grain boundaries in the material which reduced the mobility. If one assumes this to be true, there should be less extended grain boundaries on substrate A and thus the mobility should increase in comparison to substrate C. And indeed,

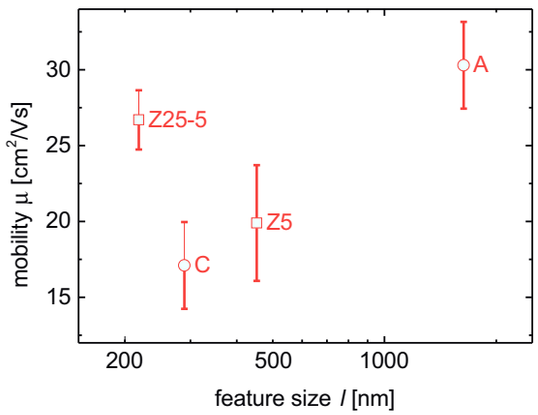

Fig. 5.17. Substrates Z25-5 and Z5, and C and A, respectively, possessed similar surface morphologies. They differed however in lateral feature size. The mobility of ZnO:Al films deposited on these two sets of substrates is shown. Non-optimized deposition conditions and Gencoa configuration were used.

Fig. 5.17 proves the expected result of higher ZnO:Al mobility on substrate A than on substrate C.

Substrates Z5 and Z25-5 are both nano-imprint substrates with a similar V-shape morphology. The major difference between both substrates was the obvious difference in lateral feature size. Substrates Z5 and Z25-5 possessed features sizes of 453 nm and 218 nm, respectively. One might assume again that the smaller feature size induces more extended grain boundaries. Thus, the mobility should be lower for substrate Z25-5. However, Fig. 5.17 shows the mobility to be higher for substrate Z25-5 in comparison to substrate Z5. Reasons for this surprising result will be discussed in Section 5.3.3.

Inverted textures Sharp features with high curvature of pyramidal textures are lines whereas craters possess a single point at the bottom that might induce extended grain boundaries. Thus, the number of extended grain boundaries should be higher on pyramidal than on crater-like textures. And indeed, pyramidal, V-shaped surface morphologies were shown to induce rather low ZnO:Al charge carrier mobilities whereas crater-like, U-shaped structures led to higher ZnO:Al mobilities on rough substrates. In theory, the inversion of a pyramidal texture should lead to a crater structure and the inversion of a crater-like morphology should lead to a pyramidal texture. Thus, ZnO:Al charge carrier mobility on inverted pyramidal and crater

textures should increase and decrease, respectively, in comparison to values on the original texture.

Fig. 5.18 shows the comparison of ZnO:Al mobility on original and inverted textures E-AZO and Z5. Within the error bars, substrate Z5 showed no difference with regard to mobility between original and inverted texture. The inversion of E-AZO reduced the mobility by 14% only.

Obviously, the experimental results differ from the theoretical prediction in particular for substrate Z5. Reasons for this behavior will be discussed in Section 5.3.3.

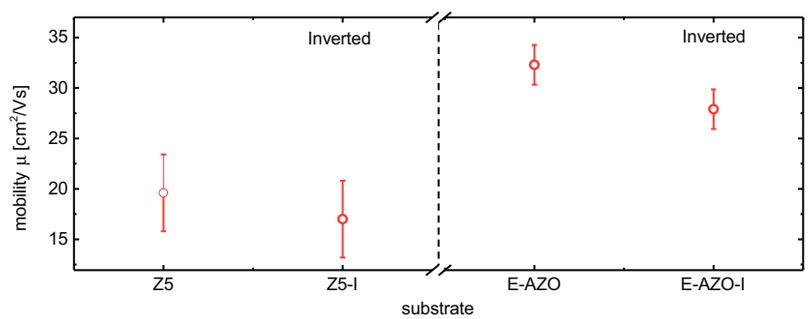

Fig. 5.18. The graph compares ZnO:Al mobility of films on original and inverted textures E-AZO and Z5. Nano-imprint lithography was used to produce the textured substrates. Non-optimized deposition conditions and Gencoa configuration were used.

5.2.2. Damp heat stability

Textured substrates induce extended grain boundaries (eGB) within the ZnO:Al layer that were given as reason for stronger ZnO:Al damp heat degradation on textured substrates compared to flat references [33, 34]. Here, the damp heat degradation of ZnO:Al resistivity was investigated as a function of substrate texture.

In Fig. 5.19, the resistivity is plotted over damp heat time for V-shaped (red data) and U-shaped (blue data) texture-etched glass (a) and nano-imprint (b) substrates. ZnO:Al films were grown using optimized (closed symbols) and non-optimized (open symbols) deposition conditions. V-shaped substrates showed stronger degradation than U-shaped substrates. The lowest degradation was observed for the flat reference. The damp heat degradation was to a lesser extent influenced by deposition conditions

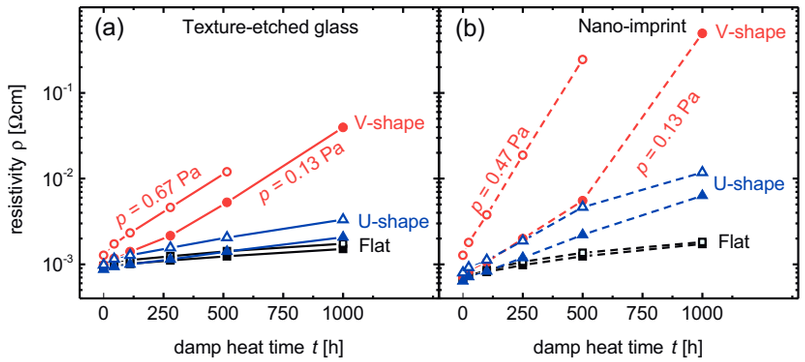

Fig. 5.19. The resistivity was measured as a function of damp heat degradation time. Texture-etched glass substrates (a) and nano-imprint substrates (b) were investigated. ZnO:Al was deposited on flat reference substrates, V-shaped textures (C, Z5) and U-shaped textures (C120, E-AZO). Optimized (closed symbols) and non-optimized (open symbols) were used (see Section 5.1.1.1).

than by substrate texture. Nevertheless, textured substrates showed a stronger degradation for non-optimized than for optimized deposition conditions.

The stronger damp heat degradation on V- than on U-shaped substrates might be explained in terms of the higher number of extended grain boundaries. V-shaped substrates induced a higher number of extended grain boundaries that led to lower initial mobility and damp heat stability.

5.2.3. Etch characteristics

It was revealed in Section 5.1 that etching of ZnO:Al on textured substrates induces deep holes or even trenches in the layer. These holes or trenches are observed as black spots or lines in SEM top view images. I argued that extended grain boundaries are etched faster than the rest of the ZnO:Al films. Thus, the number of holes or trenches is an indicator for the number of extended grain boundaries.

Fig. 5.20 shows SEM top view images of ZnO:Al films on V- and U-shaped substrates after etching of ZnO:Al for 5 s in dilute hydrochloric acid (HCl 0.5 wt%). Holes were observed on U-shaped substrates whereas V-shaped substrates showed trenches. The number of holes or trenches was lower on U-shaped than on V-shaped substrates. This observation holds for texture-etched glass and nano-imprint substrates. Thus,

Fig. 5.20. SEM top view images of ZnO:Al layers on V- and U-shaped substrates that were etched for 5 s in dilute hydrochloric acid (HCl 0.5 wt%). The films were deposited with non-optimized deposition conditions (see Section 5.1.1.1). Texture-etched glass substrates C (a) and C120 (b) as well as nano-imprint substrates Z5 (c) and E-AZO (d) were investigated. Black spots indicate holes in the ZnO:Al films.

U-shaped substrates induced less extended grain boundaries than V-shaped substrates. As a consequence, initial mobility and damp heat stability was higher on U- than on V-shaped substrates.

5.2.4. Summary

ZnO:Al films were deposited onto texture-etched glass and nano-imprint substrates. Subsequently, charge carrier mobility, damp heat stability, and etching characteristics were investigated. ZnO:Al on U-shaped substrates showed higher mobility and improved damp heat stability than on V-shaped substrates. A lower number of extended grain boundaries was assumed to be the reason for the beneficial film properties. This interpretation was supported by etching experiments. Consequently, the higher ZnO:Al mobility before and after damp heat degradation on U-shaped

structures compared to V-shaped morphologies could be explained by a lower number of extended grain boundaries constricting the current in the ZnO:Al layer.

5.3. Electrical simulation

The results in Section 5.2 proved the strong influence of substrate texture on the mobility of ZnO:Al films. Qualitatively, the textures were characterized as V- or U-shaped. Here, a model shall be developed that is able to quantitatively describe various textures. The aim is the prediction of ZnO:Al mobility on textured substrates for non-optimized deposition conditions. Additionally, the electrical model shall be able to evaluate substrate texture in terms of their suitability for ZnO:Al film growth independent of specific deposition conditions.

5.3.1. Model description

General description Sharp, V-shaped features were identified as reason for the occurrence of extended grain boundaries. The suitability of substrate features for ZnO:Al growth may be described by the local surface curvature [213]. The proposed electrical simulation will assume a high convex curvature to induce an extended grain boundary within the material. The curvature will be described by the curvature radius r_{curv}.

The local surface curvature can be extracted from substrate topographies obtained by AFM measurements. A home-built software was used for this purpose[6]. Fig. 5.21 shows the local curvature for the investigated substrates. Dark spots and lines indicate high convex curvature. One observes a decrease of spots and lines with high convex curvature when going from V- to U-shaped substrates, e.g. substrate C shows high convex curvature within the deep trenches whereas substrate C120 is free of spots with high convex curvature.

The sheet resistance and thus the mobility is modeled by a two-dimensional resistance network depicted in Fig. 5.22. A sheet resistance will be assigned to each data point of the AFM curvature images. If the local curvature exceeds a certain threshold $r_{\mathrm{curv}}^{\mathrm{thr}}$, a high sheet resistance R_{eGB} will be assigned to this data point. This corresponds to the assumption of high convex curvature inducing extended grain boundaries with

[6] K. Bittkau, private communication

high resistance. If the local curvature is below $r_{\mathrm{curv}}^{\mathrm{thr}}$, the sheet resistance of the flat reference substrate R_{flat} will be assigned to the data point. One ends up with a network that contains two different sheet resistance values. Such a resistance network can be solved with programs such as *Spice* or *Gnucap*.

Fig. 5.21. The local curvature of various textured substrates has been extracted from AFM measurements. Dark and bright parts indicate convex and concave curvature, respectively. From left to right, the surface morphology changes from V- to U-shape. Substrates (a) - (e) are texture-etched glasses. Substrates (f) - (k) are nano-imprint substrates. Substrates Z5-I (j) and E-AZO-I (k) were inverted from Z5 (f) and E-AZO (h). Substrates A and C, and Z5 and Z25-5, respectively, possess similar surface features, but the lateral feature size differs. Note that substrate A has a different length scale than the other substrates.

Determination of free parameters The electrical simulation contains two free parameters, namely the curvature threshold $r_{\mathrm{curv}}^{\mathrm{thr}}$ and the sheet resistance of extended grain boundaries R_{eGB}. Both parameters were determined by a two-dimensional optimization routine. Experimentally determined mobility values of substrates C, C040, C080, and C120 were compared to values that were determined by the electrical simulation. R_{eGB} was varied from 100 to 2800 $\Omega/\square$. For each value of R_{eGB}, $r_{\mathrm{curv}}^{\mathrm{thr}}$ was determined by an optimization routine such that the sum of squared differences between experimental and simulated mobility values was minimal. In other words, the texture-etched glass substrates C through C120 were used to calibrate the electrical simulation.

Fig. 5.22. The electrical simulation consists of a network whereby a sheet resistance value will be assigned to each data point of the curvature image. If the convex curvature lies above a threshold value $r_{\mathrm{curv}}^{\mathrm{thr}}$, a high sheet resistance R_{eGB} will be assigned to this point (red resistances). Otherwise, the sheet resistance R_{flat} of the flat reference substrates is taken.

Fig. 5.23 shows the sum of squared differences between experimental and simulated mobility as a function of R_{eGB}. Furthermore, the optimized values for R_{eGB} and $r_{\mathrm{curv}}^{\mathrm{thr}}$ are shown. The used AFM images may differ from measurement to measurement for two main reasons. First, the AFM tip geometry is crucial for the measurement, but never exactly the same. Second, the investigated substrates are randomly textured. Thus, a different measurement spot might reveal a slightly different texture.

Therefore, two different sets of AFM images were used to evaluate the impact of AFM measurements. One observes a clear minimum for both measurements. More importantly, since the obtained parameters were similar, the error due to different AFM measurements was small.

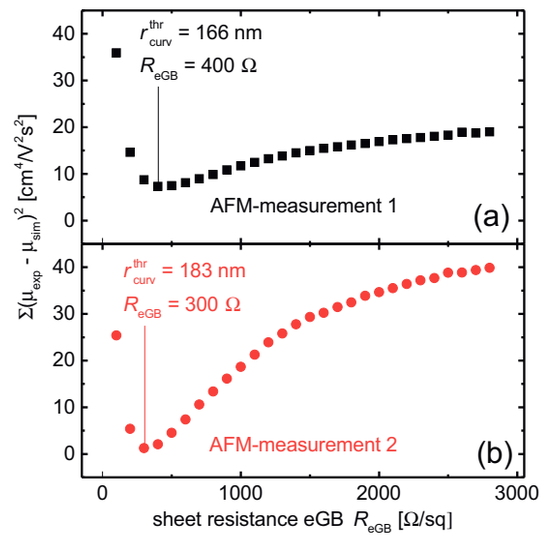

Fig. 5.23. The free parameters R_{eGB} and $r_{\mathrm{curv}}^{\mathrm{thr}}$ of the electrical simulation were determined by varying the sheet resistance of extended grain boundaries R_{eGB}. An optimization routine determined for each R_{eGB} the curvature threshold $r_{\mathrm{curv}}^{\mathrm{thr}}$ such that the sum of squared differences between experimental and simulated mobility was minimal. Two different sets of AFM images (a) and (b) were evaluated to estimate the potential error resulting from different AFM measurements. The results for R_{eGB} and $r_{\mathrm{curv}}^{\mathrm{thr}}$ are given in the graphs.

5.3.2. Application of the model

Predictive power The electrical simulation has been calibrated using texture-etched glass substrates C through C120. Calibration means the determination of the model's free parameters which are the sheet resistance of extended grain boundaries R_{eGB} and the curvature threshold $r_{\mathrm{curv}}^{\mathrm{thr}}$. Note that the calibration holds true for one specific deposition condition, that is non-optimized deposition conditions. Here, the calibrated electrical simulation shall be applied to other textured substrates under investigation, namely texture-etched glass substrate A and nano-imprint substrates.

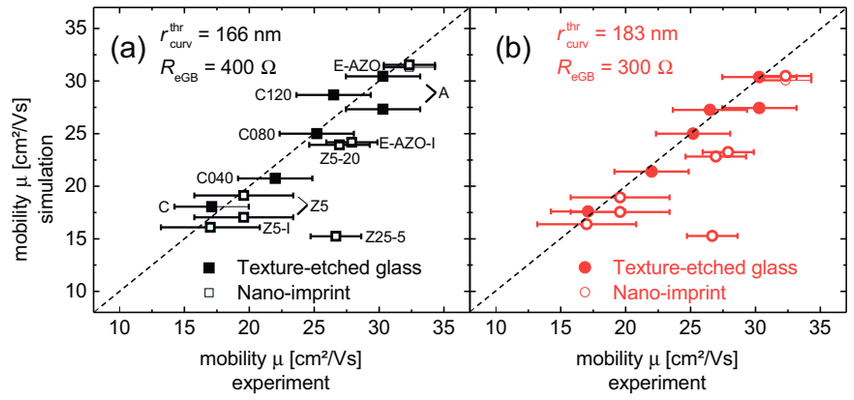

Fig. 5.24. ZnO:Al mobilities on textured substrates were determined using the electrical model described in Section 5.3.1. The graphs compare the simulated mobility values to the experimental ones. The dotted line represents equal simulated and experimental mobility. Texture-etched glass (closed symbols) and nano-imprint (open symbols) substrates were investigated. Two parameter sets for R_{eGB} and $r^{\mathrm{thr}}_{\mathrm{curv}}$ were used. Note that two AFM measurements were evaluated for substrates Z5, A, and E-AZO in order check the measurements' and simulation's reproducibility and stability.

In Fig. 5.24, the simulated mobility values are plotted as a function of the experimental mobility values. The dotted line represents equal values of experiment and simulation. Two parameter sets, that correspond to two different AFM measurements (see Fig. 5.23), were used to predict ZnO:Al mobility on textured substrates. One observes an excellent agreement between simulated and experimental values for both parameter sets. Thus, the electrical simulation seems to be very robust against deviations of their free parameter set R_{eGB} and $r^{\mathrm{thr}}_{\mathrm{curv}}$. The results are even more astonishing if one remembers that non-optimized deposition conditions for nano-imprint substrates differed slightly from the ones used for texture-etched glass substrates (see Section 5.2.1). Only the data point that corresponds to substrate Z25-5 was not well predicted by the simulation. This limitation of the model will be discussed in Section 5.3.3.

Importance of eGB distribution The proposed electrical simulation does not take into account the number of extended grain boundaries only, but also their individual positions and thus their overall distribution. Fig. 5.25 shows the importance of considering the distribution of extended grain boundaries. The sheet resistance was simulated as a function of the curvature threshold for substrate C and C120.

First, the simulation was executed by constructing the resistance network in the way described in Section 5.3.1 (closed symbols in Fig. 5.25). Second, the simulation was performed using a differently obtained resistance network. The number of points with curvature above the threshold, i.e. the number of extended grain boundaries with high sheet resistance, was counted. Then, the same number of high resistance spots was distributed randomly across the surface (open symbols in Fig. 5.25). Thus, both resistance networks agree in the density but differ in the distribution of high resistance spots.

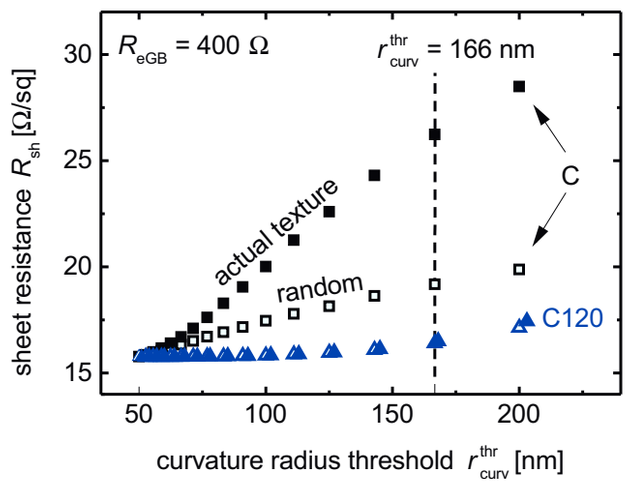

Fig. 5.25. The sheet resistance is plotted against the curvature radius threshold for substrate C and C120. On the one hand, the simulation was done for the actual texture (closed symbols). On the other hand, the number of extended grain boundaries was counted, that is the number of point with curvature above the threshold. Then, this amount of extended grain boundaries corresponding to high sheet resistance spots was distributed randomly across the surface (open symbols). Finally, the so constructed resistance network was evaluated. Note that the data points were slightly shifted for substrate C120 to ensure a better visual clarity.

Substrate C shows a higher sheet resistance if extended grain boundaries were distributed according to the actual texture in contrast to the scenario with randomly distributed extended grain boundaries. Thus, Fig. 5.25 provides evidence that the low mobility of ZnO:Al on substrate C is not only due to a high number of extended grain boundaries but also due to their specific distribution where extended grain boundaries separate individual domains. As a result of this domain-like structure, the current

was forced to cross extended grain boundaries. In contrast, for substrate C120, one obtained similar mobilities irrespective of the specific distribution of extended grain boundaries. Substrate C120 induced a distribution of extended grain boundaries where no separated domains occurred. Therefore, the current can avoid extended grain boundaries with the consequence that merely their absolute number defined the sheet resistance on substrate C120.

5.3.3. Discussion

Inverted substrates Section 5.2.1 described the initial idea of inverting pyramidal and crater structures. Theoretically, inverted pyramids should possess a crater-like structure and inverted craters should possess a rather pyramid-like texture. Consequently, the inversion of the pyramidal substrate Z5 and the crater-like substrate E-AZO should yield a variation of mobility. However, Z5 and Z5-I showed similar mobilities. The mobility on E-AZO-I was only slightly reduced in contrast to E-AZO.

The above described results may be well interpreted in the framework of the developed electrical simulation which revealed the local surface curvature as the parameter that determines the mobility. Fig. 5.21 shows qualitatively that substrate Z5 and Z5-I do not differ much in their amount and distribution of extended grain boundaries. Quantitatively, by predicting similar sheet resistances, the electrical simulation verifies that original and inverted structures are alike (see Fig. 5.24).

Fig. 5.21 suggests qualitatively that substrate E-AZO-I contains a higher amount of high curvature spots than substrate E-AZO. Indeed, experimental as well as simulated mobilities were lower for the inverted structure E-AZO-I. The obtained mobilities are not as low as e.g. for substrate C or Z5. Nevertheless, a clear effect is demonstrated.

A possible explanation for the contrast between initial idea and experiment regarding substrate Z5 might be that its structure deviates too much from the ideal pyramid. In particular, it showed a rather line-like instead of an ideal, point-like tip. As a consequence, the inverted structure Z5-I contained again deep trenches with high curvature that decreased the mobility. E-AZO-I did show the expected mobility decrease. Yet, the mobility did not decrease to values observed for the pyramidal substrates C and Z5 because the amount of spots with curvature exceeding the threshold was just not as high as for the latter substrates. Note however that E-AZO-I showed a domain-like structure comparable to substrates C and Z5.

Limitations of the model ZnO:Al on substrate Z25-5 was expected to show even lower mobilities than on Z5. Both substrates possessed similar morphologies, but Z25-5 had a smaller lateral features size. Fig. 5.21 illustrates Z25-5 to have a similar or even higher amount of spots with high curvature than Z5. Consequently, the electrical simulation predicted for Z25-5 the lowest mobility of all investigated substrates. However, the experimental mobility is higher than predicted by the electrical simulation and higher than the mobility on substrate Z5.

Here, only speculations can be presented about the exceptional behavior of substrate Z25-5. The lateral feature size was the lowest of all investigated substrates. Additionally, the rms roughness was lower than for the rest of the substrates. Possibly, the roughness was not high enough to disturb the ZnO:Al growth as much as one expected from the curvature based electrical simulation. Extended grain boundaries that are initially present may have vanish at a certain layer thickness because the growing films does not "see" the rough substrate anymore.

Conclusion The electrical simulation is able to predict the ZnO:Al mobility on a variety of textured substrates. The simulation is based on the assumption that substrate spots with high convex curvature induce extended grain boundaries with high resistance. The substrate topography determined by AFM measurements can be used to compute a map of local substrate curvatures. The curvature map can then be converted into a resistance network that yields the layer's sheet resistance. The prediction of mobility values is only possible for the deposition condition that the simulation was calibrated for. Nevertheless, I think that the order of simulated mobilities reflects the suitability of textured substrates for the growth of ZnO:Al layers. Thus, the presented electrical simulation is a versatile tool to evaluate surface textures in terms of their suitability for ZnO:Al growth.

5.4. Solar cells on texture-etched glass with thin textured ZnO:Al

Objective At the beginning of this chapter, the use of textured substrates for thin-film silicon solar cells was motivated with the possibility to use thin ZnO:Al layers that save material and reduce parasitic absorption. Here, a proof of concept of thin ZnO:Al layers on textured glass as substrate for a-Si:H/µc-Si:H tandem solar cells will be presented. Furthermore, solar cells that were deposited on double textures based on the etching of ZnO:Al in hydrofluoric acid will be investigated.

Experimental details The texture-etched glass substrate C120 (see Fig. 5.15) was used for the following investigations. ZnO:Al was deposited in Gencoa configuration with a deposition temperature and pressure of 500 °C and 0.13 Pa, respectively. No further etching was applied to a 250 nm thin ZnO:Al layer. 300 nm thin ZnO:Al layers were etched for 10, 20, and 30 s in 1 wt% hydrofluoric acid (HF). The surface texture after etching is shown exemplarily in Fig. 5.26. The morphology consisted of larger texture-etched glass features and smaller features that were produced by the HF etching. Subsequently, a-Si:H/µc-Si:H tandem solar cells have been deposited onto the described substrates. The thickness of a-Si:H and µc-Si:H layers were 380 nm and 1200 nm, respectively.

Fig. 5.26. SEM images of a 300 nm thin ZnO:Al layer on texture-etched glass C120. The ZnO:Al layer was etched for 20 s in 1 wt% hydrofluoric acid to obtain a double texture.

Results and discussion Fig. 5.27 shows the parameters of solar cells that have been deposited on the above described substrates. The additionally shown reference substrate consists of an 800 nm thick ZnO:Al layer on a flat glass substrate. The ZnO:Al film was subsequently etched for 40 s in 0.5 wt% hydrochloric acid to induce a rough, light scattering surface [8, 25].

For the HF0s substrate, one observed the a-Si:H top cell to produce less current than the µc-Si:H bottom cell. Etching ZnO:Al in dilute HF however increased the top and decreased the bottom cell current. The reason for the increased top cell current is supposed to be the improved light incoupling into the solar cell. Fig. 5.28 emphasizes the cell absorptance in the short wavelength range by a red box. Interference fringes can be observed that result from interference within the ZnO:Al layer that grew in a conformal manner on the textured substrate [216]. These interferences could be reduced by etching the ZnO:Al layer because the glass/ZnO:Al and the ZnO:Al/silicon interface were no longer coplanar. Consequently, the EQE was increased by the

better light incoupling as can be seen in Fig. 5.28. Note that a similar concept of ZnO:Al etching on nano-imprinted substrates was already published by Meier et al. [217].

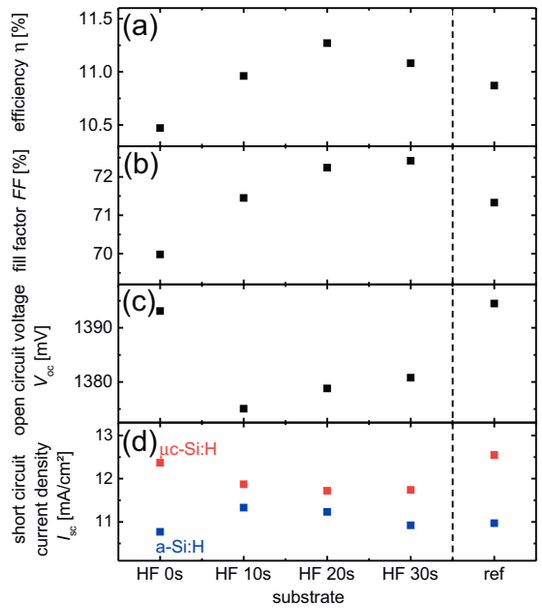

Fig. 5.27. (a) Efficiency, (b) fill factor, (c) open-circuit voltage, and (d) short-circuit current density of a-Si:H/µc-Si:H tandem solar cells are shown for various investigated substrates. Substrates denoted HF10s - HF30s represent texture-etched glass substrates of type C120. These substrates have been coated with 300 nm thin ZnO:Al layers which were then subjected to a treatment in 1 wt% HF for 10 to 30 s. HF0s denotes a C120 substrate with 250 nm of ZnO:Al that was not etched. The reference substrate consisted of 800 nm thick ZnO:Al that was etched for 40 s in 0.5 wt% hydrochloric acid.

At the rough interface, ZnO:Al and silicon can be described as an effective medium with an averaged refractive index [218]. Thus, besides the reduction of interferences, the HF etching improves the light incoupling because the light no longer "sees" an abrupt interface but a rather smooth transition from the refractive index of ZnO:Al to the refractive index of silicon. This effect requires the lateral width of the rough features to be equal or below the wavelength. This requirement is fulfilled by the small HF features [15, 61].

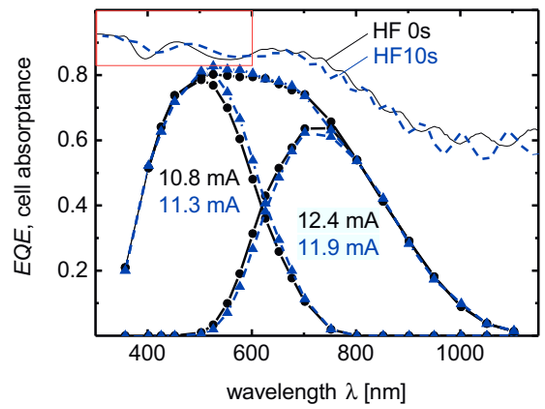

Fig. 5.28. External quantum efficiency (EQE) and cell absorptance of a-Si:H/µc-Si:H tandem solar cells on texture-etched glass substrates of the type C120. One ZnO:Al layer (blue) was subjected to a 10 s HF etch. The red box emphasizes interferences in the cell absorptance.

The bottom cell current decreased when the ZnO:Al layer was etched. I suspect this effect to be induced by a flattening of the large features as a result of the HF etching [86]. Consequently, the substrate's light scattering ability was deteriorated and the bottom cell current decreased. Note that the reference substrate showed the highest bottom cell current and thus the best light scattering capability.

The open-circuit voltage V_{oc} decreased when the HF etching was applied. The small and sharp HF features possibly induced more defects in the subsequently deposited silicon material reducing the V_{oc}. I speculate that longer HF etching widened and possibly reduced the sharpness of the etch features. Hence, one observed a slight V_{oc} improvement with increasing HF etching time.

The fill factor increased with increasing HF etching time. This is surprising because a better matching between top and bottom cell should decrease the fill factor. The opposite behavior is observed. An explanation is lacking.

The best efficiency of 11.3 % was obtained by etching the ZnO:Al layer for 20 s. However, the high efficiency was predominately induced by the better matching between top and bottom cell in comparison to other substrates. Note in particular that the reference was highly mismatched. Nevertheless, the combination of textured substrates and HF etching of ZnO:Al led to efficiencies that were comparable to the sophisticated reference substrate. Furthermore, the a-Si:H top cell profited from

the better light incoupling induced by the HF etching. As a result, thinner a-Si:H layers can be used which reduces their light induced degradation [219]. Note that Neubert et al. combined texture-etched glass substrates of type C120 with thin and highly conductive ZnO:Al films that have been subjected to a post-deposition heat treatment (see Section 4.4) under a-Si:H capping layer [199].

In conclusion, the solar cell results showed the applicability of textured substrates for thin-film silicon solar cells. A double texture was developed by HF etching of ZnO:Al layers on textured substrates.

6. Conclusion and Future Prospects

This work aims at elucidating the mechanisms that govern the conductivity in highly doped, polycrystalline ZnO:Al films that were deposited on either flat or textured substrates.

Flat substrates The understanding of scattering mechanisms that limit the charge carrier mobility in degenerately doped, polycrystalline films is the first step to improve the conductivity in these materials. To further the understanding of electron scattering mechanisms, a conductivity model for highly doped, polycrystalline semiconductors was proposed that comprises ionized impurity scattering, electron-phonon scattering, and field emission at grain boundaries. Ionized impurity scattering, described by the theory of Brooks, Herring, and Dingle, and electron-phonon scattering, implemented by the Bloch-Grüneisen law, are both scattering mechanisms which are located within the grain. However, besides these well-known and accepted intra-grain scattering mechanisms, scattering at grain boundaries had to be considered.
Grain boundaries induce defects that trap electrons which results in potential barriers that scatter electrons. Electrons can pass these potential barriers by three different mechanisms: thermionic emission, thermionic field emission, and field emission. Thermionic emission theory, predominantly applied in the framework of the Seto model, is considered by the majority of authors as dominant mechanism across potential barriers at grain boundaries. Field emission, also denoted as quantum mechanical tunneling, and thermionic field emission are neglected in most cases. The progress made in this work is the adaptation of Stratton's analytical (thermionic) field emission theory for the application to potential barriers at grain boundaries.

Criteria were presented that hint to the dominant transport path across grain boundaries. The application of these criteria revealed field emission to be the dominant transport mechanism through potential barriers at grain boundaries. In conjunction with the above outlined intra-grain scattering mechanisms, excellent fits of temperature-dependent Hall effect measurements were obtained. I discovered that only the combination of field emission and electron-phonon scattering leads to a satisfying description of temperature-dependent conductivity or mobility data. Also, mobility data, given as a function of carrier concentration, was described satisfactorily. Merely three fit parameters, namely the density of occupied traps at grain boundaries,

the electron-phonon coupling constant, and the Debye temperature, had to be considered. The fit results suggested that the trap density at grain boundaries increases linearly with carrier concentration. This observation was explained by the assumption of an energetic distribution of trap states. Only trap states equal to or below the Fermi level are occupied. Increasing carrier concentration induces a rising Fermi level with the consequence of charging formerly unoccupied trap states. As a result, the amount of occupied trap states increases.

After the development of a comprehensive conductivity model, this model is employed to analyze two optimization routes for ZnO:Al films. The first route details a seed layer approach in order to reduce the deposition temperature without deteriorating electrical, optical, and etching properties. The second route deals with post-deposition heat treatments that boost or reduce the mobility depending on whether or not an amorphous silicon capping layer is applied during treatment.

Seed layers with a high concentration of the dopant aluminum enabled a deposition temperature reduction of 100 °C for the subsequently grown, lowly doped and thus more transparent bulk layer. Highly doped seed layers were sputtered from a ZnO:Al_2O_3 target with 2 wt% of Al_2O_3 whereas the target used for the lowly doped bulk layer deposition contained only 1 wt% of Al_2O_3. Seed layers reduced grain size and surface roughness of the bulk layer. I proposed that the dopant aluminum acts as a surfactant that increases the surface diffusion length whereby a 2D-growth mode is favored. The beneficial 2D-growth of the highly doped seed layer is then adopted by the thereafter grown, lowly doped bulk layer. Additionally, the seed layer induced increasing tensile stress. The tensile stress was interpreted in terms of the grain boundary relaxation model. The grain boundary relaxation model assumes grain boundaries to induce a horizontal attractive force between adjacent grains that results in tensile stress. More grain boundaries or equally, a lower grain size, induce higher tensile stress. Thus, in the framework of the grain boundary relaxation model, I explained the augmented tensile stress to result from the reduction of grain size upon seed layer application. Furthermore, etching characteristics, temperature-dependent conductivity measurements, and optical fits suggested the seed layer induced grain size reduction to be accompanied by an improved grain boundary morphology. The improved grain boundary morphology leads to less grain boundary scattering and thus a higher mobility. Note that a seed layer thickness of 5 nm was sufficient to induce the beneficial effects.

Raman spectroscopy and temperature-dependent Hall effect measurements were used to analyze the impact of post-deposition heat treatments on charge carrier

mobility and concentration of ZnO:Al films. It is known in literature that the application of an amorphous silicon capping layer during the annealing process yields improved mobilities, whereas an annealing without capping layer commonly decreases carrier concentration and mobility. In this work, two conclusions were drawn from Raman spectroscopy: First, the trap density at grain boundaries was reduced by a post-deposition heat treatment irrespective of whether or not a capping layer was present. Second, the capping layer possibly prevented the incorporation of oxygen into ZnO:Al films. The combination of Raman spectroscopy and temperature-dependent Hall effect measurements yielded the following explanation for the different electrical properties of annealed films. I proposed that annealing under a capping layer reduces the grain boundary trap density as well as the number of acceptors. Therefore, grain boundary scattering becomes negligible and ionized impurity scattering is diminished to a minimum. In contrast, annealing without capping layer increases the number of acceptors and thus the compensation such that ionized impurity scattering is amplified. Similar to annealing with capping layer, the grain boundary trap density is reduced resulting in a decrease of barrier height at the grain boundaries. However, since the Fermi Level and the barrier height decrease simultaneously, field emission through potential barriers at grain boundaries, i.e. grain boundary scattering, is still present.

Textured substrates The deposition of ZnO:Al films on textured substrates is challenging due to the occurrence of extended grain boundaries that reduce charge carrier mobility and damp heat stability. The influence of ZnO:Al deposition conditions and substrate morphology was investigated in order to optimize ZnO:Al conductivity and stability on textured substrates for the application in thin-film silicon and chalcopyrite-based solar cells.

Optimized, low-temperature and low-pressure deposition conditions led to ZnO:Al films with similar charge carrier mobility on randomly textured glass substrates as on flat reference substrates. Generally, the mobility gap between ZnO:Al films on rough and flat substrates can be decreased to a minimum by applying a low-temperature post-deposition annealing process with an amorphous silicon capping layer at 300 °C. A model substrate with periodically recurring trenches was developed that verified the results obtained on randomly textured substrates. The model structure enabled the estimation of resistivity for extended grain boundaries when non-optimized, low-temperature and high-pressure deposition conditions were used. The resistivity of extended grain boundaries was determined to be between $5.72 \times 10^{-1}\,\Omega\,\mathrm{cm}$ and $7.15 \times 10^{-2}\,\Omega\,\mathrm{cm}$. A growth model was presented that qualitatively explains the observed mobility trends for various deposition conditions. The model assumes that

grains which grow perpendicular to the local substrate surface induce more and larger extended grain boundaries with the result of a more severe reduction of mobility. The grain orientation depends on the deposition conditions. High-temperature deposition conditions led, irrespective of deposition pressure, to grains that were oriented perpendicular to the local substrate surface. Using low-temperature deposition conditions, the grain growth was suspected to depend on the deposition pressure. Low pressures induced grains to be bent towards the rather direct incident particle flux whereas high pressures induced grains to be oriented according to the local substrate surface. The qualitative model explains why the mobility of ZnO:Al films that were deposited at low deposition temperatures and pressures on textured substrates was only very slightly diminished in comparison to films on flat substrates.

ZnO:Al films were deposited on a variety of texture-etched glass and nano-imprint substrates. ZnO:Al on U-shaped substrates showed higher mobility and lower degradation under damp heat than on V-shaped substrates. Etching experiments supported the assumption of U-shaped substrates to induce less extended grain boundaries than V-shaped substrates. Hence, the high mobility and damp heat stability of ZnO:Al on U-shaped substrates was explained by the lower number of extended grain boundaries.

The rather qualitative description of substrate texture as V- or U-shaped was developed further and implemented into a quantitative electrical simulation. The simulation is based on the assumption that local spots on the substrate with high convex curvature induce extended grain boundaries with high resistance. The substrate topography determined by AFM measurements was used to compute a map of local substrate curvatures, which was converted into a resistance network with high and low values. The determination of the network's total resistance yielded the resistance and thus the mobility of ZnO:Al films on the specific substrate texture. After the calibration of the simulation for particular deposition conditions, an excellent prediction of ZnO:Al mobility on textured substrates was achieved. Even without calibration, the order of simulated mobilities reflects the suitability of textured substrates for the growth of ZnO:Al layers. Thus, the presented electrical simulation is a versatile tool for the evaluation of surface textures in terms of their suitability for ZnO:Al growth.

At last, a double textured ZnO:Al was developed for the application in a-Si:H/µc-Si:H tandem solar cells. The double texture consisted of a 300 nm thin ZnO:Al film deposited onto a texture-etched glass substrate. The ZnO:Al layer was furthermore etched in dilute hydrofluoric acid. As a consequence, the resulting double texture

possessed large ($\varnothing \approx 1\,\mu m$) and small ($\varnothing \lessapprox 300\,nm$) features. The applicability of this texture in a-Si:H/µc-Si:H tandem solar cells was successfully proven.

Future Prospects The proposed conductivity model on flat substrates has to be further tested by its application to more data of temperature-dependent Hall effect measurements. Furthermore, the model's fit parameters should be independently determined by other methods, e.g. the Debye temperatures can be obtained by specific heat measurements.

Seed layers with higher aluminum concentrations than the ones used in this work should be investigated. A further decrease of deposition temperature might thus be possible.

Further investigations to elucidate the microscopic changes induced by the annealing process are needed. A powerful tool for this purpose is atom probe tomography (APT). APT measurements with first promising results were ongoing at the end of this thesis.

The influence of substrate morphology is not only important for the growth of ZnO:Al but also for the deposition of silicon films for solar cells. The characterization of substrate textures via their local curvature was successfully used to describe ZnO:Al conductivity. It would be interesting to apply the local curvature concept to correlate substrate texture and crack formation in the absorber layer. Finally, an estimation of shunt-resistance and open-circuit voltage as a function of substrate texture is expected.

Bibliography

[1] C. G. Granqvist, *Transparent conductors as solar energy materials: A panoramic review*, Solar Energy Materials and Solar Cells **91** (2007), 1529 – 1598.

[2] C. G. Granqvist, *Handbook of inorganic electrochromic materials*, Elsevier, 1995.

[3] D. S. Ginley and C. Bright, *Transparent Conducting Oxides*, MRS Bulletin **25** (2000), 15 – 18.

[4] K. L. Chopra, P. D. Paulson, and V. Dutta, *Thin-film solar cells: an overview*, Progress in Photovoltaics: Research and Applications **12** (2004), 69 – 92.

[5] K. Ellmer, A. Klein, and B. Rech, *Transparent conductive zinc oxide: basics and applications in thin film solar cells*, Vol. 104, Springer, 2007.

[6] A. G. Aberle, *Thin-film solar cells*, Thin Solid Films **517** (2009), 4706 – 4710.

[7] J. Müller, B. Rech, J. Springer, and M. Vanecek, *TCO and light trapping in silicon thin film solar cells*, Solar Energy **77** (2004), 917 – 930.

[8] M. Berginski, J. Hüpkes, M. Schulte, G. Schöpe, H. Stiebig, B. Rech, and M. Wuttig, *The effect of front ZnO:Al surface texture and optical transparency on efficient light trapping in silicon thin-film solar cells*, Journal of Applied Physics **101** (2007), 074903.

[9] J. Y. W. Seto, *The electrical properties of polycrystalline silicon films*, Journal of Applied Physics **46** (1975), 5247–5254.

[10] R. L. Petritz, *Theory of Photoconductivity in Semiconductor Films*, Phys. Rev. **104** (1956), 1508–1516.

[11] S. Sze and K. Ng, *Physics of Semiconductor Devices*, John Wiley & Sons, Wiley, 2006.

[12] J. Orton, *Interpretation of Hall mobility in polycrystalline thin films*, Thin Solid Films **86** (1981), 351 – 357.

[13] S. Faÿ, J. Steinhauser, S. Nicolay, and C. Ballif, *Polycrystalline ZnO: B grown by LPCVD as TCO for thin film silicon solar cells*, Thin Solid Films **518** (2010), 2961 – 2966.

[14] J. ichi Nomoto, T. Hirano, T. Miyata, and T. Minami, *Preparation of Al-doped ZnO transparent electrodes suitable for thin-film solar cell applications by various types of magnetron sputtering depositions*, Thin Solid Films **520** (2011), 1400 – 1406.

[15] J. I. Owen, J. Hüpkes, H. Zhu, E. Bunte, and S. E. Pust, *Novel etch process to tune crater size on magnetron sputtered ZnO:Al*, physica status solidi (a) **208** (2011), 109–113.

[16] S. E. Pust, J.-P. Becker, J. Worbs, S. O. Klemm, K. J. J. Mayrhofer, and J. Hüpkes, *Electrochemical Etching of Zinc Oxide for Silicon Thin Film Solar Cell Applications*, Journal of The Electrochemical Society **158** (2011), D413–D419.

[17] H. Sai, H. Jia, and M. Kondo, *Impact of front and rear texture of thin-film microcrystalline silicon solar cells on their light trapping properties*, Journal of Applied Physics **108** (2010), 044505.

[18] M. Boccard, C. Battaglia, S. Hänni, K. Söderström, J. Escarré, S. Nicolay, F. Meillaud, M. Despeisse, and C. Ballif, *Multiscale Transparent Electrode Architecture for Efficient Light Management and Carrier Collection in Solar Cells*, Nano Letters (2012).

[19] D. Köhl, G. Natarajan, and M. Wuttig, *Structure control of sputtered zinc oxide films by utilizing zinc oxide seed layers tailored by ion beam assisted sputtering*, Journal of Physics D: Applied Physics **45** (2012), 245302.

[20] W. Dewald, V. Sittinger, B. Szyszka, F. Säuberlich, B. Stannowski, D. Köhl, P. Ries, and M. Wuttig, *Advanced properties of Al-doped ZnO films with a seed layer approach for industrial thin film photovoltaic application*, Thin Solid Films **534** (2013), 474 – 481.

[21] F. Claeyssens, C. L. Freeman, N. L. Allan, Y. Sun, M. N. R. Ashfold, and J. H. Harding, *Growth of ZnO thin films-experiment and theory*, J. Mater. Chem. **15** (2005), 139–148.

[22] F. Ruske, M. Roczen, K. Lee, M. Wimmer, S. Gall, J. Hupkes, D. Hrunski, and B. Rech, *Improved electrical transport in Al-doped zinc oxide by thermal treatment*, Journal of Applied Physics **107** (2010), 013708.

[23] J. Hüpkes, J. Owen, M. Wimmer, F. Ruske, D. Greiner, R. Klenk, U. Zastrow, and J. Hotovy, *Damp heat stable doped zinc oxide films*, Thin Solid Films **555** (2014), 48 – 52.

[24] M. Warzecha, J. I. Owen, M. Wimmer, F. Ruske, J. Hotovy, and J. Hüpkes, *High mobility annealing of Transparent Conductive Oxides*, IOP Conference Series: Materials Science and Engineering **34** (2012), 012004.

[25] O. Kluth, G. Schöpe, J. Hüpkes, C. Agashe, J. Müller, and B. Rech, *Modified Thornton model for magnetron sputtered zinc oxide: film structure and etching behaviour*, Thin Solid Films **442** (2003), 80 – 85.

[26] W. Böttler, V. Smirnov, J. Hüpkes, and F. Finger, *Texture-etched ZnO as a versatile base for optical back reflectors with well-designed surface morphologies for application in thin film solar cells*, physica status solidi (a) **209** (2012), 1144–1149.

[27] J. Springer, B. Rech, W. Reetz, J. Müller, and M. Vanecek, *Light trapping and optical losses in microcrystalline silicon pin solar cells deposited on surface-textured glass/ZnO substrates*, Solar Energy Materials and Solar Cells **85** (2005), 1 – 11.

[28] C. Battaglia, J. Escarré, K. Söderström, L. Erni, L. Ding, G. Bugnon, A. Billet, M. Boccard, L. Barraud, S. De Wolf, F.-J. Haug, M. Despeisse, and C. Ballif, *Nanoimprint Lithography for High-Efficiency Thin-Film Silicon Solar Cells*, Nano Letters **11** (2011), 661–665.

[29] M. Meier, U. W. Paetzold, M. Prömpers, T. Merdzhanova, R. Carius, and A. Gordijn, *UV nanoimprint for the replication of etched ZnO:Al textures applied in thin-film silicon solar cells*, Progress in Photovoltaics: Research and Applications (2013).

[30] O. Isabella, F. Moll, J. Krc, and M. Zeman, *Modulated surface textures using zinc-oxide films for solar cells applications*, physica status solidi (a) **207** (2010), 642–646.

[31] N. P. Harder, D. L. Bellac, E. Royer, B. Rech, G. Schöpe, and J. Müller, *Light-Trapping in a-Si:H and* µc*-Si:H Solar Cells via Nano-Textured Glass*

Superstrates made by Plasma Etching, Proceedings of the 19th European Photovoltaic Solar Energy Conference, 2004, pp. 1355 – 1358.

[32] A. Hongsingthong, A. Aino, P. Sichanugrist, M. Konagai, H. Kuramochi, R. Akiike, H. Iigusa, K. Utsumi, and T. Shibutami, *Development of Novel Al-Doped Zinc Oxide Films Fabricated on Etched Glass and Their Application to Solar Cells*, Japanese Journal of Applied Physics **51** (2012), 10NB09.

[33] D. Greiner, N. Papathanasiou, A. Pflug, F. Ruske, and R. Klenk, *Influence of damp heat on the optical and electrical properties of Al-doped zinc oxide*, Thin Solid Films **517** (2009), 2291 – 2294.

[34] D. Greiner, S. Gledhill, C. Köble, J. Krammer, and R. Klenk, *Damp heat stability of Al-doped zinc oxide films on smooth and rough substrates*, Thin Solid Films **520** (2011), 1285 – 1290.

[35] D. Greiner, *Ursache der Leitfähigkeitsabnahme nach künstlicher Alterung in feuchter Wärme bei hochdotierten Zinkoxid-Schichten für die Dünnschichtfotovoltaik*, Ph.D. thesis, Freie Universität Berlin, 2010.

[36] B. O'Connor, C. Haughn, K.-H. An, K. P. Pipe, and M. Shtein, *Transparent and conductive electrodes based on unpatterned, thin metal films*, Applied Physics Letters **93** (2008).

[37] R. B. Pode, C. J. Lee, D. G. Moon, and J. I. Han, *Transparent conducting metal electrode for top emission organic light-emitting devices: Ca–Ag double layer*, Applied Physics Letters **84** (2004), 4614–4616.

[38] L. Groenendaal, F. Jonas, D. Freitag, H. Pielartzik, and J. R. Reynolds, *Poly(3,4-ethylenedioxythiophene) and Its Derivatives: Past, Present, and Future*, Advanced Materials **12** (2000), 481–494.

[39] M. J. Allen, V. C. Tung, and R. B. Kaner, *Honeycomb carbon: a review of graphene*, Chemical reviews **110** (2009), 132–145.

[40] K. Baedeker, *Über die elektrische Leitfähigkeit und die thermoelektrische Kraft einiger Schwermetallverbindungen*, Annalen der Physik **327** (1907), 749–766.

[41] R. Klenk, J. Klaer, C. Köble, R. Mainz, S. Merdes, H. Rodriguez-Alvarez, R. Scheer, and H. Schock, *Development of $CuInS_2$-based solar cells and modules*, Solar Energy Materials and Solar Cells **95** (2011), 1441 – 1445.

[42] W. Hirschwald, P. Bonasewicz, L. Ernst, M. Grade, D. Hofmann, S. Krebs, R. Littbar, G. Neumann, M. CJrunze, D. Kolb, et al., *Zinc oxide*, Current Topics in Materials Science **7** (1981), 143–482.

[43] U. Özgür, Y. I. Alivov, C. Liu, A. Teke, M. A. Reshchikov, S. Doğan, V. Avrutin, S.-J. Cho, and H. Morkoç, *A comprehensive review of ZnO materials and devices*, Journal of Applied Physics **98** (2005).

[44] S. Hunklinger, *Festkörperphysik*, Oldenbourg, 2007.

[45] J. D. Jackson, *Classical Electrodynamics*, 3rd ed., John Wiley & Sons, 1999.

[46] J. Hüpkes, *Untersuchung des reaktiven Sputterprozesses zur Herstellung von aluminiumdotierten Zinkoxid-Schichten für Silizium-Dünnschichtsolarzellen*, Ph.D. thesis, RWTH Aachen University, 2005.

[47] M. Berginski, *Lichtstreuende Oberflächen, Schichten und Schichtsysteme zur Verbesserung der Lichteinkopplung in Silizium-Dünnschichtsolarzellen*, Ph.D. thesis, RWTH Aachen University, 2008.

[48] D. Mergel and Z. Qiao, *Dielectric modelling of optical spectra of thin In_2O_3:Sn films*, Journal of Physics D: Applied Physics **35** (2002), 794.

[49] E. Gerlach, *Carrier scattering and transport in semiconductors treated by the energy-loss method*, Journal of Physics C: Solid State Physics **19** (1986), 4585.

[50] A. Pflug, V. Sittinger, F. Ruske, B. Szyszka, and G. Dittmar, *Optical characterization of aluminum-doped zinc oxide films by advanced dispersion theories*, Thin Solid Films **455–456** (2004), 201 – 206.

[51] E. Burstein, *Anomalous Optical Absorption Limit in InSb*, Phys. Rev. **93** (1954), 632–633.

[52] T. S. Moss, *The Interpretation of the Properties of Indium Antimonide*, Proceedings of the Physical Society. Section B **67** (1954), 775.

[53] T. Pisarkiewicz, K. Zakrzewska, and E. Leja, *Scattering of charge carriers in transparent and conducting thin oxide films with a non-parabolic conduction band*, Thin Solid Films **174** (1989), 217 – 223.

[54] K. Ellmer, *Resistivity of polycrystalline zinc oxide films: current status and physical limit*, Journal of Physics D: Applied Physics **34** (2001), 3097.

[55] T. Minami, H. Sato, K. Ohashi, T. Tomofuji, and S. Takata, *Conduction mechanism of highly conductive and transparent zinc oxide thin films prepared by magnetron sputtering*, Journal of Crystal Growth **117** (1992), 370 – 374.

[56] B. E. Sernelius, K.-F. Berggren, Z.-C. Jin, I. Hamberg, and C. G. Granqvist, *Band-gap tailoring of ZnO by means of heavy Al doping*, Phys. Rev. B **37** (1988), 10244–10248.

[57] J. I. Pankove, *Absorption Edge of Impure Gallium Arsenide*, Phys. Rev. **140** (1965), A2059–A2065.

[58] S. Schönau, F. Ruske, S. Neubert, and B. Rech, *Analysis of Urbach-like absorption tails in thermally treated ZnO:Al thin films*, Applied Physics Letters **103** (2013).

[59] A. P. L. **103** (2013), *Product Information: Corning 1737*, 2004.

[60] B. N. Chapman, *Glow discharge processes: sputtering and plasma etching*, Wiley, 1980.

[61] J. I. Owen, *Growth, Etching, and Stability of Sputtered ZnO:Al for Thin-Film Silicon Solar Cells*, Ph.D. thesis, RWTH Aachen, 2011.

[62] N. Fujimura, T. Nishihara, S. Goto, J. Xu, and T. Ito, *Control of preferred orientation for ZnOx films: control of self-texture*, Journal of Crystal Growth **130** (1993), 269 – 279.

[63] A. Van der Drift, *Evolutionary selection, a principle governing growth orientation in vapour-deposited layers*, Philips Res. Rep **22** (1967), 267–88.

[64] J. A. Thornton, *Influence of apparatus geometry and deposition conditions on the structure and topography of thick sputtered coatings*, Journal of Vacuum Science & Technology **11** (1974), 666–670.

[65] J. Hüpkes, J. I. Owen, S. E. Pust, and E. Bunte, *Chemical Etching of Zinc Oxide for Thin-Film Silicon Solar Cells*, ChemPhys **13** (2012), 66–73.

[66] J. A. Thornton and D. Hoffman, *Stress-related effects in thin films*, Thin Solid Films **171** (1989), 5 – 31.

[67] S. O. Kucheyev, J. E. Bradby, J. S. Williams, C. Jagadish, and M. V. Swain, *Mechanical deformation of single-crystal ZnO*, Applied Physics Letters **80** (2002), 956–958.

[68] G. Carlotti, D. Fioretto, G. Socino, and E. Verona, *Brillouin scattering determination of the whole set of elastic constants of a single transparent film of hexagonal symmetry*, Journal of Physics: Condensed Matter **7** (1995), 9147.

[69] 9147, *Product Information: Eurowhite NG*, 2014.

[70] H. Windischmann, *Intrinsic stress in sputter-deposited thin films*, Critical Reviews in Solid State and Materials Sciences **17** (1992), 547–596.

[71] E. Klokholm and B. S. Berry, *Intrinsic Stress in Evaporated Metal Films*, Journal of The Electrochemical Society **115** (1968), 823–826.

[72] J. D. Finegan and R. W. Hoffman, *Stress Anisotropy in Evaporated Iron Films*, Journal of Applied Physics **30** (1959), 597–598.

[73] F. D'Heurle and J. Harper, *Note on the origin of intrinsic stresses in films deposited via evaporation and sputtering*, Thin Solid Films **171** (1989), 81 – 92.

[74] D. Köhl, M. Luysberg, and M. Wuttig, *Structural improvement of zinc oxide films produced by ion beam assisted reactive sputtering*, Journal of Physics D: Applied Physics **43** (2010), 205301.

[75] M. A. Green, K. Emery, Y. Hishikawa, W. Warta, and E. D. Dunlop, *Solar cell efficiency tables (version 39)*, Progress in Photovoltaics: Research and Applications **20** (2012), 12–20.

[76] A. V. Shah, H. Schade, M. Vanecek, J. Meier, E. Vallat-Sauvain, N. Wyrsch, U. Kroll, C. Droz, and J. Bailat, *Thin-film silicon solar cell technology*, Progress in Photovoltaics: Research and Applications **12** (2004), 113–142.

[77] A. Goetzberger, J. Luther, and G. Willeke, *Solar cells: past, present, future*, Solar Energy Materials and Solar Cells **74** (2002), 1 – 11.

[78] D. L. Staebler and C. R. Wronski, *Reversible conductivity changes in discharge produced amorphous Si*, Applied Physics Letters **31** (1977), 292–294.

[79] O. Vetterl, F. Finger, R. Carius, P. Hapke, L. Houben, O. Kluth, A. Lambertz, A. Mück, B. Rech, and H. Wagner, *Intrinsic microcrystalline silicon: A new material for photovoltaics*, Solar Energy Materials and Solar Cells **62** (2000), 97 – 108.

[80] P. Würfel and U. Würfel, *Physics of solar cells: from basic principles to advanced concepts*, John Wiley & Sons, 2009.

[81] R. Waser, *Nanoelectronics and information technology*, John Wiley & Sons, 2012.

[82] G. Schöpe, *DC-Sputtern transparenter, leitfähiger Zinkoxidschichten für Dünnschichtsolarzellen von metallischen Zn:Al-Targets*, Master's thesis, Fachhochschule Aachen, 1998.

[83] O. Kluth, *Texturierte ZinkoxidschiZinkoxid Silizium-Dünnschichtsolarzellen*, Ph.D. thesis, RWTH Aachen University, 2001.

[84] S. Fearn, D. McPhail, R. Morris, and M. Dowsett, *Sodium and hydrogen analysis of room temperature glass corrosion using low energy Cs SIMS*, Applied Surface Science **252** (2006), 7070 – 7073.

[85] C. Wang, W. Häfner, G. Krausch, E. Rädlein, S. Tratzky, M. Schramm, and K.-P. Martinek, *Study of surface changes on industrial glasses with AFM, FE-SEM, EDX, SNMS and LM. Part 1. Glass skin and corrosion*, Glass science and technology **77** (2004), 103–110.

[86] G. Jost, *Analyse der Lichtstreuung zur Textur-Optimierung von Zinkoxid-Frontkontakten für Silizium-Dünnschichtsolarzellen*, Ph.D. thesis, RWTH Aachen, 2013.

[87] G. Jost, T. Merdzhanova, T. Zimmermann, and J. Hüpkes, *Process monitoring of texture-etched high-rate ZnO:Al front contacts for silicon thin-film solar cells*, Thin Solid Films **532** (2013), 66 – 72.

[88] J. Woerdenweber, T. Merdzhanova, T. Zimmermann, A. Flikweert, H. Stiebig, W. Beyer, and A. Gordijn, *Cross-contamination in single-chamber processes for thin-film silicon solar cells*, Journal of Non-Crystalline Solids **358** (2012), 2183 – 2186.

[89] A. J. Flikweert, T. Zimmermann, T. Merdzhanova, D. Weigand, W. Appenzeller, and A. Gordijn, *Microcrystalline thin-film solar cell deposition on moving substrates using a linear VHF-PECVD reactor and a cross-flow geometry*, Journal of Physics D: Applied Physics **45** (2012), 015101.

[90] T. Repmann, *Stapelsolarzellen aus amorphem und mikrokristallinem Silizium*, Ph.D. thesis, 2003.

[91] S. Haas, *Untersuchung und Optimierung der Serienverschaltung von Silizium-Dünnschicht-Solarmodulen*, Ph.D. thesis, RWTH Aachen University, 2010.

[92] L. Van der Pauw, *A method of measuring the resistivity and Hall coefficient on lamellae of arbitrary shape*, Philips technical review **20** (1958), 220–224.

[93] T. Bronger, *Electronic properties of µc-Si:H layers investigated with Hall measurements*, Ph.D. thesis, RWTH Aachen University, 2007.

[94] Quantum Design, *Physical Property Measurement System (http://www.qdusa.com/sitedocs/productBrochures/1070-002.pdf)*.

[95] H. Lüth, *Solid surfaces, interfaces and thin films*, Vol. 4, Springer, 2001.

[96] P. Scherrer, *Bestimmung der Größe und der inneren Struktur von Kolloidteilchen mittels Röntgenstrahlen*, Nachrichten von der Gesellschaft der Wissenschaften zu Göttingen, Mathematisch-Physikalische Klasse **1918** (1918), 98–100.

[97] R. Cebulla, R. Wendt, and K. Ellmer, *Al-doped zinc oxide films deposited by simultaneous rf and dc excitation of a magnetron plasma: Relationships between plasma parameters and structural and electrical film properties*, Journal of Applied Physics **83** (1998), 1087–1095.

[98] D. Köhl, *The influence of energetic bombardment on the structure formation of sputtered zinc oxide films: development of an atomistic growth model and its application to tailor thin film properties*, Ph.D. thesis, RWTH Aachen University, 2011.

[99] Q. Yang, F. Williams, X. Zhao, C. Reece, and M. Krishnan, *Investigating crystal microstructure of niobium materials by an x-ray diffraction reciprocal space mapping technique*, Phys. Rev. ST Accel. Beams **17** (2014), 013501.

[100] C. Raman and K. Krishnan, *The optical analogue of the Compton effect*, Nature **121** (1928), 711–711.

[101] U. Rau, D. Abou-Ras, and T. Kirchartz, *Advanced characterization techniques for thin film solar cells*, John Wiley & Sons, 2011.

[102] J. Metzdorf, *Calibration of solar cells. 1: The differential spectral responsivity method*, Appl. Opt. **26** (1987), 1701–1708.

[103] M. Theiss, *Hard and Software for Optical Spectroscopy*, Dr. Berhard-Klein-Straße 110, 52078 Aachen, Germany, www.mtheiss.com.

[104] Z. Qiao, C. Agashe, and D. Mergel, *Dielectric modeling of transmittance spectra of thin ZnO:Al films*, Thin Solid Films **496** (2006), 520 – 525.

[105] Z.-C. Jin, I. Hamberg, and C. G. Granqvist, *Optical properties of sputter-deposited ZnO:Al thin films*, Journal of Applied Physics **64** (1988), 5117–5131.

[106] J. Steinhauser, S. Fay, N. Oliveira, E. Vallat-Sauvain, and C. Ballif, *Transition between grain boundary and intragrain scattering transport mechanisms in boron-doped zinc oxide thin films*, Applied Physics Letters **90** (2007), 142107.

[107] J. Steinhauser, S. Faÿ, N. Oliveira, E. Vallat-Sauvain, D. Zimin, U. Kroll, and C. Ballif, *Electrical transport in boron-doped polycrystalline zinc oxide thin films*, physica status solidi (a) **205** (2008), 1983–1987.

[108] A. Bikowski and K. Ellmer, *A comparative study of electronic and structural properties of polycrystalline and epitaxial magnetron-sputtered ZnO:Al and $Zn_{1-x}Mg_xO$:Al Films—Origin of the grain barrier traps*, Journal of Applied Physics **114** (2013).

[109] S. Brehme, F. Fenske, W. Fuhs, E. Nebauer, M. Poschenrieder, B. Selle, and I. Sieber, *Free-carrier plasma resonance effects and electron transport in reactively sputtered degenerate ZnO:Al films*, Thin Solid Films **342** (1999), 167 – 173.

[110] H. Fujiwara and M. Kondo, *Effects of carrier concentration on the dielectric function of ZnO:Ga and In_2O_3:Sn studied by spectroscopic ellipsometry: Analysis of free-carrier and band-edge absorption*, Phys. Rev. B **71** (2005), 075109.

[111] N. Ehrmann and R. Reineke-Koch, *Ellipsometric studies on ZnO:Al thin films: Refinement of dispersion theories*, Thin Solid Films **519** (2010), 1475 – 1485.

[112] R. J. Mendelsberg, G. Garcia, and D. J. Milliron, *Extracting reliable electronic properties from transmission spectra of indium tin oxide thin films and nanocrystal films by careful application of the Drude theory*, Journal of Applied Physics **111** (2012).

[113] F. Ruske, A. Pflug, V. Sittinger, B. Szyszka, D. Greiner, and B. Rech, *Optical modeling of free electron behavior in highly doped ZnO films*, Thin Solid Films **518** (2009), 1289 – 1293.

[114] Y. S. Jung, O. V. Kononenko, and W.-K. Choi, *Electron transport in high quality undoped ZnO film grown by plasma-assisted molecular beam epitaxy*, Solid State Communications **137** (2006), 474 – 477.

[115] K. Ellmer and R. Mientus, *Carrier transport in polycrystalline transparent conductive oxides: A comparative study of zinc oxide and indium oxide*, Thin Solid Films **516** (2008), 4620 – 4627.

[116] D. Gerthsen, D. Litvinov, T. Gruber, C. Kirchner, and A. Waag, *Origin and consequences of a high stacking fault density in epitaxial ZnO layers*, Applied Physics Letters **81** (2002), 3972–3974.

[117] D. S. Ginley, H. Hosono, D. C. Paine, et al., *Handbook of transparent conductors*, (2010).

[118] D. Mergel and Z. Qiao, *Correlation of lattice distortion with optical and electrical properties of In2O3:Sn films*, Journal of Applied Physics **95** (2004), 5608–5615.

[119] B. D. Ahn, S. H. Oh, H. J. Kim, M. H. Jung, and Y. G. Ko, *Low temperature conduction and scattering behavior of Ga-doped ZnO*, Applied Physics Letters **91** (2007).

[120] V. Bhosle, A. Tiwari, and J. Narayan, *Electrical properties of transparent and conducting Ga doped ZnO*, Journal of Applied Physics **100** (2006).

[121] Z. Ovadyahu, *Nonequilibrium dephasing in two-dimensional indium oxide films*, Phys. Rev. B **63** (2001), 235403.

[122] E. Conwell and V. F. Weisskopf, *Theory of Impurity Scattering in Semiconductors*, Phys. Rev. **77** (1950), 388–390.

[123] H. Brooks, *Advances in electronics and electron physics*, Academic Press Inc., 1955.

[124] R. Dingle, *XCIV. Scattering of electrons and holes by charged donors and acceptors in semiconductors*, Philosophical Magazine Series 7 **46** (1955), 831–840.

[125] Y. Kajikawa, *Effects of grain-boundary potential barrier height and its fluctuation on conductivity of polycrystalline semiconductors in the ionized-impurity-scattering dominated case*, Journal of Applied Physics **114** (2013).

[126] G. Masetti, M. Severi, and S. Solmi, *Modeling of carrier mobility against carrier concentration in arsenic-, phosphorus-, and boron-doped silicon*, IEEE Transactions on Electron Devices **30** (1983), 764–769.

[127] D. C. Look, K. D. Leedy, L. Vines, B. G. Svensson, A. Zubiaga, F. Tuomisto, D. R. Doutt, and L. J. Brillson, *Self-compensation in semiconductors: The Zn vacancy in Ga-doped ZnO*, Phys. Rev. B **84** (2011), 115202.

[128] A. Janotti and C. G. Van de Walle, *Native point defects in ZnO*, Phys. Rev. B **76** (2007), 165202.

[129] D. C. Look, T. C. Droubay, and S. A. Chambers, *Stable highly conductive ZnO via reduction of Zn vacancies*, Applied Physics Letters **101** (2012).

[130] D. L. Young, T. J. Coutts, V. I. Kaydanov, A. S. Gilmore, and W. P. Mulligan, *Direct measurement of density-of-states effective mass and scattering parameter in transparent conducting oxides using second-order transport phenomena*, Journal of Vacuum Science & Technology A **18** (2000), 2978–2985.

[131] S. Cornelius, M. Vinnichenko, N. Shevchenko, A. Rogozin, A. Kolitsch, and W. Möller, *Achieving high free electron mobility in ZnO:Al thin films grown by reactive pulsed magnetron sputtering*, Applied Physics Letters **94** (2009).

[132] K. Ellmer and R. Mientus, *Carrier transport in polycrystalline ITO and ZnO:Al II: The influence of grain barriers and boundaries*, Thin Solid Films **516** (2008), 5829 – 5835.

[133] X. D. Liu, J. Liu, S. Chen, and Z. Q. Li, *Electrical transport properties of Al-doped ZnO films*, Applied Surface Science **263** (2012), 486 – 490.

[134] C. Agashe, O. Kluth, J. Hupkes, U. Zastrow, B. Rech, and M. Wuttig, *Efforts to improve carrier mobility in radio frequency sputtered aluminum doped zinc oxide films*, Journal of Applied Physics **95** (2004), 1911–1917.

[135] D. Zhang and H. Ma, *Scattering mechanisms of charge carriers in transparent conducting oxide films*, Applied Physics A **62** (1996), 487–492.

[136] J. Ziman, *Electrons and Phonons: The Theory of Transport Phenomena in Solids*, Oxford Classic Texts In The Physical Sciences, Oxford University Press, 2001.

[137] P. B. Allen, *Boltzmann Theory and Resistivity of Metals*, Quantum Theory of Real Metals (J. R. C. S. G. Louie, ed.), Kluwer Academic Publishers, 1996, pp. 219–250.

[138] B.-T. Lin, Y.-F. Chen, J.-J. Lin, and C.-Y. Wu, *Temperature dependence of resistance and thermopower of thin indium tin oxide films*, Thin Solid Films **518** (2010), 6997 – 7001.

[139] H. Y. Liu, V. Avrutin, N. Izyumskaya, . Özgür, A. B. Yankovich, A. V. Kvit, P. M. Voyles, and H. Morkoç, *Electron scattering mechanisms in GZO films grown on a-sapphire substrates by plasma-enhanced molecular beam epitaxy*, Journal of Applied Physics **111** (2012).

[140] T. Terasako, H. Song, H. Makino, S. Shirakata, and T. Yamamoto, *Temperature dependence of electrical properties of Ga-doped ZnO films deposited by ion plating with DC arc discharge*, Thin Solid Films **528** (2013), 19 – 25.

[141] A. Bikowski and K. Ellmer, *Analytical model of electron transport in polycrystalline, degenerately doped ZnO films*, Journal of Applied Physics **116** (2014).

[142] R. Stratton, *Volt-current characteristics for tunneling through insulating films*, Journal of Physics and Chemistry of Solids **23** (1962), 1177 – 1190.

[143] R. Stratton, *Theory of Field Emission from Semiconductors*, Phys. Rev. **125** (1962), 67–82.

[144] E. Rhoderick and R. Williams, *Metal-semiconductor Contacts*, Monographs in electrical and electronic engineering, Clarendon Press, 1988.

[145] C. Crowell and S. Sze, *Current transport in metal-semiconductor barriers*, Solid-State Electronics **9** (1966), 1035 – 1048.

[146] J. W. Orton and M. J. Powell, *The Hall effect in polycrystalline and powdered semiconductors*, Reports on Progress in Physics **43** (1980), 1263.

[147] G. Baccarani, B. Riccò, and G. Spadini, *Transport properties of polycrystalline silicon films*, Journal of Applied Physics **49** (1978), 5565–5570.

[148] J. H. Werner and H. H. Güttler, *Barrier inhomogeneities at Schottky contacts*, Journal of Applied Physics **69** (1991), 1522–1533.

[149] J. Werner, *Origin of curved Arrhenius plots for the conductivity of polycrystalline semiconductors*, Solid State Phenomena **37** (1994), 213–218.

[150] J. Oertel, K. Ellmer, W. Bohne, J. Röhrich, and H. Tributsch, *Growth of n-type polycrystalline pyrite (FeS2) films by metalorganic chemical vapour deposition and their electrical characterization*, Journal of Crystal Growth **198–199** (1999), 1205 – 1210.

[151] Y. Kajikawa, *Conduction model covering non-degenerate through degenerate polycrystalline semiconductors with non-uniform grain-boundary potential heights based on an energy filtering model*, Journal of Applied Physics **112** (2012).

[152] J. Bruneaux, H. Cachet, M. Froment, and A. Messad, *Correlation between structural and electrical properties of sprayed tin oxide films with and without fluorine doping*, Thin Solid Films **197** (1991), 129 – 142.

[153] A. P. Roth and D. F. Williams, *Properties of zinc oxide films prepared by the oxidation of diethyl zinc*, Journal of Applied Physics **52** (1981), 6685–6692.

[154] A. Kronenberger, A. Polity, D. M. Hofmann, B. K. Meyer, A. Schleife, and F. Bechstedt, *Structural, electrical, and optical properties of hydrogen-doped ZnO films*, Phys. Rev. B **86** (2012), 115334.

[155] M. V. GarciaCuenca, J. L. Morenza, and J. Esteve, *Electron tunneling in heavily In doped polycrystalline CdS films*, Journal of Applied Physics **56** (1984), 1738–1743.

[156] M. Ada-Hanifi, J. Sicart, J. M. Dusseau, and J. L. Robert, *A model of conduction in polycrystalline silicon films*, Journal of Applied Physics **62** (1987), 1869–1876.

[157] R. Holm, *The Electric Tunnel Effect across Thin Insulator Films in Contacts*, Journal of Applied Physics **22** (1951), 569–574.

[158] J. G. Simmons, *Generalized Formula for the Electric Tunnel Effect between Similar Electrodes Separated by a Thin Insulating Film*, Journal of Applied Physics **34** (1963), 1793–1803.

[159] J. G. Simmons, *Conduction in thin dielectric films*, Journal of Physics D: Applied Physics **4** (1971), 613.

[160] H. Kramers, *Wellenmechanik und halbzahlige Quantisierung*, Zeitschrift für Physik **39** (1926), 828–840.

[161] G. Wentzel, *Eine Verallgemeinerung der Quantenbedingungen für die Zwecke der Wellenmechanik*, Zeitschrift für Physik **38** (1926), 518–529.

[162] F. Padovani, *The Voltage–Current Characteristic of Metal–Semiconductor Contacts*, Applications and Devices (R. Willardson and A. C. Beer, eds.), Semiconductors and Semimetals, Vol. 7, Part A, Elsevier, 1971, pp. 75 – 146.

[163] A. Yu, *Electron tunneling and contact resistance of metal-silicon contact barriers*, Solid-State Electronics **13** (1970), 239 – 247.

[164] F. Padovani and R. Stratton, *Field and thermionic-field emission in Schottky barriers*, Solid-State Electronics **9** (1966), 695 – 707.

[165] C. Crowell and V. Rideout, *Normalized thermionic-field (T-F) emission in metal-semiconductor (Schottky) barriers*, Solid-State Electronics **12** (1969), 89 – 105.

[166] S. Y. Myong, J. Steinhauser, R. Schlüchter, S. Faÿ, E. Vallat-Sauvain, A. Shah, C. Ballif, and A. Rüfenacht, *Temperature dependence of the conductivity in large-grained boron-doped ZnO films*, Solar Energy Materials and Solar Cells **91** (2007), 1269 – 1274.

[167] J. I. Kim, W. Lee, T. Hwang, J. Kim, S.-Y. Lee, S. Kang, H. Choi, S. Hong, H. H. Park, T. Moon, and B. Park, *Quantitative analyses of damp-heat-induced degradation in transparent conducting oxides*, Solar Energy Materials and Solar Cells **122** (2014), 282 – 286.

[168] T. Tohsophon, J. Hüpkes, S. Calnan, W. Reetz, B. Rech, W. Beyer, and N. Sirikulrat, *Damp heat stability and annealing behavior of aluminum doped zinc oxide films prepared by magnetron sputtering*, Thin Solid Films **511–512** (2006), 673 – 677.

[169] E. M. Likovich, R. Jaramillo, K. J. Russell, S. Ramanathan, and V. Narayanamurti, *Scanning tunneling microscope investigation of local density of states in Al-doped ZnO thin films*, Phys. Rev. B **83** (2011), 075430.

[170] J. Hinze and K. Ellmer, *In situ measurement of mechanical stress in polycrystalline zinc-oxide thin films prepared by magnetron sputtering*, Journal of Applied Physics **88** (2000), 2443–2450.

[171] M. Suchea, S. Christoulakis, N. Katsarakis, T. Kitsopoulos, and G. Kiriakidis, *Comparative study of zinc oxide and aluminum doped zinc oxide transparent*

thin films grown by direct current magnetron sputtering, Thin Solid Films **515** (2007), 6562 – 6566.

[172] L. Ding, M. Boccard, G. Bugnon, M. Benkhaira, S. Nicolay, M. Despeisse, F. Meillaud, and C. Ballif, *Highly transparent ZnO bilayers by LP-MOCVD as front electrodes for thin-film micromorph silicon solar cells*, Solar Energy Materials and Solar Cells **98** (2012), 331 – 336.

[173] M. Copel, M. C. Reuter, E. Kaxiras, and R. M. Tromp, *Surfactants in epitaxial growth*, Phys. Rev. Lett. **63** (1989), 632–635.

[174] J. Massies and N. Grandjean, *Surfactant effect on the surface diffusion length in epitaxial growth*, Phys. Rev. B **48** (1993), 8502–8505.

[175] D. Kandel and E. Kaxiras, *Surfactant Mediated Crystal Growth of Semiconductors*, Phys. Rev. Lett. **75** (1995), 2742–2745.

[176] M. Warzecha, *Zinkoxid: Einfluss von Dotierung und Legierungen auf elektrooptische Eigenschaften, auf das Ätzverhalten und auf die Tempernachbehandlung*, Ph.D. thesis, RWTH Aachen University, 2014.

[177] C. Charpentier, P. Prod'homme, and P. R. i Cabarrocas, *Microstructural, optical and electrical properties of annealed ZnO:Al thin films*, Thin Solid Films **531** (2013), 424 – 429.

[178] Y. Kim, W. Lee, D.-R. Jung, J. Kim, S. Nam, H. Kim, and B. Park, *Optical and electronic properties of post-annealed ZnO:Al thin films*, Applied Physics Letters **96** (2010).

[179] C. Roy, S. Byrne, E. McGlynn, J.-P. Mosnier, E. de Posada, D. O'Mahony, J. Lunney, M. Henry, B. Ryan, and A. Cafolla, *Correlation of Raman and X-ray diffraction measurements of annealed pulsed laser deposited ZnO thin films*, Thin Solid Films **436** (2003), 273 – 276.

[180] S. Ghosh, A. Sarkar, S. Bhattacharya, S. Chaudhuri, and A. Pal, *Microstructure of ZnO films produced by reactive DC sputtering technique*, Journal of Crystal Growth **108** (1991), 534 – 540.

[181] B.-Y. Oh, M.-C. Jeong, and J.-M. Myoung, *Stabilization in electrical characteristics of hydrogen-annealed ZnO:Al films*, Applied Surface Science **253** (2007), 7157 – 7161.

[182] M. Wimmer, F. Ruske, S. Scherf, and B. Rech, *Improving the electrical and optical properties of DC-sputtered ZnO:Al by thermal post deposition treatments*, Thin Solid Films **520** (2012), 4203 – 4207.

[183] K.-K. Kim, H. Tampo, J.-O. Song, T.-Y. Seong, S.-J. Park, J.-M. Lee, S.-W. Kim, S. Fujita, and S. Niki, *Effect of Rapid Thermal Annealing on Al Doped n-ZnO Films Grown by RF-Magnetron Sputtering*, Japanese Journal of Applied Physics **44** (2005), 4776–4779.

[184] E. Johnson, P. Prod'homme, C. Boniface, K. Huet, T. Emeraud, and P. R. i Cabarrocas, *Excimer laser annealing and chemical texturing of ZnO:Al sputtered at room temperature for photovoltaic applications*, Solar Energy Materials and Solar Cells **95** (2011), 2823 – 2830.

[185] Q. Xu, R. Hong, H. Huang, Z. Zhang, M. Zhang, X. Chen, and Z. Wu, *Laser annealing effect on optical and electrical properties of Al doped ZnO films*, Optics & Laser Technology **45** (2013), 513 – 517.

[186] E. Schumann, *Entwicklung eines Laserprozesses zur gezielten Veränderung elektrooptischer Eigenschaften von Zinkoxid*, Master's thesis, RWTH Aachen University, 2012.

[187] N. Ohta, D. Ohba, S. Sato, Z. Tang, H. Shimizu, and H. Shirai, *Rapid thermal-plasma annealing of ZnO:Al films for silicon thin-film solar cells*, Thin Solid Films **519** (2011), 6920 – 6927.

[188] T. C. Damen, S. P. S. Porto, and B. Tell, *Raman Effect in Zinc Oxide*, Phys. Rev. **142** (1966), 570–574.

[189] N. Ashkenov, B. N. Mbenkum, C. Bundesmann, V. Riede, M. Lorenz, D. Spemann, E. M. Kaidashev, A. Kasic, M. Schubert, M. Grundmann, G. Wagner, H. Neumann, V. Darakchieva, H. Arwin, and B. Monemar, *Infrared dielectric functions and phonon modes of high-quality ZnO films*, Journal of Applied Physics **93** (2003), 126–133.

[190] F. J. Manjón, B. Marí, J. Serrano, and A. H. Romero, *Silent Raman modes in zinc oxide and related nitrides*, Journal of Applied Physics **97** (2005).

[191] M. Tzolov, N. Tzenov, D. Dimova-Malinovska, M. Kalitzova, C. Pizzuto, G. Vitali, G. Zollo, and I. Ivanov, *Vibrational properties and structure of undoped and Al-doped ZnO films deposited by RF magnetron sputtering*, Thin Solid Films **379** (2000), 28 – 36.

[192] C. Charpentier, P. Prod'homme, I. Maurin, M. Chaigneau, and P. R. i Cabarrocas, *X-Ray diffraction and Raman spectroscopy for a better understanding of ZnO:Al growth process*, EPJ Photovolt. **2** (2011), 25002.

[193] I. Lorite, L. Villaseca, P. Díaz-Carrasco, M. Gabás, and J. L. Costa-Krämer, *Doping, carriers and intergrain fields in ZnO films: An impedance and confocal Raman spectroscopy study*, Thin Solid Films **548** (2013), 657 – 660.

[194] C. Bundesmann, N. Ashkenov, M. Schubert, D. Spemann, T. Butz, E. M. Kaidashev, M. Lorenz, and M. Grundmann, *Raman scattering in ZnO thin films doped with Fe, Sb, Al, Ga, and Li*, Applied Physics Letters **83** (2003), 1974–1976.

[195] J. M. Calleja and M. Cardona, *Resonant Raman scattering in ZnO*, Phys. Rev. B **16** (1977), 3753–3761.

[196] P. Emelie, J. Phillips, B. Buller, and U. Venkateswaran, *Free carrier absorption and lattice vibrational modes in bulk ZnO*, Journal of Electronic Materials **35** (2006), 525–529.

[197] O. Lupan, T. Pauporté, L. Chow, B. Viana, F. Pellé, L. Ono, B. R. Cuenya, and H. Heinrich, *Effects of annealing on properties of ZnO thin films prepared by electrochemical deposition in chloride medium*, Applied Surface Science **256** (2010), 1895 – 1907.

[198] M. Gabás, P. Díaz-Carrasco, F. Agulló-Rueda, P. Herrero, A. Landa-Cánovas, and J. Ramos-Barrado, *High quality ZnO and Ga:ZnO thin films grown onto crystalline Si by RF magnetron sputtering*, Solar Energy Materials and Solar Cells **95** (2011), 2327 – 2334.

[199] S. Neubert, S. Ring, F. Welker, S. Götzendörfer, F. Ruske, B. Stannowski, R. Schlatmann, and B. Rech, *Very thin, highly-conductive ZnO:Al front electrode on textured glass as substrate for thin-film silicon solar cells*, physica status solidi (RRL) – Rapid Research Letters (2013).

[200] J. Wang, S. Venkataraj, C. Battaglia, P. Vayalakkara, and A. G. Aberle, *Analysis of Optical and Morphological Properties of Aluminium Induced Texture Glass Superstrates*, Japanese Journal of Applied Physics **51** (2012), 10NB08.

[201] P. Reinhard, A. Chirila, P. Blosch, F. Pianezzi, S. Nishiwaki, S. Buechelers, and A. Tiwari, *Review of Progress Toward 20%; Efficiency Flexible CIGS*

Solar Cells and Manufacturing Issues of Solar Modules, IEEE Journal of Photovoltaics **3** (2013), 572–580.

[202] J. Nieuwenhuizen and H. Haanstra, *Microfractography of thin films*, Philips Tech Rev **27** (1966), 87–91.

[203] S. Lichter and J. Chen, *Model for Columnar Microstructure of Thin Solid Films*, Phys. Rev. Lett. **56** (1986), 1396–1399.

[204] R. Tait, T. Smy, and M. Brett, *Modelling and characterization of columnar growth in evaporated films*, Thin Solid Films **226** (1993), 196 – 201.

[205] Y. E. Lee, S. G. Kim, H. Joon Kim, and H. J. Kim, *Effect of oblique sputtering on microstructural modification of ZnO thin films*, Journal of Vacuum Science Technology A: Vacuum, Surfaces, and Films **15** (1997), 1194–1199.

[206] S. Mukhtar, A. Asadov, and W. Gao, *Microstructure of ZnO thin films produced by magnetron sputter oblique deposition*, Thin Solid Films **520** (2012), 3453 – 3457.

[207] J. Leem and J. Yu, *Structural, optical, and electrical properties of AZO films by tilted angle sputtering method*, Thin Solid Films **518** (2010), 6285 – 6288.

[208] Y. Sato, K. Yanagisawa, N. Oka, S.-i. Nakamura, and Y. Shigesato, *Sputter deposition of Al-doped ZnO films with various incident angles*, Journal of Vacuum Science Technology A: Vacuum, Surfaces, and Films **27** (2009), 1166–1171.

[209] J. I. Owen, W. Zhang, D. Köhl, and J. Hüpkes, *Study on the in-line sputtering growth and structural properties of polycrystalline ZnO:Al on ZnO and glass*, Journal of Crystal Growth **344** (2012), 12 – 18.

[210] C. Eisenmenger-Sittner, A. Bergauer, H. Bangert, and W. Bauer, *Measurement of the angular distribution of sputtered neutrals in a planar magnetron geometry*, Journal of Vacuum Science & Technology A **12** (1994), 536–541.

[211] M. Horkel, K. V. Aeken, C. Eisenmenger-Sittner, D. Depla, S. Mahieu, and W. P. Leroy, *Experimental determination and simulation of the angular distribution of the metal flux during magnetron sputter deposition*, Journal of Physics D: Applied Physics **43** (2010), 075302.

[212] V. Sittinger, F. Ruske, W. Werner, B. Szyszka, B. Rech, J. Hüpkes, G. Schöpe, and H. Stiebig, *ZnO:Al films deposited by in-line reactive AC magnetron sputtering for a-Si:H thin film solar cells*, Thin Solid Films **496** (2006), 16 – 25.

[213] M. Python, E. Vallat-Sauvain, J. Bailat, D. Dominé, L. Fesquet, A. Shah, and C. Ballif, *Relation between substrate surface morphology and microcrystalline silicon solar cell performance*, Journal of Non-Crystalline Solids **354** (2008), 2258 – 2262.

[214] M. Addonizio and A. Antonaia, *Surface morphology and light scattering properties of plasma etched ZnO:B films grown by LP-MOCVD for silicon thin film solar cells*, Thin Solid Films **518** (2009), 1026 – 1031.

[215] J. Bailat, D. Domine, R. Schluchter, J. Steinhauser, S. Fay, F. Freitas, C. Bucher, L. Feitknecht, X. Niquille, T. Tscharner, A. Shah, and C. Ballif, *High-Efficiency P-I-N Microcrystalline and Micromorph Thin Film Silicon Solar Cells Deposited on LPCVD ZnO Coated Glass Substrates*, Conference Record of the 2006 IEEE 4th World Conference on Photovoltaic Energy Conversion, Vol. 2, 2006, pp. 1533–1536.

[216] U. W. Paetzold, W. Zhang, M. Prömpers, J. Kirchhoff, T. Merdzhanova, S. Michard, R. Carius, A. Gordijn, and M. Meier, *Thin-film silicon solar cell development on imprint-textured glass substrates*, Materials Science and Engineering: B **178** (2013), 617 – 622.

[217] M. Meier, U. Paetzold, M. Ghosh, W. Zhang, T. Merdzhanova, G. Jost, N. Sommer, S. Michard, and A. Gordijn, *Fabrication of Light-Scattering Multiscale Textures by Nanoimprinting for the Application to Thin-Film Silicon Solar Cells*, IEEE Journal of Photovoltaics **4** (2014), 772–777.

[218] D. A. G. Bruggeman, *Berechnung verschiedener physikalischer Konstanten von heterogenen Substanzen. I. Dielektrizitätskonstanten und Leitfähigkeiten der Mischkörper aus isotropen Substanzen*, Annalen der Physik **416** (1935), 636–664.

[219] A. Gordijn, S. Schicho, S. Muthmann, T. Kilper, H. Zhu, E. Bunte, and J. Hüpkes, *Significantly decreased production times for a-Si/µc-Si tandem cells on texture-etched ZnO:Al*, physica status solidi (a) **207** (2010), 678–681.

Glossary

Common Abbreviations

Acronym	Meaning
µc-Si:H	hydrogenated, microcrystalline silicon
a-Si:H	hydrogenated, amorphous silicon
ac	alternating current
AFM	atomic force microscopy
Al_2O_3	aluminum oxide
BB	Bragg-Brentano
CdS:In	indium-doped cadmium sulfide
DARS	disorder-activated Raman scattering
dc	direct current
E-AZO	etched aluminum doped zinc oxide
EFIRS	electric field induced Raman scattering
eGB	extended grain boundary
EQE	external quantum efficiency
FE	field emission
FWHM	full width at half maximum
GB	grain boundary
GBRM	grain boundary relaxation model
HCl	hydrochloric acid
HF	hydrofluoric acid
HHCL	height-height correlation length
IEK-5	Institut für Energie- und Klimaforschung 5
ii	ionized impurity
In_2O_3:Sn	tin-doped indium oxid
KOH	potassium hydroxide
LPCVD	low pressure chemical vapour deposition
mpp	maximum power point
mf	mid-frequency
NIR	near infrared
PECVD	plasma enhanced chemical vapor deposition
ph	electron-phonon

PLD	pulsed laser deposition
PPMS	physical property measurement system
rf	radio frequency (13.56 MHz)
RC	rocking curve
RT	room temperature
sccm	standard cubic centimeter per minute
SEM	scanning electron microscopy
SIMS	secondary ion mass spectroscopy
SiO_2	silicon oxide
SnO_2:F	fluorine-doped tin oxid
SR	spectral response
TCO	transparent conductive oxide
TDC	target doping concentration
TE	thermionic emission
TFE	thermionic field emission
UV	ultraviolet
XRD	x-ray diffraction
ZnO:Al	aluminum-doped zinc oxide
ZnO:B	boron-doped zinc oxide
ZnO:Ga	gallium-doped zinc oxide

Formula Abbreviations

Symbol	Description
a_0	unstrained lattice spacing in xy-direction
A	absorptance, area
A^*	Richardson constant
$\vec{B}$	magnetic field
b_1, c_1, f_1	field emission coefficients
b_m, c_m, f_m	thermionic field emission coefficients
c_0	speed of light in vacuum
C	non-parabolicity parameter of non-parabolic conduction band
d	thickness
d_0	unstrained lattice spacing in z-direction
d_{xy}	lattice spacing parallel to the substrate
d_{z}	lattice spacing perpedicular to the substrate
$\vec{D}$	electric displacement field

e	elementary charge
E	Young modulus
$\vec{E}$	electric field
$\widetilde{E}$	parameter in field emission theory
E_{00}	field emission (tunneling) constant
E_{B}	barrier height
E_{C}	conduction band energy
E_{F}	Fermi energy
E_{g}	band gap energy
E_{m}	specific energy for thermionic field emission
E_{photon}	energy of incident light
E_{V}	valence band energy
FF	fill factor
h	Planck constant
I	current
j	current density
j_0	dark saturation current density
j_{sc}	short circuit current density
k	wave vector
k_{B}	Boltzmann constant
K	compensation ratio
L	grain size
m^*	effective mass
m_0^*	effective mass at the bottom of the conduction band
n	charge carrier concentration
$n_{\mathrm{A}}, n_{\mathrm{D}}$	acceptor, donor concentration
n_{op}	refractive index
$\widetilde{n}_{\mathrm{op}}$	complex index of refraction
N_{c}	effective density of states in the conduction band
p	pressure
P	power, polarization, probability
Q_{t}	trap density at grain boundary
$Q_{\mathrm{t0}}, C_{\mathrm{t}}$	parameters to determine trap density at grain boundary
r_0	ionic radius
$r_{\mathrm{curv}}^{\mathrm{thr}}$	curvature threshold
R	resistance, reflectance
R_{eGB}	sheet resistance of extended grain boundaries
R_{sh}	sheet resistance

t	time
T	temperature, transmittance
u	amplitude of harmonic oscillator
V	volume
V_H	Hall voltage
V_{oc}	open circuit voltage
v_{D}	effective diffusion velocity
v_{ph}	phase velocity
$\bar{v}$	average thermal velocity
$Z_{\mathrm{D}}, Z_{\mathrm{A}}$	donor, acceptor charge

Greek symbols

Symbol	Description
α	thermal expansion coefficient, constant in field emission theory
α_{op}	absorption coefficient
Γ	damping constant of harmonic oscillator
Γ_{Dr}	damping constant of Drude model
Γ_{H}	high-frequency damping factor of extended Drude model
Γ_{L}	low-frequency damping factor of extended Drude model
$\Gamma_{\Gamma\mathrm{Dr}}$	function width of extended Drude model
ϵ	dielectric function, permittivity
ϵ'	real part of dielectric function, permittivity
ϵ''	imaginary part of dielectric function, permittivity
ϵ_0	dielectric constant, vacuum permittivity
ϵ_r	static dielectric constant
η	efficiency
Θ	Debye temperature
κ	extinction coefficient
λ	wavelength
λ_{tr}	electron-phonon coupling constant
μ	charge carrier mobility
μ_{op}	charge carrier mobility obtained by optical fits
μ^{M}	magnetic permeability
μ_0^{M}	vacuum permeability
ν	frequency, Poisson ratio, Raman shift
ρ	resistivity

σ	electric conductivity, biaxial stress
ω	angular frequency
Ω_{Dr}	plasma frequency
$\Omega_{\Gamma\mathrm{Dr}}$	changeover frequency of extended Drude model
Ω_0	eigenfrequency of non-damped oscillator
Φ	barrier potential
χ	electric susceptibility

List of Figures

List of Tables

A. Appendix

A.1. Field Emission: Evaluation of coefficients

The evaluation of coefficients b_1, c_1, f_1 needs the definition of the barrier $\phi(x)$. Using the abrupt depletion approximation, a simple parabolic expression for the Schottky barrier potential

$$\begin{aligned} \phi(x) &= a\,(x-l)^2 \\ \text{with} \qquad a &= \frac{e^2 n}{2\epsilon_0 \epsilon_\mathrm{r}} \\ l &= \left[\frac{2\epsilon_0\epsilon_\mathrm{r}}{e^2 n}(E_\mathrm{B} - eV + E_\mathrm{F})\right]^{1/2} \end{aligned} \tag{A.1}$$

can be given. n is the carrier concentration, e is the electron charge, and ϵ_0 and ϵ_r are the static dielectric constant and the vacuum permittivity. l describes the width of the depletion zone. It is defined by the barrier height E_B, the Fermi level E_F, and the applied voltage V. The abrupt depletion approximation assumes the carrier density to fall abruptly from the density in the bulk to a negligible value in the depletion zone. This simplification might be too drastic in the degenerate case as also pointed out by Padovani and Stratton [164].

The coefficient b_1 is defined as

$$b_1 = \alpha \int_{x_1}^{x_2} (\phi(x) - E_\mathrm{F})^{1/2} \mathrm{d}x \tag{A.2}$$

with $\alpha = 2(2m^*)^{1/2}/\hbar$. The condition $\phi = E_\mathrm{F}$ yields x_1, x_2. Inserting ϕ into

Eq. (A.2) and performing a hyperbolic substitution gives

$$\begin{aligned} b_1 &= -\frac{\alpha E_\mathrm{F}}{\sqrt{a}} \int_{w_1}^{w_2} (\sinh(w))^2 \,\mathrm{d}w \\ \text{with} \qquad w_1 &= 0 \\ w_2 &= \operatorname{arccosh}\left(\sqrt{\frac{a}{E_\mathrm{F}}} l\right). \end{aligned} \tag{A.3}$$

The antiderivative of this integral is $1/2(\sinh(w)\cosh(w) - w)$. One defines

$$\widetilde{E} = \frac{E_\mathrm{B} - eV}{E_\mathrm{F}} \tag{A.4}$$

$$E_{00} = \frac{2e}{\alpha}\sqrt{\frac{n}{2\epsilon_0 \epsilon_\mathrm{r}}} = \frac{\hbar}{2}\sqrt{\frac{n}{\epsilon_0 \epsilon_\mathrm{r} m^*}} \tag{A.5}$$

and obtains

$$b_1 = 2\,\frac{E_\mathrm{F}}{E_{00}}\left[\sqrt{\widetilde{E}^2 + \widetilde{E}} - \ln\left(\sqrt{\widetilde{E}+1} + \sqrt{\widetilde{E}}\right)\right]. \tag{A.6}$$

As the integral in Eq. (A.2) is axially symmetric with respect to the energy axis, b_1 for a double Schottky barrier is just twice the value of a simple Schottky barrier. Hence, one finds a factor 2 in Eq. (A.6).

The coefficient c_1 is defined as

$$c_1 = \frac{1}{2}\,\alpha \int_{x_1}^{x_2} (\phi(x) - E_\mathrm{F})^{-1/2} \mathrm{d}x. \tag{A.7}$$

A hyperbolic substitution results in the expression

$$\begin{aligned} c_1 &= \frac{\alpha}{2\sqrt{a}} \int_{w_1}^{w_2} w \,\mathrm{d}w \\ \text{with} \qquad w_1 &= \operatorname{arccosh}\left(\sqrt{\frac{a}{E_\mathrm{F}}} l\right) \\ w_2 &= 0. \end{aligned} \tag{A.8}$$

The evaluation of the integral leads to

$$c_1 = 2\,\frac{1}{E_{00}}\,\ln\left(\sqrt{\widetilde{E}+1}+\sqrt{\widetilde{E}}\right) \tag{A.9}$$

with the factor 2 for a double Schottky barrier.

The coefficient f_1 is defined as

$$\begin{aligned} f_1 = \frac{\alpha}{4}\Bigg[& \overbrace{\frac{1}{x_2-x_1}\left\{\frac{1}{\phi'(x_1)}-\frac{1}{\phi'(x_2)}\right\}\int_{x_1}^{x_2}(\phi(x)-E_\mathrm{F})^{-1/2}\,\mathrm{d}x}^{\equiv f_{11}} \\ & \underbrace{-\frac{1}{2}\int_{x_1}^{x_2}(\phi(x)-E_\mathrm{F})^{-3/2}\left\{1-\frac{\phi'(x)}{x_2-x_1}\left(\frac{x-x_1}{\phi'(x_2)}+\frac{x_2-x}{\phi'(x_1)}\right)\right\}\mathrm{d}x}_{\equiv f_{12}}\Bigg]. \end{aligned} \tag{A.10}$$

The upper part f_{11} of Eq. (A.10) can be solved easily as the integral resembles the one of c_1. The result is

$$f_{11} \approx \frac{1}{4E_\mathrm{F}\sqrt{a(\widetilde{E}+1)}}\,\ln(4\widetilde{E}). \tag{A.11}$$

Note that the approximation

$$\ln\left(\sqrt{\widetilde{E}+1}+\sqrt{\widetilde{E}}\right) \approx \ln(4\widetilde{E}) \tag{A.12}$$

was used. The lower part f_{12} of Eq. (A.10) consists of the difference between two diverging integrals. Stratton circumvented this problem by introducing a special linear transformation [142]. Here, the obstacle was removed by solving the expression

$$\begin{aligned} f_{12} &= \int_{x_1}^{x_2}\{...\} = \lim_{\bar{x}\to x_2}\int_{x_1}^{\bar{x}}\{...\} \\ &= \frac{\sqrt{\widetilde{E}}-\frac{1}{2}\ln(4\widetilde{E})}{2E_\mathrm{F}\sqrt{a(\widetilde{E}+1)}} \end{aligned} \tag{A.13}$$

with the mathematical software tool *Mathematica* from *Wolfram Research*. The

combination of Eqs. (A.11) and (A.13) yields

$$\begin{aligned} f_1 &= 2\,\frac{1}{4E_{00}E_\mathrm{F}}\sqrt{\frac{\widetilde{E}}{\widetilde{E}+1}} \\ &= 2\,\frac{1}{4E_{00}E_\mathrm{F}}\sqrt{\frac{E_\mathrm{B}-eV}{E_\mathrm{B}-eV+E_\mathrm{F}}}. \end{aligned} \tag{A.14}$$

Again, the factor 2 marks the difference between a simple and a double Schottky barrier.

Eq. (A.14) differs from the expression

$$f_1 = 2\,\frac{1}{4E_{00}E_\mathrm{F}}\sqrt{\frac{E_\mathrm{B}}{E_\mathrm{B}-E_\mathrm{F}}} \tag{A.15}$$

given by Padovani [162]. Two reasons favor our result: (1) Let us assume a Schottky barrier with a highly doped semiconductor. In that case, it holds that $k_\mathrm{B}T/E_{00} \ll 1$. Thus, field emission should be the dominant transport mechanism. Furthermore, I assume that E_F measured with respect to the conduction band is large, and that E_B measured with respect to the Fermi level is small. In particular, $E_\mathrm{B} < E_\mathrm{F}$ might occur. Using Padovani's expression, this situation would imply that f_1 is not defined. In consequence, the inequality $1 > k_\mathrm{B}T(\sqrt{2f_1}+c_1)$ can not be computed. But that would be a contradiction as the inequality relation must be fulfilled in the case of field emission. (2) A situation as described above occurs if one chooses $n = 2\times10^{20}\,\mathrm{cm}^{-3}$ and $Q_\mathrm{t} = 7\times10^{13}\,\mathrm{cm}^{-2}$. It yields $E_\mathrm{F} = 459\,\mathrm{meV}$ and $E_\mathrm{B} = 206\,\mathrm{meV}$, thus $E_\mathrm{B} < E_\mathrm{F}$. We solved Eq. A.10 numerically for the above given parameters using the *scipy* package of *Python*. We obtained a perfect agreement between the numerical result and Eq. A.14.

For $E_\mathrm{B} \gg E_\mathrm{F}$ and small applied voltages, Eqs. (A.6), (A.9), and (A.14) can be simplified to

$$b_1 = 2\,\frac{E_\mathrm{B}-eV}{E_{00}} \tag{A.16}$$

$$c_1 = 2\,\frac{1}{2E_{00}}\ln\left(4\widetilde{E}\right) \tag{A.17}$$

$$f_1 = 2\,\frac{1}{4E_{00}E_\mathrm{F}}. \tag{A.18}$$

These expressions, except for the factor 2, have been given by Padovani and Stratton for simple Schottky barriers in their publication [164].

A.2. Field emission: Fluctuating barriers

Fluctuating barriers shall be implemented into the tunneling equations according to the approach by Werner for thermionic emission outlined in Section 4.1.3.1 [148]. The current density J_{FE} is multiplied with a Gaussian distribution $P(E_{\mathrm{B}})$ resembling the barrier fluctuations. This expression is then integrated over the barrier energy E_{B}. One obtains the expression for the conductivity

$$\begin{aligned}\sigma_{\mathrm{FE}}^{\mathrm{f}}(\bar{E}_{\mathrm{B}},\tilde{\sigma}_{\mathrm{B}}) &= L\frac{\mathrm{d}}{\mathrm{d}V}\int\limits_{-\infty}^{\infty} J_{\mathrm{FE}}(E_{\mathrm{B}})P(E_{\mathrm{B}})\mathrm{D}E_{\mathrm{B}} = L\int\limits_{-\infty}^{\infty}\frac{\mathrm{d}J(E_{\mathrm{B}})}{\mathrm{d}V}P(E_{\mathrm{B}})\mathrm{D}E_{\mathrm{B}} \\ &= \int\limits_{-\infty}^{\infty}\sigma_{\mathrm{FE}}(E_{\mathrm{B}})P(E_{\mathrm{B}})\mathrm{d}E_{\mathrm{B}}\end{aligned} \tag{A.19}$$

by interchanging derivation and integration. $\sigma_{\mathrm{FE}}(E_{\mathrm{B}})$ is described by Eq. (4.28). It is repeated here for completeness.

$$\sigma_{\mathrm{FE}} = \frac{eLA^{*}\pi\, T}{k_{\mathrm{B}}\sin\left(\pi c_1 k_{\mathrm{B}}T\right)}\exp\left(-b_1\right) - \frac{eLA^{*}c_1}{(c_1k_{\mathrm{B}})^2}\exp\left(-b_1 - c_1E_{\mathrm{F}}\right). \tag{A.20}$$

The exponential functions as well as their prefactors contain the integration variable E_{B}. However, the exponential functions will be considered for the integration only. In the prefactors, one defines $E_{\mathrm{B}} = \bar{E}_{\mathrm{B}}$. The integrals to solve are thus

$$\int\limits_{-\infty}^{\infty}\exp\Big(\underbrace{-b_1}_{\equiv e_1}\Big)P(E_{\mathrm{B}})\mathrm{d}E_{\mathrm{B}} \qquad \text{and} \qquad \int\limits_{-\infty}^{\infty}\exp\Big(\underbrace{-b_1 - c_1E_{\mathrm{F}}}_{\equiv e_2}\Big)P(E_{\mathrm{B}})\mathrm{d}E_{\mathrm{B}}. \tag{A.21}$$

The expressions e_1 and e_2 have to be simplified in order to perform the integration because these expressions contain the parameters b_1 and c_1 which are rather complex functions of the integration variable E_{B}. Fits using the uniform barrier height model yield values $\tilde{E} < 1$. Therefore, $\tilde{E} \ll 1$ will be assumed for the approximation of e_1 and e_2.

First, the expression

$$e_1 = -b_1 = -2\frac{E_{\mathrm{F}}}{E_{00}}\Bigg[\underbrace{\sqrt{\tilde{E}^2+\tilde{E}}}_{\approx\sqrt{\tilde{E}}} - \underbrace{\ln\left(\sqrt{\tilde{E}+1}+\sqrt{\tilde{E}}\right)}_{\equiv(\star)}\Bigg] \tag{A.22}$$

will be estimated. The term $(\star)$ can be further simplified

$$\begin{aligned}(\star) &= \ln\left\{\sqrt{\widetilde{E}+1}+\sqrt{\widetilde{E}}\right\}\\ &= \ln\left\{\sqrt{\left(\sqrt{\widetilde{E}+1}+\sqrt{\widetilde{E}}\right)^2}\right\}\\ &= \ln\left\{\sqrt{\widetilde{E}+1+2\sqrt{\widetilde{E}^2+\widetilde{E}}+\widetilde{E}}\right\}\\ &\approx \ln\left\{\sqrt{2\sqrt{\widetilde{E}}+1}\right\}\\ &= \frac{1}{2}\ln\left\{2\sqrt{\widetilde{E}}+1\right\}\\ &\approx \frac{1}{2}\left(2\sqrt{\widetilde{E}}-\frac{4\widetilde{E}}{2}\right)\\ &= \sqrt{\widetilde{E}}-\widetilde{E}\end{aligned} \tag{A.23}$$

by taking the square and the square root in the argument of the logarithm and using the relation $\ln\left(x^{1/2}\right) = 1/2\ln\left(x\right)$. Furthermore, one can expand the logarithm into a power series according to the expression $\ln\left(x+1\right) \approx x - x^2/2$. The power series converges for $|x| < 1$. Accordingly, the boundary condition for Eq. (A.23) is $\widetilde{E} < 1/4$. Inserting Eq. (A.23) into Eq. (A.22), one obtains

$$e_1 = -b_1 = -2\,\frac{E_\mathrm{F}}{E_{00}}\left[\sqrt{\widetilde{E}}-\sqrt{\widetilde{E}}+\widetilde{E}\right] = -2\,\frac{E_\mathrm{F}}{E_{00}}\widetilde{E} = -2\,\frac{E_\mathrm{B}}{E_{00}}. \tag{A.24}$$

The relation $\widetilde{E} = E_\mathrm{B}/E_\mathrm{F}$ was used for the last transformation. Finally, a numerical comparison of the full and approximated expression for e_1 reveals that the best agreement is achieved by

$$e_1 = -b_1 = -\frac{E_\mathrm{B}}{2E_{00}}. \tag{A.25}$$

Next, the expression e_2 has to be evaluated for $\widetilde{E} \ll 1$. The approximation is

$$\begin{aligned} e_2 =& - b_1 - c_1 E_\mathrm{F} \\ =& - 2\,\frac{E_\mathrm{F}}{E_{00}}\left[\sqrt{\widetilde{E}^2+\widetilde{E}} - \ln\left(\sqrt{\widetilde{E}+1}+\sqrt{\widetilde{E}}\right)\right] - 2\,\frac{E_\mathrm{F}}{E_{00}}\left[\ln\left(\sqrt{\widetilde{E}+1}+\sqrt{\widetilde{E}}\right)\right] \\ =& - 2\frac{E_\mathrm{F}}{E_{00}}\sqrt{\widetilde{E}^2+\widetilde{E}} \\ \approx& - 2\,\frac{E_\mathrm{F}}{E_{00}}\sqrt{\widetilde{E}} \\ =& - 2\,\frac{E_\mathrm{F}}{E_{00}}\sqrt{\frac{E_\mathrm{B}}{E_\mathrm{F}}} \end{aligned} \tag{A.26}$$

Inserting Eqs. (A.25) and (A.26) into Eq. (A.21) yields

$$\int_{-\infty}^{\infty} \exp\left(-\frac{E_\mathrm{B}}{2E_{00}}\right) P(E_\mathrm{B})\mathrm{d}E_\mathrm{B} \tag{A.27}$$

and

$$\int_{-\infty}^{\infty} \exp\left(-2\,\frac{E_\mathrm{F}}{E_{00}}\sqrt{\frac{E_\mathrm{B}}{E_\mathrm{F}}}\right) P(E_\mathrm{B})\mathrm{d}E_\mathrm{B}. \tag{A.28}$$

The integrand of Eq. (A.28) is not defined for $E_\mathrm{B} < 0$. Therefore, the integral (A.28) cannot be solved. In contrast, integral (A.27) is solvable. One obtains the expression

$$\int_{-\infty}^{\infty} \exp\left(-\frac{E_\mathrm{B}}{2E_{00}}\right) P(E_\mathrm{B})\mathrm{d}E_\mathrm{B} = \exp\left\{-\frac{1}{2E_{00}}\left(\bar{E}_\mathrm{B} - \frac{\tilde{\sigma}_\mathrm{B}^2}{4E_{00}}\right)\right\} \tag{A.29}$$

with $\tilde{\sigma}_\mathrm{B}$ being the standard deviation around the mean value $\bar{E}_\mathrm{B}$.

The comparison of the first and second summand of Eq. (A.20) reveals the first summand to be roughly one order of magnitude larger than the second one. Potential fluctuations might thus be neglected in the second term. This assumption is beneficial because the second summand contained the integral that was analytically unsolvable. The final equation describing tunneling through fluctuating barriers is thus given

by

$$\sigma_{\mathrm{FE}}^{\mathrm{f}} = \frac{eLA^{*}\pi\, T}{k_{\mathrm{B}} \sin\left(\pi \bar{c}_1 k_{\mathrm{B}} T\right)} \exp\left\{-\frac{1}{2E_{00}}\left(\bar{E}_{\mathrm{B}} - \frac{\tilde{\sigma}_{\mathrm{B}}^{2}}{4E_{00}}\right)\right\} - \frac{eLA^{*}\bar{c}_1}{(\bar{c}_1 k_{\mathrm{B}})^{2}} \exp\left\{-\bar{b}_1 - \bar{c}_1 E_{\mathrm{F}}\right\} \tag{A.30}$$

in which the parameters

$$\bar{b}_1 = b_1(\bar{E}_{\mathrm{B}}) \qquad \text{and} \qquad \bar{c}_1 = c_1(\bar{E}_{\mathrm{B}}) \tag{A.31}$$

were defined.

Eq. (A.20) contains two boundary conditions: (1) Potential fluctuations were neglected in the second summand. (2) Approximations are only valid for $E_{\mathrm{B}}/E_{\mathrm{F}} < 1/4$. Especially this second constraint might not be fulfilled. Fits assuming uniform barrier heights yield values of $E_{\mathrm{B}}/E_{\mathrm{F}} \approx 0.1 - 0.45$. In conclusion, the two boundary conditions reduce the applicability of the model strongly. This drawback overcompensates the possibly better physical description of grain boundaries.

B. Publications

Journal Articles

N. Sommer, S. Götzendörfer, F. Köhler, M. Ziegner, and J. Hüpkes, *Influence of deposition conditions and substrate morphology on the electrical properties of sputtered ZnO:Al grown on texture-etched glass*, Thin Solid Films **568** (2014), 25-30

M. Meier, U.W. Paetzold, M. Ghosh, W. Zhang, T. Merdzhanova, G. Jost, N. Sommer, S. Michard, and A. Gordijn, *Fabrication of Light-Scattering Multiscale Textures by Nanoimprinting for the Application to Thin-Film Silicon Solar Cells*, IEEE Journal of Photovoltaics **4** (2014), 772-777

J. Hegmann, R. Jahn, S. Schönau, N. Sommer, and P. Löbmann, *SiO2–TiO2 scattering layers prepared by sol–gel processing for light management in thin film solar cells*, Journal of Sol-Gel Science and Technology (2015), 1-9

N. Sommer, M. Stanley, F. Köhler, J. Mock, and J. Hüpkes, *Role of the dopant aluminum for the growth of sputtered ZnO:Al investigated by means of a seed layer concept*, Journal of Applied Physics **118** (2015), 035301

N. Sommer, J. Hüpkes, and U. Rau, *Field emission at grain boundaries – Modeling the conductivity in highly doped polycrystalline semiconductors*, Physical Review Applied **5** (2016), 024009

N. Sommer, J. Hüpkes, N. Wilck, F. Lentz, and U. Rau, *ZnO:Al on rough substrates: From surface texture to conductivity prediction*, 42nd IEEE Photovoltaic Specialist Conference (PVSC), New Orleans, USA, (2015), 1-3.

C. Zhang, T. Merdzhanova, M. Meier, Nicolas Sommer and O. Astakhov, *Impact of transparent conductive oxide front side texture on the open-circuit voltage of a-Si:H solar cells*, physica status solidi (a), (2016)

Oral Presentations

N. Sommer, S. Götzendörfer, and J. Hüpkes, *Zinc oxide growth on textured substrates*, 8th International Symposium on Transparent Oxide and Related Materials for Electronics and Optics, Tokyo, Japan, May 13-15, 2013

N. Sommer, M. Stanley, J. Mock, F. Köhler, and J. Hüpkes, *Seed layer approach to reduce sputter temperature of lowly doped ZnO:Al*, 5th International Symposium on Transparent Conductive Materials, Crete, Greece, October 12-17, 2014

N. Sommer, J. Hüpkes, and U. Rau, *Modeling the conductivity of highly doped, polycrystalline semiconductors*, European Materials Research Society – Spring Meeting 2015, Lille, France, May 11-15, 2015

Poster Presentations

N. Sommer, S. Götzendörfer, J. Hüpkes, *Double texture obtained by etching of ZnO:Al on textured glass*, European PV Solar Energy Conference and Exhibition, Paris, France, September 30 - October 4, 2013

N. Sommer, J. Hüpkes, N. Wilck, F. Lentz, and U. Rau, *ZnO:Al for thin-film solar cell application: Optimization and prediction of conductivity on textured substrates*, 42nd IEEE Photovoltaic Specialists Conference, New Orleans, USA, June 14-19, 2015

Danksagung

Viele Personen haben zum Gelingen dieser Arbeit beigetragen. Ihnen zu danken, soll der Zweck der folgenden Seiten sein:

- Mein besonderer Dank gilt meinem Betreuer, intellektuellem Sparringspartner, nimmermüdem Korrekturleser und kritischem Begleiter in allen Wissenschaftslagen Herrn Dr. Jürgen Hüpkes. Seine Tür war immer offen, um jedes Projekt, jedes Problem, jedes Ergebnis mit Akribie und Begeisterung zu diskutieren und mir jederzeit mit Rat und Tat zur Seite zu stehen. Diese Doktorarbeit wäre in der vorliegenden Form ohne seine Ideen und seine konstruktive Kritik nicht möglich gewesen. Danke, Jürgen!

- Herrn Prof. Dr. Uwe Rau danke ich für die Möglichkeit, meine Doktorarbeit am Institut durchführen zu können. Ich bedanke mich für die intensiven Diskussionen, die kleinen und großen Ideen, die diese Arbeit besser gemacht haben, für seinen freundlichen und respektvollen Umgang mit den Mitarbeiter des Instituts, für sein ehrliches Interesse an der Situation der Doktoranden und für die Aufklärung darüber, wer Katsche Schwarzenbeck war.

- Bei Herrn Prof. Dr. Matthias Wuttig möchte ich mich für die freundliche Übernahme des Zweitgutachtens bedanken. Weiterhin danke ich für die wissenschaftlichen Diskussionen zum Tempern von ZnO:Al und für die Möglichkeit, mit den Doktoranden seines Instituts so intensiv zusammenarbeiten zu können.

- Der TCO-Gruppe danke ich für die Unterstützung und Hilfsbereitschaft bei allen wissenschaftlichen und technischen Themen, bei Problemen und Problemchen und bei der Glühweinvernichtung. Mein Dank für das nette und angenehme Arbeitsklima geht an Dr. Gabrielle Jost, Alain Doumit, Hildegard Siekmann, Ulrike Gerhards, Dr. Sascha Pust, Mishael Stanley, Oleg Tremmel, Dr. Marek Warzecha, Brigitte Zwaygardt, Dr. Jorj Owen, Dr. Wendi Zhang, Alexander Hamri, David Wippler und Juraj Hotovy.

- Meinen Doktorandenkollegen André Hoffmann (Büro 24!), Bugra Turan, Stephan Michard, Chao Zhang, Jan-Philipp Becker und Tobias Knüttel danke ich für unzählige wissenschaftliche Diskussionen, gegenseitige Unterstützung in allen

Belangen und die beste Mittagessengruppe, wo gibt. Ihr seid mir gute Freunde geworden.

- Allen Partner im Verbundprojekt LIST möchte ich für die hervorragende und konstruktive Zusammenarbeit danken: Dr. Florian Ruske, Dr. Stefan Götzendörfer, Steffi Schönau, Daniel Dorow-Gerspach, Jan Hegmann, Roland Sittner, Dr. Volker Sittinger, Prof. Dr. Peer Löbmann, Patrick Ries, Dr. Wilma Dewald und Alexandra Yatim. In diesem Zusammenhang geht mein Dank insbesondere auch an das Bundeswirtschaftsministerium für die finanzielle Unterstützung dieser Arbeit.

- Ein großer Dank geht an alle Kolleginnen und Kollegen, die durch die Betreuung der vielfältigen Mess- und Depositionsanlagen, durch Hilfe bei der Interpretation der Messergebnisse oder durch die Unterstützung bei organisatorischen Angelegenheiten zum Gelingen dieser Arbeit beigetragen haben. Zu Dank verpflichtet bin ich Dr. Florian Köhler, Dr. Tsvetelina Merdzhanova, Dr. Matthias Meier, Noel Wilck, Dr. Bart Pieters, Dr. K.Bittkau, Oliver Thimm, Thomas Fink, Mirko Ziegner, Dr. Florian Lentz, Dr. Ulrich Paetzold, Hans-Peter Bochem, Dr. Elmar Neumann, Markus Hülsbeck, Andrea Mülheims, Petra Lorbach, Daniel Weigand, Joachim Kirchhoff, Wilfried Reetz, Christoph Zahren, Sabine Kasper, Gunnar Schöpe, Andreas Bauer, Dr. Torsten Bronger, Josef Klomfaß, Sandra Tillmanns, Dr. Michael Ghosh, Andreas Schmalen, Johannes Wolff, Andreas Mück, Pascal Foucart und all jenen, die ich vergessen habe. Speziell danken möchte ich Wolfgang Appenzeller, der die kurz vor dem Ableben begriffene Ami-Sputteranlage gerettet und zu neuer Blüte geführt hat. Außerdem geht mein Dank an meine HITEC-Mentoren Dr. Paul Konopka und Dr. Bradley Tinkham sowie an Dr. Bärbel Köster stellvertretend für die HITEC-Graduiertenschule, die ein sehr bereicherndes Element meiner Promotionszeit war.

- Ein besonderer Dank geht an meine Freundin Wiebke. Ohne Dich wäre Alles Nichts!

- Danke an meine Mutter, meine Schwester und Hagü, auf deren Unterstützung ich immer bauen kann.

Schriften des Forschungszentrums Jülich
Reihe Energie & Umwelt / Energy & Environment

Band / Volume 316
Oxidation Mechanisms of Metallic Carrier Materials for Gas Separation Membranes
M. Schiek (2016), 148 pp
ISBN: 978-3-95806-138-5

Band / Volume 317
Thermoschockverhalten und temperaturabhängige Eigenschaften kohlenstoffarmer und -freier Feuerfestwerkstoffe
A. Böhm (2016), VI, 153 pp
ISBN: 978-3-95806-139-2

Band / Volume 318
Theoretical and experimental studies of runaway electrons in the TEXTOR tokamak
S.S. Abdullaev, K.H. Finken, K. Wongrach, O. Willi (2016), X, 109 pp
ISBN: 978-3-95806-140-8

Band / Volume 319
Modelling Thermodynamic Properties of Intercalation Compounds for Lithium Ion Batteries
S. O. Dang (2016), x, 133 pp
ISBN: 978-3-95806-141-5

Band / Volume 320
Atmospheric Mixing in a Lagrangian Framework
M. Tao (2016), 146 pp
ISBN: 978-3-95806-142-2

Band / Volume 321
Statistical analysis and combination of active and passive microwave remote sensing methods for soil moisture retrieval
K. Rötzer (2016), XIV, 112 pp
ISBN: 978-3-95806-143-9

Band / Volume 322
Langzeitstabilität der Polymerelektrolyt-Wasserelektrolyse bei reduziertem Iridiumgehalt
C. G. Rakousky (2016), VII, 199 pp
ISBN: 978-3-95806-147-7

Band / Volume 323
Light induced water splitting using multijunction thin film silicon solar cells
F. Urbain (2016), xi, 173, XLVI pp
ISBN: 978-3-95806-148-4

Schriften des Forschungszentrums Jülich
Reihe Energie & Umwelt / Energy & Environment

Band / Volume 324
Properties of convective gravity waves derived by combining global modeling and satellite observations
Q. T. Trinh (2016), 140 pp
ISBN: 978-3-95806-150-7

Band / Volume 325
Feasible and Reliable Ab initio Atomistic Modeling for Nuclear Waste Management
G. Beridze (2016), xix, 128 pp
ISBN: 978-3-95806-151-4

Band / Volume 326
Sauerstoffspeicher für die oxidkeramische Batterie: Herstellung, Charakterisierung und Betriebsverhalten
C. M. Berger (2016), XV, 128 pp
ISBN: 978-3-95806-154-5

Band / Volume 327
Institute of Energy and Climate Research IEK-6: Nuclear Waste Management Report 2013 / 2014
Material Science for Nuclear Waste Management
S. Neumeier, M. Klinkenberg, D. Bosbach (Eds.)
(2016), 219 pp
ISBN: 978-3-95806-155-2

Band / Volume 328
Conductivity and Structure of Sputtered ZnO:Al on Flat and Textured Substrates for Thin-Film Solar Cells
N. Sommer (2016), vii, 195, XIV
ISBN: 978-3-95806-156-9

Weitere ***Schriften des Verlags im Forschungszentrum Jülich*** unter
http://wwwzb1.fz-juelich.de/verlagextern1/index.asp

Energie & Umwelt
Energy & Environment

328

Conductivity and Structure of Sputtered ZnO

Nicolas Sommer

Member of the Helmholtz Association

Conductivity and Structure of Sputtered ZnO:Al on Flat and Textured Substrates for Thin-Film Solar Cells

Nicolas Sommer

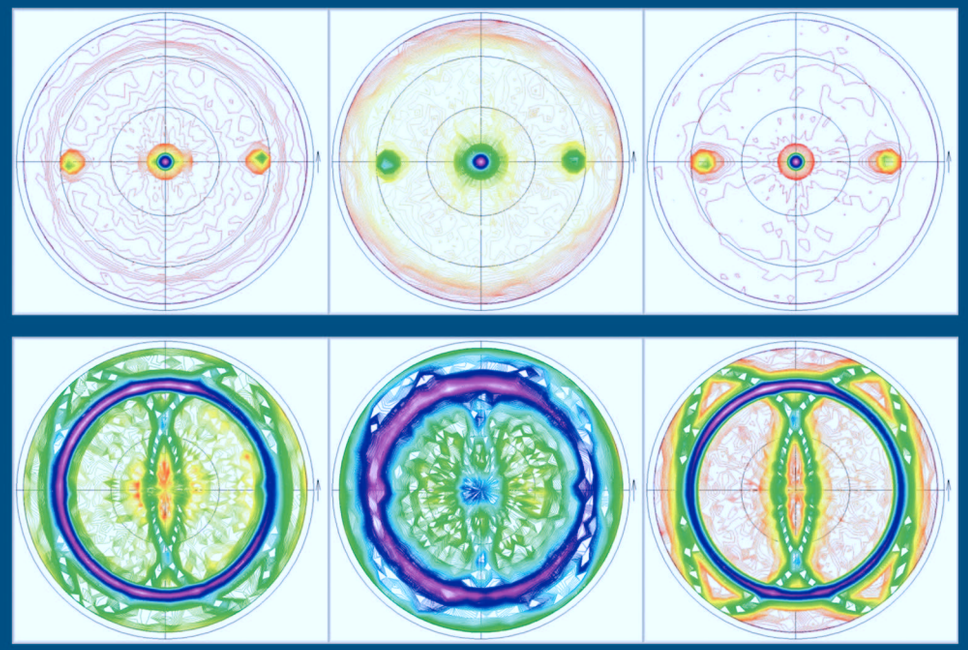

Energie & Umwelt / Energy & Environment
Band / Volume 328
ISBN 978-3-95806-156-9

JÜLICH
FORSCHUNGSZENTRUM

Energie & Umwelt / Energy & Environment
Band / Volume 328
ISBN 978-3-95806-156-9

JÜLICH
FORSCHUNGSZENTRUM